Enhancing multi-scale cardiac simulations by coupling electrophysiology and mechanics

A flexible high performance approach to cardiac electromechanics

Doctoral Dissertation submitted to the
Faculty of Informatics of the Università della Svizzera Italiana
in partial fulfillment of the requirements for the degree of
Doctor of Philosophy

presented by
Sonia Pozzi

under the supervision of
Prof. Rolf Krause

December 2018

Dissertation Committee

Prof. Rolf Krause	Università della Svizzera italiana, Switzerland
Prof. Limongelli Vittorio	Università della Svizzera italiana, Switzerland
Prof. Igor Pivkin	Università della Svizzera italiana, Switzerland
Prof. Luca F. Pavarino	Dept. of Mathematics, University of Pavia, Italy
Prof. Gernot Plank	Medizinische Universität Graz, Austria

Dissertation accepted on 15 December 2018

Research Advisor	PhD Program Director
Prof. Rolf Krause	**Prof. Walter Binder, Prof. Olaf Schenk**

I certify that except where due acknowledgement has been given, the work presented in this thesis is that of the author alone; the work has not been submitted previously, in whole or in part, to qualify for any other academic award; and the content of the thesis is the result of work which has been carried out since the official commencement date of the approved research program.

Sonia Pozzi
Lugano, 15 December 2018

$$\frac{4}{3}\pi r^3$$

Abstract

This work focuses on the development of computational methods for the simulation of the propagation of the electrical potential in the heart and of the resulting mechanical contraction. The interaction of these two physical phenomena is described by an electromechanical model which consists of the monodomain system, which describes the propagation of the action potential in the cardiac tissue, and the equations of incompressible elasticity, which describe its mechanical response. In fully-coupled electromechanical simulations, two main computational challenges are usually identified in literature: the time integration of the monodomain system and the efficient solution of the equations of incompressible elasticity. These two are the actual bottlenecks in the realization of accurate and efficient fully-coupled electromechanical simulations.

The first computational challenge arises from the discretization in time of the equations that describe the electrical activation of cardiac tissue. The monodomain system should be discretized employing both fine spatial grids and small time-steps, to capture the spatial steep gradients typical of the action potential and the behavior of the stiff gating variables, respectively. To obtain an accurate and computationally-cheap numerical solution, we propose a novel method based on coupling high-order backward differentiation formulae with high-order exponential time stepping schemes for the time integration of the monodomain system. We propose a novel quasi-Newton approach for the implicit discretization of the monodomain equation. We also compare this latter approach against a complex step differentiation-based approach.

As a result, we show by means of numerical tests the accuracy of the developed strategies and how the use of high-order time integration schemes affects the simulation of post-processed quantities of clinical relevance such as the conduction velocity.

The second computational challenge is due to the structure the discretization of the equations of incompressible elasticity. Due to the incompressibility constraint, the arising linear system has a saddle point structure for which standard solution methods such as multigrid or domain decomposition do not provide optimal convergence if not properly adapted. In order to overcome this problematic, we propose a segregated multigrid preconditioned solution method. The segregated approach allows to recast the saddle-point problem into two elliptic problems for which multigrid methods are shown to provide optimal convergence.

The electromechanical model is employed to evaluate the effects of geometrical changes due to the contraction of the heart on simulated electrocardiograms. Finally, the effect of different electrical activations on the resulting pressure-volume loops is investigated by coupling the electromechanical model with a lumped model of the circulatory system.

Acknowledgements

Foremost, I would like to thank my advisor Prof. Rolf Krause for the support and his encouragement over the last years. His patient supervision and guidance have been fundamental in this growth. The possibility to present my work at various international conferences was greatly appreciated. I am also grateful to my co-advisor, Dr. Marco Favino, for his teaching and valuable suggestions. I want to thank Prof. Angelo Auricchio and Prof. Frits Prinzen for their time and for the constant discussions. I also want to express my gratitude to the other members of my dissertation committee, Prof. Vittorio Limongelli, Prof. Igor Pivkin, Prof. Luca F. Pavarino, and Prof. Gernot Plank for their time and interest. I am grateful to my fellow colleagues of the Institute of Computational Science and of the Center for Computational Medicine in Cardiology for their help and suggestions and for the friendly working atmosphere.

Voglio ringraziare la mia famiglia, Flavio e gli amici per il supporto continuo e per tutti i modi in cui mi rendono felice, giornalmente.

I gratefully acknowledge the financial support by the Theo Rossi di Montelera Foundation, the Metis Foundation Sergio Mantegazza, the Fidinam Foundation, and the Horten Foundation. This work was also supported by the Swiss National Science Foundation, project 205321_149828 “A Flexible High Performance Approach to Cardiac Electromechanics".

Contents

Figures

Tables

List of Algorithms

Introduction and motivation

Electromechanical models of the whole heart have been extensively used to investigate heart failure, including arrhythmia and ischemia, and ventricular pacing. The simulation of the heartbeat is one of the "Grand Challenges" in computational science, in that it requires the analysis of various coupled single-physics fields. The modeling of the mechanical and of the electrophysiological behavior of the tissue is an essential tool to describe the leading mechanisms underlying every single heartbeat. The *multiscale* nature of the problem represents the prominent hurdle in coupled electromechanical simulations. From the mechanical point of view, the cardiac muscle behaves as an hyperelastic, incompressible, orthotropic material and its functionalities occur at the macroscale level. The propagation of the electrical signal throughout the cardiac tissue is described through the bidomain model (or its reduced forms). Ionic models describe, through the representation of the behavior of the gating variables, the interaction of the ionic channels responsible of the electrical activation of the cells. Cardiac electrophysiology involves functionalities occurring at the microscales. A fine spatial grid is required to capture the gradient of the action potential and a fine temporal grid is required to capture the behavior of the gating variables. This peculiarity implies an high number of degrees of freedom involved in simulations and the need of an high-performance scalable setup.

This thesis is concerned with *fully coupled electromechanical models of cardiac behavior*. We exploited solution methods constructed *ad hoc* for single-physics problems. The aim of this work was to *design novel segregated solution techniques* for the electromechanical coupled model. *Appropriate solution strategies* for the underlying *electrophysiological* and *mechanical* problems were proposed and investigated.

We proposed novel *high-order* numerical schemes for the time integration of the equations that describe cardiac electrophysiology. Starting from exponential integrators theory, we generalized the Rush-Larsen approach presenting high-order exponential time differencing and integrating factor schemes for the time integration of the gating variables. These exponential schemes were coupled to implicit-explicit and backward differentiation formula for the solution of the monodomain equation. Considering high-order backward differentiation formulae, we introduced of a novel quasi-Newton approach for the solution of the algebraic problem arising from the implicit discretization of the monodomain equation. As an alternative, we proposed the evaluation of the complex dependence of the ionic currents on the action potential considering the complex step derivative approximation. We showed how accurate methodologies for the numerical integration of cardiac electrophysiology represents a key point for accurate and low-cost simulations of the propagation of the electrical signal in the cardiac tissue.

We presented an efficient *segregated multigrid preconditioned strategy* for the solution of the system of equations describing incompressible nonlinear elasticity for anisotropic materials with an additional active stress component. The elasticity operator in the tangent problem is not positive definite and may exhibit a non-trivial kernel. This prevents a straight-forward application of segregated solution methods for saddle point problems, which are usually based on the Schur complement of the system. In order to overcome the hurdle associated to the elasticity operator, we considered a linear and a nonlinear augmenting strategies, which ensure that the elasticity operator is invertible. In a mixed finite element framework, the system is written as a generalized nonlinear saddle point problem and solved by means of Newton's method. For the solution of the Schur complement system, we employed a strategy based on a *two multigrid of V-cycle type*: one for a mass matrix, preconditioner of the Schur complement matrix, and one for the elasticity operator. Numerical results showed the convergence rate of the proposed strategy to be independent of the grid size.

Various electromechanical coupling strategies were introduced, implemented, and compared in terms of the outcome of numerical simulations. Numerical experiments are presented to assess the performance of the proposed strategies. To study the impact of the mechanical deformation on the *morphology of the simulated electrocardiograms*, different coupling strategies were compared. The numerical experiments showed an impact of mechanics on the T-wave and, under specific circumstances, on the QRS complex as well. To study the impact of synchronous and asynchronous electrical activation of the tissue on simulated pseudo-ECGs, a finite element model of cardiac electromechanics was additionally coupled to a lumped model of circulation.

The collaboration with the *Cardio Centro Ticino* (CCT) inside the *Center for Computational Medicine in Cardiology* (CCMC) at the Institute of Computational Science (ICS) gave us the opportunity to discuss the outcomes of numerical simulations with the medical community. Moreover, this collaboration provided a cardiac anatomy represented with high geometric fidelity electromechanical parameters involved.

These models and strategies were implemented inside the novel framework HART, developed at CCMC/ICS. HART is based on the open source general purpose C++ finite element framework *MOOSE*, Multiphysics Object Oriented Simulation Environment. Mainly developed at Idaho National Lab, where the author has worked for three months, MOOSE is specifically designed to simplify development of multi-physics tools. Making use of the very modular formulation of MOOSE, HART is easily extendible to incorporate additional mechanical material laws and cell membrane models. The code relies on the widely used and well developed solver library PETSc. To perform coupled electromechanical simulation of interest required the transfer of discrete fields such as stresses, pressure, displacement and action potential. For this purpose, the Multipurpose Object Oriented Numerics Library *MOONOLITH* is integrated into the HART suite. We present and discuss scaling benchmark problems for the coupled problem on both a Linux cluster and a state-of-the-art Cray supercomputer.

Chapter 1

Governing equations in electromechanics

1.1 Mathematical modeling of passive mechanics

The human heart is a muscle which main function is to pump the blood throughout the body. During the last decades, many efforts have been done in order to model the cardiac activity. The heart has been described as a mechanical pump for the first time in 1628 by William Harvey. The heart consists of four chambers, namely the *left atrium* (LA) and *right atrium* (RA) and the *left ventricle* (LV) and *right ventricle* (RV). The periodic contractions, generated by biochemical processes, determine the so called *heartbeat*. Each heartbeat lasts approximately 800 ms. Two distinct phases regulate each chamber during the cardiac cycle: the *systole* (contraction phase), and the *diastole* (dilatation phase). During the different phases of the cardiac cycle, the four chambers undergo different workloads. After the ejection of the blood from the ventricles, the aortic and pulmonic valves close. This closure represents the beginning of the diastolic phase, which lasts approximately 400 ms. A steep drop of blood pressure of about 80 to 100 mmHg occurs in conjunction with an isovolumetric relaxation. The volume relaxation is due to the deactivation of the myofibrils of the myocytes. The mitral and tricuspid valves open when atrial pressures are higher than ventricular ones. This results in a rapid blood flows into the ventricles. In this filling phase no mechanical activation is involved. The last point of the filling stage is just before the mitral and tricuspid valves closure. At this point the ventricles reaches their maximum volumes, also called *end-diastolic volumes*, and the *systolic phase* starts. During systole the left and right ventricles contract and eject blood into the aorta and the pulmonary artery, respectively. In this phase an external work is performed by the muscle. Atrioventricular valves close and therefore no blood is entering in the ventricles. However, the atria are filled though the vena cavae and pulmonary veins. The closure of the aortic and pulmonic valves indicate the beginning of a new cardiac cycle. The heart wall is composed by three layers which are namely the *endocardium* (inner layer), the *myocardium* (middle layer) and the *epicardium* (outmost layer). The heart wall not only exhibits different thickness along the apicobasal direction (being thinnest at the apex and thickest at base), but the wall thickness changes also according to the different (in space and time) workloads that the tissues have to sustain. From a mechanical point of view, the myocardial fiber architecture plays a crucial role (quantitatively investigated in e.g. [LeGrice

et al., 1997, 2001b]). LeGrice and co-workers have shown that myocardial fibers are oriented and arranged into laminar sheets. Transmural specimen of the left and of the right ventricles, traversed from the outer side to the inner side, contain fibers that rotate approximately from $\pi/3$ to $-\pi/3$ and from $\pi/4$ to $-\pi/4$, respectively. Recent histological studies of the myocardium show that the fibers are organized into laminar sheets. Each sheet is composed by an ensemble of cells tightly bounded together by endomysial collagen [LeGrice et al., 1995; Gilbert et al., 2007]. Through the myocardium the orientation of these sheets varies, but this effect is negligible if compared with the change of the fibers orientation; therefore in this work we consider the normal direction of the sheets parallel to the longitudinal direction of the ventricles. In the last decades, several models for the passive mechanics of the ventricle have been proposed. The first proposed model was isotropic [Demiray, 1976]. To account for the microstructure of the myocardium, more realistic transversely isotropic models have been proposed [Chadwick, 1982; Humphrey et al., 1990; Taber, 1991; Guccione et al., 1995]. In more recent works the myocardium was considered to be an inhomogeneous orthotropic body [Hunter et al., 1997; Costa et al., 2001; Schmid et al., 2006]. Holzapfel and Ogden [Holzapfel and Ogden, 2009] summarized many of them. Moreover, they proposed a model in which the strain-energy is defined in terms of generalized invariants.

In the present section, we investigate the passive mechanical properties of cardiac tissue. We focus on continuum mechanics theory, which aim is the mathematical description of media as a continuous body. It is basically a review of classical framework of continuum mechanics. The Piola transformation and the equations related to the balance principles are deduced. The two main approaches to incompressibility in cardiac mechanics, the Lagrange multiplier method and the penalty method, are presented. Moreover we introduce the Guccione-Costa and the Holzapfel-Odgen constitutive models of cardiac tissue.

1.1.1 Kinematics

This section deals with the kinematics of finite deformation, which is the study of motion and deformation without reference to their cause. Let $\mathscr{B}_r$ be an open set of $\mathbb{R}^3$ called body. The elements thereof are called particles. Considering a orthonormal basis $\{\mathbf{E}_i\}_{i=1}^3$, particles are labelled by the coordinates $\mathbf{X}$. These coordinates are known as *material coordinates*. We consider $\mathscr{B}_r$ to be the reference configuration, a fixed domain in space employed to define physical quantities in the course of motion. Following [Bonet, 2008], the current position of these particles (at time t) is described with respect to the same basis.
A *deformation* of $\mathscr{B}_r$ is a mapping χ

$$\chi : \mathbb{R}^3 \mapsto \mathbb{R}^3, \quad \mathbf{x} = \chi(\mathbf{X}). \tag{1.1}$$

Defined $\mathscr{T} = [t_0, t_{\text{fin}}]$, a *motion* $\mathscr{M}$, is a collection of time-dependent deformations

$$\mathscr{M} = \{\chi_t : \mathbf{x} = \chi(\mathbf{X}, t)\}_{t\in\mathscr{T}}. \tag{1.2}$$

For a fixed time, it represents a mapping between the undeformed and deformed body configuration. The image $\mathscr{B}_t$ of the reference configuration through the deformation χ_t is called deformed configuration at time t. The reference configuration is used in solid mechanics to reinterpret physical quantities usually defined in the current configuration of the body. We define the displacement vector $\mathbf{u}$ as

$$\mathbf{u}(\mathbf{X}, t) := \chi(\mathbf{X}, t) - \mathbf{X} = \mathbf{x} - \mathbf{X}. \tag{1.3}$$

Fig. 1.1 sketches the plot of the configuration and of the deformation. We refer to the gradient of the motion with respect to the material coordinates as deformation gradient and we denote it with $\mathbf{F}$. We have

$$\mathbf{F}(\mathbf{X},t) := \nabla\chi(\mathbf{X},t) = \mathbf{I} + \nabla\mathbf{u}(\mathbf{X},t). \tag{1.4}$$

We consider only tensors defined in the Euclidean space. Formally $\mathbf{F}$ is a two-point tensor with components

$$\mathbf{F}_{ij} = \frac{\partial\chi_i}{\partial\mathbf{X}_j}. \tag{1.5}$$

Its determinant $J(\mathbf{X},t) = \det F(\mathbf{X},t)$ is called deformation determinant. For $d = 3$, consider an infinitesimal rectilinear parallelepiped in $\mathscr{B}_r$ with edges $\{\,\mathrm{d}\mathbf{Y}_i\,\}_{i=1}^3$. The elemental volume defined by this vectors is

$$dV = (\mathrm{d}\mathbf{Y}_1 \times \mathrm{d}\mathbf{Y}_2)\cdot\mathrm{d}\mathbf{Y}_3. \tag{1.6}$$

In the current configuration, the volume of the parallelepiped is

$$dv = ((\mathbf{F}\mathrm{d}\mathbf{Y}_1)\times(\mathbf{F}\mathrm{d}\mathbf{Y}_2))\cdot(\mathbf{F}\mathrm{d}\mathbf{Y}_3) = J\,(\mathrm{d}\mathbf{Y}_1 \times \mathrm{d}\mathbf{Y}_2)\cdot\mathrm{d}\mathbf{Y}_3. \tag{1.7}$$

The substitution of Eq. (1.6) into Eq. (1.7) yields

$$dv = JdV. \tag{1.8}$$

Therefore J accounts for local volume changes between the reference and the current configuration. Local invertibility of $\boldsymbol{\chi}$ requires the Jacobian determinant to be non-zero. We define the *trajectory* as

$$\mathrm{T}_\chi := \{\,(\mathbf{x},t)\in\mathbb{R}^3\times\mathscr{T} \mid \mathbf{x} = \chi(\mathbf{X},t),\ \mathbf{X}\in\mathscr{B}_r,\ t\in\mathscr{T}\,\}. \tag{1.9}$$

If, for each t, the map χ is invertible, we define the inverse of motion

$$\mathbf{X} = \chi^{-1}(\mathbf{x},t), \tag{1.10}$$

which domain is T_χ. The following properties hold

$$\mathbf{x} = \chi(\chi^{-1}(\mathbf{x},t),t), \quad \text{and} \quad \mathbf{X} = \chi^{-1}(\chi(\mathbf{X},t),t). \tag{1.11}$$

Denoting by $\mathrm{Lin}(\mathbb{R}^3)$ the vector space of all linear transformation from $\mathbb{R}^3$ to $\mathbb{R}^3$, we define its the subset

$$\mathrm{Lin}^+(\mathbb{R}^3) = \{\,L\in\mathrm{Lin}(\mathbb{R}^3)\colon J>0\,\}. \tag{1.12}$$

A configuration $\mathbf{F}$ is said to be admissible if $\mathbf{F}\in\mathrm{Lin}^+(\mathbb{R}^3)$. Let $\partial\mathscr{B}_r$ be the boundary of $\mathscr{B}_r$, and two distinct subsets of it, namely Γ_D , on which Dirichlet boundary conditions are considered, and Γ_N, for the natural one. We require that the intersection of this two subset is an empty set and moreover that $\partial\mathscr{B}_r$ corresponds to the closure of the union of the two subsets.

Under the regularity assumption that χ is C^2 with respect to time, it is defined the material velocity

$$\dot{\mathbf{x}}(\mathbf{X},t) = \frac{\partial\chi(\mathbf{X},t)}{\partial t}, \tag{1.13}$$

and the material acceleration as

$$\ddot{\mathbf{x}}(\mathbf{X},t) = \frac{\partial^2\chi(\mathbf{X},t)}{\partial t^2}. \tag{1.14}$$

Composing the material velocity and acceleration with the inverse motion we define the spatial velocity and acceleration as

$$\mathbf{v}(\mathbf{x},t) := \dot{\mathbf{x}}(\pi(\mathbf{x},t),t), \tag{1.15}$$

and the material acceleration as

$$\mathbf{a}(\mathbf{x},t) := \ddot{\mathbf{x}}(\pi(\mathbf{x},t),t). \tag{1.16}$$

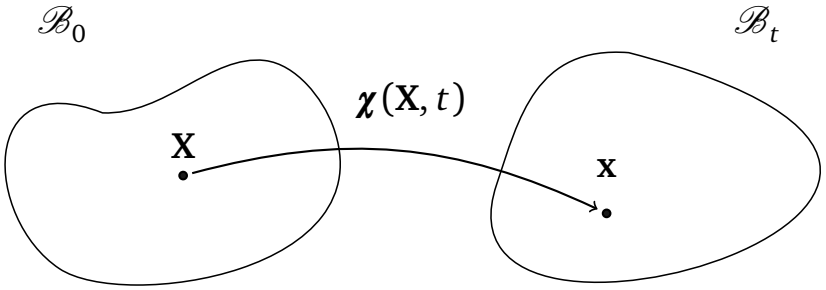

Figure 1.1. Deformation map between reference and current configurations using coordinates.

1.1.2 Material and spatial description

In finite deformation analysis an important distinction has to be made in the description of fields and quantities of interest. A *material description* refers to the behavior of a material particle. In this case the quantity of interest is described with respect to the initial coordinate $\mathbf{X}$ obtained at time $t = t_0$. Formally, a *material field* is a tensorial function defined as

$$\mathscr{B}_r \times \mathscr{T} \ni (\mathbf{X},t) \to \Upsilon(\mathbf{X},t), \tag{1.17}$$

where Υ is a tensor of Lin_n for $n \in \mathbb{N}$. Materials fields are also referred to as *Lagrangian fields*. A *spatial description* refers to the behavior of a spatial position. In this case the description is performed in terms of the coordinate $\mathbf{x}$, obtained during the deformation. A *spatial field* is a tensorial function defined as

$$\mathscr{T}_\chi \ni (\mathbf{x},t) \to \Psi(\mathbf{x},t), \tag{1.18}$$

where Ψ is a tensor. To obtain a material description, we can compose its spatial field Ψ with the motion as follows

$$\Psi_m(\mathbf{X},t) = \Psi(\chi(\mathbf{X},t),t). \tag{1.19}$$

Vice versa, to obtain a spatial description, we compose its material field Υ with the inverse of the motion as follows

$$\Upsilon_s(\mathbf{x},t) = \Upsilon(\chi^{-1}(\mathbf{x},t),t). \tag{1.20}$$

With respect to the material coordinates we define the operators

$$\nabla\Upsilon = D_{\mathbf{X}}\Upsilon \quad \text{and} \quad \operatorname{Div}\Upsilon = \operatorname{tr}(\nabla\Upsilon), \tag{1.21}$$

while with respect to the spatial ones we define

$$\operatorname{grad}\Psi = D_{\mathbf{x}}\Psi \quad \text{and} \quad \operatorname{div}\Psi = \operatorname{tr}(\operatorname{grad}\Psi). \tag{1.22}$$

Here we are supposing the order of the tensors to be greater than or equal to 1. We define the convective derivative D_t of a spatial field Ψ to be

$$D_t\Psi = \left(\frac{d}{dt}\Psi_m\right)_s. \tag{1.23}$$

1.1.3 Piola transformation

Piola transformations allow to map balance laws written considering spatial coordinates to balance laws written using material coordinates. Let $\mathscr{P}$ denotes a subset of the reference configuration $\mathscr{B}_r$ and $\mathscr{P}_t = \boldsymbol{\chi}(\mathscr{P}, t)$ be its image at time t through the motion. Hereafter we describe the Piola transformations of gradient of scalar and vector functions and of the divergence of vector and tensor functions. Let ϕ be a spatial scalar field. The integral of its gradient can be written in material coordinates as

$$\int_{\mathscr{P}_t} \nabla\phi \,\mathrm{d}\mathbf{x} = \int_{\mathscr{P}} (\nabla\phi)_m J \,\mathrm{d}\mathbf{X}. \tag{1.24}$$

Applying the chain rule to the right hand side of Eq. (1.24), we get

$$\int_{\mathscr{P}_t} \nabla\phi \,\mathrm{d}\mathbf{x} = \int_{\mathscr{P}} \mathbf{F}^{-T}\nabla\phi_m J \,\mathrm{d}\mathbf{X}. \tag{1.25}$$

Let $\boldsymbol{\psi} \in \mathrm{Lin}_1$ be a spatial vector field. Exploiting Eq. (1.25), we obtain

$$\int_{\mathscr{P}_t} \nabla\boldsymbol{\psi} \,\mathrm{d}\mathbf{x} = \int_{\mathscr{P}} \nabla\boldsymbol{\psi}_m \mathbf{F}^{-1} J \,\mathrm{d}\mathbf{X}. \tag{1.26}$$

The transformation of the divergence of $\boldsymbol{\psi}$ can derived using the Piola identity $\mathrm{Div}(J\mathbf{F}^{-T}) = \mathbf{0}$ [Marsden and Hughes, 1994b] and the fact that

$$\mathrm{div}\,\boldsymbol{\psi} = \mathrm{tr}\,(\nabla\boldsymbol{\psi}). \tag{1.27}$$

We obtain the Piola transformation

$$(\mathrm{div}\,\boldsymbol{\phi})_m J = \mathrm{Div}(J\mathbf{F}^{-1}\boldsymbol{\phi}_m). \tag{1.28}$$

Let us now consider the divergence of $\mathbf{T} \in \mathrm{Lin}_2$. Exploiting Eq. (1.28), we obtain

$$(\mathrm{div}\,\mathbf{T})_m J = \mathrm{Div}(J\mathbf{T}_m\mathbf{F}^{-T}). \tag{1.29}$$

1.1.4 Balance principles

Balance of mass

We consider a density function to compute the mass of a body. Let $\rho_r(\mathbf{X}, t)$ indicate the mass density in material coordinates and $\rho(\mathbf{x}, t)$ indicate the same quantity in spatial coordinates. Conservation of mass reads

$$\int_{\mathscr{P}} \rho_r \,\mathrm{d}\mathbf{X} = \int_{\mathscr{P}_t} \rho \,\mathrm{d}\mathbf{x}. \tag{1.30}$$

Changing the variable of integration in the right hand side of Eq. (1.30), we obtain

$$\int_{\mathscr{P}} \rho_r \mathrm{d}\mathbf{X} = \int_{\mathscr{P}} \rho_m J \mathrm{d}\mathbf{X}. \tag{1.31}$$

The arbitrariness of $\mathscr{P}$ allows to convert the integral relation (1.31) into the pointwise equality

$$\rho_r(\mathbf{X}, t) = \rho_m(\mathbf{X}, t) J(\mathbf{X}, t), \tag{1.32}$$

which represents the Piola transformation of a scalar field. The density ρ obeys the mass conservation law which states that the mass of each subpart $\mathscr{P}_t \subset \mathscr{B}_t$ is constant during the motion. This is expressed as

$$\frac{\mathrm{d}}{\mathrm{d}t} \int_{\mathscr{P}_t} \rho \mathrm{d}\mathbf{x} = 0. \tag{1.33}$$

The independence of the integral (1.33) on time can be obtained writing the integral in material coordinates. Exploiting again the arbitrariness of $\mathscr{P}$, we obtain

$$\frac{\mathrm{d}}{\mathrm{d}t}(\rho_m J) = 0. \tag{1.34}$$

From Eq. (1.32) and Eq. (1.34) we obtain that density in material coordinates cannot be time depend. Time derivative (1.34) can be computed exploiting Eq. (1.23) as

$$(\rho')_m J + (\operatorname{grad} \rho)_m \mathbf{x} J + \rho_m \dot{J} = 0. \tag{1.35}$$

Balance of linear and angular momentum

Momentum balance principle are essential postulates in continuum mechanics. Balance of linear and angular momentum are assumed to hold each subpart $\mathscr{P}_t$ of the body. We define the total *linear momentum* $\mathbf{L}$ as

$$\mathbf{L}(t) = \int_{\mathscr{P}_t} \rho \mathbf{v} \mathrm{d}\mathbf{x}. \tag{1.36}$$

We define the total *angular momentum* $\mathbf{J}$ as

$$\mathbf{J}(t) = \int_{\mathscr{P}_t} \mathbf{x} \times \rho \mathbf{v} \mathrm{d}\mathbf{x}. \tag{1.37}$$

Sometimes in the literature $\mathbf{L}$ and $\mathbf{J}$ are also referred-to as *translational momentum* and *rotational momentum*, respectively. Let $\mathbf{b} = \mathbf{b}(\mathbf{x}, t)$ be a spatial vector field called the *body force*. It represent the contribution of external volumetric forces. The conservation of linear momentum reads

$$\dot{\mathbf{L}}(t) = \frac{\mathrm{d}}{\mathrm{d}t} \int_{\mathscr{P}_t} \rho \mathbf{v} \mathrm{d}\mathbf{x} = \int_{\partial \mathscr{P}_t} \mathbf{t}(\mathbf{x}, t, \mathbf{n}) \mathrm{d}\mathbf{a} + \int_{\mathscr{P}_t} \mathbf{b} \mathrm{d}\mathbf{x}, \tag{1.38}$$

i.e. the rate of change of the linear momentum of $\mathscr{P}_t$ equals the force acting on it. The existence of the *Cauchy* traction vector $\mathbf{t} = \mathbf{t}(\mathbf{x}, t, \mathbf{n})$ is postulated [Marsden and Hughes, 1994a]. It represents the force per unit current surface area of $\partial \mathscr{P}_t$. Here $\mathbf{n}$ is the outward normal to an infinitesimal surface element of $\partial \mathscr{P}_t$. As proved by Cauchy, the dependence of $\mathbf{t}$ on $\mathbf{n}$ is linear,

i.e. we can write $\mathbf{t}(\mathbf{x},t,\mathbf{n}) = \boldsymbol{\sigma}(\mathbf{x},t)\mathbf{n}$. Here $\boldsymbol{\sigma}$ is a second-order tensor called *Cauchy stress tensor*. The existence and uniqueness of this tensor is given by the Cauchy's fundamental theorem, also called Cauchy stress theorem We apply the divergence theorem to the right hand side of Eq. (1.38) to obtain

$$\int_{\partial \mathscr{P}_t} \sigma \mathbf{n}\, \mathrm{d}\mathbf{a} = \int_{\mathscr{P}_t} \operatorname{div} \boldsymbol{\sigma}\, \mathrm{d}\mathbf{x}. \tag{1.39}$$

Exploiting the time-independence of ρ_r, the time derivative in(1.38) can be written as

$$\frac{\mathrm{d}}{\mathrm{d}t}\int_{\mathscr{P}_t} \rho \mathbf{v}\mathrm{d}\mathbf{x} = \int_{\mathscr{P}_t} \rho \mathbf{a}\mathrm{d}\mathbf{x}. \tag{1.40}$$

Eq. (1.38) can be reformulated using the divergence theorem (1.39) and the formulae (1.40). Hence, we deduce the *Cauchy' first equation of motion* in local form, i.e.

$$\rho \mathbf{a} = \operatorname{div} \boldsymbol{\sigma} + \mathbf{b}, \tag{1.41}$$

for each $\mathbf{x}$ and for all times t. Assuming $\rho\mathbf{a} \ll \operatorname{div}\boldsymbol{\sigma} + \mathbf{b}$, Eq. (1.41) becomes

$$\operatorname{div} \boldsymbol{\sigma} + \mathbf{b} = \mathbf{0}, \tag{1.42}$$

which is referred to as *Cauchy's equation of equilibrium*. The conservation of angular momentum reduces to $\boldsymbol{\sigma} = \boldsymbol{\sigma}^T$. This result is often referred to as *Cauchy's second equation of motion*.

Balance of momentum in material coordinates

The *first Piola-Kirchhoff* (or nominal) stress tensor is defined as

$$\mathbf{P}(\mathbf{X},t) = J(\mathbf{X},t)\,\boldsymbol{\sigma}(\boldsymbol{\chi}(X,t),t)\mathbf{F}^{-T}(\mathbf{X},t)$$

The tensor $\mathbf{P}$ relates an area in the reference configuration to the corresponding force in the current configuration and so it is typically interpreted as the current force for unit of deformed area. In material coordinates, we define the passive symmetric *second Piola- Kirchhoff stress tensor* as

$$\mathbf{S}(\mathbf{X},t) = \mathbf{F}^{-1}(\mathbf{X},t)\mathbf{P}(\mathbf{X},t). \tag{1.43}$$

Let $\mathbf{b} = \mathbf{b}(\mathbf{x},t)$ denote a spatial vector field called the *body force*. It represents an external bulk force per unit volume. We introduce $\mathbf{B} = \mathbf{B}(\mathbf{X},t)$, the reference body force expressed in local form as $\mathbf{B}(\mathbf{X},t) = J(\mathbf{X},t)\mathbf{b}(\mathbf{x},t)$. Conservation of linear momentum for an elastic body reads

$$-\operatorname{Div}\mathbf{P}(\mathbf{X},t) + \mathbf{B}(\mathbf{X},t) = \rho_r \frac{\partial^2 \chi(\mathbf{X},t)}{\partial t^2}(\mathbf{X},t), \tag{1.44}$$

where ρ_r is the mass density in the reference configuration. In [Tallarida et al., 1970] it is shown that the inertial terms represents negligible contributions in the linear momentum. For this reason a quasi-static approximation is considered. This approach leads to

$$-\operatorname{Div}\mathbf{P}(\mathbf{X},t) + \mathbf{B}(\mathbf{X},t) = 0. \tag{1.45}$$

We define the left Cauchy-Green deformation tensor and the Green-Lagrange strain tensor as

$$\mathbf{C} := \mathbf{F}^T\mathbf{F} \quad \mathbf{E} := \frac{(\mathbf{C}-\mathbf{I})}{2}$$

, where $\mathbf{I}$ denotes the second-order unit tensor.

1.1.5 Incompressible materials

For incompressible material we assume the material density to be constant. This means that Eq. (1.34) in material coordinates reduces to the constraint equation $\dot{J} = 0$. Consistently with the literature we impose

$$J(\mathbf{X}, t) = 1. \tag{1.46}$$

For incompressible materials, the Cauchy stress tensor is usually written as

$$\boldsymbol{\sigma}_{\mathrm{p}} = \boldsymbol{\sigma}_{\mathrm{dev}} + p\mathbf{I}, \tag{1.47}$$

where $\boldsymbol{\sigma}_{\mathrm{dev}}$ is a deviatoric tensor and p is the pressure, which, as discussed in [Holzapfel, 2000], represents the workless reaction to the kinematic constraint on the deformation field. Eq. (1.47) represents the elastic response of the material to external loads. Since no active contraction is involved, this response is said to be passive. This is denoted in Eq. (1.47) by the subscript p. The first Piola-Kirchhoff tensor can hence be written as

$$\mathbf{P} = J\boldsymbol{\sigma}_{\mathrm{p}}\mathbf{F}^{-T} = \mathbf{P}_{\mathrm{dev}} + Jp\mathbf{F}^{-T}, \tag{1.48}$$

where $\mathbf{P}_{\mathrm{dev}}$ is the Piola transformation of $\boldsymbol{\sigma}_{\mathrm{dev}}$. We define $\mathbf{P}_{\mathrm{vol}} := Jp\mathbf{F}^{-T}$. For hyperelastic materials, we postulate the existence of an *Helmholtz free-energy function*

$$\Psi\colon \mathscr{B}_r \times \mathrm{Lin}^+ \to \mathbb{R}, \qquad \Psi = \Psi(\mathbf{F}), \tag{1.49}$$

such that

$$\mathbf{P} = \frac{\partial \Psi}{\partial \mathbf{F}}. \tag{1.50}$$

The fact that Ψ is a function of $\mathbf{C}$, is referred to as *objectivity* property of Ψ. In particular we consider *homogeneous materials*, i.e. materials in which the distributions of the internal constituents are assumed to be uniform on the continuum scale. For this particular class of ideal materials Ψ does not depend on the material point. We consider the following multiplicative split of the deformation gradient

$$\mathbf{F} = \mathbf{F}_{\mathrm{vol}} \cdot \mathbf{F}_{\mathrm{dev}}, \quad \text{where } \mathbf{F}_{\mathrm{vol}} = J^{1/3}\mathbf{I}, \text{ and } \mathbf{F}_{\mathrm{dev}} = J^{1/3}\mathbf{F}. \tag{1.51}$$

We define

$$\mathbf{C}_{\mathrm{dev}} := \mathbf{F}_{\mathrm{dev}}^T\mathbf{F}_{\mathrm{dev}} \quad \mathbf{E}_{\mathrm{dev}} := \frac{(\mathbf{C}_{\mathrm{dev}} - \mathbf{I})}{2}. \tag{1.52}$$

Any function of $\mathbf{F}_{\mathrm{dev}}$ alone is independent of the volumetric deformation since $\det(\mathbf{F}_{\mathrm{dev}}) = 1$. For incompressible hyperelastic materials, the energy is assumed not to depend on the on the third invariant J and hence on volumetric changes. For this reason, the energy is usually defined as $\bar{\Psi} = \bar{\Psi}(\mathbf{F}) := \Psi(\mathbf{F}_{\mathrm{dev}})$. The energy $\bar{\Psi}$ does not depend on the volumetric changes. We observe that

$$\frac{\partial \bar{\Psi}}{\partial \mathbf{F}} = \frac{\partial \bar{\Psi}}{\partial \bar{\mathbf{F}}}\frac{\partial \bar{\mathbf{F}}}{\partial \mathbf{F}} = J^{-1/3}\left(\frac{\partial \bar{\Psi}}{\partial \mathbf{F}_{\mathrm{dev}}} - \frac{1}{3}\left(\frac{\partial \bar{\Psi}}{\partial \mathbf{F}_{\mathrm{dev}}} : \mathbf{F}\right)\mathbf{F}^{-T}\right) = J^{-1/3}\left(\mathbf{P} - \frac{1}{3}(\mathbf{P} : \mathbf{F})\mathbf{F}^{-T}\right) = \mathbf{P}_{\mathrm{dev}}. \tag{1.53}$$

Considering Eq. (1.53) and noticing that

$$\mathrm{tr}(\mathbf{P}\,\mathbf{F}^T) = \frac{1}{3}\,\mathrm{tr}\,(\mathbf{I})\mathbf{P} : \mathbf{F}, \tag{1.54}$$

it follows that

$$\mathrm{tr}(\boldsymbol{\sigma}_{\mathrm{dev}}) = 0. \tag{1.55}$$

For incompressible hyperelastic materials, it is postulated the strain-energy function

$$\Psi_{\mathrm{p}} = \bar{\Psi} + p(J-1). \tag{1.56}$$

The scalar p is an indeterminate *Lagrange multiplier* and, if $\bar{\Psi}$ does not depend on p, it can be identified as a *pressure*. This scalar may only be determined from equilibrium equations and boundary conditions.

1.1.6 Nearly-incompressible materials

For *nearly-incompressible* hyperelastic materials, it is postulated the strain-energy function

$$\Psi_{\mathrm{n}} = \bar{\Psi} + \Psi_{\mathrm{vol}}(J). \tag{1.57}$$

The term Ψ_{vol} is the volumetric energy. Several form for Ψ_{vol} can be found in literature. Usually Ψ_{vol} is a convex function of the variable J and bounded from below, increasing when $J \neq 1$ and with null derivative for $J = 1$. In the upcoming chapters we consider

$$\Psi_{\mathrm{vol}}(J) = \frac{k}{2}(J-1)^2. \tag{1.58}$$

The scalar k, referred to as *bulk modulus*, is determined. The requirement of finite energy for $k \to \infty$ implies $J \to 1$. In order to approach an incompressible behavior of the material the bulk modulus is therefore required to be very large. In the literature, nearly-incompressible materials are also referred to as *quasi-incompressible*.

1.1.7 Anisotropy and fibers

LeGrice et al. [LeGrice et al., 1995] have shown that the myocardial fibers are organized in laminar sheets and oriented. Proceeding through the wall thickness from the epicardium to the endocardium of the left (resp. right) ventricle, the muscle fiber orientation changes following a cubic function, with an angle varying from about $\frac{\pi}{3}$ to $-\frac{\pi}{3}$ (resp. from about $\frac{\pi}{4}$ to $-\frac{\pi}{4}$) with respect to the transmural direction. For the description of the microstructure of the cardiac tissue, a *coordinate system* is usually adopted. Bayer et al. [Bayer et al., 2018] proposed a universal ventricular coordinate system for describing position within the heart and transferring data. Locally, at every point it is possible to define an orthogonal set of material axes. Distinct material responses are associated to the planes identified by this mutually orthogonal directions. In this thesis the model for the distribution of fiber directions is deduced from the approach presented in [M. Potse et al., 2006]. A slight modification accounting for the distinction among LV and RV is proposed. The local fiber orientation is denoted by the orthonormal coordinate system

$$\vec{\mathbf{e}}_n, \vec{\mathbf{e}}_f, \vec{\mathbf{e}}_s, \tag{1.59}$$

that define the sheet normal, fiber, and sheet directions, respectively. For every point $\mathbf{X}$ in the biventricular geometry $\mathscr{B}_r$ are computed the distances d_{epi}, d^L_{endo}, and d^R_{endo} from the epicardium,

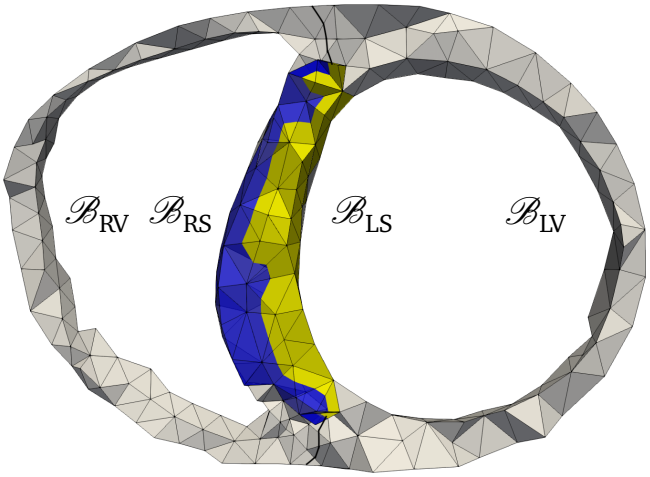

Figure 1.2. Sections of ventricular $\mathscr{B}_{\text{RV}}, \mathscr{B}_{\text{LV}}$ and septal $\mathscr{B}_{\text{RS}}, \mathscr{B}_{\text{LS}}$ regions in the biventricular meshed geometry.

from the left ventricle and from the right endocardium respectively. We consider the ventricular $\mathscr{B}_{\text{RV}}, \mathscr{B}_{\text{LV}}$ and septal $\mathscr{B}_{\text{RS}}, \mathscr{B}_{\text{LS}}$ regions depicted in Fig. 1.2. These subdomains are defined as

$$\begin{aligned}
\mathscr{B}_{\text{LV}} &= \{\mathbf{X} \in \mathscr{B}_{\text{r}} \text{ s.t. } d^R_{\text{endo}}(\mathbf{X}) > d^L_{\text{endo}}(\mathbf{X}) \text{ and } d^R_{\text{endo}}(\mathbf{X}) > d_{\text{epi}}(\mathbf{X})\}, \\
\mathscr{B}_{\text{RV}} &= \{\mathbf{X} \in \mathscr{B}_{\text{r}} \text{ s.t. } d^L_{\text{endo}}(\mathbf{X}) \geq d^R_{\text{endo}}(\mathbf{X}) \text{ and } d^L_{\text{endo}}(\mathbf{X}) > d_{\text{epi}}(\mathbf{X})\}, \\
\mathscr{B}_{\text{LS}} &= \{\mathbf{X} \in \mathscr{B}_{\text{r}} \text{ s.t. } d^R_{\text{endo}}(\mathbf{X}) > d^L_{\text{endo}}(\mathbf{X}) \text{ and } d_{\text{epi}}(\mathbf{X}) \geq d^R_{\text{endo}}(\mathbf{X})\}, \\
\mathscr{B}_{\text{RS}} &= \{\mathbf{X} \in \mathscr{B}_{\text{r}} \text{ s.t. } d^L_{\text{endo}}(\mathbf{X}) > d^R_{\text{endo}}(\mathbf{X}) \text{ and } d_{\text{epi}}(\mathbf{X}) \geq d^L_{\text{endo}}(\mathbf{X})\}.
\end{aligned} \tag{1.60}$$

We define the transmural coordinate as

$$\rho(\mathbf{X}) = \begin{cases}
\dfrac{d_{\text{epi}}}{d_{\text{epi}} + d^L_{\text{endo}}} & \text{in } \mathscr{B}_{\text{LV}}, \\
-\dfrac{d_{\text{epi}}}{d_{\text{epi}} + d^R_{\text{endo}}} & \text{in } \mathscr{B}_{\text{RV}}, \\
\dfrac{d^R_{\text{endo}}(\mathbf{X}) + d^L_{\text{endo}}(\mathbf{X})}{2\left(2^{-1}\left(d^R_{\text{endo}}(\mathbf{X}) + d^L_{\text{endo}}(\mathbf{X})\right) + d^L_{\text{endo}}(\mathbf{X})\right)} & \text{in } \mathscr{B}_{\text{LS}}, \\
-\dfrac{d^R_{\text{endo}}(\mathbf{X}) + d^L_{\text{endo}}(\mathbf{X})}{2\left(2^{-1}\left(d^R_{\text{endo}}(\mathbf{X}) + d^L_{\text{endo}}(\mathbf{X})\right) + d^R_{\text{endo}}(\mathbf{X})\right)} & \text{in } \mathscr{B}_{\text{RS}}.
\end{cases} \tag{1.61}$$

It is a normalized coordinate null for points on the epicardium, equal to one for points on the endocardium of the left ventricle, to minus one for points on the endocardium of the right ventricle and varies linearly in between. If a single ventricle is considered, for every point in the domain we define $d^R_{\text{endo}}(\mathbf{X}) = +\infty$. The proposed method ensures the alignment of the fibers with the cardiac surfaces together with angles that vary smoothly. As an alternative, the transmural coordinate can be computed as the solution of the Laplace's equation. In this case, as boundary conditions, the abovementioned values of ρ at the endocardium and epicardium are assigned as

boundary conditions. A similar approach to this latter alternative is discussed in [Bayer et al., 2018], in which the Laplace's equation is solved separately for the LV and for the RV and the additional variable is used to distinguish if a point belongs to the LV or to the RV. In this thesis the construction of the local fiber basis is currently performed as follows (where $\mathbf{e}_w$ is the unit vector of the w-axis). The sheet normal direction is chosen to be the gradient of the transmural coordinate ρ:

$$\vec{\mathbf{e}}_n = \text{sgn}(\rho(\mathbf{X}))\frac{\nabla\rho}{|\nabla\rho|}.$$

In the definition of $\vec{\mathbf{e}}_n$ the factor $\text{sgn}(\rho(\mathbf{X}))$ is considered to obtain $\vec{\mathbf{e}}_n$ pointing from the endocardium to the epicardium. We construct $\vec{\mathbf{e}}_w$ lying in the plane spanned by $\vec{\mathbf{e}}_n$ and $\vec{\mathbf{e}}_z$:

$$\vec{\mathbf{e}}_w = w_z\vec{\mathbf{e}}_z + w_n\vec{\mathbf{e}}_n, \quad w_z = -\frac{1}{\sqrt{1-(\vec{\mathbf{e}}_z\cdot\vec{\mathbf{e}}_n)}}, \quad w_n = -w_z(\vec{\mathbf{e}}_z\cdot\vec{\mathbf{e}}_n). \tag{1.62}$$

We construct $\vec{\mathbf{e}}_v$ lying in the plane spanned by $\vec{\mathbf{e}}_n$ and $\vec{\mathbf{e}}_w$:

$$\vec{\mathbf{e}}_v = \frac{\mathbf{e}_w\times\mathbf{e}_n}{|\mathbf{e}_w\times\mathbf{e}_n|} \tag{1.63}$$

The fiber direction $\vec{\mathbf{e}}_f$ lies in the plane spanned by $\vec{\mathbf{e}}_w$ and $\vec{\mathbf{e}}_v$ and $\measuredangle(\vec{\mathbf{e}}_f,\vec{\mathbf{e}}_v)=\alpha$ as

$$\vec{\mathbf{e}}_f = \sin\alpha\vec{\mathbf{e}}_w + \cos\alpha\vec{\mathbf{e}}_v \tag{1.64}$$

We consider the helix angle $\alpha = R(2e-1)^3$. Here R is the inclination angle at the endocardium and it is defined as described in [M. Potse et al., 2006]

$$R(\mathbf{X}) = \begin{cases} \frac{\pi}{4} & \text{if } e(\mathbf{X})<0, \\ \frac{\pi}{3} & \text{if } e(\mathbf{X})\geq 0. \end{cases} \tag{1.65}$$

The sheet direction $\vec{\mathbf{e}}_s$ is defined as

$$\vec{\mathbf{e}}_s = \vec{\mathbf{e}}_f\times\vec{\mathbf{e}}_n. \tag{1.66}$$

1.1.8 Constitutive models

Constitutive theory describes the physical behavior of materials by means of appropriately fitted mathematical models. *A priori* cardiac tissue constitutive models assume the deformation of the muscle to be *volume preserving*. In this section we report two models that we will use in the upcoming proposed numerical tests.

Guccione-Costa constitutive model

Guccione-Costa [Guccione et al., 1995] constitutive law is characterized by the exponential transversely isotropic, strain energy function

$$\Psi(\mathbf{F}_{\text{dev}}) = \frac{a_1}{2}\left(e^Q-1\right), \tag{1.67}$$

where

$$Q = a_2\mathbf{E}^2_{\text{dev},ff} + a_3(\mathbf{E}^2_{\text{dev},ss}+\mathbf{E}^2_{\text{dev},nn}+2\mathbf{E}^2_{\text{dev},sn}) + 2a_4(\mathbf{E}^2_{\text{dev},fs}+\mathbf{E}^2_{\text{dev},fn}). \tag{1.68}$$

The strain components $\mathbf{E}_{\text{dev},ij}$ (expressed as functions of $\mathbf{F}_{\text{dev}}$) are referred to the system of local coordinates $\left(\vec{\mathbf{e}}_n,\vec{\mathbf{e}}_f,\vec{\mathbf{e}}_s\right)$.

Holzapfel-Odgen constitutive model

The strain-energy function $\bar{\Psi}$ of an hyperelastic material can be expressed in invariant based formulation. Given two orthogonal versors $\mathbf{a}$ and $\mathbf{b}$, we define the following scalar functions of the right Cauchy-Green strain tensor $\mathbf{C}_{\text{dev}}$:

$$\begin{aligned}\mathscr{I}_1(\mathbf{C}_{\text{dev}}) &= \operatorname{tr}\mathbf{C}_{\text{dev}},\\ \mathscr{I}_{4,\mathbf{a}}(\mathbf{C}_{\text{dev}}) &= \mathbf{a}\cdot\mathbf{C}_{\text{dev}}\mathbf{a},\\ \mathscr{I}_{8,\mathbf{a}b}(\mathbf{C}_{\text{dev}}) &= \mathbf{a}\cdot\mathbf{C}_{\text{dev}}\mathbf{b}.\end{aligned}$$

The first invariant $\mathscr{I}_1$ is purely isotropic, while $\mathscr{I}_{4,\mathbf{a}}$ measures the stretching in direction $\mathbf{a}$. The relative shear between the directions $\mathbf{a}$ and $\mathbf{b}$ is accounted for through the anisotropic invariant $\mathscr{I}_{8,\mathbf{a}b}$. The incompressible Holzapfel-Ogden [Holzapfel and Ogden, 2009] law is characterized by the following strain energy function

$$\Psi(\bar{\mathbf{C}}) = \frac{a}{2b}e^{b(\mathscr{I}_1-3)} + \sum_{i=\mathbf{f},\mathbf{s}}\frac{a_i}{2b_i}e^{b(\max\{\mathscr{I}_{4,i}-1,0\}^2-1)} + \frac{a_{\mathbf{fs}}}{2b_{\mathbf{fs}}}e^{b(\mathscr{I}_{8,\mathbf{fs}}^2)^2-1.} \tag{1.69}$$

The parameters a, b, $a_{\mathbf{f}}$, $b_{\mathbf{f}}$, $a_{\mathbf{s}}$, $b_{\mathbf{s}}$, $a_{\mathbf{fs}}$, $b_{\mathbf{fs}}$ are positive material constants with identification is based on shear tests on pig myocardium [Dokos et al., 2002].

1.2 Mathematical modeling of electrophysiology

In this section we introduce the governing equations used to simulate the electrical activation of the human heart. This introduction is largely based on [Keener and Sneyd, 2008b,a]. During the cardiac cycle, an electrical stimulus spreads actively throughout the cardiac tissue causing the mechanical contraction of the muscle. A coordinate active propagation of the electrical signal is essential for a physiological heartbeat. The electrical activation of the heart involves processes occurring at the microscopic and macroscopic levels. The biochemical processes responsible for cells activation occur at the microscale. Ionic models describe the reaction of the cellular membrane to an external stimulus. The electrical macroscopic behavior of the cardiac tissue is usually described by means of the *bidomain equation* [Tung, 1978]. This homogenized partial differential equation is generally accepted as the governing equation for the electrical propagation in cardiac tissue [Keener and Sneyd, 2008b]. *Monodomain equation* is derived assuming linearly dependent intra- and extra-cellular conductivity tensors [Colli Franzone et al., 2015]. In several circumstances, for large-scale models monodomain simulations can approximate bidomain simulations well [M. Potse et al., 2006; Bordas et al., 2009].

1.2.1 Modeling electrical properties of cardiac cells

The electrical activity of cardiac cells is usually mathematically formalized by dynamic cell membrane equations, also known as ionic models. Ionic concentration balance between the intra- and the extra- cellular spaces of cardiac cells is governed by ionic channels, such as Na^+-channel, K^+-channel, and ionic pumps. The imbalance of ionic concentrations between intra- and extra-cellular spaces causes a difference between the intra-cellular potential φ_{i} and the extra-cellular potential φ_{e}. Due to its role of ions separator, the cell membrane can be compared to a capacitor.

We define $V = \varphi_\mathrm{i} - \varphi_\mathrm{e}$, the potential difference between the internal and the external of the cell (usually measured in mV). It holds

$$C_\mathrm{m} V = \Delta Q, \tag{1.70}$$

where C_m represents the membrane capacitance and Q the charge difference between the intra- and the extra- cellular domain. Removing/adding charges to any side of the membrane a purely capacitive current

$$I_\mathrm{c} = C_\mathrm{m} \frac{\mathrm{d}V}{\mathrm{d}t} \tag{1.71}$$

arises. Because of the passage of ions through the membrane a current I_{ion} arises. In a isolated cell the membrane current balances the capacitive one. Highlighting the balance between the two currents we obtain

$$C_\mathrm{m} \frac{\mathrm{d}V}{\mathrm{d}t} + I_{ion}(V) = 0. \tag{1.72}$$

In Eq. (1.72) we underline the dependence of the ionic channels on the action potential (AP) V. If case an external stimulus I_app is applied to the cell, this contribution as to be added in Eq. (1.72). In this case we obtain

$$C_\mathrm{m} \frac{\mathrm{d}V}{\mathrm{d}t} + I_{ion}(V) = I_\mathrm{app}. \tag{1.73}$$

1.2.2 Fitz-Hugh Nagumo model

The Fitz-Hugh Nagumo (FHN) model is a simplified model useful for testing numerical methods. This phenomenological model contains a single slow gating variable ω, called the *recovery variable*. We consider the variant proposed in [Rogers and McCulloch, 1994], in which I_{ion} and ω are defined as

$$\begin{cases} I_{ion} & = \eta_1 (V - V_\mathrm{r})(V - V_\mathrm{unst})(V - V_\mathrm{p}) + \eta_2 \omega (V - V_\mathrm{r}), \\ \frac{\partial w}{\partial t} & = \eta_3 (V_\mathrm{n} - \eta_4 \omega). \end{cases} \tag{1.74}$$

Here $V_\mathrm{n} = (V - V_\mathrm{r})/(V_\mathrm{p} - V_\mathrm{r})$, where V_r and V_p represent the model dependent resting and peak values. The model parameters η_1, η_2 and V_unst define the shape of the propagation wave while η_3, η_4 control the recovery potential evolution. The trivial dependence of the ionic current on the action potential allows for a straightforward analytic computation of the linearized problem. In case the contribution of the recovery variable ω in (1.74.1) is neglected, Eq. 1.72 is also known as *bistable or Nagumo equation*. Considered parameters, partially taken from [Pezzuto et al., 2016], are reported in Tab. (5.1) of Chpt. 3.

1.2.3 Hodgkin-Huxley formalism

In 1952 Hodgkin and Huxley [Hodgkin and Huxley, 1952] proposed a model for I_{ion} for squid giant axon. The profound impact of their work earn them a Nobel prize in Physiology and Medicine in 1963. They introduced the concept of dimensionless vector of gating variables $\mathbf{s}\colon \mathscr{B}_r \times \mathscr{T} \to \mathbb{R}^{n_g}$. Following the Hodgkin-Huxley formalism the ionic current can be expressed as sum of N currents as

$$I_\mathrm{ion}(V, \mathbf{s}) = \sum_{n=1}^{N} I_n(V, \mathbf{s}, \mathbf{c}), \tag{1.75}$$

where

$$I_n(V, \mathbf{s}, \mathbf{c}) = g_n(V, \mathbf{s}, \mathbf{c})(V - V_n), \tag{1.76}$$

and $g_n \colon \mathscr{B}_r \times \mathscr{T} \to \mathbb{R}$. Each gating variable s_i for $i = 1, \dots, n_g$ obeys to the first-order *rate equation*

$$\frac{\mathrm{d}s_i}{\mathrm{d}t} = \alpha_i(V)(1 - s_i) - \beta_i(V). \tag{1.77}$$

In Eq. (1.77) the likelihood that a closed ionic channel i opens and vice versa are described by the functions $\alpha_i(V)$, $\beta_i(V)$. We define the vectors $\boldsymbol{\alpha}, \boldsymbol{\beta}$ such that $(\boldsymbol{\alpha})_i = \alpha_i$ and $(\boldsymbol{\beta})_i = \beta_i$ Eq. (1.77) can be reformulated as

$$\frac{\mathrm{d}s_i}{\mathrm{d}t} = \frac{1}{\theta_i(V)}(s_{i,\infty}(V) - s_i(V)), \tag{1.78}$$

with

$$s_{i,\infty}(V) = \frac{\alpha_i(V)}{\alpha_i(V) + \beta_i(V)} \text{ and } \theta_i(V) = \frac{1}{\alpha_i(V) + \beta_i(V)}. \tag{1.79}$$

Here $s_{i,\infty}$ and θ_i represent the voltage dependent *steady state* and the *channel inactivation time constant*, respectively. For fixed membrane voltage V on the time interval $(0, t)$, this equation is solved by

$$s_i(t) = s_{i,\infty}(V) - (s_{i,\infty}(V) - s_i(0))e^{\frac{-t}{\theta_i(V)}}. \tag{1.80}$$

We focus our attention on ionic models based on the Hodgkin-Huxley formalism, but we recall that those models are sometimes not sufficient to capture some features of channels behavior [Armstrong and Bezanilla, 1977]. For this reason, Markov-type kinetic models, which represent each ionic channel as a collection of states and a set of transition between them, have been proposed, see e.g. [Balbi et al., 2017].

1.2.4 Membrane models for human ventricular cells

Several membrane equations have been proposed to reproduce the extremely complex behavior of cardiac cells. A generic model for mammalian ventricular cells was proposed in [Beeler and Reuter, 1977 Jun]. Luo and Rudy published membrane models based on experimental information from guinea pigs. Those membrane models are known as *phase-1* and *phase-2 Luo Rudy* models [Luo and Rudy, 1991 Jun, 1994]. Priebe and Beuckelmann [Priebe and Beuckelmann, 1998] adapted phase-2 Luo Rudy model using human data. In 2002, Bernus at al. [Bernus and et al., 2002] proposed a reduced version of Priebe and Beuckelmann model in which five gating variables and fixed ionic concentration are considered. Ten Tusscher [ten Tusscher et al., 2004] et al. proposed a different model for human ventricular cells in 2004 (with an update in 2006 [Ten Tusscher and Panfilov, 2006]). In 2008 Bueno-Orovio et al. [Bueno-Orovio et al., 2008] proposed a minimal model for human ventricular APs in tissue. The works by O'Hara et al. [O'Hara et al., 2011] and Grandi et al. [Grandi et al., 2010] represent the most recent works in the modeling of diseased human cardiac ventricular action potential. The early developed models considered the ionic concentrations as parameters of the problem. The need for time dependent ionic concentrations led to *second generation* models [Rasmusson et al., 1990; Noble et al., 1998; Arce et al., 2000; Endresen and Skarland, 2000]. For $m_c \in \mathbb{N}$, we define the vector of the ionic concentrations $\mathbf{c} : \mathscr{B}_r \times \mathscr{T} \to \mathbb{R}^{m_c}$ (expressed in millimole). Second generation models

read

$$\begin{cases} C_m \frac{dV}{dt} + I_{\text{ion}}(V, \mathbf{s}, \mathbf{c}) &= I_{\text{app}}, \\ \frac{ds_i}{dt} &= \alpha_i(V)(1-s_i) - \beta_i(V)s_i, \quad i = 1, \dots, n_g, \\ \frac{d\mathbf{c}}{dt} &= \mathbf{Z}(V, \mathbf{s}). \end{cases} \tag{1.81}$$

Here the functions I_{ion}, $\mathbf{Z}$, $\boldsymbol{\alpha}$, $\boldsymbol{\beta}$, and $\mathbf{c}$ depends on the choice of the ionic model. Second generation models may be numerically unstable and show degeneracy associated with non-uniqueness of the equilibrium solutions. Moreover, some of the ionic concentrations usually present slow long-term trends that require several milliseconds to reproduce the complete cell dynamic [Bernus and et al., 2002]. For these reasons *first generation* models [Beeler and Reuter, 1977 Jun; Luo and Rudy, 1991 Jun] are still widely used. In our numerical tests, we mainly consider the Bernus-Wilders-Zemlin-Verschelde-Panfilov first generation model, the ten Tusscher-Noble-Noble-Panfilov second generation model, and the Bueno Orovio-Cherry-Fenton minimal model.

1.2.5 Bernus-Wilders-Zemlin-Verschelde-Panfilov model

As first generation model we consider the Bernus-Wilders-Zemlin-Verschelde-Panfilov (BWZVP) model [Bernus and et al., 2002]. This model of a single human ventricular cell was developed to improve large scale computation of reentrant arrhythmias. It is a stable reformulation of the second generation Priebe and Beuckelmann (PB) model. The PB model (and consequently the BWZVP model) successfully reproduces basic properties of APs of normal and failing human ventricular cells. Incorporating data on human cardiac cells, it is largely based on animal data. The BWZVP model features five gating variables: while v and X are introduced for the first time in [Bernus and et al., 2002], the gating variables m, f, to are inherited from the original PB model. The variables m and v regulate the fast Na^+ current, the variable f the slow Ca^{2+} current, to the transient outward current, and X the inward delayed rectifier K^+ current. The model has three extra variables: d^∞, r^∞, K_1^∞. These gating variables, for which Eq. (1.77) does not apply, are characterized by steady-states which are independent on V. The model involves nine ionic currents. The equilibrium value for the AP for this model is $V_r = -90.2$ mV.

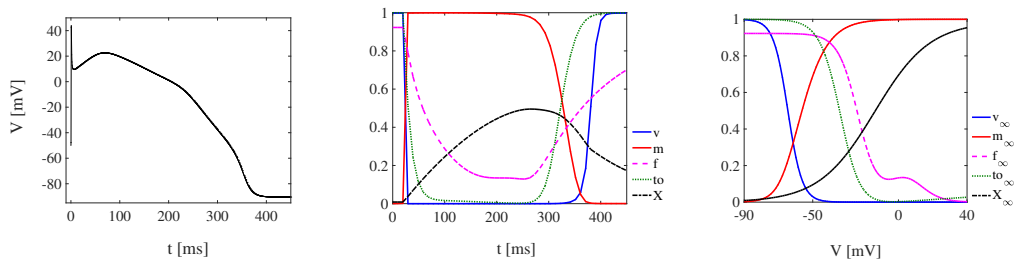

(a) (b) (c)

Figure 1.3. Simulated single cell action potential for the BWZVP model (a), associated solutions (b) and steady states of the gating variables (c).

1.2.6 ten Tusscher-Noble-Noble-Panfilov model

The ten Tusscher-Noble-Noble-Panfilov (TNNP) model [ten Tusscher et al., 2004] is based on experimental data concerning major ionic currents. In detail, the fast sodium, L-type calcium, transient outward, rapid and slow delayed rectifier, and inward rectifier currents are considered. This second generation model includes a basic calcium dynamics, allowing for the realistic modeling of calcium transients, calcium current inactivation, and the contraction staircase. Considering the differences in transient outward and slow delayed rectifier currents, human epicardial, endocardial, and M cell action potentials are reproduced. Approximating accurately the action potential duration restitution curve, the model is able to simulate the characteristic for reentrant arrhythmias. The model was extended in 2006 [Ten Tusscher and Panfilov, 2006]. The TNNP 2006 model features fourteen gating variables and twelve ionic currents. In the updated model a more extensive description of intracellular calcium handling is included. Moreover a subspace calcium variable that controls the dynamics of the L-type calcium current and the Ryanodine receptor current is included. Finally, some minor changes to parameter values and to slow delayed rectifier time dynamics are considered.

1.2.7 Bueno Orovio-Cherry-Fenton model

The Bueno Orovio-Cherry-Fenton (BOCF) model is a *minimal model* that reproduces in detail experimentally measured characteristics of human ventricular APs in in isolated cells and in tissue [Bueno-Orovio et al., 2008]. This minimal model differs from the previously described ionic models in that instead of reproducing a wide range of ion channel currents, it represents fast inward, slow inward, and outward currents as sum of the related transmembrane currents. Based on the three-variables model proposed by Fenton and Karma [Fenton and Karma, 1998], the model involves an additional variable [Fenton, 1999]. This variable reproduces the experimentally measured characteristics of human ventricular APs, which important role in dynamics, especially during alternans, is underlined in the works by Fenton, Bueno-Orovio and colleagues [Fenton et al., 2002] and by ten Tusscher and colleagues [Ten Tusscher and Panfilov, 2006].

1.2.8 Modeling electrical properties of cardiac tissue

In physiological conditions, the AP originates at the sinoatrial node. From here it spread via cell-to-cell conduction as described in [Klabunde, 2011]. The AP enters the ventricles through the atrioventricular node which is connected to the *bundle of His* and to the *Purkinje system*. The conduction velocity in the Purkinje system is about eight times higher than the conduction velocity in the surrounding ventricular myocyte tissue. In order to accurately model the electrophysiology of the heart it is therefore important to study the propagation of the AP through excitable tissue.

1.2.9 The bidomain equation

The *bidomain equation* [Tung, 1978] describes the cardiac tissue as consisting of an intra-cellular and an extra-cellular domain characterized by the conductivity tensors $\mathbf{G}_{\mathrm{i}}$ and $\mathbf{G}_{\mathrm{e}}$, respectively. It is generally accepted as the governing equation for the electrical propagation in cardiac tissue [Keener and Sneyd, 2008a] and it is based on the description of two overlapping interpenetrating domains representing the intra-cellular and extra-cellular space. In absence of external

current and assuming Ohmic materials, conservation of the total current reads

$$\nabla \cdot (\mathbf{G}_\mathrm{i} \nabla \varphi_\mathrm{i}) + \nabla \cdot (\mathbf{G}_\mathrm{e} \nabla \varphi_\mathrm{e}) = 0. \tag{1.82}$$

The *membrane current* is the sum of the capacitive and ionic current. Up to the *surface-to-volume ratio* β multiplicative factor, it equals the current of intra-cellular space, i.e.

$$\beta \left(C_\mathrm{m} \frac{\mathrm{d}V}{\mathrm{d}t} + I_\mathrm{ion}(V, \mathbf{s}, \mathbf{c}) \right) = \nabla \cdot (\mathbf{G}_\mathrm{i} \nabla \varphi_\mathrm{i}). \tag{1.83}$$

Substituting $V = \varphi_\mathrm{i} - \varphi_\mathrm{e}$ in Eq. (1.82) the following relation between AP and extracellular potential arises

$$\nabla \cdot (\mathbf{G}_\mathrm{i} \nabla V) + \nabla \cdot ((\mathbf{G}_\mathrm{i} + \mathbf{G}_\mathrm{e}) \nabla \varphi_\mathrm{e}) = 0. \tag{1.84}$$

Considering $\varphi_\mathrm{i} = V + \varphi_\mathrm{e}$ in Eq. (1.83) and the application of an external stimulus I_app in the intra-cellular space we obtain

$$\beta \left(C_\mathrm{m} \frac{\mathrm{d}V}{\mathrm{d}t} + I_\mathrm{ion}(V, \mathbf{s}, \mathbf{c}) \right) = \nabla \cdot (\mathbf{G}_\mathrm{i} \nabla (V + \varphi_\mathrm{e})) + I_\mathrm{app}. \tag{1.85}$$

The coupled system constituted by Eq. (1.84) and Eq.(1.85) is known as the *parabolic-elliptic* formulation of the bidomain equation. Coupling this formulation with a set of $n_g + m_c$ ODEs describing the gating variables behavior and the ionic concentration dynamics and imposing boundary conditions we obtain

$$\begin{cases} \nabla \cdot (\mathbf{G}_\mathrm{i} \nabla V) + \nabla \cdot ((\mathbf{G}_\mathrm{i} + \mathbf{G}_\mathrm{e}) \nabla \varphi_\mathrm{e}) = 0 & \text{in } \mathscr{B}_r \times \mathscr{T}, \\ \beta \left(C_\mathrm{m} \dfrac{\mathrm{d}V}{\mathrm{d}t} + I_\mathrm{ion}(V, \mathbf{s}, \mathbf{c}) \right) = \nabla \cdot (\mathbf{G}_\mathrm{i} \nabla (V + \varphi_\mathrm{e})) + I_\mathrm{app} & \text{in } \mathscr{B}_r \times \mathscr{T}, \\ \dfrac{d\mathbf{s}}{dt} = \mathbf{S}(V, \mathbf{c}) & \text{in } \mathscr{B}_r \times \mathscr{T}, \\ \dfrac{d\mathbf{c}}{dt} = \mathbf{Z}(V, \mathbf{s}) & \text{in } \mathscr{B}_r \times \mathscr{T}, \\ \mathbf{n}(\mathbf{G}_\mathrm{i} \nabla (V + \varphi_\mathrm{e})) = 0 & \text{in } \partial \mathscr{B}_r \times \mathscr{T}, \\ \mathbf{n} \cdot (\mathbf{G}_\mathrm{i} \nabla V + (\mathbf{G}_\mathrm{i} + \mathbf{G}_\mathrm{e}) \nabla \varphi_\mathrm{e}) = 0 & \text{in } \partial \mathscr{B}_r \times \mathscr{T}, \\ V(\mathscr{B}_\mathrm{r}, t_0) = V_0, \quad \mathbf{s}(\mathscr{B}_\mathrm{r}, t_0) = \mathbf{s}_0, \quad \mathbf{c}(\mathscr{B}_\mathrm{r}, t_0) = \mathbf{c}_0. \end{cases} \tag{1.86}$$

In the system above, the unknowns are the intra- and extra-cellular potential $\varphi_\mathrm{i}, \varphi_\mathrm{e} : \mathscr{B}_r \times \mathscr{T} \to \mathbb{R}$ (expressed in mV), the vector of the gating variables $\mathbf{s} : \mathscr{B}_r \times \mathscr{T} \to \mathbb{R}^{n_g}$ (dimensionless), and the vector of the ionic concentrations $\mathbf{c} : \mathscr{B}_r \times \mathscr{T} \to \mathbb{R}^{m_c}$ (expressed in mmol). The function I_{ion} is the ionic current and I_{app} is the applied current stimulus (both expressed in $\mu\mathrm{Acm}^{-1}$). The functions $I_\mathrm{ion}, \mathbf{S}, \mathbf{Z}$ depend on the choice of the ionic model. The parameters are the transmembrane capacitance C_m (in $\mu\mathrm{Fcm}^{-2}$), the conductivity tensors $\mathbf{G}_\mathrm{i}$, $\mathbf{G}_\mathrm{e}$ (both in $\mu\mathrm{S\ cm}^{-1}$), and the surface to volume ratio β (in cm^{-1}). Representative values for these constants can be found in [Clayton, 2011]. Suitable initial conditions depend on the ionic model and of the performed simulation. Using mathematical homogenization techniques, it is possible to obtain a more rigorous derivation of the bidomain equation [Keener and Sneyd, 2008a].

1.2.10 Conductivity tensors

The conductivity tensors $\mathbf{G}_\mathrm{i}$, $\mathbf{G}_\mathrm{e}$ in fiber-aligned coordinates are usually expressed as

$$\mathbf{G}_\mathrm{i} = \sum_{j=f,s,n} G_{\mathrm{i,j}}(\vec{e}_j \otimes \vec{e}_j), \tag{1.87}$$

$$\mathbf{G}_\mathrm{e} = \sum_{j=f,s,n} G_{\mathrm{e,j}}(\vec{e}_j \otimes \vec{e}_j), \tag{1.88}$$

in units of mScm^{-1}. Here, $\vec{e}_j$ with $j \in \{f,s,n\}$ are the previously described unit vectors in the coordinate system align with the fibers. The scalars $G_{\mathrm{i,j}}, G_{\mathrm{e,j}}$ represent scalar diffusion coefficients.

1.2.11 Activation time, wavefront, action potential duration

The duration of the electrical excitation is an important indicator of a physiological cardiac functionality. Following the book by Colli Franzone, Pavarino and Scacchi [Colli Franzone et al., 2014], we define the activation time (AT) as the first-hitting-time for the AP to assume the value $(V_r+V_p)/2$. Here V_r and V_p represent the model dependent resting and peak values, respectively. Formally we define $\psi\colon \mathscr{B}_r \to \mathbb{R}^+ \cup 0$ as

$$\psi(\mathbf{x}) = \inf\{t \in (0, T_{\mathrm{fin}}] \text{ s.t. } V(\mathbf{x},t) = (V_r + V_p)/2\}.$$

The AT represents the depolarization time at the point $\mathbf{x}$. It can be correlated with the local peak conductance of the sodium channel. We define the excitation wavefront as the level surface of the AP. Formally $\mathscr{S}\colon \mathbb{R}^+ \cup 0 \to \mathscr{B}_r$,

$$\mathscr{S}(t) = \{\mathbf{x} \in \mathscr{B}_r \text{ s.t. } \psi(\mathbf{x}) = t\}.$$

We define the repolarization time at 90% as the first time at which, after the activation phase, the action potential V reaches the value $V_p - 0.9(V_p - V_r)$. Formally we define $\varrho\colon \mathscr{B}_r \to \mathbb{R}^+ \cup 0$ as

$$\varrho(\mathbf{x}) = \inf\{t \in (\psi(\mathbf{x}), T_{\mathrm{fin}}] \text{ s.t. } V(\mathbf{x},t) = V_p - 0.9(V_p - V_r)\}.$$

Finally we define the action potential duration $\mathrm{APD}_{90}\colon \mathscr{B}_r \to \mathbb{R}^+ \cup 0$ as

$$\mathrm{APD}_{90}(\mathbf{x}) = \varrho(\mathbf{x}) - \psi(\mathbf{x}). \tag{1.89}$$

The physiological simulation of the excitation wavefront requires the numerical solution of the bidomain equation with space and time steps of the order of 0.1 mm and 0.01 ms, respectively. Reduced macroscopic approximations of the bidomain equation, less demanding in terms of required computational resources, can be considered for large scale simulations involving the whole ventricles. The monodomain equation and the Eikonal-diffusion model presented in the next section are widespread approximations of the bidomain equation.

1.2.12 The reduced monodomain equation

The *monodomain equation* system an important simplification of the bidomain system which can be written as a parabolic PDE coupled with a set of $n_g + m_c$ ODEs:

$$\begin{cases} \beta(C_m \dfrac{\mathrm{d}V}{\mathrm{d}t} + I_{\text{ion}}(V, \mathbf{s}, \mathbf{c})) = \nabla \cdot \mathbf{G}_{\text{m}} \nabla V + I_{\text{app}}, & \text{in } \mathscr{B}_r \times \mathscr{T}, \\ \dfrac{d\mathbf{s}}{dt} = \mathbf{S}(V, \mathbf{c}) & \text{in } \mathscr{B}_r \times \mathscr{T}, \\ \dfrac{d\mathbf{c}}{dt} = \mathbf{Z}(V, \mathbf{s}) & \text{in } \mathscr{B}_r \times \mathscr{T}, \\ \mathbf{n} \cdot \mathbf{G}_{\text{m}} \nabla V = 0 & \text{in } \partial\mathscr{B}_r \times \mathscr{T}, \\ V(\mathscr{B}_{\text{r}}, t_0) = V_0, \quad \mathbf{s}(\mathscr{B}_{\text{r}}, t_0) = \mathbf{s}_0, \quad \mathbf{c}(\mathscr{B}_{\text{r}}, t_0) = \mathbf{c}_0. \end{cases} \tag{1.90}$$

When $\mathbf{G}_{\text{e}} = \lambda \mathbf{G}_{\text{i}}$ for $\lambda \in \mathbb{R}$, the Eq. (1.84) simplifies to

$$\nabla \cdot (\mathbf{G}_{\text{i}}(1+\lambda)\nabla\varphi_{\text{e}}) = -\nabla \cdot (\mathbf{G}_{\text{i}} \nabla V). \tag{1.91}$$

Substituting Eq. (1.84) into Eq. (1.86.1) we get the so called monodomain equation Eq. (1.90.1). Practically this condition is never verified, but it offers a convenient way to significantly reduce the computational complexity. In fact, in this case, Eq. (1.86.1) and Eq. (1.86.2) are decoupled. We consider

$$\mathbf{G}_{\text{m}} = \mathbf{G}_{\text{i}}(\mathbf{G}_{\text{i}} + \mathbf{G}_{\text{e}})^{-1}\mathbf{G}_{\text{e}} \tag{1.92}$$

In the system above, the unknowns are the action potential $V : \mathscr{B}_r \times \mathscr{T} \to \mathbb{R}$ (expressed in mV), the vector of the gating variables $\mathbf{s} : \mathscr{B}_r \times \mathscr{T} \to \mathbb{R}^{n_g}$ (dimensionless), and the vector of the ionic concentrations $\mathbf{c} : \mathscr{B}_r \times \mathscr{T} \to \mathbb{R}^{m_c}$ (expressed in mmol). The parameters are the transmembrane capacitance C_m (in μFcm^{-2}), the monodomain conductivity tensor $\mathbf{G}_{\text{m}}$ (in $\mu\text{S cm}^{-1}$), and the surface to volume ratio β (in cm^{-1}). The PDE (1.90.1) describes the propagation of AP in the myocardial tissue. The first set of ODEs (1.90.2) represents the opening and closing of the ion channels which are responsible for cardiac excitability. The second set of ODEs (1.90.3) describes the cellular dynamics of ionic concentrations. Eq. (1.90.4) represents the homogeneous Neumann boundary conditions imposed on Γ_N. The assumption of linearly dependent intra- and extra-cellular conductivities tensors is usually inaccurate. Moreover, it is not valid for torso-coupled human heart models because outside the heart $\mathbf{G}_{\text{i}} = 0$. However the very small differences between the bidomain and the monodomain models for large-scale simulations make the use of monodomain equation warranted [M. Potse et al., 2006].

1.2.13 The reduced Eikonal-diffusion model

Another possible way to reduce the computational complexity of the bidomain model is to consider simplified kinematic models, called Eikonal equations [Keener, 1991; Colli Franzone and Guerri, 1993; Keener and Panfilov, 1995; Colli Franzone et al., 1998]. In physiological conditions, Eikonal models can be used to computed the AT at which the excitation wavefront reaches a given point of the myocardium. Formally, the Eikonal equation can be derived by a perturbation argument applied to the bidomain equations [Colli Franzone and Guerri, 1993]. The bidomain equation and its reduced Eikonal approximation have been compared in [Pullan et al., 2002; Pezzuto et al., 2017]. Focusing only on the propagation of the electrical wavefront, Eikonal models

cannot accurately describe the AP and ionic dynamics. We compute the activation sequence of the heart considering the solution of the following Eikonal-diffusion system: find ψ such that

$$\begin{cases} c_0 \nabla \cdot (\boldsymbol{G}_{\mathrm{m}} \nabla \psi) + \frac{\theta}{\sqrt{\chi}} \sqrt{\nabla \psi \cdot \boldsymbol{G}_{\mathrm{m}} \nabla \psi} &= 1, \quad \text{in } \mathscr{B}_r \setminus \Omega_{\mathrm{in}}, \\ \psi &= \eta \quad \text{in } \Omega_{\mathrm{in}}, \end{cases} \tag{1.93}$$

for c_0, $\theta \in \mathbb{R}$. The scaling parameter θ is the velocity that the front would have if χ and the conductivity tensor were set to one and c_0 to zero. Here Ω_{in} represents the part of the domain subjected to prescribed early activation. Accounting for more realistic effects of diffusion of the fronts itself or based on different metrics [Colli Franzone et al., 2014], more advanced Eikonal models are also described in literature.

1.2.14 ECGs signals

The spatio-temporal morphology of the electrocardiogram (ECG) is the result of the motion of the cardiac extracellular APs with respect to the position of the electrodes. In the computation of the ECG, often a fixed geometry of the heart in the torso is assumed. Based on this approximation, patient-tailored ECGs can be simulated in a few minutes on HPC architectures with anatomically detailed cardiac electrophysiology models [M. Potse et al., 2006; Villongco et al., 2014]. We follow the lead-field approach presented in [Plonsey, 1964; Pezzuto et al., 2017], on which this section is mainly based. The body surface map can be simulated considering the bidomain equation

(1.94)

Each ECG lead potential Z at $\mathbf{X}'$ is computed as

$$Z(\mathbf{X}') = \int_{\mathscr{B}_r} \mathbf{G}_{\mathrm{i}} \nabla V(\mathbf{X}) \cdot \nabla \varphi(\mathbf{X}; \mathbf{X}') d\mathbf{X} \tag{1.95}$$

Here φ is the lead field [Mcfee and Johnston, 1953] on the specific ECG lead. The lead field is the potential field created by a positive unit current applied at the positive electrode location and by a negative unit current applied at the negative electrode location [Geselowitz, 1989] for the torso problem. The lead field φ is the analytical solution to

$$\nabla \cdot (\mathbf{G} \nabla \varphi) = \begin{cases} -1 \text{ at the positive electrode,} \\ 1 \text{ at the negative electrode,} \\ 0 \text{ elsewhere,} \end{cases} \tag{1.96}$$

where $\mathbf{G} = \mathbf{G}_{\mathrm{i}} + \mathbf{G}_{\mathrm{e}}$ is the *bulk conductivity*. Pseudo-ECGs assumes infinite torso with constant bulk conductivity $\mathbf{G} = \sigma_0 \mathbf{I}$. In such case, for $r = \|X - X'\|$, the lead field reads

$$\varphi(X; X') = \frac{1}{4\pi\sigma_0 r}. \tag{1.97}$$

1.3 The multiscale electromechanical coupled problem

The mechanical activation of the cardiac muscle is triggered by an electric signal. The electrical potential propagates along the conduction fibers, and dictates the release of calcium from

the sarcoplasmic reticulum. This induces the contraction of the cardiac muscle by means of the shortening of cardiomyocytes. The contraction is responsible for a change in pressure inside the cardiac chambers and of the consequent lilting opening and closure of heart valves. Through the arteries the RV pumps deoxygenated blood into the pulmonary circulation and the LV pumps oxygenated blood in the systemic circulation. The description of the synergetic interaction of mechanical and electrophysiological processes is essential for physiological simulations of cardiac functions. In the following, we analyze in detail the mathematical models that we use to capture the basic fields coupling processes. In Sec. (1.3.1) we discuss the electro-mechanical feedbacks (EMFs). In detail, in Sec. (1.3.1) we discuss possible strategies to incorporate the active contribution in the mechanical model. In Sec. (1.3.2) we describe geometrical mechano-electrical feedbacks (MEFs), direct consequences of the cardiac muscle contraction and relaxation. Making an example, the monodomain system should be evaluated in the coordinate system determined from the deformation tensor. In Sec. (1.3.2) and (1.3.2) we discuss how we take into the deformation of the domain in the monodomain system (1.90) and in the computation of the ECGs signals (1.95). The mechanical deformation of the heart also influences its electrical excitation via stretch-activated channels (SAC). These channels can change the shape of AP in response to stretch [Kohl et al., 1999]. Another interesting effect is described by the Frank-Starling law. The law states that the greater is the blood volume entering the ventricles, the more powerful is the contraction exerted by the muscle. However, since in this thesis we focused on the geometrical mechano-electrical feedbacks, these latter effects are not considered in the model.
Blood flow dynamics of the human heart is usually modelled by the Navier-Stokes model [Mittal et al., 2016; Tagliabue et al., 2017a]. To examine the effect of heart dyssynchrony and failure on LV hemodynamics, Navier-Stokes equations for the hemodynamics are coupled with a detailed model of electromechanical cardiac functionality [Choi et al., 2015]. The need of the description of the fluid behavior during each phase of the heartbeat results in the requirement of mixed time varying boundary conditions for the treatment of the aortic and of the mitral valves. Usually, the involved parameters are tuned to obtain a realistic inflow velocity profile and a regularization term for the description of mitral valve is introduced to prevent numerical instabilities [Tagliabue et al., 2017a]. As an additional feature, cardiac flows present relatively high Reynolds number. In case the solution of the complete valve plane is examined, the interaction of the fluid flow with flexible structures can be solved considering immersed boundary methods [Zheng et al., 2012; Seo and Mittal, 2013]. The contact among the different valve leaflets results in the additional requirement of the fulfillment of nonpenetration constraints. For all the above-mentioned reasons, the coupling between FE electromechanical and circulatory model represents a challenge from a computational modeling and simulation point of view. In contrast to this approach, FE models of ventricular mechanics can be coupled with lumped models of blood dynamics[Eriksson et al., 2013; Watanabe et al., 2004; Kerckhoffs et al., 2007]. In Sec. (1.3.5), equations for coupling the electromechanical model with the lumped model of circulation proposed in [Kerckhoffs et al., 2007] are presented.

1.3.1 Electro-mechanical feedbacks

In this section we describe the active strain and active stress electro-mechanical feedbacks (EMF).

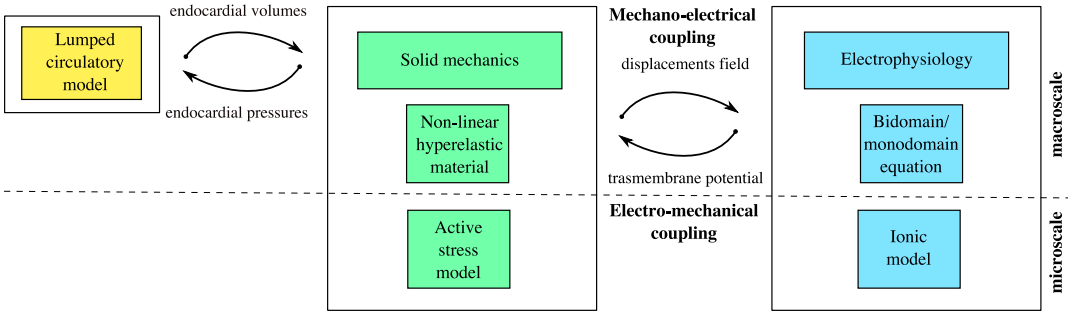

Figure 1.4. Coupling of electrophysiology, solid mechanics and lumped circulatory model. The FE mechanical model is bidirectionally coupled to FE electrophysiological model. The transfer of the displacement from the mechanical model to the electrophysiology model is required. The AP is transferred from the electrophysiological model to the mechanical model. In addition, accounting for a simplified description of the blood flow, the FE mechanical model is coupled with a lumped circulatory model. Target endocardial volumes are transferred from the circulatory model to the mechanical model. The mechanical model is then responsible for the FE description of the associated endocardial pressure which are computed and then transferred back to circulatory model.

Active strain

To include the description of the active contraction of the tissue in the balance equations, two different approaches are available in the literature. The first alternative to describe the excitation-contraction model is the *active strain formulation*. In this case the deformations arising from chemical reactions are taken into account inside a multiplicative decomposition of the deformation gradient tensor, i.e. $\mathbf{F} = \mathbf{F}_e\mathbf{F}_a$. A key assumption in this *active strain* approach is that the distortion induced by $\mathbf{F}_a$ does not store energy. The passive deformation $\mathbf{F}_e$ accommodates the material in order to preserve the compatibility of the deformation. This approach has been introduced by Taber and Perucchio in 2000 [Taber and Perucchio, 2000] and afterward investigated by others [Nardinocchi and Teresi, 2007; Cherubini et al., 2008; Rossi et al., 2012]. The second alternative is represented by the most popular *active stress* approach. In this case an active contribution is added to the stress of the material. To reproduce the contraction and torsion of the muscle, this additional contribution typically dependent on fibre orientation. As in [Smith et al., 2004; Panfilov et al., 2005; Göktepe and Kuhl, 2010], in our work we consider this latter approach which description follows.

Active stress component

The Cauchy stress tensor can be decomposed by [Lin and Yin, 1998; Wakatsuki et al., 2000]

$$\boldsymbol{\sigma} = \boldsymbol{\sigma}_p + \boldsymbol{\sigma}_a, \tag{1.98}$$

where, for incompressible materials, $\boldsymbol{\sigma}_p = \boldsymbol{\sigma}_{dev} + p\mathbf{I}$ is the passive stress representing the elastic response of the material to external loads, and $\boldsymbol{\sigma}_a$ is the active stress generated at the microscale by the contraction of the myocytes. The active component depends on a variable which represents the internal state of the cell. This state depends on multiple factors such as, i.e., the intracellular concentration of calcium ions, the history of sarcomere length changes, and the

crossbridge dynamics inside the sarcomeres [Nash and Panfilov, 2004]. Geometrical reasons suggest a dependence of the stress $\boldsymbol{\sigma}_{\mathrm{a}}$ on $\mathbf{F}$. The second Piola-Kirchhoff tensor associated to $\boldsymbol{\sigma}_{\mathrm{a}}$ reads

$$\mathbf{S}_a = J\mathbf{F}^{-1}\boldsymbol{\sigma}_{\mathrm{a}}\mathbf{F}^{-T}. \tag{1.99}$$

The associated active contribution in the first Piola-Kirchhoff tensor is expressed as $\mathbf{P}_{\mathrm{a}} = \mathbf{F}\mathbf{S}_{\mathrm{a}}$. We consider $\vec{\mathbf{e}}_{\bar{f}}$ to be the isochoric representation of $\vec{\mathbf{e}}_f$ in Eulerian coordinates. It holds that $\vec{\mathbf{e}}_{\bar{f}} = \bar{\mathbf{F}}\vec{\mathbf{e}}_f$. Following the simplified model proposed by Nash and Panfilov in 2004 [Nash and Panfilov, 2004], we consider an active stress exerted only along the fibers direction and defined as

$$\boldsymbol{\sigma}_{\mathrm{a}} = J^{-1}T_{\mathrm{a}}(\mathbf{f}\otimes\mathbf{f}) \tag{1.100}$$

where $\mathbf{f} = \dfrac{\vec{\mathbf{e}}_{\bar{f}}}{|\vec{\mathbf{e}}_{\bar{f}}|}$. The first Piola-Kirchhoff associated to $\boldsymbol{\sigma}_{\mathrm{a}}$ is

$$\mathbf{P}_{\mathrm{a}} = T_{\mathrm{a}}\mathbf{F}(\mathbf{f}\otimes\mathbf{f}), \tag{1.101}$$

and hence the Piola-Kirchhoff associated to $\boldsymbol{\sigma}$ is

$$\mathbf{P} = \mathbf{P}_{\mathrm{p}} + \mathbf{P}_{\mathrm{a}} \tag{1.102}$$

where, for incompressible materials, $\mathbf{P}_{\mathrm{p}} = \mathbf{P}_{\mathrm{dev}} + \mathbf{P}_{\mathrm{vol}}$. The scalar value T_{a} represents the active component along a fiber direction $\mathbf{f}$. In the modeling of cardiac tissue, it represents the stress generated by the contraction of the myocytes at the microscale. It depends on the internal state of the cell, see e.g. [Nash and Panfilov, 2004]. The definition of T_{a} is established by a single ODE directly dependent on the AP deviation from the myocyte resting AP V_{r}:

$$\frac{\partial T_{\mathrm{a}}}{\partial t} = \varepsilon(V)\left(k_{T_{\mathrm{a}}}(V - V_{\mathrm{r}}) - T_{\mathrm{a}}\right), \tag{1.103}$$

where $k_{T_{\mathrm{a}}} = 47.9$ kPa and

$$\epsilon(V) = \begin{cases} \epsilon_0 & \text{for} \quad V < 0.05, \\ \epsilon_\infty & \text{for} \quad V \geq 0.05. \end{cases} \tag{1.104}$$

Here function ϵ controls the delay for the activation and relaxation of T_{a}. A smoother delay function has been proposed in [Göktepe and Kuhl, 2010]:

$$\epsilon(V) = \epsilon_0 + (\epsilon_\infty - \epsilon_0)\exp\{-\exp[-\xi_{\mathrm{r}}(V - V_{\mathrm{s}})]\}. \tag{1.105}$$

Here V_{s} represents a given phase shift and ξ_{r} a transition rate. We consider $V_{\mathrm{s}} = -80$ mV, and $\xi_{\mathrm{r}} = 0.3$ mV^{-1}. As discussed in [Göktepe and Kuhl, 2010; Eriksson et al., 2013], the choice of $\epsilon_0 \leq \epsilon_\infty$ (as proposed in the original paper) results in a non-physiological short electro-mechanical delay [Panfilov et al., 2005]. For this reason, we consider the parameters $\epsilon_0 = 1$ ms^{-1} and $\epsilon_\infty = 0.01$ ms^{-1}.

1.3.2 Geometric mechano-electrical feedbacks

In this section we describe the mechano-electrical geometrical feedbacks (MEF) considered in this thesis. Additional MEFs [Colli Franzone et al., 2016, 2017] are not considered in this work, except for the ones associated to the evolution in time of the cardiac configuration. For this reason, although their importance is well known, stretch-activated channels are not considered.

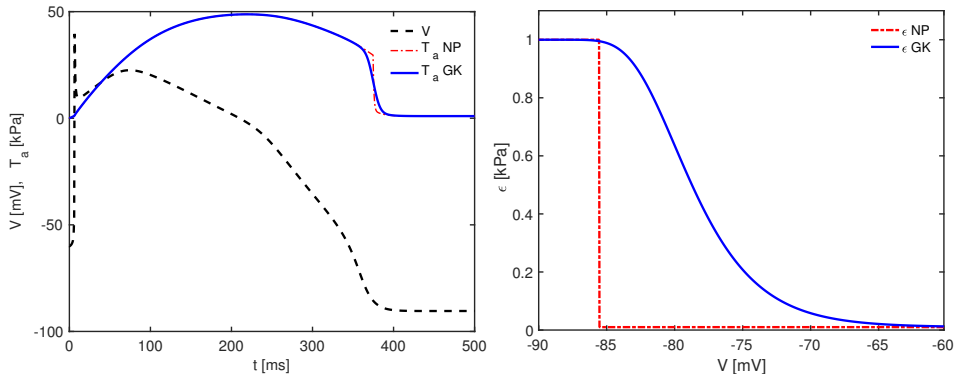

Figure 1.5. Left: Nash Panfilov (NP) and Göktepe and Kuhl (GK) active stress functions for ϵ_0=1 ms^{-1},ϵ_∞ = 0.01 ms^{-1}, V_s = -80 mV, and ξ_r = 0.3 mV^{-1}, solid lines, and action potential V, dashed line, as functions of the time. Right: delay associated to the NP and GK active stress descriptions as functions of the action potential V.

Monodomain equation on moving domain

Usually electrical simulations are performed on static meshes. However, the evolution in time of the cardiac configuration may affect the AP propagation. To account for the geometry deformation, a convenient approach, routinely adopted in computational mechanics, is to map the monodomain equation on the reference geometry $\mathscr{B}_r$. We take into account the motion of the domain inside Eq. (1.90) throughout the Piola transformation (see Sec. 1.1.3). We obtain

$$\begin{cases} J\chi(C_m\frac{\partial V}{\partial t}+I_{\text{ion}}(V,\mathbf{s},\mathbf{c})) &= \nabla\cdot\left(J\mathbf{F}^{-1}\mathbf{G}_{\text{m}}\mathbf{F}^{-T}\nabla V\right)+JI_{\text{app}}, & \text{in } \mathscr{B}_r\times\mathscr{T}\\ \dfrac{d\mathbf{s}}{dt} &= \mathbf{S}(V,\mathbf{c}) & \text{in } \mathscr{B}_r\times\mathscr{T},\\ \dfrac{d\mathbf{c}}{dt} &= \mathbf{Z}(V,\mathbf{s}) & \text{in } \mathscr{B}_r\times\mathscr{T},\\ \mathbf{n}\cdot J\mathbf{F}^{-1}\mathbf{G}_{\text{m}}\mathbf{F}^{-T}\nabla V &= 0 & \text{in } \partial\mathscr{B}_r\times\mathscr{T},\\ V(\mathscr{B}_{\text{r}},t_0)=V_0, & \mathbf{s}(\mathscr{B}_{\text{r}},t_0)=\mathbf{s}_0, & \mathbf{c}(\mathscr{B}_{\text{r}},t_0)=\mathbf{c}_0. \end{cases} \tag{1.106}$$

As a matter of fact, the electric conductivity in the reference geometry is decreased (resp. increased) if the tissue is locally stretched (resp. contracted). Moreover, mapping activation patterns arising from different models into the same reference geometry allows for easy comparison of them.

ECGs signals on moving domain

We account for the mechanical deformation of the geometry also in the computation of unipolar ECG lead potentials. We consider a rapid ECG model on moving domain under the key assumption of an infinite and homogeneous torso. For this reason, we do not consider the negligible effects of the deformation of the heart over Eq. (1.97). We consider

$$Z(\mathbf{X}')=\int_{\mathscr{B}_r} J\mathbf{F}^{-1}\mathbf{G}_{\text{i}}\mathbf{F}^{-T}\nabla V(\mathbf{X})\cdot\nabla\varphi(\mathbf{X};\mathbf{X}')d\mathbf{X}. \tag{1.107}$$

1.3.3 Electromechanics coupling strategies

In this thesis we consider two main roles played by the mechanics in modifications of the ECG signals. The first one is due to the effects of mechanical contraction on the electrical activation front [Smith et al., 2003b]. The second one is related to the change of distance from the electrodes during the cardiac cycle. These effects are taken into account replacing Eq. (1.90) and Eq. (1.95) by Eq. (1.106) and Eq. (1.107), respectively. We refer to the framework accounting for all the EMFs and MEFs described in Sec. (1.3.1) and in Sec. (1.3.2) as *bidirectional (BD)* or *fully-coupled* scenario. Accounting for both the above-mentioned mechanical roles, in our FE framework the BD scenario represents the most complete electromechanical description of the cardiac behavior. As a simplification of the BD scenario, we consider the *monodirectional (MD)* or *static-dynamic* coupling scenario, in which the electrophysiology is solved on the reference configuration neglecting the mechanical deformation of the heart. The MD approach considers all the EMFs described in Sec. 1.3.1 and the change of distance from the electrodes in the computation of the ECGs signals as described in Eq. (1.107). MD setting allows to remove all mechano-electric feedbacks (MEFs) which may affect the action potential propagation and therefore to isolate the role of the distance from the electrodes. In contrast to the BD and the MD scenario, a purely electrophysiological (PE) framework could be considered.

1.3.4 Summary of fully-coupled electromechanics governing equations

Summarizing the coupling equation of quasi-static formulation of the incompressible mechanical problem and the monodomain system we obtain the following boundary problem

Find $\mathbf{u} \in L^2(t_0, t_{\text{fin}}; H^1_{\Gamma_D}(\mathscr{B}_r)^3)$, $p \in L^2(t_0, t_{\text{fin}}; L^2(\mathscr{B}_r))$, $V \in L^2(t_0, t_{\text{fin}}; H^1(\mathscr{B}_r))$, $\mathbf{s} \in L^2(t_0, t_{\text{fin}}; (L^2(\mathscr{B}_r))^{m_g})$, $\mathbf{c} \in L^2(t_0, t_{\text{fin}}; (L^2(\mathscr{B}_r))^{m_c})$ such that

$$
\begin{cases}
-\text{Div}(\mathbf{P}) + \mathbf{B} = 0 & \text{in } \mathscr{B}_r, \\
J = 1 & \text{in } \mathscr{B}_r, \\
\mathbf{u} = 0 & \text{in } \Gamma_D, \\
\mathbf{P}\cdot\mathbf{N} = \mathbf{p}_N & \text{in } \Gamma_N, \\
J\beta(C_m \dot{V} + I_{\text{ion}}(V, \mathbf{s}, \mathbf{c})) = \nabla\cdot\left(J\mathbf{F}^{-1}\mathbf{G}_{\text{m}}\mathbf{F}^{-T}\nabla V\right) + J I_{\text{app}} & \text{in } \mathscr{B}_r \times \mathscr{T}, \\
\dot{\mathbf{s}} = \mathbf{S}(V, \mathbf{c}) & \text{in } \mathscr{B}_r \times \mathscr{T}, \\
\dot{\mathbf{c}} = \mathbf{Z}(V, \mathbf{s}) & \text{in } \mathscr{B}_r \times \mathscr{T}, \\
\mathbf{n}\cdot J\mathbf{F}^{-1}\mathbf{G}_{\text{m}}\mathbf{F}^{-T}\nabla V = 0 & \text{in } \partial\mathscr{B}_r \times \mathscr{T}, \\
V(\mathscr{B}_{\text{r}}, t_0) = V_0, \quad \mathbf{s}(\mathscr{B}_{\text{r}}, t_0) = \mathbf{s}_0, \quad \mathbf{c}(\mathscr{B}_{\text{r}}, t_0) = \mathbf{c}_0.
\end{cases}
\tag{1.108}
$$

where $\dot{V} = \frac{dV}{dt}$, $\dot{\mathbf{s}} = \frac{d\mathbf{s}}{dt}$, and $\dot{\mathbf{c}} = \frac{d\mathbf{c}}{dt}$. Moreover, it holds

$$
\mathbf{P} = \mathbf{P}_{\text{dev}} + \mathbf{P}_{\text{vol}} + \mathbf{P}_{\text{a}}. \tag{1.109}
$$

If $\Gamma_N = \emptyset$ we consider $p \in L^2(t_0, t_{\text{fin}}; L^2_0(\mathscr{B}_r))$ where $L^2_0(\Omega) = \{p \in L^2(\Omega) \colon \int_\Omega p d\Omega = 0\}$ [Quarteroni, 2009a].

1.3.5 Coupling electromechanical model with lumped models of circulations

State of the art of FE ventricular solid mechanics models involve mixed time varying boundary conditions for the description of fluid dynamics [Tagliabue et al., 2017b]. To obtain more realistic pressure and volume changes in the ventricles, FE mechanical models of the ventricles can been coupled to simple afterload models, i.e. Windkessel models [Eriksson et al., 2013]. In these models, the filling of the ventricles is prescribed by a linear increase in diastolic pressure. Coupling a left ventricular FE model (in which the left atrium is treated as a time-varying elastance) to a model of pulmonary venous return, Watanabe et al.[Watanabe et al., 2004] obtained a more realistic ventricle preload. In this thesis we coupled the FE electromechanical model outlined above with the lumped model of circulation (LMC) proposed by Kerckhoffs et al. [Kerckhoffs et al., 2007]. A similar approach has been considered in [Gurev et al., 2015]. If compared to afterload models, LMC results in a more realistic ventricles filling phase. Moreover the considered LMC accounts for the active force generated by the ventricles while the mitral and tricuspid are still open. The *Kerckhoffs et al.* time-varying elastance model includes direct ventricular interaction. Moreover, the atria are also included as time-varying elastance chambers. The model consider eight different structures, the left and right ventricles and atria, and the pulmonic and the systemic arteries and veins. Each of them is treated as a modular unit, and it is described by the time-dependent state triad $(V_i(t), p_i(t), Q_i(t))$ representing its volume, pressure and flux at the current time t. We define the time-varying vectors $\mathbf{V}, \mathbf{p}, \mathbf{Q}$ such that $(\mathbf{V})_i = V_i$, $(\mathbf{p})_i = p_i$, $(\mathbf{Q})_i = Q_i$. Pressures of modular units are obtained from modular volumes as

$$\mathbf{p} = \mathbf{E}(\mathbf{V} - \mathbf{V}_{\text{rest}}), \tag{1.110}$$

where $\mathbf{E}$ is a time-dependent matrix describing the elastance of the structures and $\mathbf{V}_{\text{rest}}$ is a vector describing of the resting volumes. The matrix $\mathbf{C} := \mathbf{E}^{-1}$ is referred to as *compliance matrix*. The flows are obtained from the difference of the pressures of subsequent modular unit as

$$\mathbf{Q} = \mathbf{R}^{-1}(\mathbf{p} - \mathbf{S}_8\mathbf{p}), \tag{1.111}$$

where $\mathbf{R}$ is the time-dependent matrix describing the module resistance and $\mathbf{S}_8$ is the matrix

$$\mathbf{S}_8 = \begin{bmatrix} \mathbf{0} & 1 \\ \mathbf{I}_7 & \mathbf{0} \end{bmatrix}.$$

Here $\mathbf{I}_7$ represents the 7×7 identity matrix. Changes in ventricular volume are purely determined by ventricular in- and outflows as

$$\frac{\mathrm{d}\mathbf{V}}{\mathrm{d}t} = (\mathbf{Q} - \mathbf{S}_8\mathbf{Q}). \tag{1.112}$$

When the circulatory model is coupled with the FE solid mechanics model, additional time dependent scalar variables V^k_{inner}, p^k_{f} representing the inner ventricular volumes and the pressures of the fluid (i.e. the radial stress at the inner wall) are introduced in the FE solid mechanics model. The flag $k = \{RV, LV\}$ distinguishes the volumes and the pressures of the left and of the right ventricles. In this case, the lumped model ventricles volumes and pressures are replaced by the V^k_{inner}, p^k_{f}. Fig. 1.6 shows a schematic representation of the biventricular FE model with the key anatomical features of the LMC embedded. We define the energy $\Psi_{\text{cm}} : \mathscr{B}_r \times \text{Lin}^+ \to \mathbb{R}$, as

$$\Psi_{\text{cm}}(\mathbf{u}, p, p^k_{\text{f}}; V^k_{\text{targ}}) = \Psi_{\text{p}} + \Psi_{\text{f}}, \tag{1.113}$$

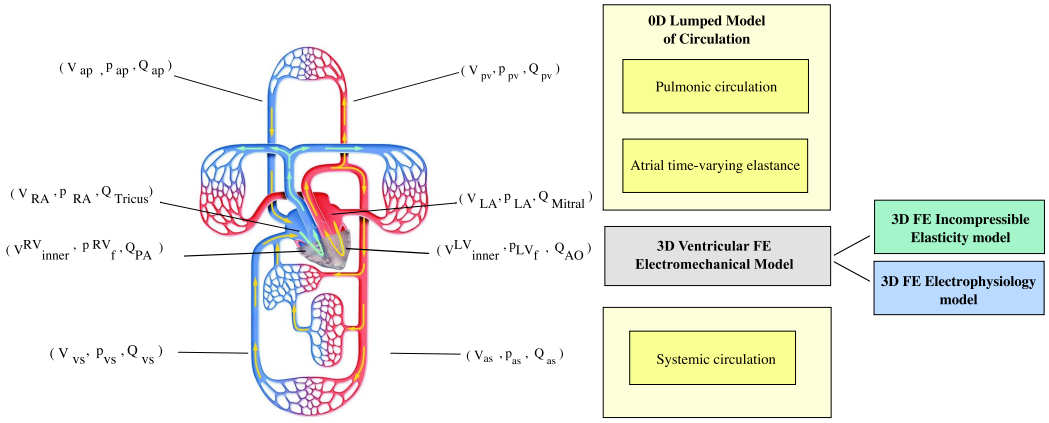

Figure 1.6. Schematic representation of the key anatomical features of the of the FE electromechanical biventricular model coupled with a LMC.

here Ψ_p is the incompressible mechanics passive hyperelastic energy described in Eq. (1.56) and Ψ_f is defined as

$$\Psi_f = p_f^k (V_{\text{inner}}^k - V_{\text{targ}}^k). \tag{1.114}$$

The parameter V_{targ}^k represents the target volume of the ventricles and it is prescribed by the LMC. Therefore Ψ_f is a penalty term accounting for the difference between the FE fluid volume V_{inner}^k and the target volume V_{targ}^k obtained from the LMC. The pressure p_f^k is the indeterminate Lagrange multiplier corresponding to such a constraint for the ventricle k. It represents an hydrostatic pressure. The construction of a FE mesh is preventable for the computation of the inner volume V_{inner}^k. In fact, consider $\mathcal{B}_{\text{inner}}^k$ to be inner cavity domain of the ventricle k. Its boundary can be represented as disjoint union of the endocardial boundary Γ_{endo}^k and of the "cap" boundary Γ_{cap}^k. The inner volume associated to the reference configuration of the domain can be computed as

$$V_{\text{inner},0}^k =:= |\mathcal{B}_{\text{inner}}^k| = \int_{\mathcal{B}_{\text{inner}}^k} d\mathbf{X} = \frac{1}{3}\int_{\mathcal{B}_{\text{inner}}^k} \text{Div}\,\mathbf{X} d\mathbf{X} = \frac{1}{3}\int_{\partial\mathcal{B}_{\text{inner}}^k} \mathbf{X}\cdot\mathbf{N} dA. \tag{1.115}$$

Suppose $\mathcal{B}_{\text{cap}}^k$ is planar, normal to $\mathbf{e}_z$ and such that each of its points has $z = 0$. Then from (1.115) we obtain

$$V_{\text{inner},0}^k = -\frac{1}{3}\int_{\Gamma_{\text{endo}}^k} \mathbf{X}\cdot\mathbf{N} dA + \frac{1}{3}\int_{\Gamma_{\text{cap}}^k} \mathbf{X}\cdot\mathbf{e}_z dA = -\frac{1}{3}\int_{\Gamma_{\text{endo}}^k} \mathbf{X}\cdot\mathbf{N} dA \tag{1.116}$$

We recall that the sign is reverse since the outer normal to Γ_{endo}^k is opposite to the one to $\partial\mathcal{B}_0$. In the current configuration we have the following formula for the inner volume

$$V_{\text{inner,t}}^k := |\chi(\mathcal{B}_{\text{inner}}^k, t)| = -\frac{1}{3}\int_{\chi(\Gamma_{\text{endo}}^k, t)} \mathbf{x}\cdot\mathbf{n} da = -\frac{1}{3}\int_{\Gamma_{\text{endo}}^k} J(\mathbf{X}+\mathbf{u})\mathbf{F}^{-T}\cdot\mathbf{N} dA, \tag{1.117}$$

in which the third equality is obtained applying the Piola transformation (see Sec. 1.1.3). In the original circulatory model, the four chambers time-varying elastance parameters are obtained

from the diastolic and systolic unloaded volumes through trigonometric activation functions. In the LMC proposed in [Kerckhoffs et al., 2007] the active stress is described as a given trigonometric function. Accounting for a progressive delayed activation of the tissue, in this thesis more physiological ATs obtained from the Eikonal-diffusion model (see Sec. 1.2.13) are considered. In this case the cellular start time of first active ventricular contraction prescribed by the LMC [Kerckhoffs et al., 2007] is shifted by the simulated AT, i.e.

$$t_{\text{active,AT}}(\mathbf{x}) = t_{\text{active}} + \psi(\mathbf{x}) \tag{1.118}$$

To summarize, the considered LMC - FE electromechanical involved the

- LMC proposed by Kerckhoffs et al. for the description of systemic and pulmonic circulations and atrial time-varying elastance;
- FE model of incompressible mechanics with Guccione-Costa constitutive law (see Sec. 1.1.8) and with active stress component (see Sec 1.3) for the description of the passive and active contraction of the geometry;
- FE Eikonal model (see Sec. 1.2.13) for the simulation of the asynchronous electrical activation of the tissue.

Circulation lumped models - FE electromechanics coupling strategies

As already discuss in the previous section, the target volume parameter V^k_{targ} is prescribed by the LMC. Two different coupling strategies arise from the choice of p^k_{f} in the circulation lumped model. In *loosely coupled* simulations the pressures of the ventricles in the circulation lumped model is considered to be independent on pressure of the FE model. In *tightly coupled* simulations the pressures of the ventricles in the circulation lumped model are imposed to be equivalent to the one of the FE mechanical model in, i.e. $p^k = p^k_{\text{f}}$. At the price of an higher number of iterations in case implicit solution methods are taken into account, we considered the tightly coupling strategy.

1.4 Computational aspects

1.4.1 Idealized ventricle geometry

The mean length, width and thickness of a human ventricle are around 1, 8.5, and 4 cm [Gupta et al., 2014], respectively resulting in a corresponding volume between 80 ÷ 120 ml. The left ventricular geometry is generally approximated by a truncated ellipsoid usually described adopting *prolate spheroidal coordinates* [LeGrice et al., 2001a; Colli Franzone and Pavarino, 2004]. Defining the idealized ventricle as a prolate ellipsoid, the fibers orientation can be analytically defined [Colli Franzone et al., 2012; Eriksson et al., 2013]. Fibers orientation can also be described by approximate geodesic [Peskin, 1989]. In this thesis, we consider the ellipsoidal idealization of a rabbit ventricle proposed by Land et al. in [Land et al., 2015a]. The position of a generic point $\mathbf{X}$ in the reference geometry is defined using the parametrization of a truncated ellipsoid

$$\mathbf{X} = \begin{bmatrix} X \\ Y \\ Z \end{bmatrix} = \begin{bmatrix} r_s \sin u \cos v \\ r_s \sin u \sin v \\ r_l \cos u \end{bmatrix} \tag{1.119}$$

The undeformed geometry is defined by the volume between

- the *endocardial surface*, obtained for $r_s = 7$mm, $r_l = 17$mm, $u \in [-\pi, -arccos\frac{5}{17}]$, $v \in [-pi, \pi]$,
- the *epicardial surface*, obtained for $r_s = 10$mm, $r_l = 20$mm, $u \in [-\pi, -arccos\frac{5}{20}]$, $v \in [-pi, \pi]$,
- the base plane $z = 5$ mm which is implicitly defined by the ranges for u.

For the correct computation of the inner volume of the ventricle (see Sec. 1.3.5), the undeformed geometry is then shifted in the $\mathbf{e}_z$ direction such that for the base plane $z = 0$. We compute the local fiber orientation following the definition discussed in Sec. 1.1.7.

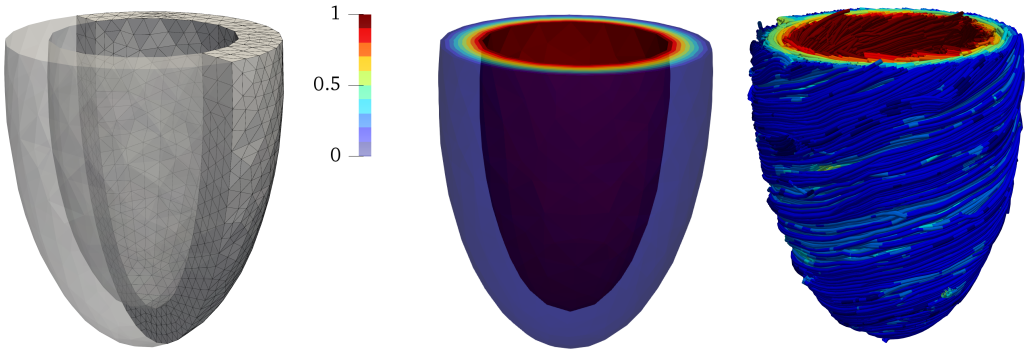

Figure 1.7. Left: idealized LV geometry with the tetrahedral finite element mesh. Middle: transmural coordinate ρ. Right: fibers distribution in anterior view. The colormap displays the trasmural coordinate ρ.

1.4.2 Biventricular geometry

A biventricular geometry for a heart failure was provided by our collaboration at Cardiocentro Ticino (Lugano, Switzerland). Left ventricular volumes were within the upper limits, mildly reduced ejection fraction (39%) and pattern of dyssynchrony compatible with left bundle branch block. The patient underwent a clinical standard magnetic resonance (Siemens, 3.0 T) before the procedure. The model, presented in [Potse et al., 2012], merges all the structures of interest in Blender [Blender Online Community]. In details, the endocardial and epicardial boundaries of the ventricles were segmented on the 3D SSFP (Steady-State Free Precessions) sequences in late diastole using a semi-automatic segmentation approach [Conti et al., 2011]. Atrial walls, lungs, big vessels and the thorax were segmented from a static, 3D, ultra-fast volume-interpolated breath-hold examination (ViBe sequence[Barnich and Van Droogenbroeck, 2011]). The locations of the surface electrodes were also manually identified in the latter. The patient provided written consent, and the institutional review board approved the use of the data for purpose of this research. A visualization of the geometry and its associated mesh and computed transmural thickness parameter are reported in Fig. 1.8. The left ventricle (LV) and right ventricle (RV) blood

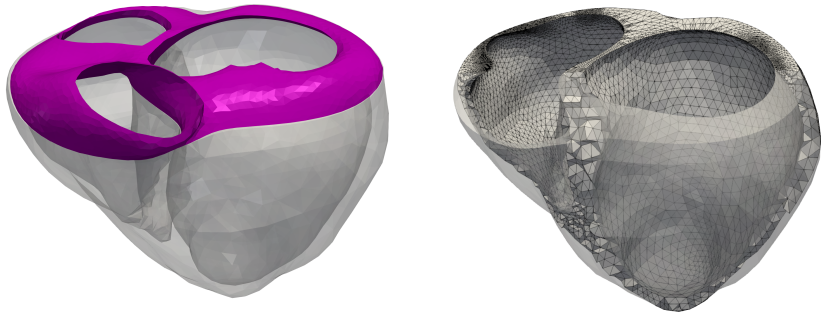

Figure 1.8. Biventricular geometry. Left: the cropped valves plane is highlighted in purple. Right: the geometry with the tetrahedral finite element mesh.

pools were ~ 140 ml and ~ 80 ml, respectively. We cropped the top of the geometry to impose Γ_D to be the valves plane. For simplicity, we cut the base at by a planar face orthogonal to $\vec{\mathbf{e}}_z$. This was reflected in a negligible internal volume loss $< 1\%$. The cropped area is highlighted in purple in Fig. 1.8. As discussed in [Augustin et al., 2016; Costa et al., 1996], the use of high order cubic Hermite Finite Elements (FE) became very popular in cardiac mechanics simulations. The main reasons is that these elements allow a tessellation of approximate ventricular anatomy using a very small number of elements For the tessellation of the geometry we considered tetrahedral elements. An accurate description of the geometry microstructure requires a consider uniform meshes with at the minimum $\sim 15\,k$ tetrahedral elements. The mesh spacing is indicative and varies with the considered simulation. The computed transmural coordinate ρ and the fibers distribution for the geometry are reported in Fig. 1.9.

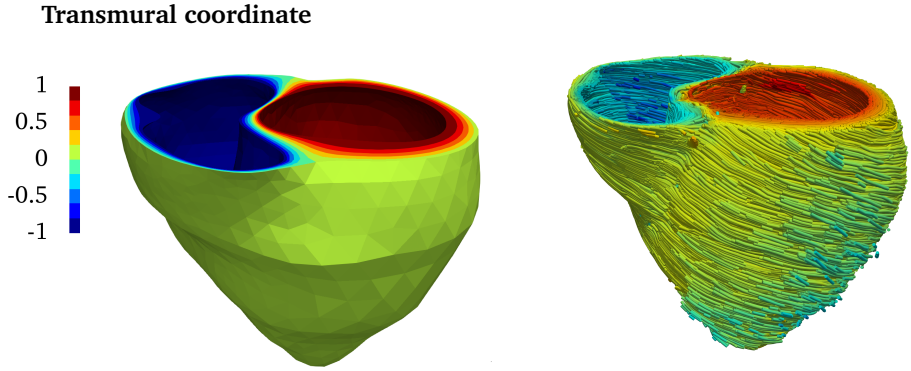

Figure 1.9. Left: transmural coordinate ρ computed for the biventricular geometry. Right: fibers distribution for the biventricular geometry in anterior view.

Chapter 2

Variational formulations and solution methods

In this chapter we discuss numerical discretization schemes for the fully coupled electromechanical model introduced in Chpt. 1. The multiscale nature of the coupled system results in the need of different spatio-temporal scales for the solution of sub-systems describing each sub-mechanism [Quarteroni et al., 2017]. In detail, cardiac electrophysiology involves functionalities occurring at the meso- (action potential) and micro- (ionic channels) scales. Therefore a high space-time resolution is necessary to capture the fast transient excitation wavefront. In particular the steep upstroke of the action potential results in a large spatial gradient in the AP field. This demands a high spatial resolution (e.g. for the human heart model in the order of 10^8 nodes). Moreover, the stiffness associated with the time-evolution of the gating variables results in the need of very small time-steps, which could go below the order of 10^{-2} ms in case explicit time stepping schemes are considered [M. Potse et al., 2006]. In contrast, the description of the mechanical response of the tissue involves functionalities occurring at the macro-scale. For this reason the elastic behavior of the cardiac muscle can be simulated using coarser spatial and temporal scales if compared to the simulation of its electrical activation. The multiple nonlinearities arising in the system (1.108) represent an addition difficulty for the solution of the electromechanical model. The nonlinearities originate, for example, from the mechanical constitutive equations, from the large deformations of the muscle, from Neumann boundary conditions in the mechanical problem and from the complex dependency of the ionic currents on the AP. Newton's method [Kantorovich, 1948] is a standard iterative solution algorithm for the solution of nonlinear problems. Using Newton's like algorithms, the entire fully coupled electromechanical system can be solved in a monolithic fashion all at once. This choice results in stable algorithms which, due to the fine (in space and in time) discretization scale required, are of considerable complexity. A more common choice is to use segregated approaches, in which each the sub-problem is solved sequentially. This allow for the use of appropriately fitted solution strategy and space-time discretization grids for each sub-problem. In the literature finite volumes methods and finite element methods (FEM) have been used to discretize the monodomain system and the mechanical equations describing the cardiac activity. In our work the discretization of the governing equations is based on the FEM. The FEM is a Galerkin discretization method commonly applied for physical problems described by PDEs [Quarteroni, 2009b; Braess, 2009; Hughes, 2009]. The chapter is organized as follows: in Sec. 2.1 we present Newton's algorithm

that we consider for the numerical solution of system (1.108). The derivation of this method requires the differentiability in Banach spaces. For this reason we first give the definition of Gâteaux differential [Lindenstrauss and Preiss, 2003]. In Sec. 2.2 we discuss the weak form of the mechanical and of the governing equations in electrophysiology. The time discretization of the weak forms follows in Sec. 2.3. In Sec. 2.4, we discuss different schemes for the time advancing of the coupled electromechanical problem. In particular, we outline segregated algorithms for the numerical solution of the fully coupled electromechanical problem. Introducing the FE approximation of the variables of interests, the fully discretized equations are presented in Sec. 2.5. Segregated solution strategies are then expressed in algebraic form. We recall that, the FE approximation can be directly generalized for the high-order time discretization schemes introduced in Chpt. 5.

2.1 Newton's method

Let V and W be two Banach spaces. A function $\mathscr{K} : V \to W$ is said to be Gâteaux differentiable at $\boldsymbol{x} \in V$ in direction $\mathbf{h} \in V$ if there exists a bounded linear operator $T_{\mathbf{x}} \in \mathscr{L}(V, W)$ such that

$$\lim_{\epsilon \to 0} \frac{\mathscr{K}(\mathbf{x} + \epsilon \mathbf{h}) - \mathscr{K}(\mathbf{x})}{\epsilon} = T_{\mathbf{x}} \mathbf{h}. \tag{2.1}$$

$\mathscr{K}$ is Gâteaux differentiable at $\mathbf{x}$ if and only if the limit above exists for all $\mathbf{h} \in V$ and there exists a bounded linear operator $T_{\mathbf{x}} : \mathbf{h} \to T_{\mathbf{x}}\mathbf{h}$. We denote the Gâteaux derivative as $\mathscr{D}\mathscr{K}(\mathbf{x})[\mathbf{h}]$. Consider a generic operator $\mathscr{R} : V \to V^*$. Newton's method to find the a root of $\mathscr{R}$ reads as described in Alg. (1). In practical cases, the computation of $\mathscr{D}\mathscr{R}$ can be very expensive. Hence, it is possible

1: **Given** $\mathbf{x}_0 \in V$;
2: **until** <convergence criteria> is satisfied:
3: **solve for** $\delta\mathbf{x}$ such that $\mathscr{D}\mathscr{R}(\mathbf{x}^k)\delta\mathbf{x} = -\mathscr{R}(\mathbf{x}^k)$;
4: **update** $\mathbf{x}^{k+1} = \mathbf{x}^k + \delta\mathbf{x}$.

Algorithm 1: Newton's method.

to approximate $\mathscr{D}\mathscr{R}$ by $\hat{\mathscr{D}}\mathscr{R}$. In this case the method is referred to as quasi-Newton method. There are two possible stopping criteria for the Newton's method: the control of residuals and the control of increments. In the former, for a given $\epsilon > 0$, the algorithm stops if

$$\|\mathscr{R}(\mathbf{u}^k, \cdot)\| \leq \epsilon. \tag{2.2}$$

In the latter, the algorithm stops when

$$\|\mathbf{u}^k - \mathbf{u}^{k-1}\|_V \leq \epsilon. \tag{2.3}$$

In this thesis we consider the former stopping criteria.

2.2 Weak formulation

2.2.1 Weak form of the incompressible mechanics system

In the following section we introduce the weak formulation of nonlinear elasticity, also known as *principle of virtual work* [Marsden and Hughes, 1994b]. We define the space $H^p(\mathscr{B}_r)$ to be

$$H^p(\mathscr{B}_r) := \{ f \in L^2(\mathscr{B}_r) \colon D^{\boldsymbol{\alpha}} f \in L^2(\mathscr{B}), \forall \boldsymbol{\alpha} \colon |\boldsymbol{\alpha}| \leq p \}. \tag{2.4}$$

Important subspaces of $H^1(\mathscr{B}_r)$ are

- $H^1_{\Gamma_D}(\mathscr{B}_r) := \{f \in H^1(\mathscr{B}_r) : f \mid_{\Gamma_D} = 0\}$;
- $H^1_0(\mathscr{B}_r) := H^1_{\Gamma_D}(\mathscr{B}_r)$ if $\Gamma_D = \partial\mathscr{B}_r$;

where the equality $f|_{\Gamma_D} = 0$ has to be intended in a weak sense. A solution $(\mathbf{u}, p)$ of the system

$$\begin{cases} -\mathrm{Div}(\mathbf{P}(\mathbf{u},p,V)) + \mathbf{B} &= 0 \quad \text{in } \mathscr{B}_r \times \mathscr{T}, \\ J(\mathbf{u}) &= 1 \quad \text{in } \mathscr{B}_r \times \mathscr{T}, \\ \mathbf{u} &= 0 \quad \text{in } \Gamma_D \times \mathscr{T}, \\ \mathbf{P}(\mathbf{u},p,V)\cdot\mathbf{N} &= \mathbf{p}_N \quad \text{in } \Gamma_N \times \mathscr{T}, \end{cases} \tag{2.5}$$

belongs to $L^2(t_0, t_{\text{fin}}; W) \times L^2(t_0, t_{\text{fin}}; Q)$ where we consider $W := H^1_{\Gamma_D}(\mathscr{B}_r)^3$ and $Q := L^2(\mathscr{B}_r)$. Detailed discussions on admissible function spaces in case of nonlinear elasticity are reported in [Tallec, 1994; Ball, 1976]. In the residual form, weak form of the incompressible elasticity problem reads
Find $\mathbf{u} \in L^2(t_0, t_{\text{fin}}; W)$, $p \in L^2(t_0, t_{\text{fin}}; Q)$ s.t.

$$\begin{cases} \int_{\mathscr{B}_r} \mathbf{P} : \nabla\mathbf{v}\,\mathrm{d}\mathbf{X} - \int_{\Gamma_N} \mathbf{p}_N \cdot \mathbf{v}\,\mathrm{d}A + \int_{\mathscr{B}_r} \mathbf{B}\cdot\mathbf{v}\,\mathrm{d}\mathbf{X} &= 0 \quad \forall \mathbf{v} \in W, \\ \int_{\mathscr{B}_r} (J-1)\,q\,\mathrm{d}\mathbf{X} &= 0 \quad \forall q \in Q. \end{cases} \tag{2.6}$$

Considering (1.109) it can be more explicitly written

$$\int_{\mathscr{B}_r} \mathbf{P}(\mathbf{u},p,V) : \nabla\mathbf{v}\mathrm{d}\mathbf{X} = \int_{\mathscr{B}_r} \left(\mathbf{P}_{\text{dev}}(\mathbf{u}) + pJ(\mathbf{u})\mathbf{F}^{-T}(\mathbf{u}) + T_{\text{a}}(V)(\mathbf{f}\otimes\mathbf{f})\mathbf{F}^{-T}\right) : \nabla\mathbf{v}\,\mathrm{d}\mathbf{X}. \tag{2.7}$$

Eq. (2.6.1) is the weak formulation of the momentum equation (2.5.1) and it is a linear functional of $\mathbf{v}$ and is nonlinear in $\mathbf{u}$, and p. Here the AP is considered as given. Equation (2.6.2) is the weak formulation of the mass balance equation (2.5.2). It is a linear functional of q and is parametrized in $\mathbf{u}$. Since the boundary integral in (2.6.1) cannot be written as a derivative of an energy, the formulation (2.6) cannot be obtained from a Hellinger-Reissner-like principle, i.e. as a Gâteaux derivative of a Lagrangian function. In contrast, in case $\Gamma_N = \emptyset$ the function

$$\mathscr{L}(\mathbf{u},p) = \int_{\mathscr{B}_r} \bar{\Psi}(\mathbf{F})\mathrm{d}\mathbf{X} + \int_{\mathscr{B}_r} p(J-1)\mathrm{d}\mathbf{X} + \int_{\mathscr{B}_r} \mathbf{B}(\mathbf{v})\cdot\mathbf{v}\mathrm{d}\mathbf{X} \tag{2.8}$$

is the Lagrangian function which stationary point $(\mathbf{u}, p)$ is solution of (2.6).

2.2.2 Weak form of the monodomain equation

We here introduce the weak formulation of the monodomain system. Defined $R := H^1(\mathscr{B}_r)$, the monodomain system reads Find $V \in L^2(t_0, t_{\text{fin}}; R)$, $\mathbf{s} \in (C^1(t_0, t_{\text{fin}}))^{m_{\text{g}}}$, $\mathbf{c} \in (C^1(t_0, t_{\text{fin}}))^{m_{\text{c}}}$ s.t.

$$\begin{cases} J(\mathbf{u})\beta(C_m\dot{V} + I_{\text{ion}}(V,\mathbf{s},\mathbf{c})) &= \nabla\cdot\left(J(\mathbf{u})\mathbf{F}^{-1}(\mathbf{u})\mathbf{G}_{\text{m}}\mathbf{F}^{-T}(\mathbf{u})\nabla V\right) + J(\mathbf{u})I_{\text{app}} \quad \text{in } \mathscr{B}_r \times \mathscr{T}, \\ \mathbf{n}\cdot J(\mathbf{u})\mathbf{F}^{-1}(\mathbf{u})\mathbf{G}_{\text{m}}\mathbf{F}^{-T}(\mathbf{u})\nabla V &= 0 \quad \text{in } \partial\mathscr{B}_r \times \mathscr{T}, \\ \dot{\mathbf{s}} &= \mathbf{S}(V,\mathbf{c}) \quad \text{in } \mathscr{B}_r \times \mathscr{T}, \\ \dot{\mathbf{c}} &= \mathbf{Z}(V,\mathbf{s}) \quad \text{in } \mathscr{B}_r \times \mathscr{T}, \\ V(\mathscr{B}_{\text{r}}, t_0) = V_0,\ \mathbf{s}(\mathscr{B}_{\text{r}}, t_0) &= \mathbf{s}_0,\ \mathbf{c}(\mathscr{B}_{\text{r}}, t_0) = \mathbf{c}_0. \end{cases} \tag{2.9}$$

Here we suppose the displacement and the pressure to be given. We recall that the definitions of $\mathbf{S}$ and $\mathbf{Z}$ do not usually involve derivative in space of $V, \mathbf{s}, \mathbf{c}$. For this reason in the FE framework, it is convenient to solve the gating variables $\mathbf{s}$ and of the ionic concentrations $\mathbf{c}$ at each nodal point [Quarteroni et al., 2017]. The weak form of Eq. (2.9) reads

Find $V \in L^2(t_0, t_{\text{fin}}; R)$, $\mathbf{s} \in (C^1(t_0, t_{\text{fin}}))^{m_g}$, $\mathbf{c} \in (C^1(t_0, t_{\text{fin}}))^{m_c}$ s.t. $\forall r \in R$

$$\begin{cases} \int_{\mathscr{B}_r} J(\mathbf{u}) \beta C_m \dot{V}\, r \mathrm{d}\mathbf{X} + \int_{\mathscr{B}_r} J(\mathbf{u})(\beta C_m I_{\text{ion}}(V, \mathbf{s}, \mathbf{c})\, r \mathrm{d}\mathbf{X} + \\ -\int_{\mathscr{B}_r} J(\mathbf{u}) \mathbf{F}^{-1}(\mathbf{u}) \mathbf{G}_{\text{m}} \mathbf{F}^{-T}(\mathbf{u}) \nabla V \cdot \nabla r \mathrm{d}\mathbf{X} - \int_{\mathscr{B}_r} J(\mathbf{u}) I_{\text{app}}\, r \mathrm{d}\mathbf{X} &= 0, \\ \dot{\mathbf{s}} &= \mathbf{S}(V, \mathbf{c}), \\ \dot{\mathbf{c}} &= \mathbf{Z}(V, \mathbf{s}), \\ V(\mathscr{B}_{\text{r}}, t_0) = V_0,\ \mathbf{s}(\mathscr{B}_{\text{r}}, t_0) = \mathbf{s}_0,\ \mathbf{c}(\mathscr{B}_{\text{r}}, t_0) &= \mathbf{c}_0. \end{cases} \tag{2.10}$$

2.2.3 Weak form of the fully coupled electromechanical problem

In the residual form, the weak form of the problem (1.108) reads:

Find $\mathbf{u} \in L^2(t_0, t_{\text{fin}}; W)$, $p \in L^2(t_0, t_{\text{fin}}; Q)$, $V \in L^2(t_0, t_{\text{fin}}; R)$, $\mathbf{s} \in (C^1(t_0, t_{\text{fin}}))^{m_g}$, $\mathbf{c} \in (C^1(t_0, t_{\text{fin}}))^{m_c}$ s.t. $\forall r \in R$, $\forall \mathbf{v} \in W$, $\forall q \in Q$,

$$\begin{cases} \int_{\mathscr{B}_r} \mathbf{P}(\mathbf{u}, p, V) : \nabla \mathbf{v} \mathrm{d}\mathbf{X} - \int_{\Gamma_N} \mathbf{p}_N \cdot \mathbf{v}\, \mathrm{d}A + \int_{\mathscr{B}_r} \mathbf{B} \cdot \mathbf{v} \mathrm{d}\mathbf{X} = & 0, \\ \int_{\mathscr{B}_r} (J - 1(\mathbf{u}))q\, \mathrm{d}\mathbf{X} = & 0, \\ \int_{\mathscr{B}_r} J(\mathbf{u}) \beta C_m \dot{V}\, r \mathrm{d}\mathbf{X} + \int_{\mathscr{B}_r} J(\mathbf{u})(\beta C_m I_{\text{ion}}(V, \mathbf{s}, \mathbf{c})\, r \mathrm{d}\mathbf{X} + & \\ -\int_{\mathscr{B}_r} J(\mathbf{u}) \mathbf{F}^{-1}(\mathbf{u}) \mathbf{G}_{\text{m}} \mathbf{F}^{-T}(\mathbf{u}) \nabla V \cdot \nabla r \mathrm{d}\mathbf{X} - \int_{\mathscr{B}_r} J(\mathbf{u}) I_{\text{app}}\, r \mathrm{d}\mathbf{X} = & 0, \\ \dot{\mathbf{s}} = & \mathbf{S}(V, \mathbf{c}), \\ \dot{\mathbf{c}} = & \mathbf{Z}(V, \mathbf{s}), \\ V(\mathscr{B}_{\text{r}}, t_0) = V_0,\ \mathbf{s}(\mathscr{B}_{\text{r}}, t_0) = \mathbf{s}_0,\ \mathbf{c}(\mathscr{B}_{\text{r}}, t_0) = & \mathbf{c}_0. \end{cases} \tag{2.11}$$

2.3 Time discretization

In this section, we discuss standard time stepping schemes for the solution of the fully coupled electromechanical problem (2.11). Low-order methods are the most common choice in literature for the solution of bidomain and monodomain equations.

In [Vigmond et al., 2002; M. Potse et al., 2006; Krause et al., 2012] an *explicit Euler* discretization for the bidomain equation in parabolic-elliptic form or the monodomain equation is considered. Let $\mathscr{T} = [t_0, t_{fin}]$ be partitioned into N subintervals $[t^n, t^{n+1}]$ of constant time step τ. Explicit or explicit-implicit low-order discretization schemes can be combined with a first-order splitting scheme resulting in decoupling state variables and the ionic equations from the bidomain or monodomain equation. Explicit discretization schemes are bound to the stability constraint $\tau << h^2$, where h denotes the minimal mesh width of the spatial discretization. This constraint renders explicit schemes inapplicable for studies involving a high spatial resolution.

In Rush-Larsen (RL) approach [Rush and Larsen, 1978], the time integration of the ODEs describing the gating variables is performed exactly by assuming the action potential constant over the interval of integration. This method is equivalent to an explicit exponential integrator [Nørsett, 1969] and prevents over- and under-shooting in the numerical solution of gating variables, ensuring that these belong to the physiological range $[0,1]$. This property is usually referred to as positivity properties of the numerical scheme [Perego and Veneziani, 2009]. The ODE describing the AP is integrated by means of an explicit Euler method. RL method improves the stability with respect to standard explicit integrators, but its convergence is limited to the first order.
In contrast to explicit methods, the stability constraint of implicit time discretization schemes are independent of the spatial discretization. However, due to their nonlinearity, these scheme typically leads to a higher computational cost.

In this section, we consider *implicit-explicit* (IMEX) time stepping schemes [Ethier and Bourgault, 2008b] which combine the simplicity and low cost per time step of the explicit schemes with the stability of implicit schemes. In these latters, the diffusion term is implicitly treated, while the reaction term is explicitly considered. Even if they are conditionally stable, these methods allow to employ larger time-steps and to solve one linear system per time-step. Moreover, we combine the scheme with a first-order splitting. In detail, we consider an explicit exponential integrator for the gating variables and an explicit integrator for the solution of ionic concentrations. We denote with a superscript n the quantities computed at time t^n. The first-order IMEX-RL scheme for the solution of the fully coupled weak electromechanical problem (2.11) reads
Given $\mathbf{u}^n \in U$, $p^n \in P$, $V^n \in R$, find $\mathbf{u}^{n+1} \in U$, $p^{n+1} \in P$, $V^{n+1} \in R$ s.t.

$$
\begin{cases}
\int_{\mathscr{B}_r} \mathbf{P}(\mathbf{u}^{n+1}, p^{n+1}, V^{n+1}) : \nabla \mathbf{v} \mathrm{d}\mathbf{X} - \int_{\Gamma_N} \mathbf{p}_N \cdot \mathbf{v}\, \mathrm{d}A + \int_{\mathscr{B}_r} \mathbf{B} \cdot \mathbf{v} \mathrm{d}\mathbf{X} = & 0, \\
\int_{\mathscr{B}_r} (J(\mathbf{u}^{n+1} - 1)\, q\, \mathrm{d}\mathbf{X} = & 0, \\
\int_{\mathscr{B}_r} J(\mathbf{u}^{n+1}) \beta C_m V^{n+1}\, r \mathrm{d}\mathbf{X} - \int_{\mathscr{B}_r} J(\mathbf{u}^{n+1}) \beta C_m V^n\, r \mathrm{d}\mathbf{X} + & \\
- \int_{\mathscr{B}_r} \tau J(\mathbf{u}^{n+1}) \mathbf{F}^{-1}(\mathbf{u}^{n+1}) \mathbf{G}_{\mathrm{m}} \mathbf{F}^{-T}(\mathbf{u}^{n+1}) \nabla V^{n+1} \cdot \nabla r \mathrm{d}\mathbf{X} + & \\
+ \int_{\mathscr{B}_r} \tau J(\mathbf{u}^n)(\beta C_m I_{\mathrm{ion}}(V^n, \mathbf{s}^{n+1}, \mathbf{c}^{n+1})\, r \mathrm{d}\mathbf{X} - \int_{\mathscr{B}_r} \tau J(\mathbf{u}^n) I_{\mathrm{app}}\, r \mathrm{d}\mathbf{X} = & 0, \\
s_i^{n+1} = s_{\infty,i}^n - (s_{\infty,i}^n - s_i^n) e^{-\frac{\tau}{\theta_i^n}}, \quad \text{for } i = 1, \ldots, m_g, & \\
\mathbf{c}^{n+1} = \mathbf{c}^n + \tau \mathbf{Z}(V^n, \mathbf{s}^n), & \\
V(\mathscr{B}_{\mathrm{r}}, t_0) = V_0,\ \mathbf{s}(\mathscr{B}_{\mathrm{r}}, t_0) = \mathbf{s}_0,\ \mathbf{c}(\mathscr{B}_{\mathrm{r}}, t_0) = \mathbf{c}_0. &
\end{cases}
\tag{2.12}
$$

2.4 Solution algorithms for the electromechanical problem

For the solution of the electromechanical problem monolithic and segregated approaches are available in the literature. In monolithic approaches the entire problem is considered and solved all at once for every time step. In contrast, in segregated approaches each sub-problem is solved sequentially and the obtained solution is used to initialize the next sub-system. This is done until all sub-systems are solved. This algorithm is iterated until convergence for the initial problem is reached. Segregated approaches allow for the use of appropriately fitted solution strategy and space-time discretization grids for each sub-problem. In this section we outline segregated schemes used for numerical simulation presented in the following chapters. In our case, the

usage of segregated schemes for the solution of the fully coupled electromechanical problem is motivated by the strain-rate independent activation model considered. Studies have reported numerical instabilities associated to these latter schemes [Niederer and Smith, 2008; Pathmanathan et al., 2010]. We recall that in our case for the proposed ionic models, we did no observed numerical instabilities associated to the proposed segregated scheme.

2.4.1 Monolithic solution of the fully coupled electromechanical problem

The solution of system (2.12) in the framework of the Newton's method requires the linearization of the problem around the point $(\mathbf{u}^k,\, p^k,\, V^k)$. This gives rise to the so-called *tangent problem*. The linearization is obtained from the computation of the Gâteaux derivative of $\mathscr{M}_u$, $\mathscr{M}_p$, and $\mathscr{E}$ with respect to the displacement $\mathbf{u}$, the pressure p and the AP. Linearizing Eq. (2.12) around the generic point $(\mathbf{u},\, p,\, V)$ we obtain

Find $(\mathbf{h}, \pi, \xi) \in W \times Q \times R$ s.t.

$$\begin{aligned}
a(\mathbf{h},\mathbf{v};\mathbf{u},p,V) \quad + \quad b(\mathbf{v},\pi;\mathbf{u}) \qquad\qquad\qquad &= -\mathscr{M}_{\mathbf{u}}(\mathbf{v};\mathbf{u},p,V) \qquad \forall \mathbf{v} \in W,\\
b(\mathbf{h},q;\mathbf{u}) \qquad\qquad\qquad\qquad\qquad &= -\mathscr{M}_p(q;\mathbf{u}) \qquad\quad \forall q \in Q,\\
c(\mathbf{h},r;V,\mathbf{s},\mathbf{c},\mathbf{u}) \qquad + \quad e(\xi,r;V,\mathbf{s},\mathbf{c},\mathbf{u}) \quad &= -\mathscr{E}(r;V,\mathbf{s},\mathbf{c},\mathbf{u}) \qquad \forall r \in R.
\end{aligned} \tag{2.13}$$

In the system above, we have that

$$\begin{aligned}
a(\mathbf{h},\mathbf{v};\mathbf{u},p,V) &:= \mathscr{D}_{\mathbf{u}}\mathscr{M}_{\mathbf{u}}(\mathbf{v};\mathbf{u},p,V)[\mathbf{h}],\\
b(\mathbf{h},q;\mathbf{u}) &:= \mathscr{D}_{\mathbf{u}}\mathscr{M}_p(q;\mathbf{u})[\mathbf{h}] \qquad = \mathscr{D}_q\mathscr{M}_{\mathbf{u}}(\mathbf{h};\mathbf{u},q,V)[\pi],\\
c(\mathbf{h},r;V,\mathbf{s},\mathbf{c},\mathbf{u}) &:= \mathscr{D}_{\mathbf{u}}\mathscr{E}(r;V,\mathbf{s},\mathbf{c},\mathbf{u})[\mathbf{h}],\\
e(\mathbf{h},r;V,\mathbf{s},\mathbf{c},\mathbf{u}) &:= \mathscr{D}_V\mathscr{E}(r;V,\mathbf{s},\mathbf{c},\mathbf{u})[\mathbf{h}],
\end{aligned} \tag{2.14}$$

where we have defined

$$\mathscr{M}_{\mathbf{u}}(\mathbf{v};\mathbf{u},p,V) := \mathscr{M}_{\text{dev}}(\mathbf{v};\mathbf{u}) + \mathscr{M}_{\text{vol}}(\mathbf{v};\mathbf{u},p) + \mathscr{M}_{\text{act}}(\mathbf{v};\mathbf{u},V) + \mathscr{M}_{\text{B}}(\mathbf{v}) + \mathscr{M}_{\text{N}}(\mathbf{v};\mathbf{u}), \tag{2.15}$$

for

$$\begin{aligned}
\mathscr{M}_{\text{dev}}(\mathbf{v};\mathbf{u}) &:= \int_{\mathscr{B}_r} \mathbf{P}_{\text{dev}} : \nabla\mathbf{v}\,\mathrm{d}\mathbf{X},\\
\mathscr{M}_{\text{vol}}(\mathbf{v};\mathbf{u},p) &:= \int_{\mathscr{B}_r} pJ\mathbf{F}^{-T} : \nabla\mathbf{v}\,\mathrm{d}\mathbf{X},\\
\mathscr{M}_{\text{act}}(\mathbf{v};\mathbf{u},V) &:= \int_{\mathscr{B}_r} T_{\text{a}}\,(\mathbf{f}\otimes\mathbf{f})\,\mathbf{F}^{-T} : \nabla\mathbf{v}\,\mathrm{d}\mathbf{X},\\
\mathscr{M}_{\text{B}}(\mathbf{v}) &:= \int_{\mathscr{B}_r} \mathbf{B}\cdot\mathbf{v}\,\mathrm{d}\mathbf{X},\\
\mathscr{M}_{\text{N}}(\mathbf{v};\mathbf{u}) &:= -\int_{\Gamma_N} \mathbf{p}_N\cdot\mathbf{v}\,\mathrm{d}A,
\end{aligned} \tag{2.16}$$

and

$$\mathscr{M}_p(q;\mathbf{u}) := \int_{\mathscr{B}_r} (J-1)q\,\mathrm{d}\mathbf{X}. \tag{2.17}$$

We observe that

$$a(\mathbf{h},\mathbf{v};\mathbf{u},p,V) = a_{\text{dev}}(\mathbf{h},\mathbf{v};\mathbf{u}) + a_{\text{vol}}(\mathbf{h},\mathbf{v};\mathbf{u},p) + a_{\text{act}}(\mathbf{h},\mathbf{v};\mathbf{u},V) + a_{\text{B}}(\mathbf{h},\mathbf{v}) + a_{\text{N}}(\mathbf{h},\mathbf{v};\mathbf{u}), \tag{2.18}$$

where the addends at the right-hand-side of the last equation are the derivatives of the terms at the right-hand-side of Eq. (2.15). Moreover, we have defined

$$\mathscr{E}(r;V,\mathbf{s},\mathbf{c},\mathbf{u}) := \mathscr{E}_{\text{in}}(r;\dot{V},\mathbf{u}) + \mathscr{E}_{\text{ion}}(r;V,\mathbf{s},\mathbf{c},\mathbf{u}) + \mathscr{E}_{\text{diff}}(r;V,\mathbf{u}) + \mathscr{E}_{\text{app}}(r;V,\mathbf{u}) \tag{2.19}$$

for

$$\begin{aligned}
\mathscr{E}_{\text{in}}(r;\dot{V},\mathbf{u}) &:= \int_{\mathscr{B}_r} J(\mathbf{u})\beta C_m \dot{V}\, r\,\mathrm{d}\mathbf{X},\\
\mathscr{E}_{\text{ion}}(r;V,\mathbf{s},\mathbf{c},\mathbf{u}) &:= \int_{\mathscr{B}_r} J(\mathbf{u})\beta C_m I_{\text{ion}}(V,\mathbf{s},\mathbf{c})\, r\,\mathrm{d}\mathbf{X},\\
\mathscr{E}_{\text{diff}}(r;V,\mathbf{u}) &:= -\int_{\mathscr{B}_r} J(\mathbf{u})\mathbf{F}^{-1}(\mathbf{u})\mathbf{G}_{\text{m}}\mathbf{F}^{-T}(\mathbf{u})\nabla V\cdot\nabla r\,\mathrm{d}\mathbf{X},\\
\mathscr{E}_{\text{app}}(r;V,\mathbf{u}) &:= -\int_{\mathscr{B}_r} J(\mathbf{u}) I_{\text{app}}\, r\,\mathrm{d}\mathbf{X}.
\end{aligned} \tag{2.20}$$

The monolithic solution strategy for the BD coupled model (see Sec. 1.3.3) is outlined in Alg. 2.

1: **Given** Given $\mathbf{u}^n$, p^n, V^n, $\mathbf{s}^n$, $\mathbf{c}^n$;
2: **update** the gating variables and the ionic concentrations, i.e. compute $\mathbf{s}^{n+1}$, $\mathbf{c}^{n+1}$ as

$$\begin{aligned}
s_i^{n+1} &= s_{\infty,i}^n - (s_{\infty,i}^n - s_i^n)e^{-\frac{\tau}{\theta_i^n}} \quad \text{for } i=1,\dots,m_g,\\
\mathbf{c}^{n+1} &= \mathbf{c}^n + \tau\mathbf{Z}(V^n,\mathbf{s}^n);
\end{aligned} \tag{2.21}$$

3: **compute** $\mathbf{u}^{n+1}$, p^{n+1}, V^{n+1} solving

$$\begin{cases}
\int_{\mathscr{B}_r}\mathbf{P}(\mathbf{u}^{n+1},p^{n+1},V^{n+1}):\nabla\mathbf{v}\mathrm{d}\mathbf{X} - \int_{\Gamma_N}\mathbf{p}_N\cdot\mathbf{v}\,\mathrm{d}A + \int_{\mathscr{B}_r}\mathbf{B}\cdot\mathbf{v}\mathrm{d}\mathbf{X} &= 0,\\
\int_{\mathscr{B}_r}(J(\mathbf{u}^{n+1}-1)q\,\mathrm{d}\mathbf{X} &= 0,\\
\int_{\mathscr{B}_r}J(\mathbf{u}^{n+1})\beta C_m V^{n+1}\, r\mathrm{d}\mathbf{X} - \int_{\mathscr{B}_r}J(\mathbf{u}^{n+1})\beta C_m V^n\, r\mathrm{d}\mathbf{X} + & \\
-\int_{\mathscr{B}_r}\tau J(\mathbf{u}^{n+1})\mathbf{F}^{-1}(\mathbf{u}^{n+1})\mathbf{G}_{\text{m}}\mathbf{F}^{-T}(\mathbf{u}^{n+1})\nabla V^{n+1}\cdot\nabla r\mathrm{d}\mathbf{X} + & \\
+\int_{\mathscr{B}_r}\tau J(\mathbf{u}^n)(\beta C_m I_{\text{ion}}(V^n,\mathbf{s}^{n+1},\mathbf{c}^{n+1})\, r\mathrm{d}\mathbf{X} - \int_{\mathscr{B}_r}\tau J(\mathbf{u}^n) I_{\text{app}}\, r\mathrm{d}\mathbf{X} &= 0.
\end{cases} \tag{2.22}$$

as described in Alg. (1).

Algorithm 2: Monolithic solution scheme for the BD coupled electromechanical problem.

2.4.2 Segregated solution of the fully coupled electromechanical problem

In segregated approaches, for every time step n an iterative process of solutions of single-physics electrophysiological and mechanical problems is considered. Fig. 2.1 shows BD and MD coupled problems solved in a segregated fashion. The considered segregated approach for the solution the BD coupled problem is outlined in Alg. 3. The segregated solution strategy for the MD coupled model similarly to the one for the BD coupled model: the difference is that, for the MD approach, Eq. (2.12.3) is computed on the undeformed configuration, i.e. considering $\mathbf{F}$ to be the second order identity tensor and consequently, $J=1$. In this latter case we have $\mathscr{D}_{\mathbf{u}}\mathscr{E}=0$ and therefore Eq. (2.12.3) is naturally decoupled from Eq. (2.12). Suppose the action potential V^{k+1} to be given. Linearizing Eq. (2.12.1) around the generic point $(\mathbf{u},p)$ we obtain

Find $(\mathbf{h},\pi)\in W\times Q$ such that

$$\begin{aligned}
a(\mathbf{h},\mathbf{v};\mathbf{u},p,V) + b(\mathbf{v},\pi;\mathbf{u}) &= -\mathscr{M}_{\mathbf{u}}(\mathbf{v};\mathbf{u},p,V) \qquad \forall\mathbf{v}\in W,\\
b(\mathbf{h},q;\mathbf{u}) &= -\mathscr{M}_p(q;\mathbf{u}) \qquad \forall q\in Q.
\end{aligned} \tag{2.23}$$

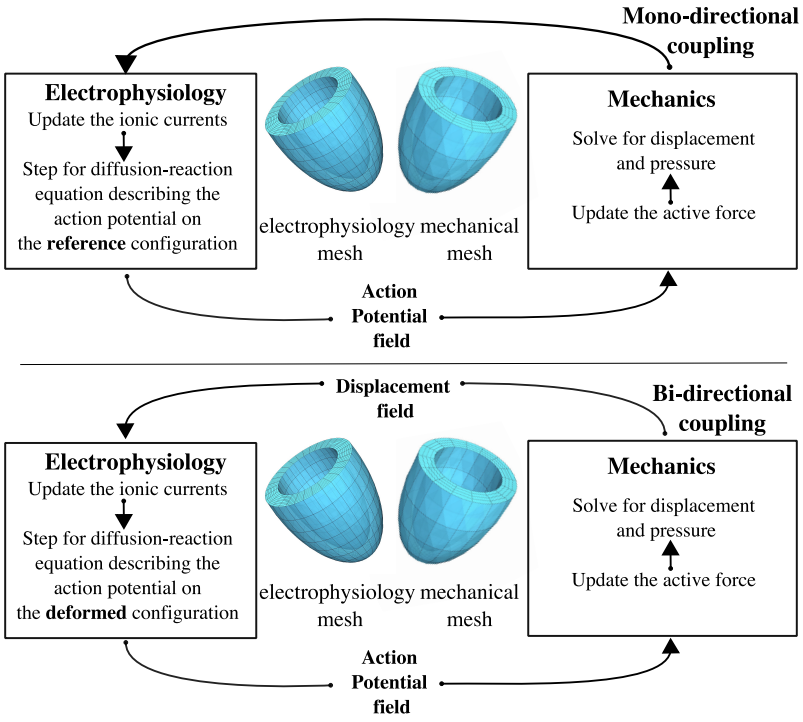

Figure 2.1. Top: segregated approach for the mono-directionally coupled problem. At each time step, the obtained AP is transferred to the mechanical solver to update the active force and, hence, to compute the new configuration. Bottom: segregated approach for the bidirectionally coupled problem. Same as the MD segregated approach with the displacement field is additionally transferred to the electrophysiological problem in order to solve the monodomain equation in the deformed configuration.

The problem tangent to the reference configuration, i.e. $(\mathbf{u}, p) = (0, 0)$, reads:
Find $(\mathbf{h}, \pi) \in W \times Q$ such that

$$\begin{aligned} a_{\text{iso}}(\mathbf{h}, \mathbf{v}; \mathbf{0}) + a_{\text{act}}(\mathbf{h}, \mathbf{v}; 0, V) + a_{\text{N}}(\mathbf{h}, \mathbf{v}; 0) \quad + \quad b(\mathbf{v}, \pi; \mathbf{0}) \quad &= \quad -\mathscr{M}_{\mathbf{u}}(\mathbf{v}; \mathbf{0}, 0, V) \qquad \forall \mathbf{v} \in W, \\ b(\mathbf{h}, q; \mathbf{0}) \qquad\qquad\qquad\qquad\qquad\qquad\quad &= \quad -\mathscr{M}_{p}(q; \mathbf{0}) \qquad\quad \forall q \in Q. \end{aligned} \tag{2.24}$$

Here, we want to remind that the system above is different from system describing incompressible linear elasticity, which reads:
Find $(\mathbf{h}, \pi) \in W \times Q$ such that

$$\begin{aligned} a_{\text{iso}}(\mathbf{h}, \mathbf{v}; \mathbf{0}) \quad + \quad b(\mathbf{v}, \pi; \mathbf{0}) \quad &= \quad -\mathscr{M}_{\mathbf{u}}(\mathbf{v}; \mathbf{0}, 0, V) \qquad \forall \mathbf{v} \in W, \\ b(\mathbf{h}, q; \mathbf{0}) \qquad\qquad\qquad\quad &= \quad -\mathscr{M}_{p}(q; \mathbf{0}) \qquad\quad \forall q \in Q. \end{aligned} \tag{2.25}$$

In particular, the bilinear form associated to the linear elasticity operator (2.24) present an additional term that makes the bilinear form non-symmetric. For the incompressible linear elasticity system (2.25), existence, uniqueness, and stability of the solution have been shown in [Brezzi and

Fortin, 1991]. Given the displacement $\mathbf{u}^k$ and the associated pressure p^k and linearizing (2.28) around the generic point V we obtain
Find $\xi \in R$ s.t.

$$e(\xi, r; V, \mathbf{s}, \mathbf{c}, \mathbf{u}) \quad = \quad -\mathscr{E}(r; V, \mathbf{s}, \mathbf{c}, \mathbf{u}) \qquad \forall r \in R. \tag{2.26}$$

1: **Given** Given $\mathbf{u}^n$, p^n, V^n, $\mathbf{s}^n$, $\mathbf{c}^n$;
2: **define** $\mathbf{u}^k = \mathbf{u}^n$, $p^k = p^n$, $V^k = V^n$, $\mathbf{s}^k = \mathbf{s}^n$, $\mathbf{c}^k = \mathbf{c}^n$;
3: **until** <convergence criteria> is satisfied:
4: **update** the gating variables and the ionic concentrations, i.e. compute $\mathbf{s}^{k+1}$, $\mathbf{c}^{k+1}$ as

$$\begin{aligned} s_i^{k+1} &= s_{\infty,i}^k - (s_{\infty,i}^k - s_i^k) e^{-\frac{\tau}{\theta_i^k}} \quad \text{for } i = 1, \dots, m_g, \\ \mathbf{c}^{k+1} &= \mathbf{c}^k + \tau \mathbf{Z}(V^k, \mathbf{s}^k); \end{aligned} \tag{2.27}$$

5: **compute** V^{k+1} solving

$$\begin{aligned} &\int_{\mathscr{B}_r} J(\mathbf{u}^k) \beta C_m V^{k+1} \, r \mathrm{d}\mathbf{X} - \int_{\mathscr{B}_r} J(\mathbf{u}^k) \beta C_m V^k \, r \mathrm{d}\mathbf{X} + \\ &- \int_{\mathscr{B}_r} \tau J(\mathbf{u}^k) \mathbf{F}^{-1}(\mathbf{u}^k) \mathbf{G}_{\mathrm{m}} \mathbf{F}^{-T}(\mathbf{u}^k) \nabla V^{k+1} \cdot \nabla r \mathrm{d}\mathbf{X} + \\ &+ \int_{\mathscr{B}_r} \tau J(\mathbf{u}^k) (\beta C_m I_{\mathrm{ion}}(V^k, \mathbf{s}^{k+1}, \mathbf{c}^{k+1}) \, r \mathrm{d}\mathbf{X} - \int_{\mathscr{B}_r} \tau J(\mathbf{u}^k) I_{\mathrm{app}} \, r \mathrm{d}\mathbf{X} \quad = 0; \end{aligned} \tag{2.28}$$

with Alg. (1).
6: **compute** $\mathbf{u}^{k+1}$, p^{k+1} solving for

$$\begin{cases} \int_{\mathscr{B}_r} \mathbf{P}(\mathbf{u}^{k+1}, p^{k+1}, V^{k+1}) : \nabla \mathbf{v} \mathrm{d}\mathbf{X} - \int_{\Gamma_N} \mathbf{p}_N \cdot \mathbf{v} \, \mathrm{d}A + \int_{\mathscr{B}_r} \mathbf{B} \cdot \mathbf{v} \mathrm{d}\mathbf{X} = & 0, \\ \int_{\mathscr{B}_r} (J(\mathbf{u}^{k+1} - 1) q \, \mathrm{d}\mathbf{X} = & 0. \end{cases} \tag{2.29}$$

with Alg. (1).
7: **set** $k = k + 1$;
8: **set** $\mathbf{u}^{n+1} = \mathbf{u}^k$, $p^{n+1} = p^k$, $V^{n+1} = V^k$, $\mathbf{s}^{n+1} = \mathbf{s}^k$, $\mathbf{c}^{n+1} = \mathbf{c}^k$;

Algorithm 3: Segregated solution scheme for the BD coupled electromechanical problem.

2.5 Finite element dicretization

For the discretization of (2.12), we consider standard FE discretizations. We denote by $\mathfrak{T}_H$, $\mathfrak{T}_h$ partitions of Ω. Here H, h denote representative mesh parameters. We consider shape-regular meshes consisting of quadrilateral or hexahedral axis-aligned elements for cuboid geometries or of triangular or tetrahedral elements for more general geometries. We consider the FE subspaces $W_H^l \subset W$, $Q_H^\sigma \subset Q$ and $R_h^\eta \subset R$, defined as

$$\begin{aligned} W_H^l &= \left\{ \mathbf{v}_H \in W : \ \mathbf{v}_H|_{Y_i} \in (\mathbb{P}_l)^3, \text{ for } i = 1, \dots, N_H \right\}, \\ Q_H^\sigma &= \left\{ \pi_H \in Q : \ \pi_H|_{Y_i} \in \mathbb{P}_\sigma, \text{ for } i = 1, \dots, N_H \right\}, \\ R_h^\eta &= \left\{ \xi_h \in R : \ \xi_h|_{Z_i} \in \mathbb{P}_\eta, \text{ for } i = 1, \dots, N_h \right\}, \end{aligned} \tag{2.30}$$

for $(\mathbb{P}_l)^3$, $\mathbb{P}_\sigma$, and $\mathbb{P}_\eta$ spaces of polynomials of degree l, σ, and η respectively. The notation $(\mathbb{P}_l)^3$ means that all components of the three-dimensional vector $\boldsymbol{\nu}_h|_{Y_i}$ are polynomials of degree l. In case of a segregated solution approach is considered, for the mechanical problem the couple (W_H^l, Q_H^σ) is also denoted with $\mathbb{P}_l - \mathbb{P}_\sigma$ in case of tetrahedral elements, or $\mathbb{Q}_l - \mathbb{Q}_\sigma$ in case of hexahedral elements. The well known Ladyzhenskaya-Babuska-Brezzi (LBB) condition is a particular instance of the so- called discrete inf-sup condition it is a necessary and sufficient condition for the well-posedness of discrete saddle point problems arising from discretization via Galerkin methods. The LBB condition states

$$\exists\, c_H \text{ s.t. } c_H \|q_H\|_{L^2} \leq \sup_{w_H \in W_H^l} \frac{\int_{\mathscr{B}_r} (\nabla \cdot w_H)\, q_H}{\|w_H\|_{H^1}} \quad \forall q_H \in Q_H^\sigma. \tag{2.31}$$

In this case, possible choices of l and σ leading to approximation spaces that satisfy the discrete LBB stability condition are discussed in [Quarteroni, 2009b]. We recall that the so called *Taylor-Hood* elements $\mathbb{P}_k - \mathbb{P}_{k-1}$ are stable for $k \geq 2$ for linear elasticity. To overcome volume locking issues, we consider second order finite elements for the approximation of the displacement field, i.e. $k = 2$. Denoting the Lagrangian basis functions of W_H^l, Q_H^σ and R_h^η by

$$\{\varphi_i\}_{i=1}^{w_d}, \{\phi_j\}_{j=1}^{q_d}, \{\psi_s\}_{s=1}^{r_d}, \tag{2.32}$$

respectively, the discrete solution $(\mathbf{h}_H, \pi_H, \xi_h)$ of problem (2.13) can be written as

$$\mathbf{h}_H = \sum_{i=1}^{w_d} h_i \boldsymbol{\varphi}_j, \qquad \pi_H = \sum_{j=1}^{q_d} \pi_j \phi_j, \qquad \xi_h = \sum_{s=1}^{r_d} \xi_s \psi_s \tag{2.33}$$

As described in [Quarteroni et al., 2017], a standard quadrature approximation of

$$\mathscr{E}_{\text{ion}}(r; V, \mathbf{s}, \mathbf{c}, \mathbf{u}) := \int_{\mathscr{B}_r} J(\mathbf{u}) \beta C_m I_{\text{ion}}(V, \mathbf{s}, \mathbf{c})\, r \mathrm{d}\mathbf{X} \tag{2.34}$$

is performed considering the *ionic current interpolation* (ICI)

$$\mathscr{E}_{\text{ion}}^{\text{ICI}}(r; V, \mathbf{s}, \mathbf{c}, \mathbf{u}) := \beta C_m \sum_{s=1}^{r_d} [\mathbb{M}]_{j,s} J(\Pi(\mathbf{u})_s) I_{\text{ion}}(V_s, \mathbf{s}_s, \mathbf{c}_s). \tag{2.35}$$

Here we have defined

$$[\mathbb{M}]_{j,s} := \int_{\mathscr{B}_r} \psi_s \psi_j \mathrm{d}\mathbf{X}, \tag{2.36}$$

and $V_s, \mathbf{s}_s, \mathbf{c}_s, \Pi(\mathbf{u})_s$ to be the coefficients of the variables $V, \mathbf{s}, \mathbf{c}, \Pi(\mathbf{u})$ expanded with respect to the basis $\{\psi_s\}_{s=1}^{r_d}$.

2.5.1 Transfer operators

L^2-projection is a fundamental tool to construct restriction and prolongation operators for MG methods applied with non-nested meshes [Krause and Zulian, 2016]. We consider two shape-regular meshes $\mathscr{T}_{h_1}$, $\mathscr{T}_{h_2}$. Following the naming convention of mortar methods, we refer to the space $S_{h_1}^{\text{p}}$ as master space, or mortar space. In contrast, we refer to $S_{h_2}^{\text{p}}$ as slave, or non-mortar space. Following [Sampath and Biros, 2010], we define the projection operator $\mathscr{F}\text{p}_{h_1}^{h_2} : S_{h_1}^{\text{p}} \to S_{h_2}^{\text{p}}$.

The mortar projection maps a function from the mortar space, to the non-mortar space. Given $v_{h_1} \in S^{\mathrm{p}}_{h_1}$ we want to find $w_{h_2} = \mathscr{F}\mathrm{p}^{h_2}_{h_1}(v_{h_1}) \in S^{\mathrm{p}}_{h_2}$, such that

$$(\mathscr{F}\mathrm{p}^{h_2}_{h_1}(v_{h_1}), q_{h_2})_{L^2} = (v_{h_1}, q_{h_2})_{L^2} \quad \forall q_{h_2} \in S^{\mathrm{p}}_{h_2}. \tag{2.37}$$

Following [Bernardi et al., 2005] we reformulate (2.37) getting the weak equality condition

$$\int_\Omega (v_{h_1} - \mathscr{F}\mathrm{p}^{h_2}_{h_1}(v_{h_1}))q_{h_2}\mathrm{d}\mathbf{X} = \int_\Omega (v_{h_1} - w_{h_2})q_{h_2}\mathrm{d}\mathbf{X} = 0 \quad \forall q_{h_2} \in S^{\mathrm{p}}_{h_2}. \tag{2.38}$$

Any coarse-grid vector v_{h_1} and fine-grid vector w_{h_2} can be expanded as

$$v_{h_1} = \sum_{m=1}^{N_{h_1}} v^m_{h_1}\psi^{h_1}_m \quad \text{and} \quad w_{h_2} = \sum_{n=1}^{N_{h_2}} w^n_{h_2}\psi^{h_2}_n, \tag{2.39}$$

respectively. In Eq. (2.39) the coefficients $v^m_{h_1}$ and $w^n_{h_2}$ are the coefficients in the basis expansion of v_{h_1} and of w_{h_2} with respect to the bases $\{\psi^{h_1}_m\}^{N_{h_1}}_{m=1}$ and $\{\psi^{h_2}_n\}^{N_{h_2}}_{n=1}$, respectively. This allows us to write the point-wise contributions to Eq. (2.38) as

$$\sum_{m=1}^{N_{h_1}} v^m_{h_1}\int_\Omega \psi^{h_1}_m\psi^{h_2}_k\mathrm{d}\mathbf{X} = \sum_{n=1}^{N_{h_2}} w^n_{h_2}\int_\Omega \psi^{h_2}_n\psi^{h_2}_k\mathrm{d}\mathbf{X} \quad \forall\, k = 1,\dots,N_{h_2}. \tag{2.40}$$

Defining the matrices $\mathscr{D}^{h_2}_{h_2}$ and $\mathscr{B}^{h_2}_{h_1}$ of entries

$$(\mathscr{D}^{h_2}_{h_2})_{k,n} = \int_\Omega \psi^{h_2}_n\psi^{h_2}_k\mathrm{d}\mathbf{X}, \quad (\mathscr{B}^{h_2}_{h_1})_{k,m} = \int_\Omega \psi^{h_1}_m\psi^{h_2}_k\mathrm{d}\mathbf{X}, \tag{2.41}$$

Eq. (2.40) admits the following algebraic representation

$$\mathscr{D}^{h_2}_{h_2}\mathbf{v} = \mathscr{B}^{h_2}_{h_1}\mathbf{w}. \tag{2.42}$$

Here the vectors $\mathbf{v}$, $\mathbf{w}$ are the vectors of coefficients with respective entries $v^m_{h_1}$ and $w^n_{h_2}$. The matrix $\mathscr{D}^{h_2}_{h_2}$ is a mass matrix and hence it is invertible. Therefore, it holds

$$\mathbf{v} = (\mathscr{D}^{h_2}_{h_2})^{-1}\mathscr{B}^{h_2}_{h_1}\mathbf{w} = \mathscr{P}^{h_2}_{h_1}\mathbf{w} \tag{2.43}$$

for $\mathscr{P}^{h_2}_{h_1} = (\mathscr{D}^{h_2}_{h_2})^{-1}\mathscr{B}^{h_2}_{h_1}$. The discrete operator $\mathscr{P}^{h_2}_{h_1}$ is the algebraic representation of the L^2-projection $\mathscr{F}\mathrm{p}^{h_2}_{h_1}$. An explicit computation of $\mathscr{P}^{h_2}_{h_1}$ is computationally unaffordable, since it would require an explicit computation of the inverse of $\mathscr{D}^{h_2}_{h_2}$ which is dense. Alternatively, the following two strategies are considered:

- solve a linear system for $\mathscr{D}^{h_2}_{h_2}$ each time the transfer operator is applied.
- consider biorthogonal basis functions of $S^{\mathrm{p}}_{h_2}$ with respect to the L^2-inner product [Wohlmuth, 2000] obtaining a diagonal $\mathscr{D}^{h_2}_{h_2}$.

Although the first-mentioned strategy may appear inconvenient, mass matrices are typically well-conditioned, having a condition number independent on the mesh size. In contrast, the second strategy is hardly applicable for $p \geq 2$, due to the difficulties in generating biorthogonal basis functions.

In case of nested grids, in particular when $\mathscr{T}_{h_2}$ is a uniform refinement of $\mathscr{T}_{h_1}$, the projection operator can be easily constructed as the interpolation operator. Due to the definition of Lagrangian basis function, for each $\psi_i^{h_2}$, there exists a unique $\mathbf{p}_i \in \Omega$ such that

$$\psi_j^{h_2}(\mathbf{p}_i) = \delta_{ij} \quad \forall i,j = 1,\dots,N_{h_2} \tag{2.44}$$

where δ represents the Kronecker delta function. The point $\mathbf{p}_i$ is the fine grid node associated with $\psi_i^{h_2}$. In case of nested grids, any coarse-grid function can be expended with respect to the basis functions of the fine space. In this case, Eq. (2.44) leads to

$$v_{h_2}^i = \sum_{j=1}^{N_{h_1}} v_{h_1}^j \psi_j^{h_1}(\mathbf{p}_i). \tag{2.45}$$

The entries of the matrix $\mathscr{P}\mathrm{p}_{h_1}^{h_2}$ are then just the coarse-grid basis functions evaluated at the fine-grid vertices

$$(\mathscr{P}\mathrm{p}_{h_1}^{h_2})_{ij} = \psi_j(\mathbf{p}_i). \tag{2.46}$$

We define the restriction operator $\mathscr{R}p_{h_2}^{h_1} : S_{h_2}^{\mathrm{p}} \to S_{h_1}^{\mathrm{p}}$ as $\mathscr{R} = \mathscr{P}^T$. Thanks to the Piola transformation, the assembling of transfer operators is performed only once on the reference configuration.

2.5.2 Discrete monolithic problem

The FE discretization of the monolithic tangent problem (2.13) reads
Find $(\mathbf{h}_H, \pi_H, \xi_h) \in W_H^l \times Q_H^\sigma \times R_h^\eta$ s.t.

$$\begin{aligned}
a(\mathbf{h}_H, \mathbf{v}_H; \mathbf{u}_H, p_H, \mathscr{R}\eta_h^H(V_h)) + b(\mathbf{v}_H, \pi_H; \mathbf{u}_H) &= -\mathscr{M}_{\mathbf{u}}(\mathbf{v}_H; \mathbf{u}_H, p_H, \mathscr{R}\eta_h^H(V_h)) \quad \forall \mathbf{v}_H \in W_H,\\
b(\mathbf{h}_H, q_H; \mathbf{u}_H) &= -\mathscr{M}_p(q_H; \mathbf{u}_H) \quad \forall q_H \in Q_H,\\
c(\mathscr{P}l_h^H(\mathbf{h}_H), r_h; V_h, \mathbf{s}_h, \mathbf{c}_h, \mathscr{P}l_h^H(\mathbf{u}_H)) + e(\xi_h, r_h; V_h, \mathbf{s}_h, \mathbf{c}_h, \mathscr{P}l_h^H(\mathbf{u}_H)) &= -\mathscr{E}(r_h; V_h, \mathbf{s}_h, \mathbf{c}_h, \mathscr{P}l_h^H(\mathbf{u}_H)) \quad \forall r_h \in R_h.
\end{aligned} \tag{2.47}$$

which considering the base defined in Eq. (2.32) becomes

Find $(\mathbf{h}_H, \pi_H, \xi_h) \in W_H^l \times Q_H^\sigma \times R_h^\eta$ s.t.

$$\begin{aligned}
a(\mathbf{h}_H, \varphi_i; \mathbf{u}_H, p_H, \mathscr{R}\eta_h^H(V_h)) + b(\varphi_i, \pi_H; \mathbf{u}_H) &= -\mathscr{M}_{\mathbf{u}}(\varphi_i; \mathbf{u}_H, p_H, \mathscr{R}\eta_h^H(V_h))\\
b(\mathbf{h}_H, \phi_j; \mathbf{u}_H) &= -\mathscr{M}_p(\phi_j; \mathbf{u}_H)\\
c(\mathscr{P}l_h^H(\mathbf{h}_H), \psi_s; V_h, \mathbf{s}_h, \mathbf{c}_h, \mathscr{P}l_h^H(\mathbf{u}_H)) + e(\xi_h, \psi_s; V_h, \mathbf{s}_h, \mathbf{c}_h, \mathscr{P}l_h^H(\mathbf{u}_H)) &= -\mathscr{E}(\psi_s; V_h, \mathbf{s}_h, \mathbf{c}_h, \mathscr{P}l_h^H(\mathbf{u}_H)).
\end{aligned} \tag{2.48}$$

for $i = 1,\dots,w_d$, $j = 1,\dots q_d$ and $s = 1,\dots,r_d$. Consider the matrices $\mathscr{A} \in \mathbb{R}^{w_d \times w_d}$, $\mathscr{B} \in \mathbb{R}^{w_d \times q_d}$, $\mathscr{C} \in \mathbb{R}^{w_d \times r_d}$, and $\mathscr{D} \in \mathbb{R}^{r_d}$ are the algebraic representations of the weak forms $a(\cdot,\cdot)$, $b(\cdot,\cdot)$, $c(\cdot,\cdot)$, and $d(\cdot,\cdot)$, respectively, and their entries are given by

$$\begin{aligned}
\mathscr{A}_{ij} &= a(\boldsymbol{\varphi}_j, \boldsymbol{\varphi}_i), \qquad \mathscr{B}_{lj} = b(\boldsymbol{\varphi}_l, \phi_j),\\
\mathscr{C}_{lj} &= c(\boldsymbol{\varphi}_j, \psi_l), \qquad \mathscr{D}_{ln} = d(\psi_n, \psi_l).
\end{aligned} \tag{2.49}$$

We consider the vectors F, G, T which entries are

$$F_i = \mathscr{M}_{\mathbf{u}}(\varphi_i; \mathbf{u}_H, p_H, \mathscr{R}\eta_h^H(V_h)), \qquad G_j = \mathscr{M}_p(\phi_j; \mathbf{u}_H), \qquad T_s = \mathscr{E}(\psi_s; V_h, \mathbf{s}_h, \mathbf{c}_h, \mathscr{P}l_h^H(\mathbf{u}_H)), \tag{2.50}$$

and the vectors U, P and E such that $U_i = h_i$, $P_j = \pi_j$, and $E_s = \xi_s$. Problem (2.48) is equivalent to the algebraic problem

$$\begin{bmatrix} \mathscr{A} & \mathscr{B}^T & \mathbf{0} \\ \mathscr{B} & \mathbf{0} & 0 \\ \mathscr{C} & \mathbf{0} & \mathscr{E} \end{bmatrix} \begin{bmatrix} U \\ P \\ E \end{bmatrix} = \begin{bmatrix} F \\ G \\ T \end{bmatrix}. \tag{2.51}$$

In the linear system above, we dropped the dependence of the submatrices $\mathscr{A}, \mathscr{B}, \mathscr{C}, \mathscr{E}$ on the Newton's step k. We choose $l = 2$, $\sigma = 1$ and $\eta = 1$. This means that for meshes with quadrilateral or hexahedral elements, we employ bi-quadratic FE to interpolate the displacement variables and bi-linear FE to interpolate the pressure and the action potential variables. For mesh with triangular or tetrahedral elements, we employ quadratic FE to interpolate the displacement variables and linear FE to interpolate the pressure and the action potential variables.

2.5.3 Discrete segregated problem

FE discretization of problem (2.23) and of problem (2.26) read

Find $(\mathbf{h}_H, \pi_H) \in W_H^l \times Q_H^\sigma$ s.t.

$$\begin{aligned} a(\mathbf{h}_H, \varphi_i; \mathbf{u}_H, p_H, \mathscr{R}\eta_h^H(V_h)) \;+\; b(\varphi_i, \pi_H; \mathbf{u}_H) &= -\mathscr{M}_{\mathbf{u}}(\varphi_i; \mathbf{u}_H, p_H, \mathscr{R}\eta_h^H(V_h)) \\ b(\mathbf{h}_H, \phi_j; \mathbf{u}_H) &= -\mathscr{M}_p(\phi_j; \mathbf{u}_H), \end{aligned} \tag{2.52}$$

and

Find $\xi_h \in R_h^\eta$ s.t.

$$c(\mathscr{P}l_h^H(\mathbf{h}_H), \psi_s; V_h, \mathbf{s}_h, \mathbf{c}_h, \mathscr{P}l_h^H(\mathbf{u}_H)) \;+\; e(\xi_h, \psi_s; V_h, \mathbf{s}_h, \mathbf{c}_h, \mathscr{P}l_h^H(\mathbf{u}_H)) = -\mathscr{E}(\psi_s; V_h, \mathbf{s}_h, \mathbf{c}_h, \mathscr{P}l_h^H(\mathbf{u}_H)), \tag{2.53}$$

for $i = 1, \ldots, w_d$, $j = 1, \ldots q_d$ and $s = 1, \ldots, r_d$, respectively. Problems (2.52) and (2.53) are equivalent to the algebraic problems

$$\begin{bmatrix} \mathscr{A} & \mathscr{B}^T \\ \mathscr{B} & \mathbf{0} \end{bmatrix} \begin{bmatrix} U \\ P \end{bmatrix} = \begin{bmatrix} F \\ G \end{bmatrix}, \tag{2.54}$$

and

$$\mathscr{E}E = T, \tag{2.55}$$

respectively. We define $\mathscr{H} \in \mathbb{R}^{(w_d+q_d)\times(w_d+q_d)}$ to be the matrix at the left hand side of (2.54). At the first step of Newton's method, the LBB condition ensures the matrix $\mathscr{H}$ to be non singular. In general, it is not possible to prove that such condition eliminates spurious modes for any tangent problem. In the specific case of incompressible elasticity, the matrix $\mathscr{A}$ is singular at the first iteration of Newton's method and singular or non-positive definite at any iteration of Newton's method. Following [Quarteroni et al., 2017], the introduced segregated approach corresponds to a block Gauss-Seidel iteration of to a *serial loosely coupled scheme*.

Chapter 3

High-order time stepping schemes for cardiac electrophysiology

In this chapter, we derive high-order numerical schemes for the time integration of cardiac electrophysiology. To this aim, we generalize the approach proposed by Rush and Larsen [Rush and Larsen, 1978]. Final aim of this study is to investigate the impact of the high-order schemes on simulated post-processing quantities of clinical interest. For the purpose of simplicity, we here neglect the deformation of the body which contribution is out of the scope of focus of the chapter.

High-order time integration of the monodomain system coupled with stiff and nonlinear ionic models is a widely known challenge in cardiac electrophysiology [Lontsi et al., 2017; Franzone and Pavarino, 2004; Sundnes et al., 2005]. The main numerical difficulties arising from the time integration of cardiac electrophysiology are the stiffness associated with the time-evolution of the gating variables and the complex dependence of the ionic currents on the action potential. The Rush-Larsen (RL) scheme is one of the most popular numerical strategy for the solution of the cellular models in which it allows to overcome the two above-mentioned problematics. In RL scheme a first-order exponential integrator is proposed for the solution the ionic channels. In detail, the time integration of the ODEs describing the gating variables is performed exactly but assuming the AP constant over the interval of integration. The RL method is equivalent to an explicit exponential integrator [Nørsett, 1969] and prevents over- and under-shooting in the numerical solution of gating variables, ensuring that they belong to the physiological range $[0, 1]$. Eventually, the ODE for the AP is integrated by means of an explicit Euler method. The RL method improves the stability w.r.t. standard explicit integrators, but its convergence is limited to the first-order. Although the RL scheme falls into the class of exponential integrators, it originates from a peculiar linearization of the original problem. Literature of exponential integrators is well established [Lawson, 1967; Beylkin et al., 1998; Boyd, 2001; Cox and Matthews, 2002; Smith et al., 2003a; Hochbruck and Ostermann, 2005; Minchev and Wright, 2005; Krogstad, 2005] but it is focused mainly on semilinear ODEs with constant coefficients of the linear terms. For this class of ODEs, the derivation of high-order methods is straightforward. When considering the ODEs describing the gating variable dynamic, the coefficients of the linear terms are not constant, rather they depend on the action potential. In this context, high order exponential integrators can not be readily derived. An attempt to derive a second order RL scheme has been proposed in [Sundnes et al., 2009]. This method consists in a predictor-corrector midpoint method. The predictor step exploits the standard RL method, then, in the fashion of Heun integrators, the

standard first-order formulae is evaluated at the midpoint of the time step. This approach has been shown to outperform standard RL and Runge-Kutta methods with a double computational cost for each time step [Gomes and dos Santos, 2015]. In [Perego and Veneziani, 2009], formulae for generalized RL schemes have been presented but they are shown not to be in general A-stable. An alternative strategy to employ high-order exponential integrators consists in transforming the original problem in an equivalent one in which the leading coefficient of the right-hand-side is constant over the discretization interval [Lontsi et al., 2017]. This coefficient is referred to as *time step dependent stabilizer*.

A further step of complexity is introduced by the monodomain or bidomain operators. Both are diffusion-like, thus contributing to the stiffness of the system. The standard choice for the integration of this kind of model is either to decouple diffusion and reaction (operator splitting) or to partially treat the ionic currents explicitly [Franzone and Pavarino, 2004; Ethier and Bourgault, 2008a; Perego and Veneziani, 2009]. In the formes, overall convergence rate is limited to first or second order (depending on the splitting scheme), albeit it is possible to attain higher-order convergence treating the reaction term with RL-like schemes and the diffusion term with implicit schemes. Implicit-explicit (IMEX) schemes allow to employ larger time steps, even if they are conditionally stable, and to solve one linear system per time step. High-order IMEX schemes can be formally derived, but the strict stability condition depending on the mesh-size prevents their use in realistic simulations. To avoid the usage of very small time steps, backward differentiation formula (BDF) can be used [Ethier and Bourgault, 2008a; Perego and Veneziani, 2009; Hundsdorfer and Verwer, 2013] but they require the expensive evaluation of the derivatives of the ionic currents. Operator-splitting methods are commonly used to avoid the implicit evaluation of derivatives [Qu and Garfinkel, 1999; Sundnes et al., 2005]. Adaptive time step methods, see e.g. [Franzone et al., 2006; Qu and Garfinkel, 1999], represent provide added value to the above-mentioned approaches. In [Krause, 2013] lightweight spatially and space-time adaptive schemes for large-scale parallel simulations are designed. In detail, two different adaptive schemes based on locally structured meshes are proposed. In [Campos et al., 2013b] different techniques (adaptive time step-methods, partial evaluation and lookup tables, and the exploitation of the code concurrency via OpenMP directives) to automatically speed up the numerical solution of cardiac models are proposed.

Starting from the standard derivation of exponential integrators, in this chapter we propose novel generalized schemes for the time-integration of the equations describing the behavior of the gating variables. Stabilized and non-stabilized schemes are hence coupled with IMEX and BDF methods for the solution of the reaction-diffusion equation describing the AP. Additional contribution of this work is the introduction of a novel quasi-Newton (qN-BDF) approach for the implicit solution of the algebraic problem arising from the implicit discretization of the monodomain system. The proposed quasi-Newton approach is applicable to every cellular model that follows the HH [Hodgkin and Huxley, 1952] formalism. As an alternative, we propose the evaluation of the complex dependence of the ionic currents on the AP considering the complex step derivative approximation (CSDA-BDF) approach.

The chapter is organized as follows. In Sec. 3.1, starting from exponential integrators theory, we present different high-order exponential (EXP) schemes for the numerical integration of the gating variables. In Sec. 3.2, we present high-order IMEX and BDF schemes for the time integration of the monodomain equation. In Sec. 3.3, our novel quasi-Newton (qN) approach and the application of the complex step derivative approximation (CSDA) approach for the approximation of the derivative of the ionic current with respect to the AP are introduced. Sec. 3.4 the convergence behavior of the above-mentioned high-order numerical strategies is assessed for

the numerical solution of an initial value problem (IVP) with trigonometric coefficient, of the FHN and the BWZVP cellular models and of the monodomain system. We recall that the FHN model, the BWZVP model and the Beeler-Reuter model [Beeler and Reuter, 1977 Jun] are suitable ionic models for testing the accuracy of high-order time integration schemes in which, in these models, the analytical definition of the ionic currents are regular enough. The last section is finalized with the study of the impact of high-order time integration on simulated AT, CV, APD_{90} and pseudo-ECGs signals for 3D simulation of the monodomain system coupled with the BWZVP cellular model.

3.1 High-order exponential schemes

Theory of exponential integrators is well established for semi-linear problems of the form

$$\begin{cases} y'(t) = c_\ell y(t) + n(y(t), t), \\ y(0) = y_0. \end{cases} \tag{3.1}$$

Given suitable initial conditions, each gating variable s obeys an equation of the form

$$s_i' = \frac{s_{i,\infty}(V) - s_i}{\tau_i(V)}. \tag{3.2}$$

For this reason, we consider the following generalization of the IVP (3.2)

$$\begin{cases} y'(t) = f(y(t)) = \ell(t)y(t) + n(t), \\ y(0) = y_0. \end{cases} \tag{3.3}$$

This section is devoted to the description of first-, and high-order EXP integration schemes for the solution to semi-linear IVP (3.3). Defining $A(t) = \int_0^t \ell(s)ds$ and multiplying the equation by the integrating factor $e^{-A(t)}$ we obtain

$$(e^{-A(t)}y(t))' = e^{-A(t)}n(t). \tag{3.4}$$

Integrating (3.4) we obtain

$$y(\tau) = e^{\int_0^\tau \ell(s)ds}y(0) + \int_0^\tau e^{\int_\omega^\tau \ell(s)ds}n(\omega)d\omega, \tag{3.5}$$

or, equivalently,

$$y(t+\tau) = e^{\int_t^{t+\tau} \ell(s)ds}y(t) + \int_t^{t+\tau} e^{\int_\omega^{t+\tau} \ell(s)ds}n(\omega)d\omega. \tag{3.6}$$

We define the function $\mathscr{I}: \mathscr{T} \to \mathbb{R}$ as

$$\mathscr{I}(\omega; [t, t+\tau]) = e^{\int_\omega^{t+\tau} \ell(s)ds}n(\omega). \tag{3.7}$$

Different numerical approximations of the integrand $\mathscr{I}$ in (3.5) lead to different numerical integration strategies. The ETD schemes are obtained by distinct polynomial approximation of the functions ℓ and n. IF methods are obtained when the whole integrand $\mathscr{I}$ is approximated. This is equivalent to apply standard time stepping schemes to Eq. (3.4). Defining $y^n := y(t^n)$, $\ell^n := \ell(t^n)$, and $n^n := n(t^n)$ Eq. (3.6) are written as

$$y(t^{n+1}) = e^{\int_{t^n}^{t^{n+1}} \ell(s)ds}y(t^n) + \int_{t^n}^{t^{n+1}} e^{\int_\omega^{t^{n+1}} \ell(s)ds}n(\omega)d\omega. \tag{3.8}$$

We define

$$E_i^j := e^{\int_{t^i}^{t^j} \ell(s)\,ds}. \tag{3.9}$$

3.1.1 Exponential time differencing schemes

ETD Adams-Bashforth schemes with stabilization procedure

ETD approaches with stabilization procedure are constructed by transformation of the IVP (3.3) in an equivalent form in which the leading coefficient in the right hand side is constant on the considered discretization interval $[t^n, t^{n+1}]$:

$$y'(t) = c_\ell^n y(t) + r^n(y(t)). \tag{3.10}$$

$c_\ell^n \in \mathbb{R}$ is usually called *time step dependent stabilizer* and $r^n(y(t)) = (\ell(t) - c_\ell^n)y(t) + n(t)$. The exact solution of Eq. (3.10) satisfies the *variation of the constant formula*

$$y^{n+1} = e^{\tau c_\ell^n}\left(y^n + \int_{t^n}^{t^{n+1}} e^{-c_\ell^n(\omega - t^n)} r^n(\omega)\,d\omega\right). \tag{3.11}$$

Following [Nørsett, 1969], we apply Adams methods to Eq. (3.11). ETD Adams-Bashforth methods have the form:

$$y^{n+1} = e^{\tau c_\ell^n} y^n + \tau \sum_{j=0}^{q-1} \alpha_j(\tau c_\ell^n)\nabla^j n_n, \tag{3.12}$$

where $\nabla^0 n_{n-1} = n_{n-1}$ and $\nabla^{j+1} n_{n-1} = \nabla^j n_{n-1} - \nabla^j n_{n-2}$ are the backward differences. The functions $\alpha_j(x)$ satisfy the following recurrence relations

$$\begin{cases} x\alpha_0(x) & = e^x - 1, \\ x\alpha_{j+1}(x) & = \alpha_j(x) + \frac{1}{2}\alpha_{j-1}(x) + \frac{1}{3}\alpha_{j-2}(x) + \cdots + + \frac{1}{j+1}\alpha_0(x). \end{cases} \tag{3.13}$$

To overcome the numerical round-off errors arising when computing the powers of the product τc_ℓ^n for small time steps we approximate the exponential function by its truncated Taylor expansion considering $c_\ell^n = \ell^n$. In the first-order ETD Adams-Bashforth method the functions ℓ and n in Eq. (3.4) are approximated in the interval $[t^n, t^{n+1}]$ by their evaluations $\ell^n = \ell(t^n)$ and $n^n = n(t^n)$ at time t^n. In this case, we obtain:

$$y^{n+1} = e^{\tau \ell^n} y^n + \frac{(e^{\tau \ell^n} - 1)}{\ell^n} n^n. \tag{3.14}$$

The first-order ETD Adams-Bashforth method is also known as exponential explicit Euler (EEE) method. As an alternative the functions ℓ and n can be implicitly evaluated. Eq. (3.14) can also be derived from the following linearization of the IVP (3.3)

$$y\prime(t+\tau) = f(y(t)) + f(y(t))'(y(t+\tau t) - y(t)). \tag{3.15}$$

The exact solution of Eq. (3.15) is

$$y(t+\tau) = y(t) + \tau\varphi_1\left(\tau f(y(t))'\right) f(t) \tag{3.16}$$

where it is defined

$$\varphi_1(z) = \frac{\exp(z) - 1}{z}. \tag{3.17}$$

The method is exact for

$$f(y(t)) = c_\ell y(t) + c_n \tag{3.18}$$

for c_ℓ and c_n constants. In case only c_ℓ is constant the error per-step is $\frac{\tau^2}{2}n'$, so the method is accurate if n is "slowly varying". EEE method has been introduced in cardiac electrophysiological simulations in [Rush and Larsen, 1978]. Since then the EEE method has been largely used for the time integration of the ODEs related to the gating variables. For this reason, disregarding the global nature of the strategy proposed in the original work for the solution of the complete electrophysiological problem, the application of EEE method in cardiac electrophysiology literature is often referred to as RL method. For the i-th Eq. (1.78-1.79) we have

$$\ell(t^n) = -1/\tau_i^n, \quad n(t^n) = s_{\infty,i}^n/\tau_i^n. \tag{3.19}$$

Applying EEE method we obtain

$$s_i^{n+1} = s_{i,\infty}^n - (s_{i,\infty}^n - s_i^n)e^{-\frac{\tau}{\tau_i^n}}.$$

For the purpose of this work we limit our study to ETD Adams-Bashforth methods. Stabilized ETD Adams-Bashforth method of order m in the plots is referred to as ETDStab_m. We refer to [Minchev and Wright, 2005] for the construction of ETD Adams-Moulton formulae.

ETD schemes without stabilization procedure

We here introduce ETD schemes without stabilization procedure which represent an alternative approach to the stabilization-based method described in the previous section. Given a function $f : \mathscr{T} \to \mathbb{R}$ and its evaluation on $p+1$ distinct points $\{t_0, \dots, t_p\} \in \mathscr{T}$, the function admits the polynomial approximation

$$P(f; [t_0, \dots, t_p]) = \sum_{i=0}^{p} y_i(f) m_i(t) \quad \text{with} \quad y_i(f) = f(t_i), \quad m_i(t) = \prod_{j=0, j\neq i}^{p} \frac{t - t_j}{t_i - t_j}. \tag{3.20}$$

We consider $P(\ell; [t_{n-m}, \dots, t_{n+1}])$ and $P(n; [t_{n-m}, \dots, t_{n+1}])$ approximations of ℓ and n, respectively. We define

$$\hat{E}_n^{n+1}([t_{n-m}, \dots, t_{n+1}]) := e^{\int_{t^n}^{t^{n+1}} P(\ell; [t_{n-m}, \dots, t_{n+1}])(s) ds}, \tag{3.21}$$

and

$$\hat{\mathscr{I}}_n^{n+1}([t_{n-m}, \dots, t_{n+1}]) := \int_{t^k}^{t^{k+1}} \left(e^{\int_\omega^{t^{k+1}} P(\ell; [t_{n-m}, \dots, t_{n+1}])(s) ds} \right) P(n; [t_{n-m}, \dots, t_{n+1}])(\omega) d\omega \tag{3.22}$$

approximations of E_n^{n+1} and $\mathscr{I}_n^{n+1}$, respectively. We define the $m+1$ order ETD scheme

$$y^{n+1}([t_{n-m}, \dots, t_{n+1}]) = \hat{E}_n^{n+1}([t_{n-m}, \dots, t_{n+1}]) y^n + \hat{\mathscr{I}}_n^{n+1}([t_{n-m}, \dots, t_{n+1}]) \tag{3.23}$$

where the computation of the integrands $\hat{E}_n^{n+1}$ and $\hat{\mathscr{I}}_n^{n+1}$ is performed using an integration method of order of accuracy at equal or bigger than $m+1$. The computation of $\hat{E}_n^{n+1}$ and $\hat{\mathscr{I}}_n^{n+1}$ require implicit evaluations of the functions ℓ and n. The ETD method of order of accuracy m without stabilization procedure in the plots is referred to as ETD_m.

ETD midpoint scheme

In the second-order ETD midpoint method we approximate the functions ℓ and n over the time interval $[t^n, t^{n+1}]$ through the constants $P(\ell;[t_{n+\frac{1}{2}}])$ and $P(n;[t_{n+\frac{1}{2}}])$, respectively. Given this approximation, integrating Eq. (3.6) we obtain

$$y^{n+1} = e^{\tau \ell^{n+\frac{1}{2}}} y^n + \frac{e^{\tau \ell^{n+\frac{1}{2}}} - 1}{\ell^{n+\frac{1}{2}}} n^{n+\frac{1}{2}}. \tag{3.24}$$

The ETD midpoint scheme is referred to in the plots as ETDMid_2.

3.1.2 Integrating factor schemes

In this section we present first-, and high-order Adams- and backward differentiation formula-based IF schemes.

IF Adams-Bashforth schemes

IFAB_1

Applying the first-order Adams-Bashforth (AB) scheme to Eq. (3.4) and multiplying the resulting equation by $e^{A(t^{n+1})}$ we obtain

$$y^{n+1} = E_n^{n+1} y^n + \tau E_n^{n+1} n^n. \tag{3.25}$$

We approximating ℓ and n by $P(\ell;[t_n]) = \ell^n$ and $P(n;[t_n]) = n^n$, and consequently E_n^{n+1} by $\hat{E}_n^{n+1} = e^{\tau \ell^n}$. We obtain

$$y^{n+1} = e^{\tau \ell^n} y^n + \tau e^{\tau \ell^n} n^n. \tag{3.26}$$

IFAB_2

Applying the second-order AB to Eq. (3.4) and multiplying the resulting equation by $e^{A(t^{n+1})}$ we obtain

$$y^{n+1} = E_n^{n+1} y^n + \frac{\tau}{2}(3E_n^{n+1} n^n - E_{n-1}^{n+1} n^{n-1}). \tag{3.27}$$

We consider $P(\ell;[t_j, t_{n+1}]), P(n;[t_j, t_{n+1}])$, for $j = n-1, n$. The factor $\hat{E}_j^{n+1}$ is computed applying the trapezoidal integration rule over the interval $[t^j, t^{n+1}]$. Even if the method is explicit with respect to the solution variable y, the computation of the coefficient $\hat{E}_j^{n+1}$ requires an implicit evaluation of the functions ℓ and n.

IFAB_3

Applying the third-order AB to Eq. (3.4) and multiplying the resulting equation by $e^{A(t^{n+1})}$ we obtain

$$y^{n+1} = E_n^{n+1} y^n + \frac{\tau}{12}(23E_n^{n+1} n^n - 16E_{n-1}^{n+1} n^{n-1} + 5E_{n-2}^{n+1} n^{n-2}). \tag{3.28}$$

We consider $P(\ell;[t_j, t_n, t_{n+1}])$, $P(n;[t_j, t_n, t_{n+1}])$ for $j = n-1, n-2$. The factor $\hat{E}_j^{n+1}$, for $j = n-2, n-1$, is computed applying the trapezoidal integration rule over the interval $[t^j, t^{n+1}]$.

IF Adams-Moulton schemes

IFAM$_1$

Applying the first-order Adams-Moulton (AM) scheme to Eq. (3.4) and multiplying the resulting equation by $e^{A(t^{n+1})}$ we obtain

$$y^{n+1} = E_n^{n+1} y^n + \tau n^{n+1}. \tag{3.29}$$

Similarly as for the IFAB1 method, we approximate ℓ and n by $P(\ell;[t_n]) = \ell^n$ and $P(n;[t_n]) = n^n$, obtaining $\hat{E}_n^{n+1} = e^{\tau \ell^n}$ as approximation for E_n^{n+1}.

IFAM$_2$

Applying the second-order AM scheme to Eq. (3.4) and multiplying the obtained equation by $e^{A(t^{n+1})}$ we obtain

$$y^{n+1} = E_n^{n+1} y^n + \frac{\tau}{2}(n^{n+1} + E_n^{n+1} n^n). \tag{3.30}$$

The factor $\hat{E}_n^{n+1}$, is computed as outlined for the IFAB$_2$ method.

IFAM$_3$

Applying the second-order AM scheme to Eq. (3.4) and multiplying the resulting equation by $e^{A(t^{n+1})}$ we obtain

$$y^{n+1} = E_n^{n+1} y^n + \frac{\tau}{12}(5n^{n+1} + 8E_n^{n+1} n^n - E_{n-1}^{n+1} n^{n-1}). \tag{3.31}$$

The factor $\hat{E}_j^{n+1}$ for $j = n-1, n$ is computed as outlined for the IFAB$_3$ method.

IF midpoint scheme

Applying the midpoint rule to Eq. (3.4) and multiplying the resulting equation by $e^{A(t^{n+1})}$ we obtain

$$y^{n+1} = E_n^{n+1} y^n + \tau E_{n+\frac{1}{2}}^{n+1} n^{n+\frac{1}{2}}. \tag{3.32}$$

Consider $P(\ell;[t_j, t_{n+1}])$, $P(n;[t_j, t_{n+1}])$ for $j = n, n+\frac{1}{2}$. The factor $\hat{E}_j^{n+1}$, is computed applying the trapezoidal integration rule over the interval $[t^j, t^{n+1}]$. The IF midpoint scheme is referred to in the plots as IFMid$_2$.

Integrating factor backward differentiation schemes

IFBDF$_2$

Applying the second-order BDF scheme to Eq. (3.4) and multiplying the resulting equation by $e^{A(t^{n+1})}$ we obtain

$$y^{n+1} = \frac{4}{3} E_n^{n+1} y^n - \frac{1}{3} y^{n-1} E_{n-1}^{n+1} + \tau \frac{2}{3} n^{n+1}. \tag{3.33}$$

The factor $\hat{E}_j^{n+1}$ for $j = n-1, n$ is computed as outlined for the IFAB$_2$ method.

IFBDF$_3$

Applying the third-order BDF scheme to Eq. (3.4) and multiplying the resulting equation by $e^{A(t^{n+1})}$ we obtain

$$y^{n+1} = \frac{18}{11}E_n^{n+1}y^n - \frac{9}{11}y^{n-1}E_{n-1}^{n+1} + \frac{2}{11}y^{n-2}E_{n-2}^{n+1} + \tau\frac{6}{11}n^{n+1}. \tag{3.34}$$

The factor $\hat{E}_j^{n+1}$ for $j = n-2, n-1, n$ is computed as outlined for the IFAB$_3$ schemes. Following similar approaches to the ones described above, we obtain the IFAB$_4$, IFAM$_4$ and IFBDF$_4$ schemes.

3.1.3 High-order RL schemes

In [Lontsi et al., 2017] exponential AB and the RL schemes are considered up to fourth-order accuracy. These methods are based on the *variation of constants formula*. The RL method of order of accuracy m (referred to as RL$_m$) is of the form

$$y^{n+1} = y^n + \tau\varphi_1(\alpha_{n,m}\tau)(\alpha_{n,m}y^n + \beta_{n,m}). \tag{3.35}$$

The coefficient $\alpha_{n,m}$ and $\beta_{n,m}$ (which explicit expressions are reported in [Lontsi et al., 2017]) are chosen to ensure the convergence at order m of the scheme (3.35). In [Lontsi et al., 2017] the canine ventricular Beeler-Reuter [Beeler and Reuter, 1977 Jun] model is considered. In our work the performance of RL$_m$ are assessed for the more stiff BWZVP model.

3.2 High-order schemes for the monodomain equation

In this section we present high-order strategies for the time discretization of the monodomain system

$$\begin{cases} \beta(C_m\dfrac{\partial V}{\partial t} + I_{\text{ion}}(V,\mathbf{s},\mathbf{c})) &= \nabla\cdot\mathbf{G}_{\text{m}}\nabla V + I_{\text{app}}, & \text{in } \mathscr{B}_r\times\mathscr{T}, \\ \dfrac{d\mathbf{s}}{dt} &= \mathbf{S}(V,\mathbf{c}) & \text{in } \mathscr{B}_r\times\mathscr{T}, \\ \dfrac{d\mathbf{c}}{dt} &= \mathbf{Z}(V,\mathbf{s}) & \text{in } \mathscr{B}_r\times\mathscr{T}, \\ \mathbf{n}\cdot\mathbf{G}_{\text{m}}\nabla V &= 0 & \text{in } \partial\mathscr{B}_r\times\mathscr{T}, \\ V(\mathscr{B}_{\text{r}},0) = V_0, \quad \mathbf{s}(\mathscr{B}_{\text{r}},0) = \mathbf{s}_0, & \quad \mathbf{c}(\mathscr{B}_{\text{r}},0) = \mathbf{c}_0. \end{cases} \tag{3.36}$$

We apply the three steps strategy designed in Alg. 4. The considered IMEX-EXP$_m$ and BDF-EXP$_m$ schemes. For both IMEX-EXP$_m$ and BDF-EXP$_m$ strategies, we solve the ODEs (3.36.2) by mean of an EXP$_m$ time stepping scheme while the ODEs (3.36.3) are solved considering the AB$_m$ scheme. The IMEX-EXP$_m$ and BDF-EXP$_m$ schemes differ each other by the numerical discretization of (3.36.1). In IMEX$_m$ schemes an implicit-explicit time integrator [Franzone and Pavarino, 2004; Ethier and Bourgault, 2008a; Perego and Veneziani, 2009] of order of accuracy m is applied for the solution of Eq. (3.36.1). In BDF$_m$ schemes this equation is solved by mean of the backward differentiation formula [Ethier and Bourgault, 2008a; Perego and Veneziani, 2009; Hundsdorfer and Verwer, 2013] of order of accuracy m.

Unless extrapolation techniques are considered, high-order IF$_m$ and ETD$_m$ (without stabilization) approaches require an implicit evaluation of the coefficients with respect to the AP. In

this case the above-mentioned strategy for the staggered solution of (3.36) need to be modified. Under these circumstances IMEX$_m$ approaches can be applied for the solution of Eq. (3.36.1) coupled with implicit or explicit schemes in V for the solution of Eq. (3.36.2) switching stage 2 and 3. On the other hand, BDF approaches for the solution of Eq. (3.36.1) can be coupled with ETDStab$_m$ and RL$_m$ approaches for the solution of Eq. (3.36.2). Alternatively, in a predictor-correct fashion, a corrective fourth step can be additionally considered. In this case in stage 2. we consider an EXP$_m$ method fully explicit with respect to V. This step can be seen as a predictor step. After the computation of the action potential in stage 3. via IMEX$_m$ or BDF$_m$ approach, we are then able to apply a EXP$_m$ method implicit with respect to V in stage 4. This step can be regarded as a corrector step. In the next sections we present IMEX and BDF approaches for the solution of Eq. (3.36.1). For simplicity, we neglect the contribution of the applied current I_{app} which, in the proposed numerical tests, is independent on V.

1: a step of AB$_m$ scheme is applied to (3.36.3) to update the ionic concentrations $\mathbf{c}$;
2: a step an EXP$_m$ scheme is then applied to (3.36.2) to update the gating variables $\mathbf{s}$;
3: a step of IMEX$_m$ or BDF$_m$ is applied to (3.36.1) to update the action potential V.

Algorithm 4: Numerical integration schemes for the solution of the monodomain system.

3.2.1 Implicit-explicit - exponential schemes

IMEX$_m$ schemes for the solution of Eq. (3.36.1) combine an implicit scheme for the discretization of the diffusive term and an explicit one for the discretization of the ionic (and applied) currents. In detail, they combine implicit and explicit Adams schemes of order of accuracy m obtaining

$$\beta C_m \sum_{j=0}^{m} a_j V^{n+1-j} + \tau \left(\sum_{j=0}^{m} b_j \nabla \cdot \mathbf{G}_{\text{m}} \nabla V^{n+1-j} + \beta \sum_{j=1}^{m} c_j I_{\text{ion}}(V^{n+1-j}, \mathbf{s}^{n+1-j}, \mathbf{c}^{n+1-j}) \right) = 0. \tag{3.37}$$

The parameters a_j, b_j, and c_j are chosen to obtain a m-th order scheme. Coupling IMEX$_m$ scheme with a EXP$_m$ scheme for the solution of Eq. (3.36.2) and with the AB$_m$ scheme for the solution of the ionic concentrations described in Eq. (3.36.3) the resulting method is referred to as IMEX-EXP$_m$ scheme. In case we consider cells dynamics, we replace Eq. (3.36.1) by

$$C_m \frac{dV}{dt} + I_{\text{ion}}(V, \mathbf{s}, \mathbf{c}) \quad = \quad 0 \tag{3.38}$$

In this case stage 3. is substituted by a step of AB$_m$ scheme applied to (3.38) to update V. Underlining the explicit nature of Bashforth schemes, we refer to the resulting strategies as EX-EXP$_m$ schemes.

3.2.2 Backward differentiation formula - exponential schemes

The application of BDF$_m$ schemes to Eq. (3.36.1) results into an implicit evaluation of the diffusive term and of the ionic (and applied) currents. Resulting schemes obey the equation

$$\beta C_m \sum_{j=0}^{m} a_j V^{n+1-j} + \tau b \left(\nabla \cdot \mathbf{G}_{\text{m}} \nabla V^{n+1} + \beta I_{\text{ion}}(V^{n+1}, \mathbf{s}^{n+1}, \mathbf{c}^{n+1}) \right) = 0, \tag{3.39}$$

where the parameters a_j, and b are chosen to obtain a m-order of accuracy scheme. We consider $a_0 = 1$. Coupling the obtained BDF$_m$ scheme with an EXP$_m$ scheme for the solution of (3.36.2) and with the AB$_m$ scheme for the solution of the ionic concentrations (3.36.3) the resulting method is referred to as BDF-EXP$_m$ scheme. In this case, we consider an explicit EXP$_m$ scheme for the solution of the gating variables. We define $r(V^{n+1})$ to be the left hand side of Eq. (3.39). The solution of the arising nonlinear problem $r(V^{n+1}) = 0$ is computed applying the Newton's algorithm. In this case, considering the time step $n+1$ (which index is neglected), stage 3 of Newton's Alg. (1) reads

$$\text{solve for} \quad \delta V \ \text{ s.t.} \quad \mathscr{D}r(V^k)\delta V = -r(V^k) \tag{3.40}$$

where

$$r(V^k) = V^k + \beta C_m \sum_{j=1}^{m} a_j V^{n+1-j} + \tau b \left(\nabla \cdot \mathbf{G}_{\mathrm{m}} \nabla V^k + \beta I_{\mathrm{ion}}(V^k, \mathbf{s}^{n+1}, \mathbf{c}^{n+1}) \right) = 0. \tag{3.41}$$

It holds

$$\mathscr{D}r(V^k)\delta V = \frac{\partial r}{\partial V^k}\delta V = \beta C_m \delta V + \tau b \left(\nabla \cdot \mathbf{G}_{\mathrm{m}} \nabla(\delta V) + \beta \frac{\partial I_{\mathrm{ion}}(V^k, \mathbf{s}^{n+1}, \mathbf{c}^{n+1})}{\partial V^k} \delta V \right). \tag{3.42}$$

Therefore the application of BDF discretization implies the need to evaluate the derivatives of the ionic currents with respect to the AP. To obtain an estimate of the derivatives finite differences (FD) method is applicable. Due to its computational cost, the resulting FD-BDF-EXP$_m$ strategy is suitable just in one-dimensional simulations. In the next sections we present two alternative to the FD approach: the quasi-Newton (qN-BDF-EXP) and the complex step derivative approximation (CSDA-BDF-EXP) backward differentiation exponential schemes.

3.3 Approximation of the derivatives of the ionic currents in backward differentiation formula-based schemes

3.3.1 Quasi-Newton schemes

Goal of quasi-Newton approaches is to propose a suitable approximation of the derivatives of interest. Slightly modifying the general form proposed by [Ambrosi et al., 2012], ionic currents can be expressed as sum of P currents as

$$I_{\mathrm{ion}}(V, \mathbf{s}, \mathbf{c}) = \sum_{p=1}^{P} I_p(V, \mathbf{s}) \quad \text{where} \quad I_p(V, \mathbf{s}) = g_p(V, \mathbf{s}, \mathbf{c})(V - V_p). \tag{3.43}$$

In detail we define

$$g_p(V, \mathbf{s}, \mathbf{c}) = k_p q_p(V, \mathbf{c}) \prod_{i=1}^{n_g} s_i^{p_{pi}}(V, \mathbf{c}). \tag{3.44}$$

Here k_p are the maximum conductances of the ionic channel p and p_{pi} are integers. Moreover $q_p : \mathscr{B}_r \times \mathscr{T} \to \mathbb{R}$. Consider the time step $n+1$ of stage 3 of Newton's Alg. 1. For the sake of simplicity, we neglect the index n. In the proposed qN approach, we approximate the derivative of the ionic currents with respect to V by

$$\frac{\partial I_{\mathrm{ion}}(V^k, \mathbf{s}^{n+1}, \mathbf{c}^{n+1})}{\partial V^k}\delta V \approx k_p q_p(V^k, \mathbf{c}^{n+1}) \prod_{i=1}^{n_g} s_i^{p_{pi}}(V^k + \delta V, \mathbf{c}^{n+1}). \tag{3.45}$$

We recall that the FHN model (see 1.2.2) does not follow the HH formalism. For this model the analytic computation of the derivative of I_{ion} with respect to the AP is straightforward. For this latter model, in the proposed qN approach we approximate the derivative of interest neglecting the contribution of the term associated to the recovery gating variable ω, i.e.

$$\begin{aligned}\frac{\partial I_{\text{ion}}(V^k,\omega^{n+1})}{\partial V^k}\delta V \approx \quad & c_1((V^k+\delta V-V_{\text{r}})(V^k+\delta V-V_{\text{unst}})+\\ & +(V^k+\delta V-V_{\text{r}})(V^k+\delta V-V_{\text{p}})+(V^k+\delta V-V_{\text{unst}})(V^k+\delta V-V_{\text{p}})).\end{aligned} \tag{3.46}$$

3.3.2 Complex step derivative approximation

Lyness and Moler [Lyness, 1967; Lyness and Moler, 1967] introduced the use of complex arithmetic for the numerical approximation of derivatives. In this section we discuss the application of the CSDA for the evaluation of the partial derivative of the function $I_{\text{ion}}(V,\mathbf{s},\mathbf{c})$, with respect to V. We consider V to be an independent variable. Given the function $I_{\text{ion}}\colon \mathbb{R}\times\mathbb{R}^{n_g}\times\mathbb{R}^{m_c}\to\mathbb{R}$, we consider its Taylor series expansion

$$\begin{aligned}I_{\text{ion}}(V+ih_v,\mathbf{s},\mathbf{c}) &= \sum_{\zeta=0}^{\infty}\frac{(ih_v)^\zeta}{\zeta!}\frac{\mathrm{d}^\zeta I_{\text{ion}}(V,\mathbf{s},\mathbf{c})}{\partial V^\zeta} =\\ &= I_{\text{ion}}(V,\mathbf{s},\mathbf{c})+ih_v\frac{\partial I_{\text{ion}}(V,\mathbf{s},\mathbf{c})}{\partial V}+\\ &-\frac{h_v}{2!}\frac{\partial^2 I_{\text{ion}}(V,\mathbf{s},\mathbf{c})}{\partial V^2}+O(h_v^3),\end{aligned}$$

where $V,h_v\in\mathbb{R}$ and $i^2=-1$. Equating the imaginary parts it holds

$$\frac{\partial I_{\text{ion}}(V,\mathbf{s},\mathbf{c})}{\partial V}=\operatorname{Im}\frac{I_{\text{ion}}(V+ih_v,\mathbf{s},\mathbf{c})}{h_v}+O(h_v^2). \tag{3.47}$$

We underline that the estimate

$$\frac{\partial I_{\text{ion}}(V,\mathbf{s},\mathbf{c})}{\partial V}\simeq\operatorname{Im}\frac{I_{\text{ion}}(V+ih_v,\mathbf{s},\mathbf{c})}{h_v} \tag{3.48}$$

is not subject to subtractive numerical cancellation errors. Applying the CSDA method, in Eq. 3.42 we consider the estimate

$$\frac{\partial I_{\text{ion}}(V^k,\mathbf{s}^{n+1},\mathbf{c}^{n+1})}{\partial V^k}\approx\operatorname{Im}\frac{I_{\text{ion}}(V^k+i\delta V,\mathbf{s}^{n+1},\mathbf{c}^{n+1})}{\delta V}. \tag{3.49}$$

Main advantages of the CSDA are that the considered approximation is not subject to roundoff errors and that the method is easily implementable in a black-box manner. The CSDA can be applied to generic functions under the hypothesis that they admit a complex analytic extension. In case, for example, the considered ionic model involves an Heaviside function, an approximation of this function that admit a complex extension need to be considered. Uses of the CSDA appear in [Kelley, 2003] and in [Martins et al., 2003]. In this latter work the automatic implementation of the CSDA is presented in detail for C/C++ and Fortran. To the best of our knowledge, the application of this approach in cardiac electrophysiology represents a novelty of our work.

Equation	Symbol	Quantity	Unit	Value
Monodomain	C_m	transmembrane capacitance	μF cm^{-2}	1
	χ	surface to volume ratio	cm^{-1}	1400
	$\mathbf{G}_i$	intra-longitudinal conductivity	mS mm^{-1}	0.17, 0.019
	$\mathbf{G}_e$	extra-longitudinal conductivity	mS mm^{-1}	0.62, 0.24
FHN	V_{r}	resting value	mV	-85.0
	V_{p}	peak value	mV	30.0
	V_{unst}	unstable value	mV	-57.6
	η_1	first param.	mScm^{-2}mV^{-2}	1.4e-3
	η_2	second param.	mScm^{-2}	10.0
	η_3	third param	ms^{-1}mV^{-1}	2.6e-3
	η_4	fourth param	ms^{-1}	2.3
BWZVP	V_{r}	resting AP value	mV	-90.2
TTNP06	V_{r}	resting AP value	mV	-85.8
	APD	restitution slope		1.1

Table 3.1. Parameters calibration for the performed numerical tests.

3.4 Numerical Results

Aim of this section is to investigate the convergence behavior of the high-order time integration schemes presented in Sec. 3.1 and in Sec. 3.2. Moreover we study their impact on post-processing quantities of clinical relevance. As a preliminary test, in Sec. 3.4.1 we assess the performances of EXP_m schemes applied to a IVP with trigonometric functions as coefficient (test A). Moreover, we discuss the numerical results for the EXP_m schemes applied to the BWZVP cellular model with given action potential (test B). To extend the results, we study of the converge of the IMEX-ETDStab_m and of the BDF-ETDStab_m schemes for the solution of the complete cellular BWZVP model (test C). In this case, due to the absence of the diffusive term, IMEX-ETDStab_m schemes reduce to EX-ETDStab_m schemes. Additionally in Sec. 3.4.2, we discuss high-order nonlinear strategies for the solution of the monodomain system. In detail, in test D, we investigate the performance of IMEX-ETDStab_m and qN-BDF-ETDStab_m schemes for the solution of the monodomain system (3.36) coupled with the FHN and the BWZVP ionic models. Moreover, the qN-BDF-ETDStab_m schemes are compared in terms of required computational time. In Sec. 3.4.3, we compare the performance of the qN-BDF-ETDStab_m, the CSDA-BDF-ETDStab_m and the FD-BDF-ETDStab_m schemes in 1D and 3D numerical tests. In detail, for this tests we consider the FHN, the BWZVP, and the TNNP06 models. Unless otherwise stated, we consider the model parameters reported in Tab. 5.1 and the absolute tolerance of $tol =$ 1e-10 as stopping criteria. We solve the linear system arising from the linearization of the monodomain equation with algebraic multigrid (AMG) method (BoomerAMG of the PETSc suite [Balay et al., 2017]).

3.4.1 Numerical results for exponential schemes

In this section, we consider the relative error in $L^\infty(t_0, t_{\text{fin}})$ norm between the numerical solution y_τ and the reference solution u_{ref} defined as

$$err_{\text{r}}(y_\tau, u_{\text{ref}}) = \frac{\|y_\tau - u_{\text{ref}}\|_{L^\infty}}{\|u_{\text{ref}}\|_{L^\infty}}. \tag{3.50}$$

Exponential schemes for trigonometric IVP - Test A

We compare the performance of the EXP schemes for the solution of the IVP problem

$$\begin{cases} y(t)' = \cos(t)y(t) + \cos^3(t), \\ y(0) = 0. \end{cases} \tag{3.51}$$

The IVP above admits analytical solution $u(t) = \sin(t)^2 + 2\sin(t) + 1 - e^{\sin(t)}$. We consider $t_{\text{fin}} = 10$. In Fig. 3.1, we compare the performance of first-, second-, third- and fourth-order EXP_m schemes, respectively, for the solution of Eq. (3.51). In particular second-, third- and fourth-rows show results obtained for the IF_m schemes on the left and for the ETD_m schemes on the right panels of the figure. For all the considered order of accuracy, results show that ETD_m (with or without stabilization) and RL_m schemes allow to achieve a smaller relative error if compared to the ones achieved using IF_m schemes. Due to the polynomial approximation required by the methods, we underline that the low errors obtained applying the non-stabilized ETD_m schemes are associated with an higher computational cost.

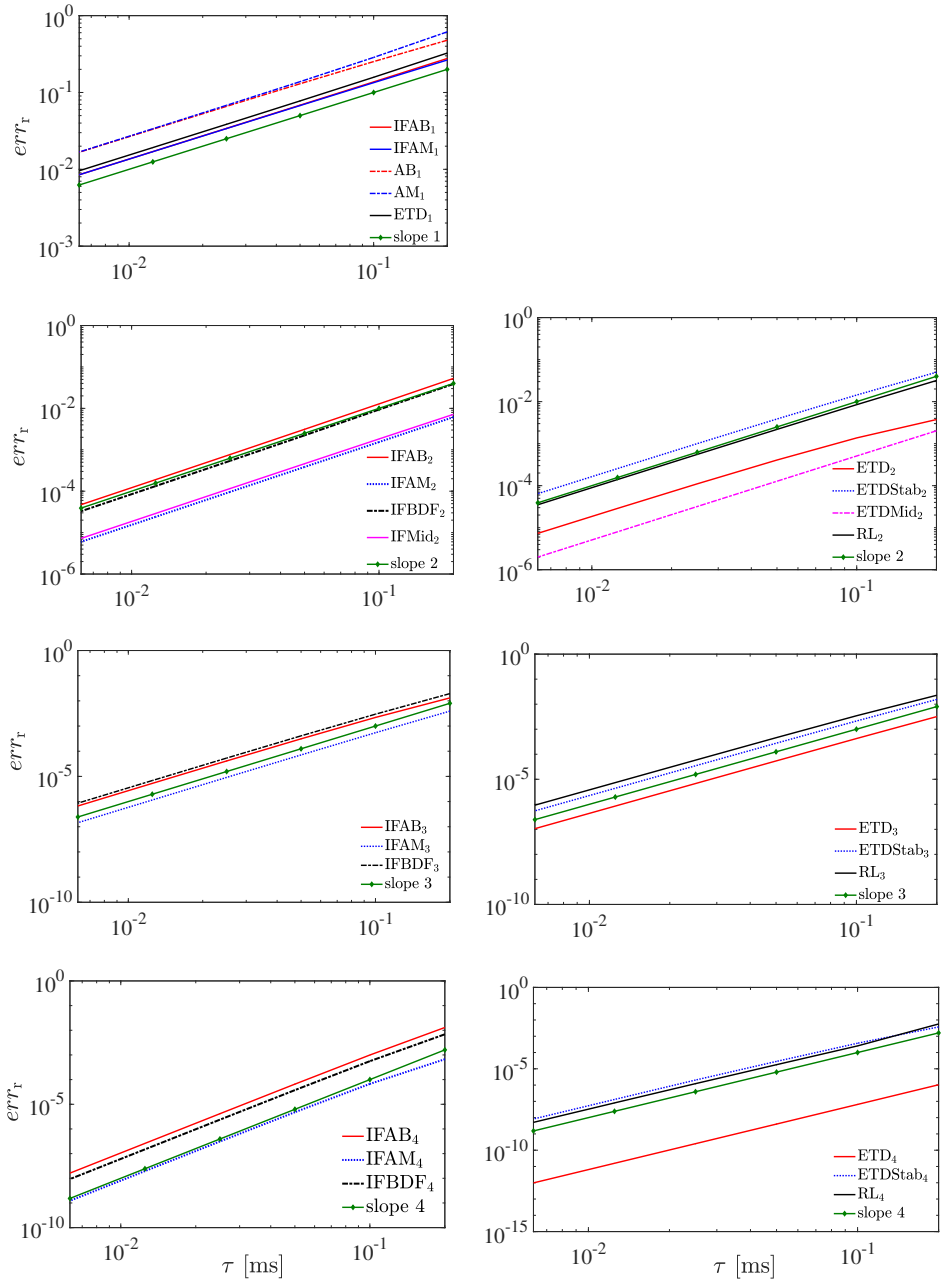

Figure 3.1. Test A. Performance of IF$_m$, BDF$_m$, ETD$_m$, and RL$_m$ schemes for the IVP (3.51). Second-, third- and fourth-rows show results obtained for the IF$_m$ schemes (left) and for the ETD$_m$ schemes (right). Relative errors in L^∞ norm are computed against the analytical solution u.

Exponential schemes for the BWZVP cellular model action potential given) - Test B

We here report the results obtained applying the ETD_m and RL_m methods for the solution of the BWZVP first generation cellular model

$$\begin{cases} C_m \frac{dV}{dt} + I_{\text{ion}}(V, \mathbf{s}) &= I_{\text{app}}, \\ \frac{ds_i}{dt} &= \alpha_i(V)(1-s_i) - \beta_i(V)s_i, \quad i = 1, \dots, n_g. \end{cases} \tag{3.52}$$

The reference solution u is obtained considering a AB_2-AM_3 predictor-corrector approach with time step $\tau = 2^{-12}$ ms. We study the performance of the schemes in an isolated fashion considering the AP as given. We consider the $C^\infty(t_0, t_{\text{fin}})$ stimulation protocol

$$I_{\text{app}}(t) = \chi_{(19,21)}(t) I_{\text{max}} e^{\left((t-20)^2-1\right)^{-1}} \quad \text{with} \quad I_{\text{max}} = 100\ \mu\text{A}. \tag{3.53}$$

We consider $[t_0, t_{\text{fin}}] = [0, 450]$ ms. First-, second- and third-rows of Fig. 3.2 show the performance of first- and second-, third- and fourth-order schemes, respectively. Relative errors in L^∞ norm are computed against the reference solution. Results are shown for the stiff gating variables v (first column) and m (second column) and for the non-stiff variable f (third column). Results show that, for all the considered order of accuracy, the non-stabilized ETD schemes allow to achieve a smaller relative error if compared to the ones achieved applying the ETDStab and RL schemes. The ETDStab and the RL schemes perform similarly for the solution of the non-stiff gating variable f. The behavior of the errors associated to the non-stiff gating variables t_o and X is similar to the one associated to f. Avoiding redundancy in the plots we report only the gating variables v, m, f.

Exponential schemes for the BWZVP cellular model - Test C

We investigate the convergence of the EX-ETDStab and of the BDF-ETDStab methods for the BWZVP cellular model (see Sec. 3.52). We consider $V_0(x) = 0$, and the naturally associated initial values for the gating variables. As in the previous test, we consider $[t_0, t_{\text{fin}}] = [0, 450]$ ms. The reference solution is obtained applying AB_2-AM_3 predictor-corrector approach with time step $\tau = 2^{-12}$ ms. Tab. 3.2 and 3.3 report the relative errors (denoted as err_{r}) of the numerical solutions computed applying the EX-ETDStab_m and qN-BDF-ETDStab_m schemes, respectively. Tables show that, considering the same time step and the same order of accuracy of the methods, the EXP-ETDStab and qN-BDF-ETDStab approaches perform similarly. However we recall that the application of high-order EX-ETDStab_m is subjected to stability conditions. In particular $\tau \leq$ 1e-1 ms and $\tau \leq$ 5e-2 ms are required to obtain the convergence of EX-ETDStab_3 and the EX-ETDStab_4 schemes, respectively. Similar stability results have been shown in [Perego and Veneziani, 2009]. The estimated convergence rates (denoted as r and computed considering nested sequence of time grids) are reported in brackets. Even if theoretical proofs of convergence for the considered schemes are not available, the estimated convergence rates of the qN-BDF-ETDStab_m approaches perfectly fit our expectations.

3.4.2 Numerical results for nonlinear high-order schemes

In this section, we consider the absolute error between the numerical solution y_τ and the reference solution u computed as

$$err_{\text{a}}(y_\tau, u) = \max_{t \in [t_0, t_{\text{fin}}]} \|y_\tau - u\|_{L^2}. \tag{3.54}$$

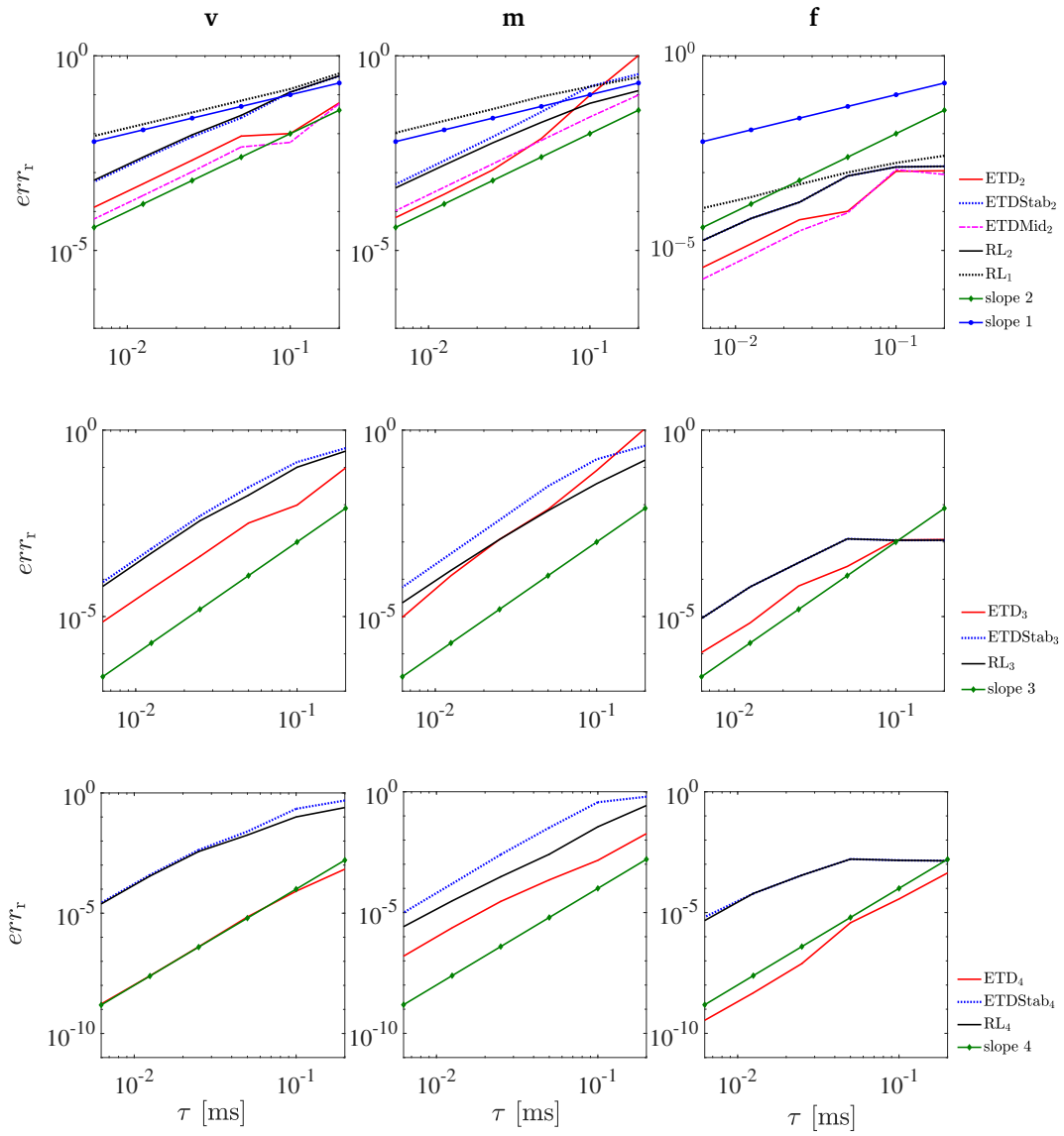

Figure 3.2. Test B. Performance of EXP$_m$ integration schemes for the solution of the stiff gating variables v (first-) and m (second-column) and for the non-stiff variable f (third column) of the BWZVP model. Results are shown for the first- and second- (first-), third- (second-) and fourth-order (third-row) schemes. The AP is considered as given. Relative errors in L^∞ norm are computed against the reference solution.

High-order schemes for 1D monodomain coupled with the BWZVP model - Test D

As idealized cardiac muscle fiber, we consider a 2 cm long fiber aligned along the x-axis. In 1D tests, we consider the intra-longitudinal and the extra-longitudinal conductivities to be equal to

	EX-ETDStab$_1$		EX-ETDStab$_2$		EX-ETDStab$_3$		EX-ETDStab$_4$	
τ [ms]	err_{r}	r	err_{r}	r	err_{r}	r	err_{r}	r
2e-1	7.09e1	(-)	6.44e1	(-)	-	-	-	-
1e-1	5.06e1	(0.48)	1.35e1	(2.16)	3.73e1	(-)	-	-
5e-2	1.61e1	(1.65)	6.52	(1.04)	4.44	(3.07)	1.10	(-)
2.5e-2	4.86	(1.73)	2.22	(1.55)	4.47e-1	(3.31)	5.89e-2	(4.22)
1.25e-2	2.42	(1.00)	6.19e-1	(1.84)	5.56e-2	(3.00)	1.78e-3	(5.04)
6.25e-3	1.21	(1.00)	1.60e-1	(1.94)	6.62e-3	(3.07)	2.61e-4	(2.76)
3.125e-3	0.60	(1.00)	4.06e-2	(1.98)	8.01e-4	(3.04)	2.41e-5	(3.43)
1.5625e-3	0.30	(1.00)	1.02e-2	(1.99)	1.00e-4	(2.99)	5.29e-7	(5.50)

Table 3.2. Test C. Relative errors (denoted as err) in L^∞ norm for the solution of the BWZVP cellular model applying EX-ETDStab$_m$ schemes. The estimated convergence rates (denoted as r), computed considering nested sequence of time grids, are reported in brackets.

1 mS mm^{-1}. We consider the stimulus

$$I_{\mathrm{app}}(x,t) = \chi_{[0,0.2]\times(0,2)}(x,t) I_{\mathrm{max}} e^{\left((t-1)^2-1\right)^{-1}} \quad \text{with} \quad I_{\mathrm{max}} = 130000\ \mu\mathrm{A},$$

for $[t_0, t_{\mathrm{fin}}] = [0, 450]$ ms. In case the FHN ionic model is considered, the exact Newton (N) method is applicable. As a preliminary test, we first study of the converge of N-BDF-BDF$_m$ and N-BDF-ETDStab$_m$ schemes for the solution of the monodomain equation coupled with the FHN ionic model. Left panel of Fig. 3.3 reports the snapshots of the numerical solutions obtained with the N-BDF-ETDStab$_m$ schemes at time $t = 10$ ms. The reference solution is computed with the time step $\tau = 2^{-9}$ ms and a spatial mesh of size h =2e-4 cm. The space-time grids considered are uniformly distributed. The reference solution is obtained with the N-BDF-BDF$_3$ scheme, which convergence for $\tau = 2^{-13}$ has been tested against the solutions obtained with the N-BDF-BDF$_1$ and the N-BDF-BDF$_2$ schemes. It is well known that, in case of travelling waves, considering sufficiently small values of h, FE schemes overestimates the analytical conduction velocities (CV) [Pezzuto et al., 2016]. Fixed a particular h, our goal is to study how the numerical time-integration schemes reproduce the CV obtained for the reference numerical solution. For the BWZVP model, considering the first-order scheme a remarkable delay in the electrical activation of the tissue is obtained. After 10 ms, the mean CV computed considering the N-BDF-BDF$_1$ and the N-BDF-ETDStab$_1$ schemes are approximatively the 6% higher of the one computed considering the corresponding second-, third-, and fourth-order schemes. The obtained absolute errors (denoted in the table as err_{a}) for the N-BDF-BDF$_m$ and N-BDF-ETDStab$_m$ schemes are reported in Tab. 3.4 and 3.5. Estimated convergence rates (denoted with r), computed considering nested sequence of time grids, are reported in brackets. For what concerns the estimated convergence rates, all the methods perfectly fit our expectations. Moreover we study of the converge of the IMEX-ETDStab$_m$ and the BDF-ETDStab$_m$ schemes for the solution of the monodomain system coupled with the BWZVP ionic model. As already discussed in the introduction, high-order IMEX-ETDStab$_m$ schemes are conditionally stable. In this test, the convergence of the IMEX-ETDStab$_3$

	qN-BDF-ETDStab$_1$		qN-BDF-ETDStab$_2$		qN-BDF-ETDStab$_3$		qN-BDF-ETDStab$_4$	
τ [ms]	err_r	r	err_r	r	err_r	r	err_r	r
2e-1	1.05e1	(-)	1.11e1	(-)	4.23e1	(-)	3.05e1	(-)
1e-1	5.34	(0.98)	4.57	(1.33)	8.57	(2.30)	1.47e1	(1.10)
5e-2	3.62	(0.55)	1.39	(1.71)	1.46	(2.55)	7.81e-1	(4.23)
2.5e-2	2.43	(0.57)	3.37e-1	(2.04)	1.97e-1	(2.88)	5.39e-2	(3.85)
1.25e-2	1.37	(0.82)	1.01e-1	(1.74)	1.95e-2	(3.33)	3.67e-3	(3.87)
6.25e-3	7.22e-1	(0.92)	2.80e-2	(1.84)	2.25e-3	(3.11)	2.34e-4	(3.94)
3.125e-3	3.70e-1	(0.96)	7.35e-3	(1.93)	2.88e-4	(2.97)	1.31e-5	(4.17)
1.5625e-3	1.87e-1	(0.98)	1.88e-3	(1.96)	3.57e-5	(3.01)	1.30e-6	(3.33)

Table 3.3. Test C: relative errors (denoted as err$_m$) in L^∞ norm for the solution of the BWZVP cellular model applying qN-BDF-ETDStab$_m$ schemes. Estimated convergence rates (denoted as r), computed considering nested sequence of time grids, are reported in brackets.

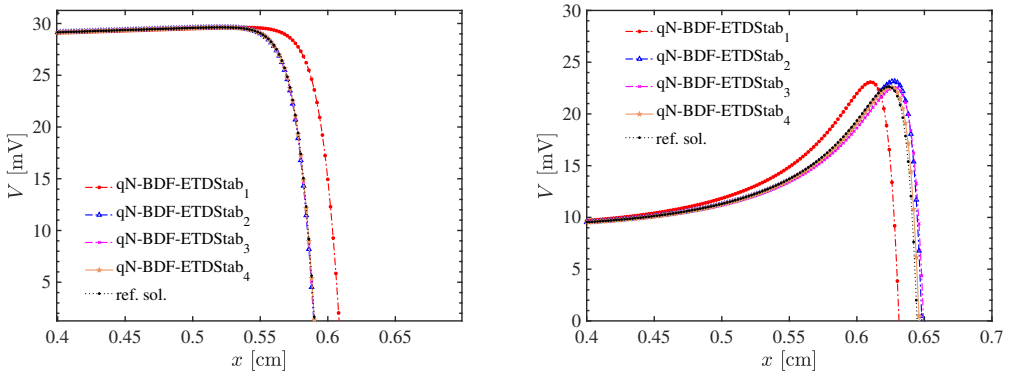

Figure 3.3. Test D: snapshot at $t = 10$ ms of the numerical solutions of the monodomain system coupled with the FHN (left) and the BWZVP (right) models computed with qN-BDF-ETDStab$_m$ schemes with $\tau =$ 5e-2 ms.

and IMEX-ETDStab$_4$ methods are subjected to $\tau \leq$ 5e-2 ms and $\tau \leq$ 2.5e-2 ms, respectively. For smaller values of τ, the sizes $h_{\min}$ of the finest spatial grids that ensure the convergence of the IMEX-ETDStab$_3$ and IMEX-ETDStab$_4$ schemes are reported in Tab. 3.6. Similar results have been reported in [Ethier and Bourgault, 2008a]. Considering the spatial grids of mesh sizes $h_{\min}$, it is not possible to observe the order of accuracy expected in time for the proposed schemes. In these cases the convergence in time is concealed by spatial effects. As discussed in Sec. 3.2.2, the application of BDF-ETDStab$_m$ methods in a Newton fashion require the evaluations of the derivatives of the currents with respect to V. We consider the numerical solutions obtained with qN-BDF-ETDStab$_m$ schemes. Right panel of Fig. 3.3 reports the snapshots of the numerical solutions at time $t = 10$ ms. Considering the first-order scheme a remarkable delay in the electrical

	N-BDF-BDF$_1$		N-BDF-BDF$_2$		N-BDF-BDF$_3$		N-BDF-BDF$_4$	
τ [ms]	err_a	r	err_a	r	err_a	r	err_a	r
2e-1	2.94e1	(-)	6.68	(-)	3.51	(-)	1.74	(-)
1e-1	1.52e1	(0.94)	2.03	(1.71)	5.61e-1	(2.64)	4.58e-1	(1.92)
5e-2	7.58	(1.00)	5.74e-1	(1.82)	1.11e-1	(2.32)	6.7e-2	(2.75)
2.5e-2	3.73	(1.02)	1.48e-1	(1.95)	1.52e-2	(2.87)	6.13e-3	(3.46)
1.25e-2	1.84	(1.01)	3.67e-2	(2.01)	1.60e-3	(3.24)	4.39e-4	(3.80)
6.25e-3	9.14e-1	(1.01)	9.06e-3	(2.01)	2.37e-4	(2.75)	2.6e-5	(4.07)
3.125e-3	4.55e-1	(1.00)	2.24e-3	(2.01)	3.17e-5	(2.90)	1.48e-6	(4.13)
1.5625e-3	2.27e-1	(1.00)	5.58e-4	(2.00)	4.10e-6	(2.95)	9.25e-8	(4.00)

Table 3.4. Test D: absolute errors (denoted with err$_a$) for the solution monodomain equation coupled with the FHN ionic model applying the N-BDF-BDF$_m$ schemes. The estimated convergence rates r, computed considering nested sequence of time grids, are reported in brackets.

	N-BDF-ETDStab$_1$		N-BDF-ETDStab$_2$		N-BDF-ETDStab$_3$		N-BDF-ETDStab$_4$	
τ [ms]	err_a	r	err_a	r	err_a	r	err_a	r
2e-1	2.94e1	(-)	6.69	(-)	3.51	(-)	1.74	(-)
1e-1	1.52e1	(0.94)	2.03	(1.71)	5.61e-1	(2.64)	4.58e-1	(1.92)
5e-2	7.58	(1.00)	5.75e-1	(1.82)	1.11e-1	(2.32)	6.79e-2	(2.75)
2.5e-2	3.35	(1.02)	1.48e-1	(1.95)	1.52e-2	(2.87)	6.13e-3	(3.46)
1.25e-2	1.84	(1.01)	3.68e-2	(2.01)	1.60e-3	(3.24)	4.45e-4	(3.78)
6.25e-3	9.14e-1	(1.01)	9.08e-3	(2.01)	2.37e-4	(2.75)	2.6e-5	(4.09)
3.125e-3	4.55e-1	(1.00)	2.21e-3	(2.03)	3.18e-5	(2.89)	1.54e-6	(4.08)
1.5625e-3	2.08e-1	(1.12)	5.48e-4	(2.01)	4.10e-6	(2.95)	9.25e-8	(4.05)

Table 3.5. Test D: absolute errors (denoted with err$_a$) for the solution monodomain equation coupled with the FHN ionic model applying the N-BDF-ETDStab$_m$ schemes. The estimated convergence rates r, computed considering nested sequence of time grids, are reported in brackets.

activation of the tissue is obtained. After 10 ms, the mean CV computed considering the qN-BDF-ETDStab$_1$ scheme is approximatively the 7% smaller of the one computed considering the qN-BDF-ETDStab$_4$ scheme. The absolute errors (denoted with err_a) associated to the numerical solutions obtained with the qN-BDF-ETDStab$_m$ schemes are reported in Tab. 3.7. The estimated convergence rates (denoted with r), computed considering nested sequence of time grids, are reported in brackets. Concerning the estimated convergence rates, qN-BDF-ETDStab$_1$, qN-BDF-ETDStab$_2$ and qN-BDF-ETDStab$_3$ perfectly fit our expectations. For the BDF-ETDStab$_4$ method, the estimated convergence rates presents some fluctuations around the expected value 4.

τ [ms]	IMEX-ETDStab$_3$	IMEX-ETDStab$_4$
5e-2	4.878e-3	$\emptyset$
2.5e-2	3.194e-3	5.263e-3
1.25e-2	2.222e-3	3.333e-3
6.25e-3	1.510e-3	2.222e-3

Table 3.6. Test D: minimum size $h_{\min}$ of the spatial uniform grids that ensure convergence of the IMEX-ETDStab$_m$ schemes given a specific time step τ. Results are reported for the IMEX-ETDStab$_3$ and IMEX-ETDStab$_4$ methods.

	qN-BDF-ETDStab$_1$		qN-BDF-ETDStab$_2$		qN-BDF-ETDStab$_3$		qN-BDF-ETDStab$_4$	
τ [ms]	err_a	r	err_a	r	err_a	r	err_a	r
2e-1	2.46e1	(-)	1.45e1	(-)	5.44	(-)	1.70e1	(-)
1e-1	1.35e1	(0.86)	2.08	(2.80)	1.42e1	(-)	2.01e1	(-)
5e-2	6.42	(1.07)	1.78	(0.22)	2.46	(2.52)	8.20e-1	(4.61)
2.5e-2	2.97	(1.11)	6.34e-1	(1.48)	3.16e-1	(2.96)	2.33e-3	(8.45)
1.25e-2	1.40	(1.08)	1.86e-1	(1.76)	3.88e-2	(3.02)	2.26e-3	(0.04)
6.25e-3	6.83e-1	(1.03)	5.03e-2	(1.88)	4.73e-3	(3.03)	2.13e-4	(3.40)
3.125e-3	3.36e-1	(1.02)	1.30e-2	(1.95)	5.77e-4	(3.03)	1.54e-5	(3.78)
1.5625e-3	1.66e-1	(1.01)	3.32e-3	(1.96)	6.99e-5	(3.04)	1.10e-6	(3.80)

Table 3.7. Test D: absolute errors (denoted with err$_a$) for the solution monodomain equation coupled with the BWZVP ionic model applying qN-BDF-ETDStab$_m$ schemes. The estimated convergence rates r, computed considering nested sequence of time grids, are reported in brackets.

Computational cost

To evaluate the computation cost of different time stepping schemes, we define

	qN-BDF-ETDStab$_1$					qN-BDF-ETDStab$_2$				
τ [ms]	$t_{\mathscr{G}}$ [s]	$t_{\mathscr{H}}$ [s]	$\mathscr{N}$	t_{ts} [s]	t_{gv}[s]	$t_{\mathscr{G}}$ [s]	$t_{\mathscr{H}}$ [s]	$\mathscr{N}$	t_{ts} [s]	t_{gv}[s]
2e-1	5.55e-3	5.68e-3	10.55	1.44e-1	4.44e-3	5.98e-3	5.98e-3	8.53	1.21e-1	5.02e-3
1e-1	5.78e-3	5.83e-3	7.71	1.08e-1	4.37e-3	6.01e-3	6.01e-3	6.74	1.00e-1	4.90e-3
5e-2	5.88e-3	5.89e-3	5.88	8.65e-2	4.23e-3	5.91e-3	6.06e-3	5.78	8.70e-2	4.74e-3
2.5e-2	6.01e-3	6.06e-3	4.90	7.67e-2	4.53e-3	6.24e-3	6.30e-3	4.87	7.86e-2	4.97e-3
1.25e-2	5.88e-3	5.85e-3	4.85	7.33e-2	4.46e-3	6.48e-3	6.58e-3	3.93	6.84e-2	5.12e-3
6.25e-3	5.89e-3	5.93e-3	3.92	6.18e-2	4.32e-3	6.32e-3	6.44e-3	3.90	6.61e-2	4.78e-3
3.125e-3	6.03e-3	5.98e-3	3.90	6.19e-2	4.37e-3	6.27e-3	6.42e-3	2.96	5.22e-2	4.87e-3
1.5625e-3	6.22e-3	6.29e-3	2.94	5.12e-2	4.37e-3	6.45e-3	6.78e-3	1.99	4.15e-2	4.75e-3
	qN-BDF-ETDStab$_3$					qN-BDF-ETDStab$_4$				
τ [ms]	$t_{\mathscr{G}}$ [s]	$t_{\mathscr{H}}$ [s]	$\mathscr{N}$	t_{ts} [s]	t_{gv} [s]	$t_{\mathscr{G}}$ [s]	$t_{\mathscr{H}}$ [s]	$\mathscr{N}$	t_{ts} [s]	t_{gv} [s]
2e-1	5.94e-3	6.12e-3	7.55	1.10e-1	5.57e-3	6.23e-3	6.58e-3	6.71	1.05e-1	6.57e-3
1e-1	6.08e-3	6.29e-3	5.86	9.08e-2	5.55e-3	6.47e-3	6.88e-3	5.83	9.76e-2	6.48e-3
5e-2	6.17e-3	6.50e-3	4.92	8.03e-2	5.60e-3	6.42e-3	6.85e-3	4.9	8.37e-2	6.51e-3
2.5e-2	6.54e-3	6.85e-3	4.87	8.35e-2	5.67e-3	6.45e-3	6.92e-3	4.83	8.29e-2	6.48e-3
1.25e-2	6.31e-3	6.81e-3	3.92	6.88e-2	5.57e-3	6.51e-3	7.10e-3	3.92	7.09e-2	6.56e-3
6.25e-3	6.63e-3	7.01e-3	3.90	7.04e-2	5.63e-3	6.55e-3	7.09e-3	3.9	7.04e-2	6.60e-3
3.125e-3	6.83e-3	7.16e-3	2.95	5.73e-2	5.64e-3	6.81e-3	7.23e-3	2.94	5.74e-2	6.38e-3
1.5625e-3	6.66e-3	6.98e-3	2.93	5.58e-2	5.65e-3	6.86e-3	7.26e-3	2.93	5.78e-2	6.43e-3

Table 3.8. Test D: $t_{\mathscr{G}}$, $t_{\mathscr{H}}$ the mean execution times for a single evaluation of the gradient and Hessian functions on the complete domain, $\mathscr{N}$ the mean number of nonlinear iterations per time step, t_{ts} the mean execution time per time step, and t_{gv} the mean evaluation time for the current value of the gating variables reported in second against the considered time step τ. We consider the qN-BDF-ETDStab$_m$ schemes for the BWZVP ionic model.

1. $t_{\mathscr{G}}$, $t_{\mathscr{H}}$: mean execution times in seconds for a single evaluation of the gradient and Hessian functions, respectively, on the complete domain;
2. $\mathscr{N}$: mean number of nonlinear iterations per time step;
3. t_{ts}: mean total assembling time in seconds per time step;
4. t_{gv}: mean execution times in seconds for the evaluation of the gating variables on the complete domain.

Tab. 3.8 reports the values of $t_{\mathscr{G}}$, $t_{\mathscr{H}}$, $\mathscr{N}$, t_{ts} computed with the qN-BDF-ETDStab$_m$ schemes considering the first 20 ms of simulation after the electrical activation of the tissue. Results are shown for the monodomain system coupled with the BWZVP ionic model. Simulations are run as single-core executions performed on MacBook Pro (Retina, Mid 2015) PC. Compared with the ones obtained for the first-order scheme, the times $t_{\mathscr{G}}$ and $t_{\mathscr{H}}$ increase respectively of approximatively the 5% and 6% for the qN-BDF-ETDStab$_2$, of the 8% and 13% for the qN-BDF-ETDStab$_3$ and

of the 10% and 17% for the qN-BDF-ETDStab$_4$ schemes. Moreover, the mean times t_{gv} increase of approximatively the 11%, the 27% and the 48% for the qN-BDF-ETDStab$_2$, the qN-BDF-ETDStab$_3$ and the qN-BDF-ETDStab$_4$ schemes, respectively. For equal values of τ, high-order methods correspond to a smaller number of nonlinear iteration per time step $\mathcal{N}$. In detail, compared with the ones obtained for the first-order scheme, a decrease of $\mathcal{N}$ of approximatively the 13%, of the 17% and of the 19% is obtained for the qN-BDF-ETDStab$_2$, qN-BDF-ETDStab$_3$ and qN-BDF-ETDStab$_4$ schemes, respectively. This results in smaller values of t_{ts} of approximatively the 7% for the -BDF-ETDStab$_2$ and qN-BDF-ETDStab$_3$ schemes and the 5% for the qN-BDF-ETDStab$_4$ scheme. Fig. 3.4 shows the cost in CPU time for the qN-BDF-ETDStab$_m$ schemes for 1 ms of simulation against the associated absolute errors. We notice that, for equal values of τ, the CPU times for the different schemes present very small fluctuations. For $m = \{1, 2, 3\}$, moving from the qN-BDF-ETDStab$_m$ scheme to the qN-BDF-ETDStab$_{m+1}$ scheme results in a reduction of the absolute errors. In detail, for values of τ smaller or equal than 2.5e-2 ms results in approximatively in a factor of 0.1.

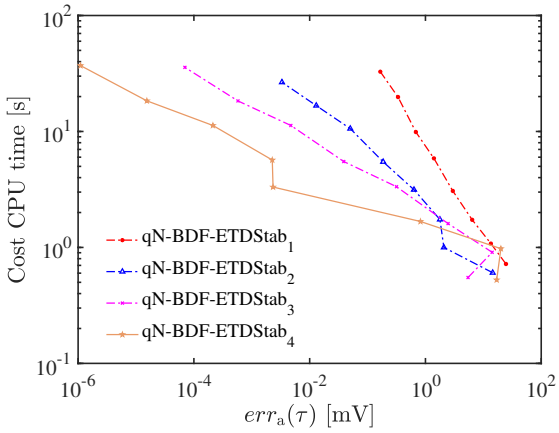

Figure 3.4. Test D: cost in CPU time for the qN-BDF-ETDStab$_m$ schemes against the absolute error (denoted with err$_a$) obtained of the scheme for 1ms of simulation of the monodomain system coupled with the BWZVP ionic model.

3.4.3 Numerical results - approximation of the derivatives of the ionic currents

In this section we compare the numerical results obtained for qN-BDF-ETDStab$_m$, CSDA-BDF-ETDStab$_m$ and FD-BDF-ETDStab$_m$ schemes in 1D and 3D numerical tests. We consider the FHN, the BWZVP, and the TNNP06 models described in Sec. 1.2.4. For Newton-BDF-ETDStab$_m$, qN-BDF-ETDStab$_m$, and CSDA-BDF-ETDStab$_m$ schemes the mean number of nonlinear iterations per time step coincides with the mean number of evaluations of the gradient (and of the Hessian) on the complete domain. For the FD-BDF-ETDStab$_m$ methods to every nonlinear step correspond four evaluations of the gradient, three of which are associated to the assembling of the Hessian matrix. As in [Martins et al., 2003], for the CSDA-BDF method we have tested a wide range of CSDA step-sizes, from $h_v = 10^{-2}$ to $h_v = 10^{-200}$. For all of the considered step sizes the complex-step method yields accurate numerical solutions and results into the same number of nonlinear iterations per time step $\mathcal{N}$.

Comparison of derivatives approximations for 1D monodomain model - Test E

We simulate the propagation of the electrical impulse through the domain $\mathscr{B}_r$ introduced in test D. We consider the exponential activation described in Eq. (3.4.2) for $I_{\text{max}} = 250000\ \mu$A and a uniform space-time grids with $h = 0.02$ mm and $\tau = 0.1$ ms. We consider $[t_0, t_{\text{fin}}] = [0, 600]$ ms. Tab. 3.9 reports $t_{\mathscr{G}}$, $t_{\mathscr{H}}$, $\mathscr{N}$, and t_{ts} for the CSDA-BDF-ETDStab$_1$, qN-BDF-ETDStab$_1$, and FD-BDF-ETDStab$_1$ schemes. Data in Tab. 3.9 are computed as mean values over the first fifty milliseconds of simulation. Results are reported for the FHN, for the BWZVP (discretized with first- and second-order BDF-ETDStab schemes), and for the TNNP06 ionic models. For the FHN model, results are reported also for the Newton's method (N-BDF-ETDStab$_1$). For the BWZVP model results are reported also for the BDF-ETDStab$_2$ scheme. The FD-BDF-ETDStab$_1$ scheme for the TNNP06 model does not converge for $\tau = 0.1$ ms. For this model results are computed also considering $\tau = 0.02$ ms, the biggest time step for which the method converges. For all the considered test cases, the CSDA-BDF-ETDStab$_m$ schemes perform similarly to the FD-BDF-ETDStab$_m$ schemes in terms of mean number $\mathscr{N}$ of nonlinear iterations per time step. On the other hand, CSDA result into a smaller mean execution times for the evaluation of the gradient and Hessian functions if compared to the FD-BDF-ETDStab$_m$ schemes. Even if for the BWZVP model the qN-BDF-ETDStab$_m$ schemes performs poorly, it results to be the best performing scheme when the TNNP06 model is considered. For the considered schemes, Fig. 3.5 shows the number of nonlinear iterations against the current simulation time considering $\tau = 0.1$ ms. For the FHN model, for the time steps for which the contribution of ω to the ionic current is relevant, the qN-BDF-ETDStab$_1$ scheme results into an higher number of nonlinear iterations. In detail in this case, the maximum number of nonlinear iteration per time step is obtained around $t = 100$ ms, see Fig. 3.5 (top left). For $t \geq 150$ ms, the contribution of ω is reduced in importance and the qN-BDF-ETDStab$_1$ scheme performs similarly to the other schemes. Simulations are run as single-core executions performed on MacBook Pro (Retina, Mid 2015) PC.

Comparison of derivatives approximations for 3D slab of tissue - Test F

We simulate the propagation of the electrical impulse through a 3D slab of tissue for 50 ms. We consider a slab of size 20 mm×7 mm×3 mm and with fibers aligned along X-axis, see Fig. 3.6. This test case has been proposed in the "N-benchmark paper" [Niederer et al., 2011]. We consider a uniform mesh of 420k elements. For this hexahedral mesh, third-order gauss quadrature rule results into 8 quadrature points for each element. As a stimulation geometry we consider a 1.5 mm ×1.5 mm ×1.5 cube from the corner $\mathbf{p}_s = \mathbf{0}$ (outlined in black in Fig. 3.6). We consider the stimulation protocol

$$I_{\text{app}}(t, \mathbf{x}) = \chi_{[0,0.15]^3 \times (0,2)}(\mathbf{x}, t) I_{\text{max}} e^{\left((t-1)^2-1\right)^{-1}} \text{ with } I_{\text{max}} = 250000\ \mu\text{A}. \tag{3.55}$$

Fig. 3.6 shows, for the reference solution, the AP propagation for the BWZVP model reported 25 ms after the application of the electrical stimulus. Tab. 3.6 reports the numerical results obtained for the CSDA-BDF-ETDStab$_1$, the qN-BDF-ETDStab$_1$, and the FD-BDF-ETDStab$_1$ schemes. As obtained in test E, for the FHN model, the qN-BDF-ETDStab$_1$ method results into an higher number of nonlinear iterations if compared to the other schemes. For the BWZVP model, the CSDA-BDF-ETDStab$_1$ scheme outperforms the qN-BDF-ETDStab$_1$ scheme. The opposite behavior can be observed for the TNNP06 model. Simulations were run on the ICS cluster, which each node runs CentOS 7.1×86_64. In detail, 3D simulations for test F and test G were run on 4 nodes with 2×Intel E5-2650 v3, 20 (2 x 10) cores.

	FHN			
	$\tau = 0.1$ ms, -BDF-ETDStab$_1$			
	$t_{\mathscr{G}}$ [s]	$t_{\mathscr{H}}$ [s]	$\mathscr{N}$	t_{ts} [s]
N-	3.315e-3	3.521e-3	3.98	2.726e-2
CSDA-	3.282e-3	3.520e-3	3.98	2.712e-2
qN-	3.395e-3	3.662e-3	5.98	4.225e-2
FD-	3.651e-3	3*3.651e-3	3.98	5.815e-2

	BWZVP							
	$\tau = 0.1$ ms, -BDF-ETDStab$_1$				$\tau = 0.1$ ms, -BDF-ETDStab$_2$			
	$t_{\mathscr{G}}$ [s]	$t_{\mathscr{H}}$ [s]	$\mathscr{N}$	t_{ts} [s]	$t_{\mathscr{G}}$ [s]	$t_{\mathscr{H}}$ [s]	$\mathscr{N}$	t_{ts} [s]
CSDA-	7.253e-3	9.961e-3	2.97	5.126e-2	7.435e-3	9.915e-3	2.96	5.146e-2
qN-	7.258e-3	7.652e-3	7.84	1.175e-1	7.675e-3	7.839e-3	6.92	1.073e-1
FD-	7.602e-3	3*7.602e-3	2.97	9.055e-2	7.915e-3	3*7.915e-3	2.96	9.390e-2

	TTNP06							
	$\tau = 0.1$ ms, -BDF-ETDStab$_1$				$\tau = 0.02$ ms, -BDF-ETDStab$_1$			
	$t_{\mathscr{G}}$ [s]	$t_{\mathscr{H}}$ [s]	$\mathscr{N}$	t_{ts} [s]	$t_{\mathscr{G}}$ [s]	$t_{\mathscr{H}}$ [s]	$\mathscr{N}$	t_{ts} [s]
CSDA-	8.501e-3	1.007e-2	4.972	9.237e-2	8.794e-3	9.968e-3	3.96	7.443e-2
qN-	8.754e-3	8.913e-3	5.014	8.858e-2	8.888e-3	8.667e-3	3.97	6.976e-2
FD-	-	-	-	-	8.777e-3	3*8.777e-3	2.99	1.050e-1

Table 3.9. Test E: $t_{\mathscr{G}}$, $t_{\mathscr{H}}$ mean execution times for a single evaluation of the gradient and Hessian functions on the complete domain, mean number of nonlinear iterations $\mathscr{N}$ per time step, and t_{ts}, mean execution time per time step for the Newton-BDF-ETDStab$_m$, the qN-BDF-ETDStab$_m$, the CDSA-BDF-ETDStab$_m$ and the FD-BDF-ETDStab$_m$ schemes. The considered ionic models are: the FHN, the BWZVP (discretized with the BDF-ETDStab$_1$ and the BDF- ETDStab$_2$ schemes), and the TNNP06 models.

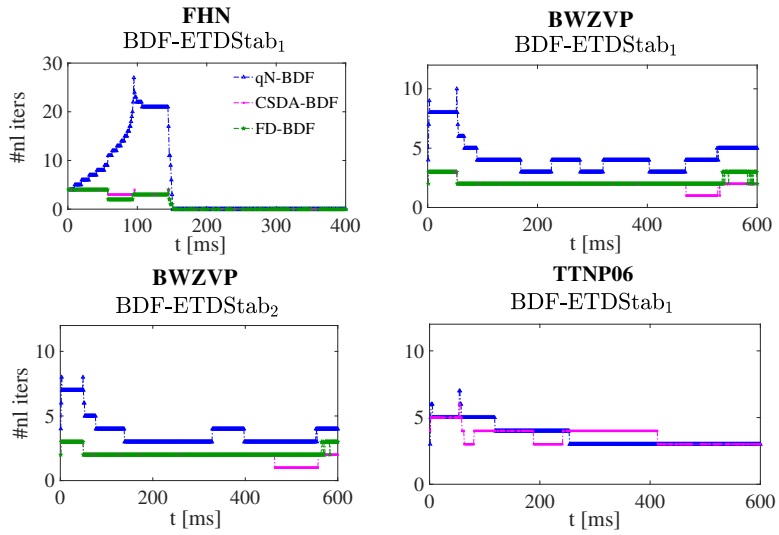

Figure 3.5. Test E: number of nonlinear iterations against the current simulation time. Results for $\tau = 0.1$ ms for the Newton-BDF-ETDStab$_m$, qN-BDF-ETDStab$_m$, CDSA-BDF-ETDStab$_m$ and FD-BDF-ETDStab$_m$ methods are reported. The considered ionic models are: the FHN, the BWZVP, and the TNNP06 models.

Comparison of derivatives approximations for the idealized left ventricle - Test G

We consider an idealized LV obtained by uniformly scaling (factor ≈ 0.37) the idealized LV geometry described in Sec. 1.4.1. Geometrical and mesh information are reported in Tab. 3.12. For the tetrahedral mesh, third-order gauss quadrature rule results into five quadrature points per element. We consider the stimulation protocol

$$I_{\text{app}}(t,\mathbf{x}) = \chi_{\mathbb{B}_r(\mathbf{x}_s)\times(0,2)}(\mathbf{x},t) I_{\text{max}} e^{\left((t-1)^2-1\right)^{-1}} \text{ with } I_{\text{max}} = 380000\ \mu\text{A},$$

where $\mathbb{B}_r(\mathbf{x}_s)$ represents a sphere of radius r and center $\mathbf{x}_s$. Tab. 3.11 reports the numerical results for the CSDA-BDF-ETDStab$_1$, qN-BDF-ETDStab$_1$, and FD-BDF-ETDStab$_1$ schemes. As in the previous test, the CSDA-BDF-ETDStab$_1$ scheme outperforms the qN-BDF-ETDStab$_1$ scheme when we consider the BWZVP model. Moreover the opposite behavior can be observed when the TTNP06 model is considered.

3.4.4 Impact of high-order time integration schemes on post-processing quantities

We consider the effects of the time integration schemes for the solution of (1.90) on the computed activation times ψ, APD$_{90}$ and pseudo-ECG signals (see Sec. 1.2.11). Results for the BWZVP model are considered. In detail,

- in the first test we consider a two-dimensional perforated cardiac tissue. In this case, we compare the ATs and the APD$_{90}$ post-processing quantities.
- to reduce the complex effects due to geometry and fiber orientation, in the second test we

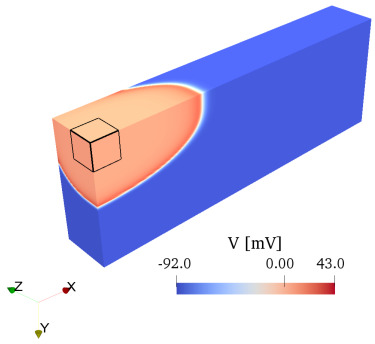

Figure 3.6. Spatial distribution of the action potential for a slab of tissue with fibers aligned along the X-axis. The configuration is reported for the BWZVP model 10 ms after the application of the electrical stimulus on the stimulation geometry (outlined in black).

consider a three-dimensional slab of tissue. In this test, we compare the morphology of the obtained pseudo-ECGs signals.

- in the third test we compare, for the different schemes, the morphology of the obtained pseudo-ECGs signals for the uniformly scaled idealized LV.

Comparison of AT, APD_{90} for a perforated cardiac tissue

We consider $\mathcal{B}_r$ to be a two-dimensional geometry of size 2 cm×2 cm presenting a 1 cm×1 cm hole in its center. We consider $C_m = 2\mu$ F cm^{-2} and $\chi = 1400$ cm^{-1}. As a stimulation geometry we consider the 1.5 mm ×1.5 mm square positioned at the corner $\mathbf{p}_s = \mathbf{0}$ and subjected to the stimulation protocol

$$I_{\text{app}}(t,\mathbf{x}) = \chi_{[0,0.15]^2\times(0,2)}(t,\mathbf{x}) I_{\text{max}} e^{\left((t-1)^2-1\right)^{-1}} \quad \text{with} \quad I_{\text{max}} = 250000\ \mu\text{A}$$

We consider the properties of the epicardial cells. The reference solution is computed applying the qN-BDF-ETDStab$_3$ scheme with τ =1.5625e-3 ms. We fix the spatial mesh of mesh size h = 5e-3 cm. Fig. 3.7 shows, from left to right, snapshots at time $t = 100$ ms of the numerical solutions obtained considering first-, second-, third- and fourth-order qN-BDF-ETDStab schemes with τ =2.5e-2 ms. Tab. 3.13 shows the ATs at the corner $\mathbf{p}_v = (2,2)$ opposite to the stimulation geometry. In particular, we consider $\tau \in$ {2e-1,1e-1,5e-2, 2.5e-2, 1.25e-2}. Post-processing the reference solution we obtain $\psi_{\text{ref}}(\mathbf{p}_v) = 125.209375$ ms. Results obtained with the qN-BDF-ETDStab$_1$ scheme show a smaller CV if compared to the ones obtained with third-order scheme. In detail

- for τ=1e-1 we obtain $\psi(\mathbf{p}_v) = 131$ ms. If compared to ψ_{ref}, a delay of about 5 ms (≈4%) in the AT for $\mathbf{p}_v$ is obtained.

- τ=2.5e-2 we obtain $\psi(\mathbf{p}_v) = 127.075$ ms. If compared to ψ_{ref}, a delay of about 2 ms (<1%) in the AT for $\mathbf{p}_v$ is obtained.

- as expected, ATs for $\mathbf{p}_v$ converge to the reference value for $\tau \to 0$.

	FHN				**TTNP06**			
	$\tau = 0.1$ ms, -BDF-ETDStab$_1$				$\tau = 0.1$ ms, -BDF-ETDStab$_1$			
	$t_{\mathscr{g}}$ [s]	$t_{\mathscr{H}}$ [s]	$\mathscr{N}$	t_{ts} [s]	$t_{\mathscr{g}}$ [s]	$t_{\mathscr{H}}$ [s]	$\mathscr{N}$	t_{ts} [s]
N-	0.1310	0.1995	3.99	1.319	-	-	-	-
CSDA-	0.1321	0.2026	3.99	1.3355	0.393	0.6003	8.134	8.08
qN-	0.1325	0.1997	5.794	1.9254	0.4444	0.4595	5.048	4.5631
	BWZVP							
	$\tau = 0.1$ ms, -BDF-ETDStab$_1$				$\tau = 0.1$ ms, -BDF-ETDStab$_2$			
	$t_{\mathscr{g}}$ [s]	$t_{\mathscr{H}}$ [s]	$\mathscr{N}$	t_{ts} [s]	$t_{\mathscr{g}}$ [s]	$t_{\mathscr{H}}$ [s]	$\mathscr{N}$	t_{ts} [s]
CSDA-	0.3875	0.6793	2.978	3.1774	0.4651	0.7126	2.934	3.4556
qN-	0.3548	0.42	7.908	6.128	0.4118	0.4603	6.902	6.0202

Table 3.10. Test F: $t_{\mathscr{g}}$, $t_{\mathscr{H}}$ mean execution times for a single evaluation of the gradient and Hessian functions on the complete domain, mean number of nonlinear iterations $\mathscr{N}$ per time step, and t_{ts}, mean execution time per time step. Results are shown for the N-, qN-, CSDA- and FD- BDF-ETDStab$_m$ methods. Solution of a 3D slab of tissue for the FHN, BWZVP and TNNP06 ionic models.

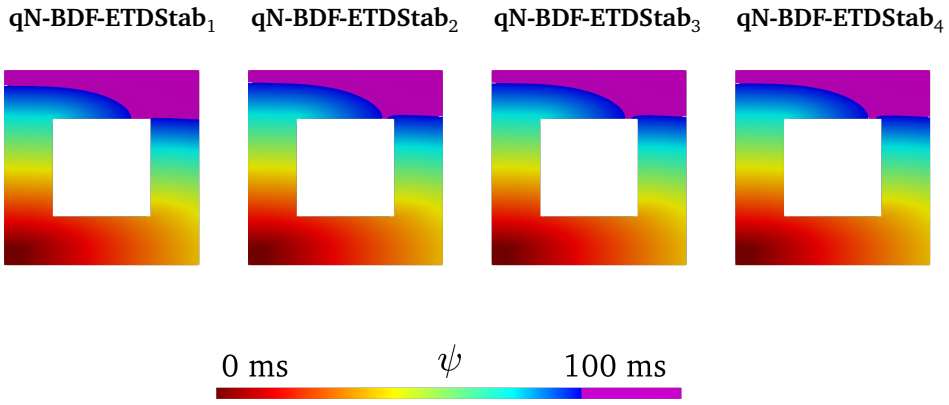

Figure 3.7. Perforated cardiac tissue: comparison of the activation times ψ obtained with the qN-BDF-ETDStab$_m$ schemes for τ =2.5e-2 ms.

Even considering finer grids in space, the qN-BDF-ETDStab$_4$ scheme is not convergent for τ =2e-1 ms. In Fig. 3.8 we compare the APD$_{90}$ obtained with the different schemes for τ =5e-2 ms. From left to right, results are shown for the first-, second-, third-, and fourth-order qN-BDF-ETDStab$_m$ schemes. No significant changes arise in the simulated APD$_{90}$ considering the different schemes: the APD$_{90}$ is accurately estimated using τ =5e-2 ms independently on the order of the accuracy of the numerical scheme. In conclusion the obtained results show how, fixed the time step and the spatial-grid, the choice of the numerical method affects the AT and, consequently, the excitation

	FHN				**TTNP06**			
	$\tau = 0.1$ ms, -BDF-ETDStab$_1$				$\tau = 0.1$ ms, -BDF-ETDStab$_1$			
	$t_{\mathscr{g}}$ [s]	$t_{\mathscr{H}}$ [s]	$\mathscr{N}$	t_{ts} [s]	$t_{\mathscr{g}}$ [s]	$t_{\mathscr{H}}$ [s]	$\mathscr{N}$	t_{ts} [s]
N-	0.1778	0.2093	3.007	1.1641	-	-	-	-
CSDA-	0.1796	0.2121	3.007	1.1781	0.7556	1.0512	7.874	13.8970
qN-	0.1764	0.2053	4.888	1.8662	0.7973	0.7013	4.931	7.3903
	BWZVP							
	$\tau = 0.1$ ms, -BDF-ETDStab$_1$				$\tau = 0.1$ ms, -BDF-ETDStab$_2$			
	$t_{\mathscr{g}}$ [s]	$t_{\mathscr{H}}$ [s]	$\mathscr{N}$	t_{ts} [s]	$t_{\mathscr{g}}$ [s]	$t_{\mathscr{H}}$ [s]	$\mathscr{N}$	t_{ts} [s]
CSDA-	0.7285	1.1635	2.652	5.0177	0.8638	1.2366	2.772	5.8226
qN-	0.6493	0.6377	6.421	8.2642	0.7346	0.6821	5.933	8.4013

Table 3.11. Test G: $t_{\mathscr{g}}$, $t_{\mathscr{H}}$ mean execution times for a single evaluation of the gradient and Hessian functions on the complete domain, mean number of nonlinear iterations $\mathscr{N}$ per time step, and t_{ts}, mean execution time per time step. Results are shown for the N-, qN-, CSDA- and FD- BDF-ETDStab$_m$ methods. Solution of the idealized LV geometry for the FHN, BWZVP, and TNNP06 ionic models.

Element	Information
LV bounding box	X = [-1,1], Y = [-1,1], Z = [-2.5,0]
LV Tetmesh	Total Nodes: $\sim$ 240k
Stimulated AV node	Sphere of radius $r = 0.15$ cm, center $\mathbf{x}_s = (0.8,0,-0.2)$ cm
$\mathbf{V}_1$	(2,2,-1) cm
$\mathbf{V}_2$	(1,2,-1) cm
$\mathbf{V}_3$	(0.5,1,-1.5) cm
$\mathbf{V}_4$	(0,2,-2) cm
$\mathbf{V}_5$	(-0.8,2,-2) cm
$\mathbf{V}_6$	(-1.2,1.8,-1.7) cm

Table 3.12. Test G: idealized scaled LV geometry and mesh information, and relative position of the pseudo-electrodes.

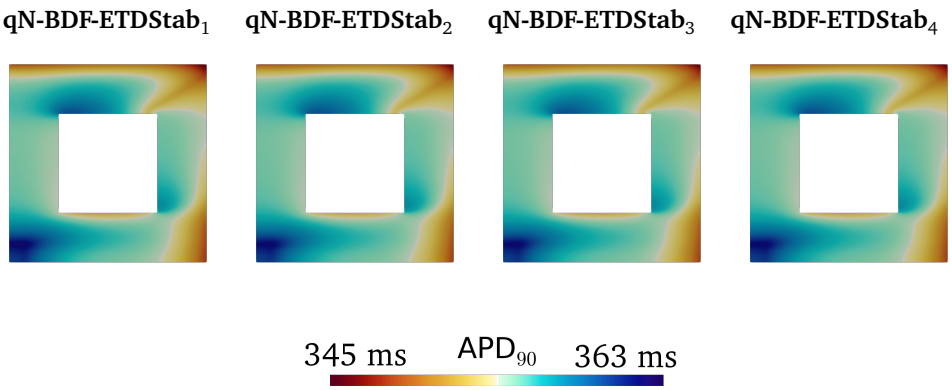

Figure 3.8. Perforated cardiac tissue: comparison of the action potential duration at 90% obtained with the qN-BDF-ETDStab$_m$ schemes for τ = 5e-2 ms.

wavefronts. However the choice of the numerical scheme does not affect the simulated APD$_{90}$. This suggests that main differences are detectable at the tissue level but are not evident at the cellular one.

Comparison of pseudo-ECG signals for a 3D slab of tissue

We systematically study the effects of high-order BDF time-stepping schemes on the simulated pseudo-ECGs signals. The domain, the stimulation geometry and the stimulation protocol are the same as described in test F . We consider a uniform spatial mesh of size $h = 0.1$ mm. In 3.9, zero isopotential surfaces obtained with the qN-BDF-ETDStab$_m$ schemes for the BWZVP model are reported after 20 ms (left) and 30 ms (right) after the application of the electrical stimulus on the stimulation geometry for τ =1e-1 ms. We compute the pseudo-ECGs signals at six

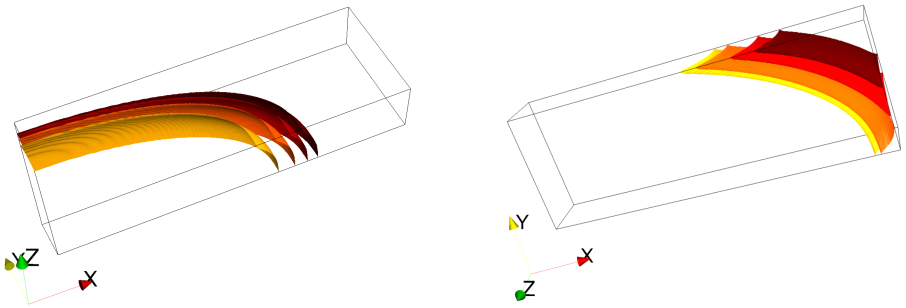

Figure 3.9. Tissue slab: zero isopotential surfaces obtained with the qN-BDF-ETDStab$_m$ schemes for τ =1e-1 ms. Fibers are aligned along the X-axis. The configuration is reported for the BWZVP model 20 ms (left) and 30 ms (right) after the application of the electrical stimulus. Zero isopotential surfaces are represented in yellow for qN-BDF-ETDStab$_1$, in orange for qN-BDF-ETDStab$_2$, in red for qN-BDF-ETDStab$_3$ and in brown for qN-BDF-ETDStab$_4$.

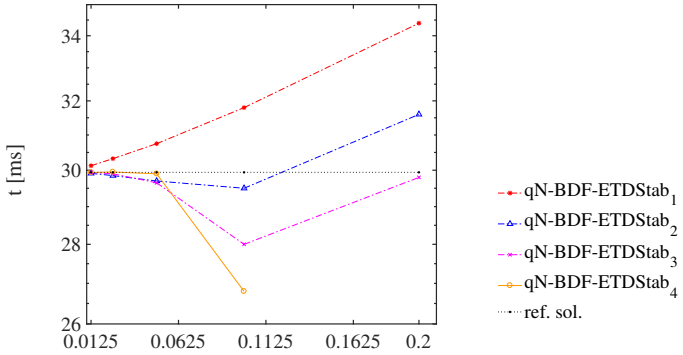

Figure 3.10. Tissue slab: time associated to the achievement of the peak values of the simulated R-waves obtained with qN-BDF-ETDStab$_m$ schemes against the considered time step τ.

τ [ms]	qN-BDF-ETDStab$_1$ ψ	qN-BDF-ETDStab$_2$ ψ	qN-BDF-ETDStab$_3$ ψ	qN-BDF-ETDStab$_4$ ψ
2e-1	147.0 ms	132.2 ms	124.4 ms	-
1e-1	131.0 ms	122.90 ms	123.05 ms	110.9 ms
5e-2	129.25 ms	124.05 ms	124.05 ms	125.05 ms
2.5e-2	127.075 ms	124.825 ms	125.075 ms	125.225 ms
1.25e-2	126.1000 ms	125.1000 ms	125.2000 ms	125.2125 ms

Table 3.13. Perforated cardiac tissue: activation times at the corner opposite to the stimulation geometry obtained with the qN-BDF-ETDStab$_m$ schemes.

unipolar electrodes, two for each Cartesian axis. They are arranged symmetrically with respect to the center of the domain, and 4 cm far from $\partial\mathscr{B}_r$. Different order of accuracy schemes lead to some variances in the simulated pseudo-ECGs. These variances, mostly visible in X-direction, are shown in Fig. 3.11. In detail, from left to right, results for τ =2.5e-2 ms, τ =5e-2 ms, τ =1e-1 ms, and τ =2e-1 ms for the positive pseudo-electrode in fiber direction are reported. The qN-BDF-ETDStab$_4$ scheme does not converge for τ=2e-1. First row shows the impact of low-order numerical schemes on the simulated QRS-complex. Fig. 3.10 shows the times associated to the achievement of the peak values of the simulated R-waves obtained with qN-BDF-ETDStab$_m$ schemes against the considered time step τ. Results are compared with the time associated to the achievement of the peak value for the reference solution which is computed considering the qN-BDF-ETDStab$_3$ scheme with τ =1.5625e-3 ms. As shown in the figure, low-order methods are associated with a delay in the achievement of the peak values of the simulated R-waves. In particular if compared to the reference solution, the qN-BDF-ETDStab$_1$ scheme with τ=2e-1 ms results into a delay of more then 5 ms (about a 16% time shift is observed). Second row of Fig. 3.11 shows the effects of the different strategies on the simulated T-waves. In general, different order of accuracy schemes produce T-waves of different amplitudes. If compared to the reference solution, the qN-BDF-ETDStab$_1$ scheme with τ=2e-1 ms results into a T-wave of amplitude increased of about 14%. No relevant changes in the simulated pseudo-ECGs configuration are present in the ST segments, during which the simulated pseudo-ECG are almost equal.

Comparison of pseudo-ECG signals for the idealized scaled LV

We consider the effect of different schemes on the morphology of the simulated pseudo-ECGs for idealized scaled LV. Fig. 3.12 shows the considered geometry and the six unipolar pseudo-electrodes $\mathbf{V}_i$. We consider the stimulation protocol

$$I_{\text{app}}(t,\mathbf{x}) = \chi_{\mathscr{B}_r(\mathbf{x}_s)\times(0,2)}(\mathbf{x},t) I_{\max} e^{\left((t-1)^2-1\right)^{-1}} \text{ with } I_{\max} = 250000\ \mu\text{A}$$

where $\mathscr{B}_r(\mathbf{x}_s)$ represents a sphere of radius $r = 0.15$ cm and center $\mathbf{x}_s = (0.8, 0, -0.2)$ cm. Fig. 3.13 shows, from left to right, anterior coronal, posterior coronal, transverse and bottom views of the ATs obtained with the different time integration schemes for τ =1e-1ms. From top to bottom, results for the qN-BDF-ETDStab$_1$, qN-BDF-ETDStab$_2$, qN-BDF-ETDStab$_3$ schemes

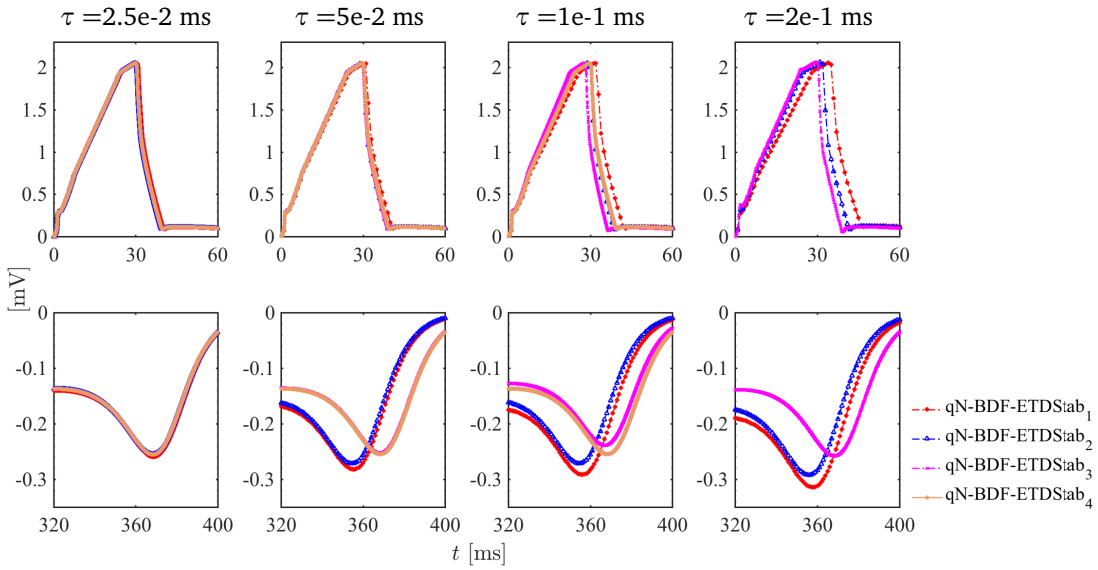

Figure 3.11. Tissue slab: simulated QRS-complex (first row) and T-waves (second row) obtained with qN-BDF-ETDStab$_m$ schemes. From left to right results are shown at the positive pseudo-electrode in X-direction for τ =2.5e-2 ms, τ =5e-2 ms, τ =1e-1 ms and for τ =2e-1 ms.

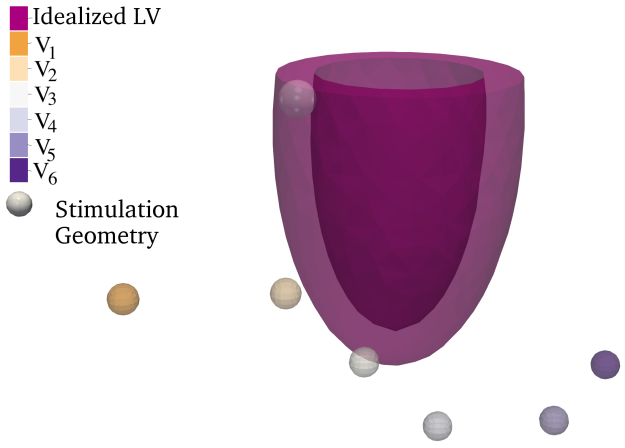

Figure 3.12. Idealized scaled LV: relative position of the pseudo-electrodes.

are shown. Fig. 3.14 and Fig. 3.15 show the simulated pseudo-ECGs for the different schemes focusing on the simulated QRS-complex (left) and T-waves (right) for τ =5e-2 ms and τ =1e-1ms, respectively. As obtained for the previous test, low-order methods are associated with a delay in the achievement of the peak values of the simulated R- and T-waves. Moreover they result into T-waves of increased amplitudes. If compared with the solution obtained with the qN-BDF-ETDStab$_3$ scheme, for τ =5e-2 the qN-BDF-ETDStab$_1$ scheme results in a delay of about 2 ms (about 4% time shift is observed) in the achievement of the R- and T- waves peak values and in an increase of amplitude of the T-wave of about the 5% for the pseudo-electrodes $\mathbf{V}_1, \mathbf{V}_2, \mathbf{V}_3, \mathbf{V}_4$ and of about the 30% for $\mathbf{V}_5$ and $\mathbf{V}_6$. For τ =5e-2 ms no significant changes are visible comparing the pseudo-ECGs obtained applying the qN-BDF-ETDStab$_2$ and qN-BDF-ETDStab$_3$ schemes. As shown in Fig. 3.15, if compared with the solution obtained with the qN-BDF-ETDStab$_3$ scheme, for τ =1e-1 ms the qN-BDF-ETDStab$_1$ scheme results in a delay of about 8-10 ms (about 19%-23% time shift is observed) in the achievement of the R- and T- waves peak values and in an increase of amplitude of the T-wave of about the 8% for the pseudo-electrodes $\mathbf{V}_1, \mathbf{V}_2, \mathbf{V}_3$ and of about the 50% for $\mathbf{V}_5$ and $\mathbf{V}_6$. A different behavior is observable for $\mathbf{V}_4$ for which the first-order scheme underestimates the T- waves peak value obtained with the third-order scheme of about the 3%. For τ =1e-1 ms changes are visible comparing the pseudo-ECGs obtained applying the qN-BDF-ETDStab$_2$ and qN-BDF-ETDStab$_3$ schemes. In particular, these changes are remarkable for the pseudo-ECG signals obtained with the second-order scheme for $\mathbf{V}_5$ and $\mathbf{V}_6$ for which a delay of about 3-6 ms (about 7%-14% time shift is observed) in the achievement of the R- and T- waves peak values and in an increase of amplitude of the T-wave of about the 25%

3.5 Comments

The qN-BDF-ETDStab$_1$, qN-BDF-ETDStab$_2$, and qN-BDF-ETDStab$_3$ methods for the solution of the monodomain system in one-dimension coupled with the FHN and BWZVP ionic model, have been show to perfectly fit our expectations in terms of order of accuracy of the methods. The qN-BDF-ETDStab$_4$ method perfectly fits our expectation for the FHN ionic model, and presents some fluctuation for the BWZVP ionic model for $\tau \approx$ 2.5e-2 ms. The advantage of the usage of the third- and fourth-order time stepping schemes has been shown comparing the computational costs of the different qN-BDF-ETDStab strategies against the obtained errors. The two-dimensional numerical experiment conducted on the perforated tissue geometry shows how the choice of the numerical method affects the conduction velocities, and, consequently, the activation times and the excitation wavefronts. As expected, the choice of the numerical scheme does not affect the simulated APD$_9$0. Three-dimensional numerical experiments simulated show an impact of high-order integration strategies on the simulated conduction velocities and pseudo-ECG signals. In detail, low-order methods are associated to a delay in the achievement of the R- and T- waves peak values and in an increase of amplitude of the T-wave. These effects is obviously dampen by the usage of small time-steps.

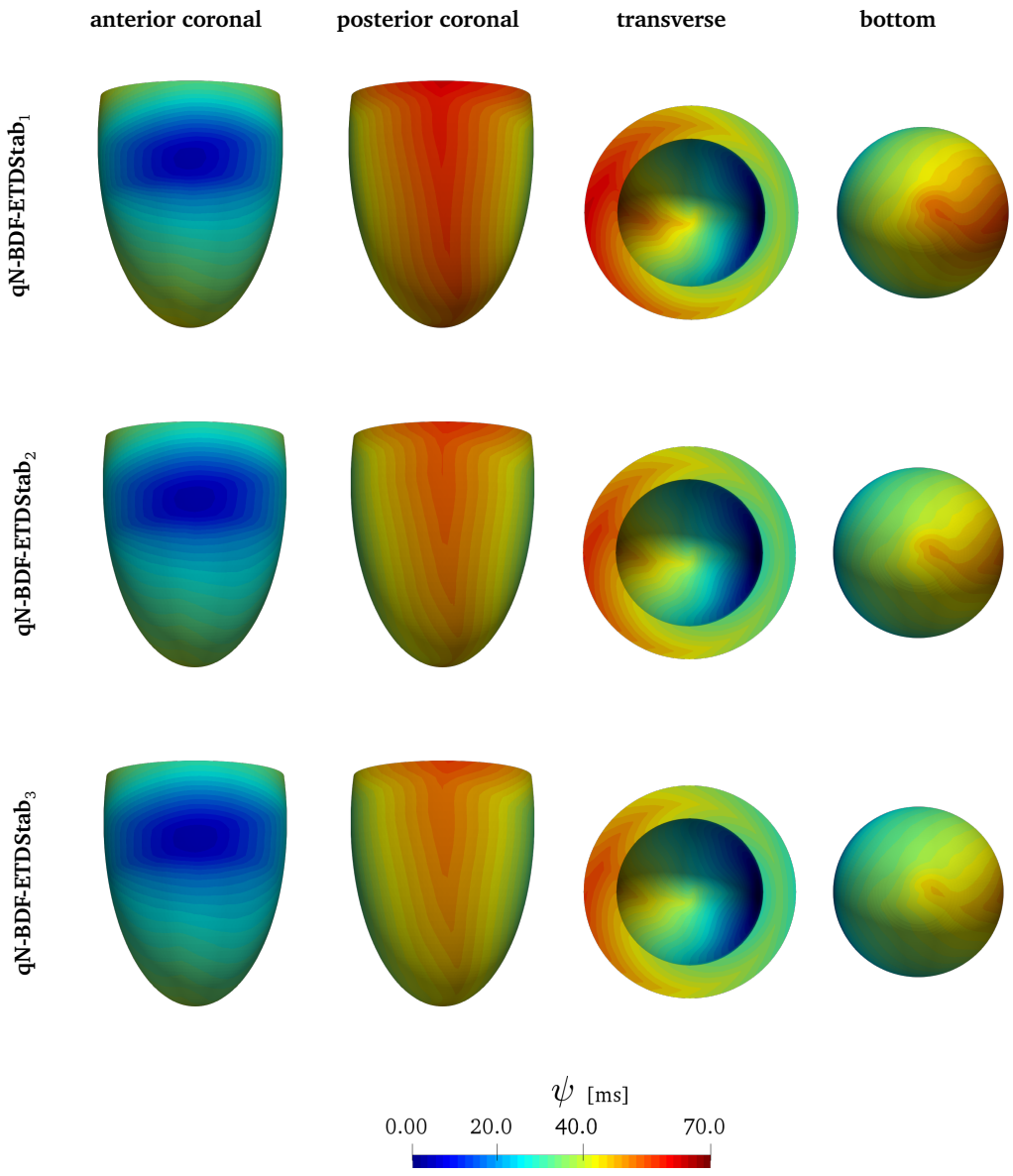

Figure 3.13. Idealized scaled LV: anterior coronal view (first column), posterior coronal view (first column), transverse view (third column) and bottom view (fourth column) of the ATs obtained with the different order of accuracy schemes. From top to bottom: results for qN-BDF-ETDStab$_1$, qN-BDF-ETDStab$_2$, and qN-BDF-ETDStab$_3$, schemes for the time step τ =1e-1 ms.

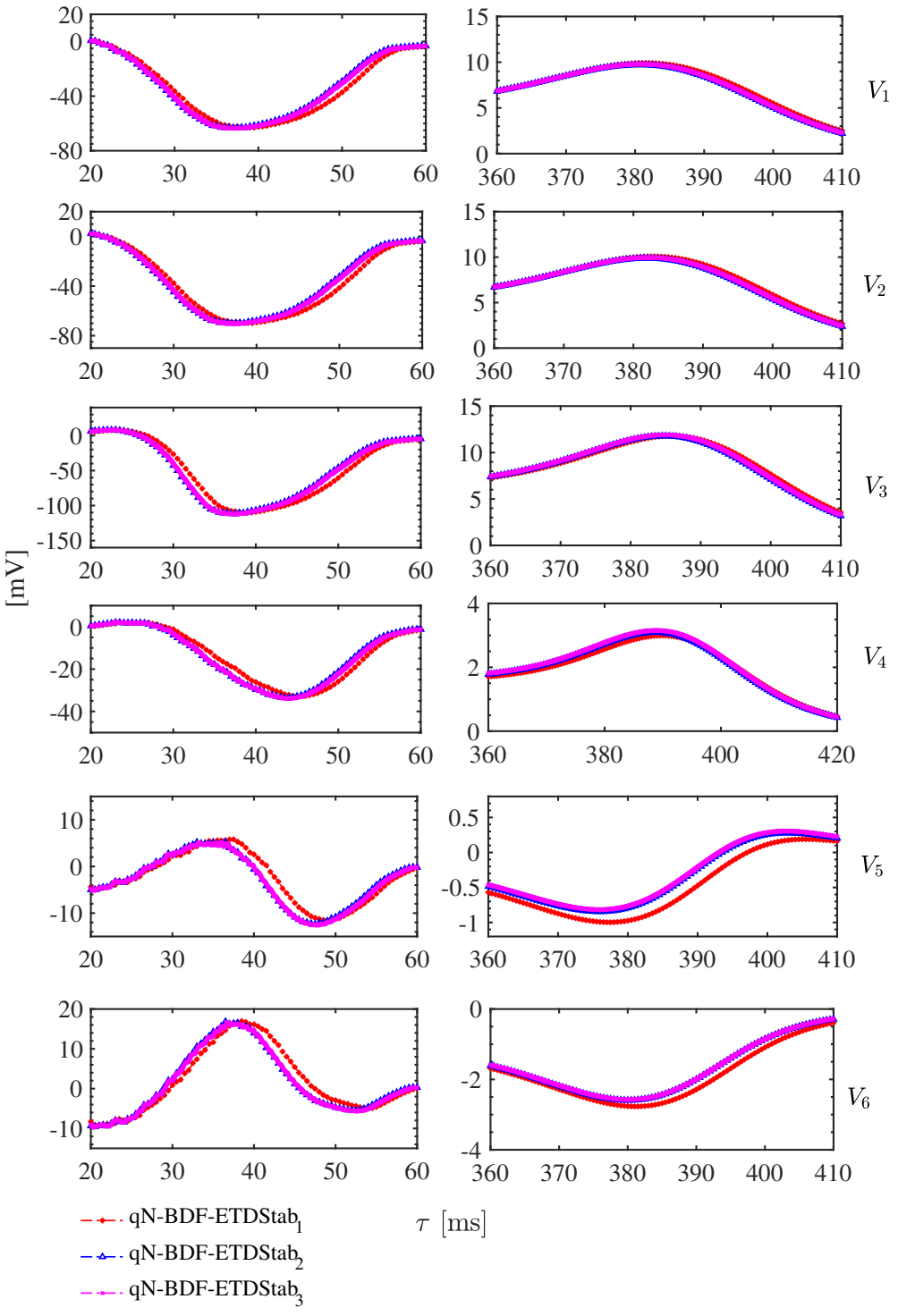

Figure 3.14. Idealized scaled LV: obtained QRS-complex (left) and T-waves (right) for the qN-BDF-ETDStab$_m$ schemes. Results are shown for the six pseudo-electrodes $\mathbf{V}_1, \ldots, \mathbf{V}_6$ considering the time step τ =5e-2 ms.

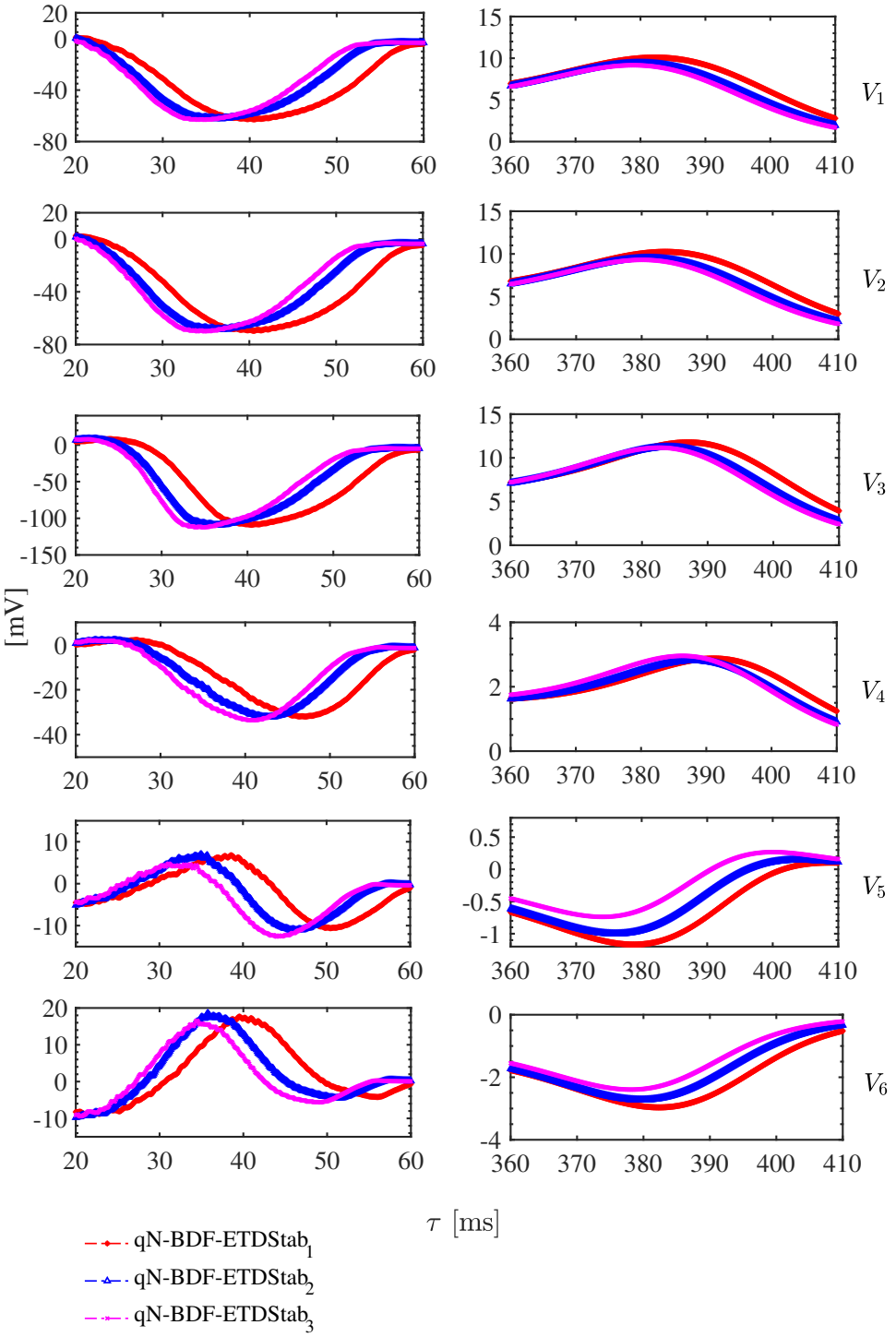

Figure 3.15. Idealized scaled LV: obtained QRS-complex (left) and T-waves (right) for the qN-BDF-ETDStab$_m$ schemes. Results are shown for the six pseudo-electrodes $\mathbf{V}_1, \ldots, \mathbf{V}_6$ considering the time step τ =1e-1 ms.

Chapter 4

Numerical algorithms for the solution of incompressible mechanics

Biological tissues are usually described as incompressible nonlinear elastic material in that they are mainly composed by water. A typical example comes from the modeling of cardiac tissue [Rossi et al., 2012; Favino et al., 2016; Ambrosi and Pezzuto, 2012] whose elastic response is highly nonlinear, anisotropic, and characterized by an active stress or an active strain component. The incompressible or nearly-incompressible behavior of the myocardium is still an open debate [Land et al., 2012; Yin et al., 1996], in that the myocardium is extensively perfused with distensible vessels which volumes vary in time. In this chapter we deal with the computational hurdles arising in the numerical solution of the equation of cardiac mechanics under the incompressibility hypothesis.

Incompressible elasticity is a constrained problem in which the unknowns are the *primal* variable, the displacement, and the *dual* variable, the pressure. This latter variable plays the role of a Lagrange multiplier to enforce the incompressibility constraint. In the most general cases of volume and boundary loads, the system of equation describing incompressible elasticity is written as a generalized nonlinear saddle point (SP) problem, i.e. a system of equations that cannot be derived from an inf-sup principle.

The development of efficient solution methods for the solution of this kind of systems is a very active field of research. Although, a lot of effort has been put in the development of nonlinear solution methods, almost no work focuses on the efficient solution of the linearized *tangent* problem that has be solved at each iteration of Newton-like methods. The mathematical properties of the tangent problem render particularly complicated the analysis: it is a generalized saddle-point problem where the elasticity operator is singular at the first iteration of Newton's method and singular or non-positive definite at any iteration of Newton's method. This is in contrast with other well-studied SP problems, such as Navier-Stokes equations, Stokes equation, and incompressible linear elasticity.

Geometric multigrid (MG) methods allow to smooth the error in the solution transferring a correction from a coarse level to a finer one. MG methods for solving partial differential equations (PDEs) have been extensively developed for linear elliptic problems [Braess, 2009] and some extensions can be found for SP problems [Bacuta, 2006; Bacuta and Shu, 2013]. For these latter, MG, as other solution methods, can be applied in a *coupled* or in a *segregated* fashion. Coupled MG approaches consist in the application of MG methods in the "primitive variables" [Vanka,

1986]. They do not require any a-priori hypothesis on the elasticity operator and in general they are not characterized by an optimal convergence rate, i.e. the number of iterations needed to reach a given tolerance is mesh dependent. The application of coupled MG methods is also connected to some technical overheads:

- they require prolongation and restriction operators able of dealing with variables of possibly different order,

- they require the implementation of modified smoothers, since standard iterative methods cannot be employed.

In contrast, segregated approaches involve the solution of the Schur complement system of the original SP problem. MG methods coupled with Schur-complement-like approaches represent valuable approaches in which they can be constructed exploiting standard tools and here we follow this approach. In case of incompressible linear elasticity, when the elasticity operator is positive definite, Schur-complement-based approaches are favourable since they deal with the solution of two elliptic problems at the price of nested iterations [Benzi et al., 2005]. In this case, optimal preconditioners are known [Verfurth, 1984] and they provide also mesh optimality of MG methods.

In the field of nonlinear elasticity, MG methods have been applied to incompressible [Campos et al., 2018; Hadjicharalambous et al., 2014] and to nearly-incompressible [Augustin et al., 2016; Colli Franzone et al., 2015] formulations. In [Augustin et al., 2016; Colli Franzone et al., 2015, 2018; Pavarino et al., 2015] purely *primal* formulations are considered and the incompressibility constraint is imposed by means of penalty terms. Mechanically speaking, the penalization parameter corresponds to the bulk modulus. The primal formulation results in a sequence of elliptic problems, the nearly-incompressible formulation leads to ill-conditioned stiffness matrices which deteriorate the performance of iterative solution methods [Campos et al., 2018]. In contrast, MG methods have been applied for the solution of the incompressible formulation considering the static condensation of the pressure variable [Campos et al., 2018] or its approximations [Hadjicharalambous et al., 2014].

Several augmenting strategies have been proposed to improve the convergence of Newton's and multigrid methods for incompressible nonlinear elasticity. In [Land et al., 2015b], it has been numerically shown that adding a penalty term improves the convergence of Newton's method. In [Gurev et al., 2015], the same strategy has been used to improve the performance of multigrid solution methods for the tangent problem. In the same work, an alternative strategy based on augmented Lagrangian methods has been discussed. This second strategy is purely algebraic and consists in the transformation of the considered linear system in an equivalent one [Benzi and Liu, 2007]. In this chapter, we present the two approaches proposed in [Gurev et al., 2015] and compare their performance when multigrid methods are applied. We refer to the resulting strategies as physics-based segregated multigrid preconditioned (SMGP) strategy and augmented Lagrangian SMGP strategy.

To the best of our knowledge, the only work where MG solution methods are used for incompressible nonlinear elasticity is [Gurev et al., 2015]. Here, a segregated approach is proposed for the solution of the tangent problem. For the inversion of the elasticity operator, a first-order approximation is employed as coarse level for a second-order approximation, allowing for a large reduction of degrees of freedom in the coarse level. The coarse level is solved by means of an algebraic MG strategy. Moreover, different preconditioners for the Schur complement have been considered.

As an alternative to geometric MG, p-multigrid methods can be considered. In p-multigrid methods the construction of the coarse spaces rely on a sequence of solution approximation of different polynomial order. In the context of the high order spectral volume and difference methods, p-multigrid methods have been extensively studied [Kannan and Wang, 2009; Kannan, 2011; Liang et al., 2009].

In this chapter, we propose a segregated approach with a geometric MG. A mass matrix is used as preconditioner for the Schur complement system. In detail, MG is employed for the solution of an elasticity problem and of a pressure mass matrix, for which standard smoothing strategies are effective. Our method can be summarized in the following steps:

1. the nonlinear problem is discretized by mixed FE formulation,
2. the discrete nonlinear problem is solved by means of Newton's method,
3. an augmenting strategy in employed to remove the singularity of the elasticity operator,
4. a segregated approach is used to solve the augmented linear system: this corresponds to the solution of the Schur complement of the augmented system, for which a mass matrix is used as a preconditioner,
5. two MG preconditioners are used to solve for the elasticity operator - in the application of the Schur complement - and for the mass matrix preconditioner.

Convergence and optimality proofs are quite complicated for these kinds of problems. We apply our SMGP strategy to solve two- and three-dimensional problems in order to numerically evaluate its properties. Several tests are employed to study the convergence behavior of the strategy and in particular to evaluate the influence of the number of degrees-of-freedom in the discretization, the value of the augmenting parameters, and the number of MG levels. The parallel implementation of the proposed solution strategy relies on the PCFIELDSPLIT and PCMG preconditioners in the PETSc suite [Balay et al., 2017]. The MOONoLith library [Krause and Zulian, 2016] allows for a fast and parallel construction of the projection and prolongation operators.

The chapter is organized following the above-mentioned steps. In Sec. 4.1 motivational benchmark problems are introduced and the results obtained for the incompressible and for the nearly-incompressible formulations compared. In Sec. 4.2 the augmenting strategies are introduced. Moreover, we introduce the standard notation of MG approaches and we present our novel SMGP solution strategy. Finally, in Sec. 4.3, numerical tests in two- and three-dimensional settings are employed to show the optimality of the proposed approach and to study the scaling properties of its implementation in the PETSc suite [Balay et al., 2017].

4.1 Motivation

Verification of computational models and of solution strategies is an important stage of software development. In [Land et al., 2015a] a framework for verifying mechanical models of cardiac tissue has been proposed. To verifying the implemented mathematical models and their correct solutions, our research group carried out the proposed benchmark problems participating to this latter work. In this section we compare the numerical results obtained for these problems for the incompressible and the nearly compressible formulations. We reproduce and extend the three benchmarks problems proposed in [Land et al., 2015a] of which we report a small description. We tested the nearly incompressible formulation for the penalty parameter (often referred to as

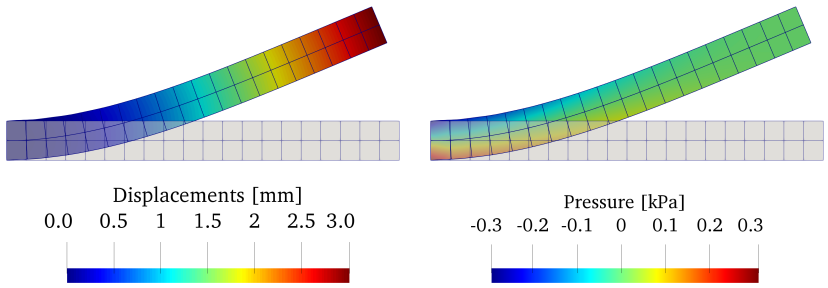

Figure 4.1. Norm of the obtained displacement (left) and pressure (right) reported in the deformed configuration. Results for the solution of setting 1 (Neo-Hookean hyperelastic law describing the passive behavior of the beam) on the mesh composed by uniform quadrilaterals of size 0.5 mm.

bulk modulus) k_n belonging to a broad spectrum of values. It is often assumed that the bulk modulus becomes very large as a material approaches *incompressibility*. However, high values of k_n may lead to very ill-conditioned problems. We recall that the choice of the penalty parameter is not standard. Even if estimates for k_n for soft human tissues exist [Saraf et al., 2007], there is a lack of data on the dynamic behavior of cardiac tissues. This is due to the difficulty of obtaining human tissues in sufficient quantities and to the lack of standard techniques for testing the loading of soft tissues.

4.1.1 Benchmark problems

Problem 1: deformation of a rectangular beam

The undeformed geometry is defined by the region $\mathcal{B}_r = [0, 10] \times [0, 1] \times [0, 1]$ mm. Homogeneous Dirichlet boundary conditions are imposed for all the directions on the left edge at $X = 0$. A constant normal force g per unit area is applied on the bottom edge at $Y = 0$. We consider three different settings, corresponding to three material laws for the description of the passive cardiac tissue. Material laws, parameters, and boundary forces are

setting 1: Neo-Hookean law [Rivlin, 1948; Bonet and Wood, 1997] with $\mu = 2.0$ kPa, and $g = 1.6$ Pa in inward-pointing normal direction. Fig. 4.1 reports the norm of the obtained displacement (left) and pressure (right) in the deformed configuration. The solution is computed on the mesh composed by uniform quadrilaterals of size 0.5 mm.

setting 2: isotropic Guccione-Costa law with $C = 10$ kPa, $b_f = 1$, $b_t = 1$, $b_{fs} = 1$ and $g = 4$ Pa.

setting 3: anisotropic Guccione-Costa law with $C = 2$ kPa, $b_f = 8$, $b_t = 2$, $b_{fs} = 4$. Fibers are aligned along the x-axis and $g = 4$ Pa.

Here C, b_f, b_t, b_{fs} represent the constitutive parameters of the Guccione-Costa law defined as in [Guccione et al., 1995].

Problem 2: inflation of an isotropic ellipsoid

Considering the ellipsoide-like LV presented in Sec. 1.4.1 , this problem tests a deformation pattern similar to cardiac inflation. Constitutive parameters are $C = 10$ kPa, $b_f = 1$, $b_t = 1$, $b_{fs} = 1$. Dirichlet boundary conditions are imposed at the base plane $z = 5$ mm, which is fixed in all directions. A pressure of 10 kPa is applied to the endocardial surface. A constant pressure of 15 kPa is applied to the endocardium.

Problem 3: inflation and active contraction of a transversely isotropic ellipsoid

Using the geometry already proposed for the second problem, this test used a transversely isotropic material with $C = 2$ kPa, $b_f = 8$, $b_t = 2$, $b_{fs} = 4$. The complex realistic fibers distribution described in Sec. 1.1.7 and an active contraction of the tissue are considered. The active stress is given by a constant, homogeneous, stress of 60 kPa in the direction of the fibers.

The use of high-order cubic Hermite elements became very popular in cardiac mechanics simulations [Costa et al., 1996]. The main reason is that these elements allow a tessellation of stylized ventricular anatomy using a small number of elements. To accommodate more complex geometries the use of tetrahedral elements has been recently introduced [Gurev et al., 2015; Fritz et al., 2014]. To investigate the differences between the two approaches, results for the first problem are compared considering tetrahedral elements ($\mathbb{P}_2$-$\mathbb{P}_1$ for the incompressible case and $\mathbb{P}_2$ for the nearly-incompressible formulation) and hexahedral elements ($\mathbb{Q}_2$-$\mathbb{Q}_1$ for the incompressible case and $\mathbb{Q}_2$ for the nearly-incompressible formulation). In the second and third problems tetrahedral elements are considered. Sixth-order quadrature rule is applied. In the nearly-incompressible case, the Newton's method is applied to solve the nonlinear problem with a fixed number of load increments. Following [Campos et al., 2013a], we used 10 load increments for the second and the third problems. As Newton's method convergence criterion we consider for the residual norm the absolute tolerance of 10^{-10}.

4.1.2 Comparison of incompressible and nearly-incompressible formulations

Comparison for benchmark problem 1

We compare the results obtained for the incompressible and for the nearly-incompressible formulations for the bending of the rectangular beam. Taking into consideration the setting 3., we consider different problem sizes and elements types. Tab. 4.1 shows, for the hexahedral $\mathscr{H}$ and tetrahedral $\mathscr{T}$ considered meshes, the total number of DOFs for the incompressible and nearly-incompressible formulations. Fig. 4.2 shows the maximal deflections of the point $(10, 0.5, 1)$ plotted against the number of DOFs used. In this test, the selected bulk parameter in the nearly-incompressible formulation is $k_n = 2000$ kPa. In addition, the graphs report the results obtained with the codes tested in the benchmark paper. The average solution of the maximal deflection obtained from the results of the cardiac mechanical benchmark was 4.161 mm (with a standard deviation of 0.032 mm). Considering the incompressible formulation we obtain for $\mathscr{T}_7$ a maximal deflection in z of 4.16914 mm and for $\mathscr{H}_9$ a maximal deflection of 4.16963 mm. In general, the solution obtained considering HEX elements overestimates the reference numerical solution. In contrast, considering the nearly-incompressible formulation we obtain for $\mathscr{T}_6$ a maximal deflection in z of 4.17135 mm and for $\mathscr{H}_9$ a maximal deflection of 4.16582 mm. For both the in-

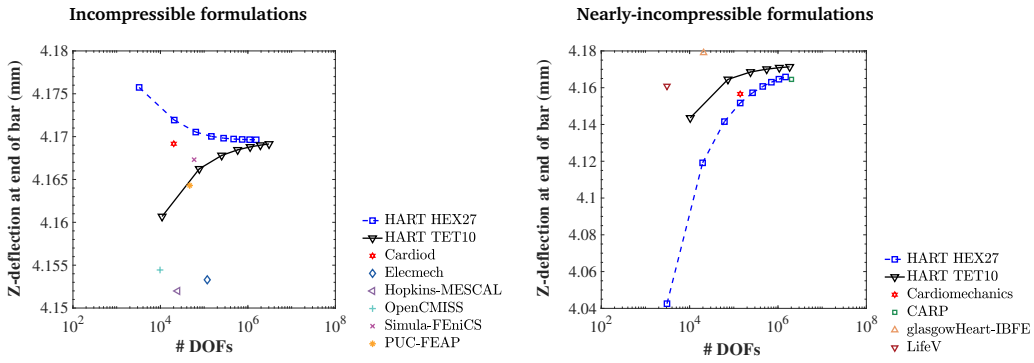

Figure 4.2. Maximal deflection of the beam across different solutions plotted against the number of degrees of freedom for the incompressible formulation (left) and for the nearly-incompressible one (right).

compressible and the nearly-incompressible formulations the solution obtained considering TET elements underestimates the reference numerical solution. For the nearly-incompressible formu-

	Formulation / Mesh	$\mathcal{H}_1$	$\mathcal{H}_2$	$\mathcal{H}_3$	$\mathcal{H}_4$	$\mathcal{H}_5$	$\mathcal{H}_6$	$\mathcal{H}_7$	$\mathcal{H}_8$	$\mathcal{H}_9$
No. DOFs	Incompressible	3k	20k	64k	146k	278k	472k	740k	1095k	1547k
	Nearly-inc.	3k	19k	61k	139k	265k	451k	708k	1048k	1482k
	Formulation / Mesh	$\mathcal{T}_1$	$\mathcal{T}_2$	$\mathcal{T}_3$	$\mathcal{T}_4$	$\mathcal{T}_5$	$\mathcal{T}_6$	$\mathcal{T}_7$		
No. DOFs	Incompressible	10k	77k	251k	583k	1125k	1928k	3044k		
	Nearly-inc.	10k	73k	238k	555075	1071k	1836k	2898k		

Table 4.1. Comparison of the number of DOFs for the considered meshes for the incompressible and the nearly-incompressible formulations.

lation, Fig. 4.3 reports the maximal deflection of the beam plotted against the bulk modulus k_n. Results, here reported for the grid $\mathcal{T}_4$, show the for relative small values of the bulk modulus k_n the deflection of the bar in the z-direction is overestimated at the end of the bar. Fig. 4.4 reports the obtained strains plotted against the considered bulk modulus k_n. Following [Land et al., 2015a], to calculate strain S_i, we track changes in the distance between pairs of n points with coordinates X_1^i and X_2^i in the undeformed FE geometries and coordinates x_1^i and x_2^i of the deformed geometry, where $i = 0, 1, \ldots, n$. We use the finite difference scheme

$$s_i = \left(\frac{\|x_1^i - x_2^i\|}{\|X_1^i - X_2^i\|} - 1 \right) \times 100\%. \tag{4.1}$$

We use the points along the line $(x, 0.5, 0.5)$ to calculate axial strain in the x-direction: $X_1^i = (i-1, 0.5, 0.5)$ and $X_2^i = (i, 0.5, 0.5)$, where $i = 1, \ldots, 9$. For transverse strain, we use $X_1^i = (i, 0.5, 0.5)$, where i= 1, ..., 10 and $X_2^i = (i, 0.9, 0.5)$ and $X_2^i = (i, 0.5, 0.9)$ for strain calculations in the y- and z-directions, respectively. Results, here reported for the grid $\mathcal{T}_4$, show that the simulated strains are well recovered considering the nearly-incompressible formulation even for small values of the bulk modulus k_n. For $k_n = 20$, the strains in z-direction are the ones subjected to higher variance of the results.

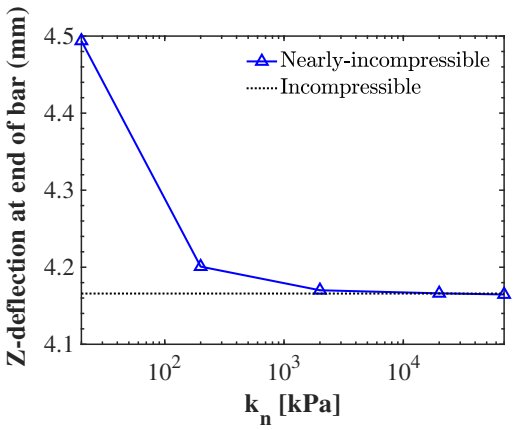

Figure 4.3. Maximal deflection of the beam across different solutions plotted against the bulk modulus k_n for the nearly-incompressible formulation. Result for the incompressible formulation are also plotted (dashed line). Results are shown for the grid $\mathscr{T}_4$.

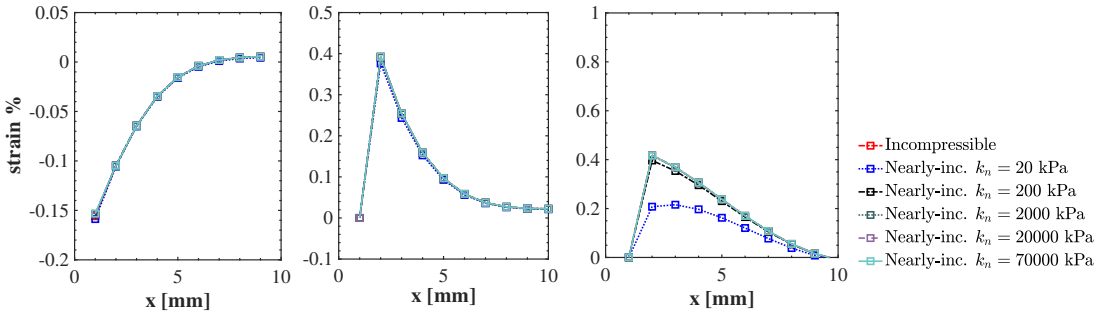

Figure 4.4. Nearly-incompressible formulation: strains computed on the beam plotted against the considered bulk modulus k_n. Result for the incompressible formulation are also plotted (red dashed line). Plot of strain in directions of x-, y- and z-axes along the line $(x, 0.5, 0.5)$. Results are computed for the grid $\mathscr{T}_4$.

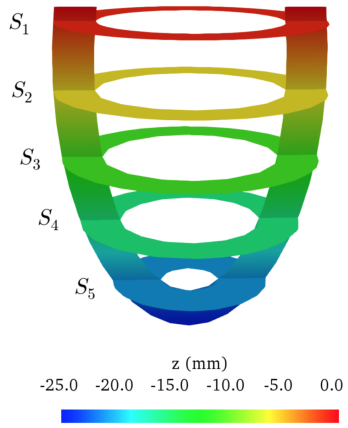

Figure 4.5. Idealized scaled LV: slices for the computation of the wall thickening

Comparison for benchmark problem 2

We compare the results obtained for the nearly-incompressible formulation with the results obtained with the incompressible formulation for the benchmark problem 2. In detail, we evaluate the wall thickening at the maximum ventricle inflation at the height $S_i = -(0.1 + 0.5(i-1))$ for $i = 1, \ldots, 5$, see Fig. 4.5. We consider $k_n = \{10C, 100C, 1000C, 3000C\}$. Results are shown in Fig. 4.6, for a mesh of tetrahedral elements with $\simeq 236k$ total nodes. The mesh (for $\mathbb{P}_2$-$\mathbb{P}_1$ discretization) results in $\simeq 707k$ DOFs for the nearly-incompressible formulation and $\simeq 739k$ DOFs for the incompressible formulation. The considered geometry has an internal volume of $\simeq 32.272$ mm^3.

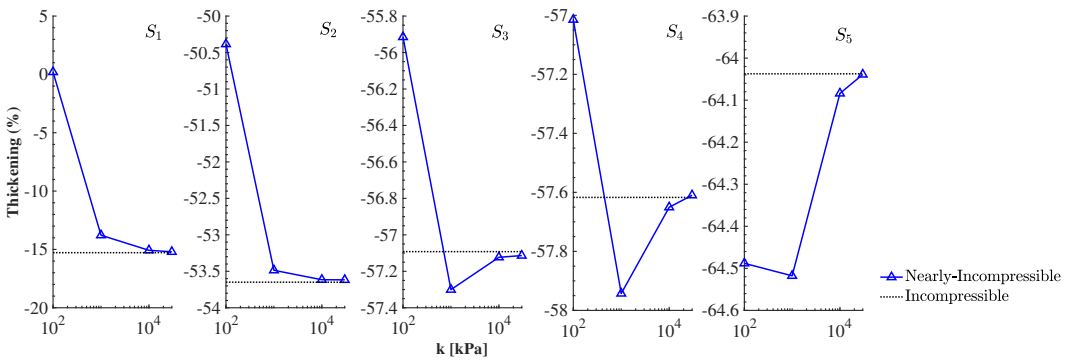

Figure 4.6. Idealized scaled LV: wall thickening computed at the slices

4.2 Segregated multigrid strategies for incompressible nonlinear elasticity

4.2.1 Segregated approaches for the solution of saddle-point problems

Iterative algorithms for the solution of SP problems are usually divided into two categories [Benzi et al., 2005]: *segregated* and *coupled* methods. In coupled method the linear system is solved "all at once". Segregated approaches are based on the splitting of primal and dual variables. In general they rely on the invertibility of the matrix $\mathscr{A}$. State-of-the-art segregated approaches focus on SP systems with $\mathscr{A}$ symmetric and positive definite. They can be formally derived from static condensation of the primal variable, from the use of specific preconditioners, or on a formal application of a block LU decomposition.

Following this latter approach, assuming that $\mathscr{A}$ is nonsingular, the SP problem (2.54) is equivalent to

$$\begin{bmatrix} \mathscr{A} & \mathscr{B}^T \\ \mathbf{0} & \mathscr{S} \end{bmatrix} \begin{bmatrix} U \\ P \end{bmatrix} = \begin{bmatrix} F \\ G - \mathscr{B}\mathscr{A}^{-1}F \end{bmatrix} \tag{4.2}$$

where $\mathscr{S}$ is the Schur complement of the system and it is defined as $\mathscr{S} = -\mathscr{B}\mathscr{A}^{-1}\mathscr{B}^T$. Segregated approaches involve the solution of a linear system of size M

$$\mathscr{S}P = G - \mathscr{B}\mathscr{A}^{-1}F. \tag{4.3}$$

Once P has been computed, U can be computed solving the N dimensional system

$$\mathscr{A}U = F - \mathscr{B}^T P. \tag{4.4}$$

In realistic large-scale simulations, the Schur complement $\mathscr{S}$ is not explicitly constructed. The application of iterative methods for the solution of (4.3) involves the solution of $\mathscr{A}$ at each iteration.

In order to precondition the linear system (4.3), alternatives can be considered:

- the *pressure mass matrix* $\mathscr{M}_p$; such a matrix is known to be an efficient preconditioner for the Schur complement for passive solid mechanics [El Maliki et al., 2010] and in particular has been shown to be an optimal preconditioner for linear elasticity; In [Verfurth, 1984], Verfürth showed that in the FE setting of the Stokes flow problem the Schur complement is spectrally equivalent to the mass or L^2-projection matrix. Verfürth's proof is based on the LBB condition and shows that the mass matrix is a suitable approximation to the Schur complement. Following [Verfurth, 1984], we consider the mass matrix in the pressure field $\mathscr{M}_p$ as a preconditioner for $\mathscr{S}$.

- *least square commutators* [Elman et al., 2006] which assuming $\mathscr{B}^T\mathscr{B}$ is not a singular matrix approximate the inverse of interest as

$$\mathscr{S} \approx (\mathscr{B}^T\mathscr{B})^{-1}\mathscr{B}^T\mathscr{A}\mathscr{B}(\mathscr{B}^T\mathscr{B})^{-1}. \tag{4.5}$$

- *sparse approximate inverse* (SPAI) approaches [Benzi and Tuma, 1999]; a possible choice is to approximate the inverse of $\mathscr{A}$ with the inverse of a fixed sparsity pattern matrix arising from the solution of a least squares problem.

In the context of cardiac mechanics, these strategies have been compared in [Gurev et al., 2015] for passive soft tissue deformation and also considering an active stress. In this latter case the pressure mass matrix was found to be less effective. Similar strategies for the approximation of the Schur complement for the Oseen's problem and for the Stokes problem are available in the literature [Verfurth, 1984; Elman et al., 2014]. Due to the cost of the construction of the approximation and to its lack of robustness with respect to mesh size, these approximation strategies are not always beneficial.

As discussed in Sec. 2.5, for the incompressible elasticity case the matrix $\mathscr{A}$ is singular at the first iteration of Newton's method (see Eq. (2.24)) and a priori not definite for all the other iterations. This is due to the considered volumetric/isochoric splitting of the deformation gradient. In the next section we present two augmenting strategies that allow for the application of segregated approaches.

4.2.2 Augmented approaches

Due to the singularity of the matrix $\mathscr{A}$ in the system (2.54), segregated strategies are not directly applicable to incompressible elasticity problems. Augmented methods allow to remove such problems replacing the original algebraic system (2.54) with one of the form

$$\begin{bmatrix} \tilde{\mathscr{A}} & \mathscr{B}^T \\ \mathscr{B} & \mathbf{0} \end{bmatrix} \begin{bmatrix} \tilde{U} \\ \tilde{P} \end{bmatrix} = \begin{bmatrix} \tilde{F} \\ G \end{bmatrix}. \tag{4.6}$$

where $\tilde{\mathscr{A}}$ and $\tilde{F}$ are obtained from the application of augmented Lagrangian methods to (2.54). We define $\tilde{\mathscr{H}} \in \mathbb{R}^{(N+M)\times(N+M)}$ to be the matrix at the left hand side of (4.6). Considering (4.6) instead of (2.54) the two-stage strategy described in (4.3)-(4.4) results in the successive solution of

$$\tilde{\mathscr{S}}\tilde{P} = G - \mathscr{B}\tilde{\mathscr{A}}^{-1}\tilde{F}, \tag{4.7}$$

and

$$\tilde{\mathscr{A}}\tilde{U} = \tilde{F} - \mathscr{B}^T\tilde{P}. \tag{4.8}$$

In the following, we discuss two possible strategies for augmenting the linear system (2.54) obtaining a system of the form (4.6).

Physics-based augmenting strategy

The first evaluated approach considers the additional term

$$\Psi_{\text{pb}}(J) = \int_{\mathscr{B}_r} \frac{k}{2}(J-1)^2 \mathrm{d}\mathbf{X} \tag{4.9}$$

to the elastic energy. Here $k \in \mathbb{R}^+$. This contribution modifies Eq. (1.45) into

$$-\operatorname{Div}\left(\mathbf{P}_{\text{dev}} + Jp\,\mathbf{F}^{-T} + k(J-1)J\,\mathbf{F}^{-T}\right) = \mathbf{0} \quad \text{in} \quad \mathscr{B}_r. \tag{4.10}$$

We underline that, differently from the nearly incompressible formulation, the volumetric constraint is still forced by Eq. (1.108.2) and the role of the additional term is to remove the singularity of the elasticity matrix $\mathscr{A}$. For this reason, relatively small values of k can be considered. The additional contribution vanishes when we are close to the numerical solution $(\tilde{\mathbf{u}}^*, \tilde{p}^*)$. Defining

$$\mathscr{M}_{\mathbf{u},\text{aug}}(\mathbf{v};\mathbf{u}) \quad = \quad k\int_{\mathscr{B}_r}(J-1)J\mathbf{F}^{-T} : \mathbf{V}\mathrm{d}\mathbf{X}, \tag{4.11}$$

we consider

$$\tilde{\mathscr{M}}_{\mathbf{u}}(\mathbf{v};\mathbf{u},p) \quad = \quad \mathscr{M}_{\mathbf{u}}(\mathbf{v};\mathbf{u},p) + \mathscr{M}_{\mathbf{u},\mathrm{aug}}(\mathbf{v};\mathbf{u}). \tag{4.12}$$

Defining

$$\tilde{a}(\mathbf{h},\mathbf{v};\mathbf{u},p) \quad := \quad d_{\mathbf{u}}\tilde{\mathscr{M}}_{\mathbf{u}}(\mathbf{v};\mathbf{u},p)[\mathbf{h}] \tag{4.13}$$

the tangent problem (2.13) is replaced by

$$\begin{array}{rcl} \tilde{a}(\mathbf{h},\mathbf{v};\mathbf{u},p) + b(\mathbf{v},\pi;\mathbf{u}) = -\tilde{\mathscr{M}}_{\mathbf{u}}(\mathbf{v};\mathbf{u},p) & \forall \mathbf{v}\in W, \\ b(\mathbf{h},q;\mathbf{u}) = -\mathscr{M}_p(q;\mathbf{u}) & \forall q \in Q. \end{array} \tag{4.14}$$

The discretization of (4.14) leads to the algebraic problem of the form (4.6). To underline the dependence of the augmented elasticity block on the parameter k, we denote $\tilde{\mathscr{A}}$ as $\mathscr{A}_k$. The matrix $\mathscr{A}_k$ retains the sparsity pattern of $\mathscr{A}$. Advantage of this augmenting strategy is that, if the equations of nearly incompressible mechanics are available in the considered FE framework, the application of the method is straightforward. In contrast, the proposed method is model dependent. Therefore it is not directly applicable to generalized SP problems arising in a context other than incompressible mechanics or fluids motion for large Reynolds numbers.

Augmented Lagrangian strategy

The second approach consists in transforming (2.54) in the equivalent system [Powell, 1969; Glowinski and Le Tallec, 1989; Fortin and Glowinski, 2000; Benzi and Liu, 2007]

$$\begin{bmatrix} \mathscr{A}+\gamma\mathscr{B}^T\mathscr{W}^{-1}\mathscr{B} & \mathscr{B}^T \\ \mathscr{B} & \mathbf{0} \end{bmatrix}\begin{bmatrix} \tilde{U} \\ \tilde{P} \end{bmatrix} = \begin{bmatrix} F+\gamma\mathscr{B}^T\mathscr{W}^{-1}G \\ G \end{bmatrix} \tag{4.15}$$

where $\gamma \in \mathbb{R}^+$ and $\mathscr{W} \in \mathbb{R}^{m\times m}$. For

$$\tilde{\mathscr{A}} = \mathscr{A}_\gamma := \mathscr{A} + \gamma\mathscr{B}^T\mathscr{W}^{-1}\mathscr{B}, \tag{4.16}$$

and

$$\tilde{F} = F + \gamma\mathscr{B}^T\mathscr{W}^{-1}G, \tag{4.17}$$

the system (4.15) can be written as (4.6). It holds that $(\tilde{U},\tilde{P}) = (U,P)$. The matrix $\mathscr{W}$ is symmetric and positive definite. A sufficiently large γ makes the augmented elasticity block "less asymmetric and indefinite" [Benzi and Liu, 2007].

This augmenting strategy is uniquely based on algebraic considerations. It could be applied to any SP problem [Gulliksson et al., 2002] but at the potential price of an high number of nonzero elements arising in the matrix $\tilde{\mathscr{A}}$. In particular, the sparsity pattern of $\mathscr{W}$ can change the one of $\tilde{\mathscr{A}} = \mathscr{A}_\gamma$, making this latter potentially dense. This is reflected in a large memory usage and large computing times for iterative solution methods. In this work, we consider $\mathscr{W}$ to be the *lumped pressure mass matrix* $\bar{\mathscr{M}}_p$. Alternative choices for $\mathscr{W}$ are:

A. $\mathbb{I}$; in this case the choice of $\gamma = \|\mathscr{A}\|_2/\|\mathscr{B}\|_2^2$ has been found to perform nicely [Benzi et al., 2005];

B. *pressure mass matrix* $\mathscr{M}_p$; In [Benzi and Olshanskii, 2006] it has been shown that $\mathscr{W} = \mathscr{M}_p$ represents a good choice. However, this choice is associated to a dense matrix $\mathscr{A}_\gamma$;

The choice $\mathscr{W} = \bar{\mathscr{M}}_p$ represents a compromise between the above-mentioned strategies. In fact $\bar{\mathscr{M}}_p$ represents an approximation of $\mathscr{M}_p$ and this choice reduces the sparsity pattern of $\mathscr{A}_\gamma$ to the one obtained following alternative A.. In the next section we describe the segregated multigrid preconditioned strategy proposed to solve the augmented system (4.6).

4.2.3 Multigrid strategy

We briefly illustrate a geometric MG method for arbitrarily shaped meshes. Given $\{\mathcal{T}_{h_1},\dots,\mathcal{T}_{h_L}\}$, conforming meshes, consider the following hierarchy of L nested interpolation spaces

$$\mathcal{N} = \{S^{\mathrm{p}}_{\mathrm{h}_1},\dots,S^{\mathrm{p}}_{\mathrm{h}_L}\}, \tag{4.18}$$

defined as in 2.5. Here the mesh $\mathcal{T}_{h_\ell}$ at level ℓ is obtained as uniform refinement of the mesh at level $\ell-1$, such that $K_{h_\ell} \subseteq K_{h_{\ell-1}}$. The prolongation operator $\mathscr{P}p^{h_\ell}_{h_{\ell-1}}\colon S^{\mathrm{p}}_{h_{\ell-1}} \to S^{\mathrm{p}}_{h_\ell}$, defined in Sec. 2.5.1, relates coefficients on level $\ell-1$ with the ones on level ℓ. To simplify the notation we write $\mathscr{P}p^{\ell}_{\ell-1}$ instead of $\mathscr{P}p^{h_\ell}_{h_{\ell-1}}$. We define the restriction operator $\mathscr{R}\mathrm{p}^{\ell-1}_{\ell}\colon S^{\mathrm{p}}_{h_\ell} \to S^{\mathrm{p}}_{h_{\ell-1}}$ as $\mathscr{R}\mathrm{p}^{\ell-1}_{\ell} = (\mathscr{P}\mathrm{p}^{\ell}_{\ell-1})^T$. The solution of the system

$$\mathscr{L}\mathbf{u} = \mathbf{f}, \tag{4.19}$$

for $\mathscr{L} \in \mathbb{R}^{N_{h_L}\times N_{h_L}}$ and $\mathbf{u},\mathbf{f} \in \mathbb{R}^{N_{h_L}}$, requires the assembling of $\mathscr{L}$ and $\mathbf{f}$ on level L. We construct the stiffness matrices $\mathscr{L}$ on the coarser levels by Galerkin projection, i.e.

$$\mathscr{L}_{\ell-1} = \mathscr{R}\mathrm{p}^{\ell-1}_{\ell}\mathscr{L}_{\ell}\mathscr{P}p^{\ell}_{\ell-1}. \tag{4.20}$$

In a similar fashion, we define

$$\mathbf{r}_{\ell-1} = \mathscr{R}\mathrm{p}^{\ell-1}_{\ell}\mathbf{r}_{\ell}, \tag{4.21}$$

where $\mathbf{r}_L = \mathbf{r} = \mathbf{f} - \mathscr{L}\mathbf{u}$. We consider MG of V-cycle type. We write the step ν of the MG algorithm for the solution of (4.19) in Alg. 5. In the algorithm, we consider s_b pre- and s_a post-smoothing steps (of GMRES type) for the solution of $\mathscr{L}_\ell\mathbf{u}_\ell = \mathbf{f}_\ell$. This is denoted with $S(\mathscr{L}_\ell,\mathbf{r}_\ell,s_b,s_a)$. We denote the MG algorithm as $MG(\mathscr{L},\mathbf{f},L,s_b,s_a)$.

for *each* $\ell \in \{L-1,\dots,1\}$ **do**
  compute: $\mathscr{L}_{\ell-1} = \mathscr{R}p^{\ell-1}_{\ell}\mathscr{L}_{\ell}\mathscr{P}p^{\ell}_{\ell-1}$ (Galerkin restriction of stiffness matrix)
end
Multigrid Iteration:
given: $\mathbf{u}^\nu \in \mathbb{R}^n$
compute: $\tilde{\mathbf{u}}^\nu = \mathbf{u}^\nu + S(\mathscr{L},\mathbf{f},s_b)$ (fine grid pre smoothing)
initialize: $\mathbf{r} = \mathbf{f} - \mathscr{L}\tilde{u}^\nu$
for *each* ℓ *in* $\{L-1,\dots,1\}$ **do**
  $\mathbf{v}_\ell = S(\mathscr{L}_\ell,\mathbf{r}_\ell,s_b)$ (pre smoothing)
  $\mathbf{r}_\ell = \mathbf{r}_\ell - \mathscr{L}_\ell\mathbf{v}_\ell$ (update of residual)
  $\mathbf{r}_{\ell-1} = \mathscr{R}p^{\ell-1}_{\ell}\mathbf{r}_\ell$ (restriction of residual)
end
compute: coarse grid correction $\mathbf{v}_0$ (direct solver)
for *each* $\ell \in \{L-1,\dots,1\}$ **do**
  $\mathbf{v}_\ell = \mathbf{v}_\ell + \mathscr{P}p^{\ell}_{\ell-1}\mathbf{v}_{\ell-1}$ (interpolation)
  $\mathbf{v}_\ell = S(\mathscr{L}_\ell,\mathbf{r}_\ell,s_a)$ (post smoothing)
end
compute: $\tilde{\mathbf{u}}^\nu = \tilde{\mathbf{u}}^\nu + \mathscr{P}p^{L}_{L-1}\mathbf{v}_{L-1}$
compute: $\mathbf{u}^{\nu+1} = \mathbf{u}^\nu + S(\mathscr{L},\mathbf{f},s_a)$ (fine grid post smoothing)

Algorithm 5: Multigrid strategy: $\mathbf{u} = MG(\mathscr{L},\mathbf{f},L,s_b,s_a)$

4.2.4 Segregated multigrid preconditioned strategy

In this section we describe the *segregated multigrid preconditioned strategy* (SMGP) that we propose for the solution of (4.6). It is based on the two-stage strategy (4.7)-(4.8). We recall that Cholesky factorization and CG method cannot be applied inasmuch $\tilde{\mathscr{S}}$ and $\tilde{\mathscr{A}}$ are not symmetric and positive definite. In the proposed algorithm, $\tilde{\mathscr{A}}$ and $\tilde{\mathscr{S}}$ are solved employing GMRES preconditioned strategies.

In particular, we employ

I) an L-levels MG strategy (Alg. 5) for the solution of the systems associated to the matrix $\tilde{\mathscr{A}}$. In detail, we refer to the computation of the left hand side of Eq. (4.7) and of the solution to Eq. (4.8).

II) an L-levels MG strategy (Alg. 5) for the application of the inverse of the mass matrix $\mathscr{M}_p$, that we employ as preconditioner for $\tilde{\mathscr{S}}$. Each GMRES iteration for $\tilde{\mathscr{S}}$ requires the solution of a system with matrix $\tilde{\mathscr{A}}$ which is performed following I). We remind that the mass matrix has a condition number which is independent of the mesh size. The application of this preconditioner could be replaced by running a few GMRES cycles on the finest level.

The construction of interpolation operators (see Sec. 2.5.1) is performed only once for all nonlinear iterations. The SMGP strategy for the computation of the solution $(\tilde{U}^*, \tilde{P}^*)$ consists in the following steps:

0. for $\ell = 1, \dots, L-1$, compute $\mathscr{P}1_{\ell-1}^{\ell}$ $\mathscr{P}2_{\ell-1}^{\ell}$, $\mathscr{R}1_{\ell}^{\ell-1}$, $\mathscr{R}2_{\ell}^{\ell-1}$;

1. compute $Z = \tilde{\mathscr{A}}^{-1}\tilde{F}$ following the strategy described in I);

2. solve Eq. (4.7) following the strategy described in II);

3. solve Eq. (4.8) following the strategy described in I).

Details on the SMGP algorithm are reported in Alg. 6. We refer to the GMRES method for the solution of $\mathscr{G}\mathbf{x} = \mathbf{b}$ with a L-levels MG preconditioner as $u = GMRES(\mathscr{L}, \mathscr{G}, \mathbf{b}, MG(L,s))$. Here $\mathscr{L}$ is the preconditioner for the matrix $\mathscr{G}$ and MG represents the solution method. In this case $MG(L,s)$ is shortcut for $MG(\mathscr{L}, \mathbf{d}, L, s, s)$ where $\mathbf{d}$ is the right hand side associated to the preconditioned system. Here s represents the number of pre- and post-smoothing steps of GMRES type, which, for the solution of a given matrix, we consider to be equal. We consider $\mathbf{s}_{\tilde{\mathscr{A}}}$ to be the number of smoothing iterations for the solution of $\tilde{\mathscr{A}}$ and $\mathbf{s}_{\tilde{\mathscr{S}}}$ the one for $\tilde{\mathscr{S}}$. The resulting SMGP strategy is denoted with $SMGP(\mathscr{M}_p, \tilde{\mathscr{H}}, \mathbf{rhs}, L, \mathbf{s}_{\tilde{\mathscr{S}}}, \mathbf{s}_{\tilde{\mathscr{A}}})$.

In the description above and in the numerical tests described in the next section, we considered the same number of MG levels for the solution of $\tilde{\mathscr{A}}$ and $\tilde{\mathscr{S}}$. We remind that different preconditioning strategies for the two systems can be used. On the fine level L, given the linear iteration k, we computed the approximate asymptotic convergence rate $\tilde{\rho}_L^k$ according to

$$\tilde{\rho}_L^k = \frac{\|r^{k+1}\|}{\|r^k\|}.$$

if $t = t_0$ **then**
  for *each* $\ell \in \{1, \dots, L-1\}$ **do**
    compute: $\mathscr{P}1_{\ell-1}^{\ell}$ $\mathscr{P}2_{\ell-1}^{\ell}$, $\mathscr{R}1_{\ell}^{\ell-1}$, $\mathscr{R}2_{\ell}^{\ell-1}$
  end
end
for *each linear step* k **do**
  solve: $\tilde{\mathscr{A}}Z = \tilde{F}$ as $\mathbf{z} = GMRES(\tilde{\mathscr{A}}, \tilde{\mathscr{A}}, \tilde{F}, MG(L, \mathbf{s}_{\tilde{\mathscr{A}}}))$
  compute: $\text{rhs}_{\mathbf{p}} = G - \mathscr{B}Z$
  solve: $\tilde{\mathscr{S}}\tilde{P}^* = \text{rhs}_{\mathbf{p}}$ as $\tilde{P}^* = GMRES(\mathscr{M}_{\mathbf{p}}, \tilde{\mathscr{S}}, \text{rhs}_{\mathbf{p}}, MG(L, \mathbf{s}_{\tilde{\mathscr{S}}}))$
  compute: $\text{rhs}_{\mathbf{x}} = \tilde{F} - \mathscr{B}^T\tilde{P}^*$
  solve: $\tilde{\mathscr{A}}\tilde{U}^* = \text{rhs}_{\mathbf{x}}$ as $\tilde{U}^* = GMRES(\tilde{\mathscr{A}}, \tilde{\mathscr{A}}, \text{rhs}_{\mathbf{x}}, MG(L, \mathbf{s}_{\tilde{\mathscr{A}}}))$
end

Algorithm 6: Segregated approach: $(\tilde{U}^*, \tilde{P}^*) = SMGP(\mathscr{M}_{\mathbf{p}}, \tilde{\mathscr{H}}, \mathbf{rhs}, L, \mathbf{s}_{\tilde{\mathscr{S}}}, \mathbf{s}_{\tilde{\mathscr{A}}})$

4.3 Numerical results

In this section we investigate the performance of the proposed SMGP approach by means of numerical experiments. The first numerical experiment consists in the bending of a two-dimensional rectangular beam of size 10×1 mm (Subsection 4.3.1). In particular, we consider three different settings, corresponding to three material laws: 1) Neo-Hookean [Rivlin, 1948; Bonet and Wood, 1997], 2) isotropic Guccione-Costa, and 3) anisotropic Guccione-Costa [Guccione et al., 1995]. For all these settings, we first study the performance of the two different augmenting strategies on the SMGP approach and the effect of different numbers of smoothing steps (Test **A**). Then, we study the optimality of the SMGP approach employing a two- and three-level MG strategies (Tests **B** and **C**). Finally, we study the performance of the physics-based SMGP approach increasing the number of MG levels, and keeping fixed the coarse level (Test **D**).

The second numerical experiment consists in the passive inflation and active contraction of an idealized left ventricle (LV) with anisotropic material properties (Subsection 4.3.2). This latter experiment has been proposed in [Land et al., 2015a] and here it is employed to assess the performance of the physics-based SMGP approach on a realistic geometry. In particular, with this experiment, we want to evaluate performance and optimality in presence of active forces.

The numerical experiments have been performed in HART, a novel application for fully coupled electromechanical cardiac simulations, implemented in the FE framework MOOSE [R Gaston et al., 2014].

HART is developed at CCMC (Center for Computational Medicine in Cardiology) and ICS (Institute of Computational Science, Università della Svizzera italiana). MOOSE relies upon PETSc [Balay et al., 2017] in which our solution strategy has been implemented. The parallel implementation of the proposed solution strategy relies on the PCFIELDSPLIT and PCMG preconditioners. The MOONoLith library [Krause and Zulian, 2016] allows for a fast and parallel construction of the projection and prolongation operators.

4.3.1 Bending of a rectangular beam

The coarsest mesh $\mathscr{H}_0$ is composed of uniform quadrilaterals of size 0.5 mm. Mesh $\mathscr{H}_\ell$ is obtained by ℓ uniform refinements of the coarsest mesh. Tab. 4.2 reports the number of vertices and

Level	Grid	# Vertices	# DOFs
0	$\mathscr{H}_0$	63	148
1	$\mathscr{H}_1$	205	473
2	$\mathscr{H}_2$	729	1663
3	$\mathscr{H}_3$	2737	6203
4	$\mathscr{H}_4$	10593	23923
5	$\mathscr{H}_5$	41665	93923
6	$\mathscr{H}_6$	165249	372163
7	$\mathscr{H}_7$	658177	1481603
8	$\mathscr{H}_8$	2627073	5912323

Table 4.2. Refinement history of the meshes associated to the beam geometry.

degrees of freedom (DOFs) of the hierarchy of considered meshes. Relative tolerances of 10^{-10}, 10^{-11} and 10^{-13} are employed as stopping criteria for the external Newton method, the solver for $\tilde{\mathscr{S}}$, and the solver for $\tilde{\mathscr{A}}$, respectively. All tests were run on a 4-core Intel processor with 2.2 GHz with MPI task parallelism.

Test A: comparison of augmenting strategies and effects of smoothing steps

As first test, we compare the augmented Lagrangian and physics-based augmenting strategies with $\gamma \in \{2, 20, 200\}$ and $k \in \{2, 20\}$. We consider a two-grid approach with $\mathscr{H}_1$ as fine mesh. In particular, we study the impact of these strategies and parameters on the number of iterations for the solution of $\tilde{\mathscr{S}}$ and of $\tilde{\mathscr{A}}$ at different steps of Newton's method setting $s_{\tilde{\mathscr{A}}} = 6$ and $s_{\tilde{\mathscr{S}}} = 2$. For all three settings, Newton's method converged to the relative tolerance in 7 iterations. Fig. 4.7 reports the convergence history for the setting 1. The plots report the obtained residuals(first and third columns) and the estimated convergence rates $\tilde{\rho}_1$ (second and fourth columns) against the iteration number. Results are reported for the first, second and second to last iterations of Newton's method (first, second and third rows). Since the solver for $\tilde{\mathscr{A}}$ is called at each iteration of the Schur complement solution process, the convergence history for $\tilde{\mathscr{A}}$ is reported at first iteration of the solution of $\tilde{\mathscr{S}}$. For both the SMGP strategies, the convergence of $\tilde{\mathscr{A}}$ deteriorates considering high values of the augmenting parameters γ and k. This behavior is partially balanced by an improvement of the convergence for the solution of $\tilde{\mathscr{S}}$. Results show that, for relatively small and comparable values of k and γ, the physics-based SMGP approach performs better then the augmented Lagrangian one. In contrast, the physics-based SMGP approach does not converge for high values of k. This is due to a failure for the solver for $\tilde{\mathscr{A}}$. For this specific setting, optimal parameters for γ and k belong the range $[2, 20]$. Comparing the different nonlinear iterations considered, the augmented Lagrangian and the physics-based SMGP approach presents a stable behavior. If compared to the augmented Lagrangian approach, for $k = 20$ the physics-based SMGP approach results in a better convergence for the solution of $\tilde{\mathscr{S}}$. Similarly, Fig. 4.8 and 4.9 report the convergence histories for the settings 2 and 3, respectively. Comparing the results settings 2 and 3, we notice that the anisotropy does not affect the convergence history.

As a second test, we study the impact of the number of smoothing steps on the convergence of the SMGP approach. For setting 3, first row of Fig. 4.10 reports the mean number of iterations for the solution of $\tilde{\mathscr{S}}$ and of $\tilde{\mathscr{A}}$ for the SMGP approach against the augmenting parameters

considered. The mean is computed over all the Newton's iterations. Second row of Fig. 4.10 reports total simulation time (in seconds) for the solution of the beam problem against the considered augmenting parameter. Results for different augmenting strategies and number of smoothing steps are shown (reported in the figure). As smoothing steps, we consider the couples $(s_{\tilde{\mathscr{P}}}, s_{\tilde{\mathscr{A}}}) \in \{(2,2),(4,4),(6,6),(8,8)\}$. To show the stability of the obtained results with respect to the size of the fine level mesh and with respect to the number of levels, we consider two-grid SMGP approach on mesh $\mathscr{H}_1$ (left) and on mesh $\mathscr{H}_2$ (center), and three-grid SMGP approach for the solution on $\mathscr{H}_2$ (right). Results show a stronger dependence of the physics-based approach on the augmenting parameter k with respect to the augmented Lagrangian one. We observe that two smoothing steps are sufficient for the solution of the Schur complement, while in general a larger number of smoothing steps improves the convergence for the elasticity matrix. The physics-based SMGP approach does not converge for $k > 50$. The augmented Lagrangian SMGP approach is associated with a fill in of the sparsity pattern of the augmented matrix $\tilde{\mathscr{A}}$ with respect to $\mathscr{A}$. This is reflected in a larger memory usage and computing times per SMGP iteration for the solution of the block $\tilde{\mathscr{A}}$. This numerical drawback makes the usage of this approach for big-size problems unfeasible.

As a third test, we investigate the stability of the obtained results with respect to the size of the fine level. Fig. 4.11 reports the number of iterations for the physics-based SMGP approach for the solution of $\tilde{\mathscr{P}}$ (left) and $\tilde{\mathscr{A}}$ (right) plotted against the considered fine level mesh size and augmenting parameter. In this case, results for the second nonlinear iteration are reported. We consider a two-level approach with meshes $\mathscr{H}_\ell$ - $\mathscr{H}_{\ell-1}$, for $\ell = 1,\dots,5$. In this case, we fix the number of smoothing steps to $s_{\tilde{\mathscr{P}}} = s_{\tilde{\mathscr{A}}} = 6$. Obtained results show that the number of iterations for the solution of $\tilde{\mathscr{P}}$ and $\tilde{\mathscr{A}}$ slightly depends on the mesh size, suggesting an optimality of the approach in a plausible range of the augmenting parameter.

Our final goal is the large scale simulation of anisotropic cardiac tissue. For this reason, in successive tests, we consider the physics-based SMGP approach for the solution of setting 3 fixing $k = 20$.

Test B-C-D: Optimality of the proposed approach

In test **B**, we evaluate the optimality of the two-grid physics-based SMGP approach with respect to the mesh size h of the fine level. We apply a uniform refinement to the meshes associated to all the levels. Fig. (4.12) reports the obtained convergence history. Results are shown for the second nonlinear iteration. Results for the solution of $\tilde{\mathscr{A}}$ are reported for the second iteration of the Schur complement. The obtained number of iterations for $\tilde{\mathscr{P}}$ and $\tilde{\mathscr{A}}$ remain constant. This suggest an extension of the theoretical optimality results well known for the linear case. Similar results are obtained in test **C**, where three-grid physics-based SMGP approach is considered. Results for this test are shown in Fig. 4.13. For the solution on the three finest grids, we notice a small decrease in the performance of the approach for the solution of $\tilde{\mathscr{P}}$ at iteration 5. In test **D**, we compare the performance of physics-based SMGP approach against the number of levels considered. For all the simulations we consider $\mathscr{H}_0$ to be the coarsest grid. Fig. 4.14 reports the results associated to this test. The obtained number of iterations for $\tilde{\mathscr{P}}$ and $\tilde{\mathscr{A}}$ remain constant with respect to the number of levels.

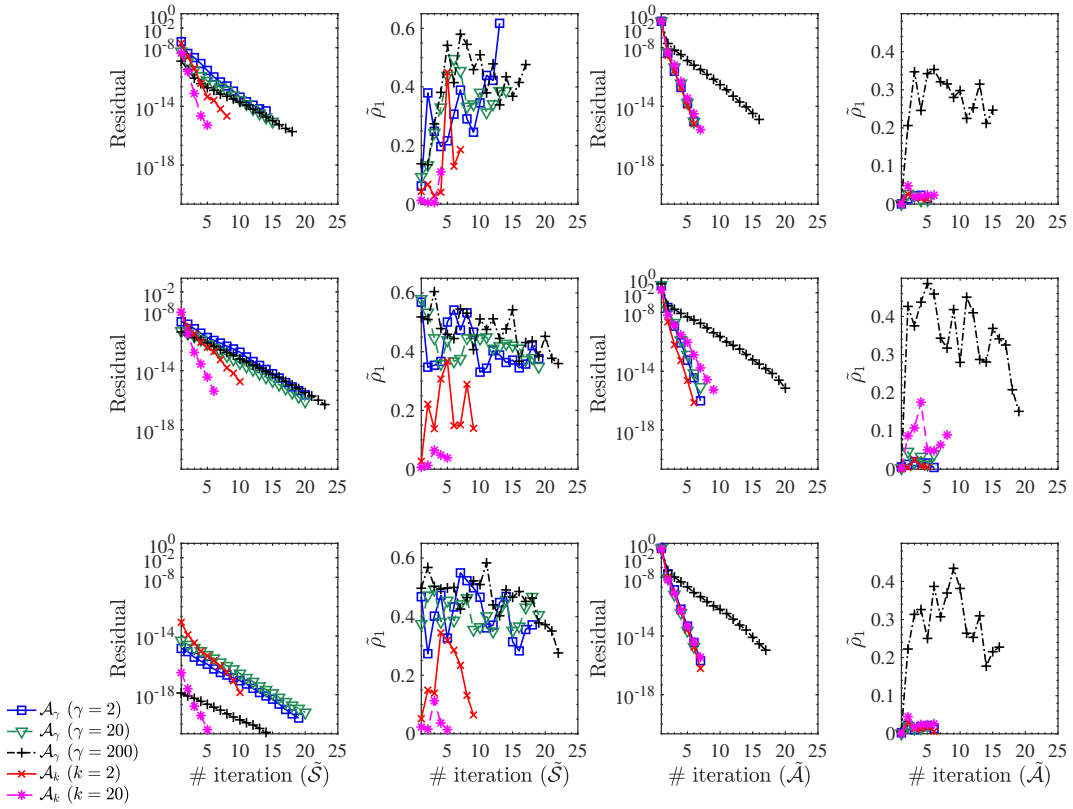

Figure 4.7. Test A, setting 1. Residuals (first and third columns) and estimated convergence rate $\tilde{\rho}_1$ (second and fourth columns) for the solution of $\tilde{\mathscr{S}}$ and $\tilde{\mathscr{A}}$ considered against the number of iteration for the the SMGP strategies. Obtained results are reported for the first, the second and the second to last nonlinear iterations in the first, second and third rows, respectively.

4.3.2 Inflation-contraction of an idealized left ventricle

We consider the problem of passive inflation and active contraction of a LV. Geometry, fiber orientation and material parameters are the same as described in third benchmark problem of [Land et al., 2015a]. Tab. 4.3 reports the number of vertices and DOFs of the considered hierarchy of nested meshes. The passive force per unit area of 15 kPa and the active stress of 60 kPa are simultaneously applied in ten incremental loading steps [Campos et al., 2013a]. We set as stopping criteria for Newton's method a relative tolerances of 10^{-6} as in [Campos et al., 2018]. Moreover, we set 10^{-9} and 10^{-11} as stopping criteria for the solution of the systems associated to the matrix $\tilde{\mathscr{S}}$ and $\tilde{\mathscr{A}}$, respectively.

Simulations are run on Linux cluster with nodes of 2×Intel E5-2650 v3 processors.

Fig. 4.15 shows the norm of the obtained displacement after ten incremental loading steps. The bottom view shown in the central part of the figure reports the LV twist due to the anisotropy

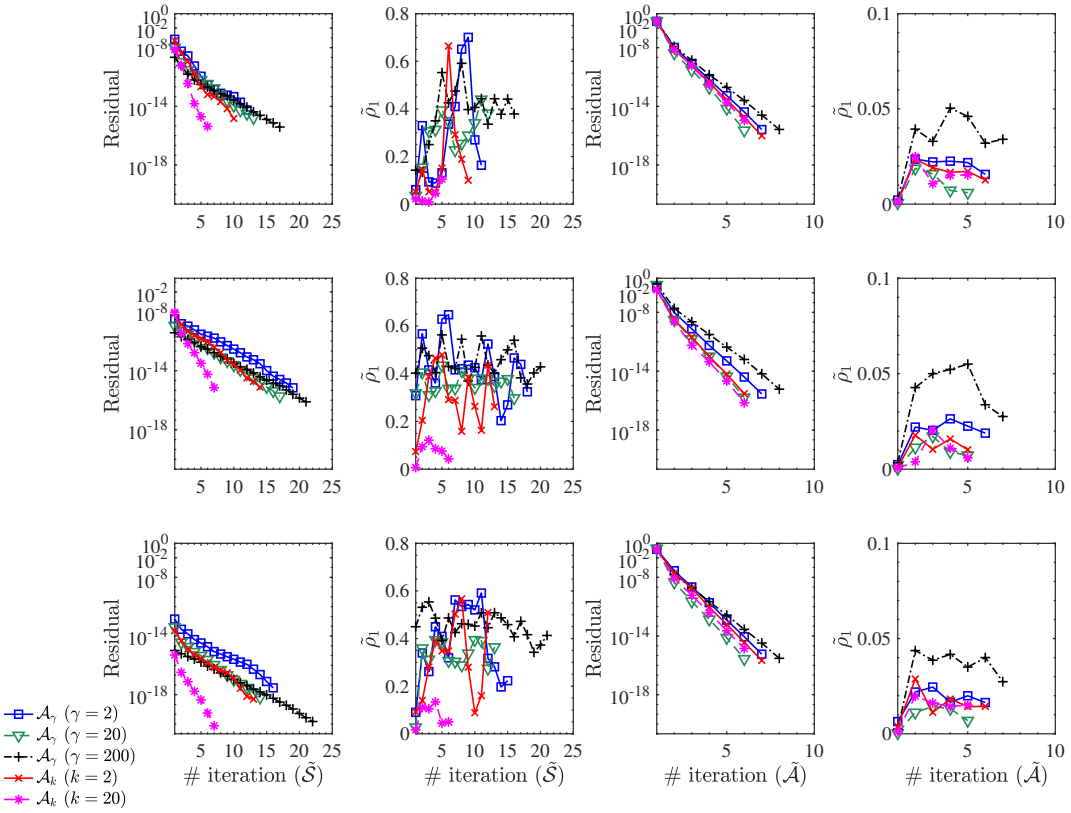

Figure 4.8. Test A, setting 2. Residuals (first and third columns) and estimated convergence rate $\tilde{\rho}_1$ (second and fourth columns) for the solution of $\tilde{\mathscr{S}}$ and $\tilde{\mathscr{A}}$ considered against the number of iteration for the SMGP strategy. Obtained results are reported for the first, the second and the second to last nonlinear iterations in the first, second and third rows, respectively.

of the material law.

Comparison of augmenting parameters and effects of smoothing steps

We study the impact of the augmenting parameter and of the number of smoothing steps on the convergence of the SMGP approach for the idealized LV. Fig. 4.16 reports the mean number of iterations for the solution of $\tilde{\mathscr{S}}$ and of $\tilde{\mathscr{A}}$ for the SMGP approach against the augmenting parameter considered. The mean is computed over all the Newton's iterations. In particular, we consider the physics-based SMGP approach for the solution on the mesh $\mathscr{T}_1$ with $(s_{\tilde{\mathscr{S}}}, s_{\tilde{\mathscr{A}}}) \in \{(2,3),(2,5)\}$. Results show that the augmenting parameter that minimizes the number of iterations for the solution of $\tilde{\mathscr{A}}$ is $k = 50$. For $k \in [1,200]$, the number of iterations for the solution of $\tilde{\mathscr{S}}$ are monotonically decreasing with respect to k. The increase of the number of smoothing steps from 3 to 5 has a small impact on the solution of $\tilde{\mathscr{A}}$.

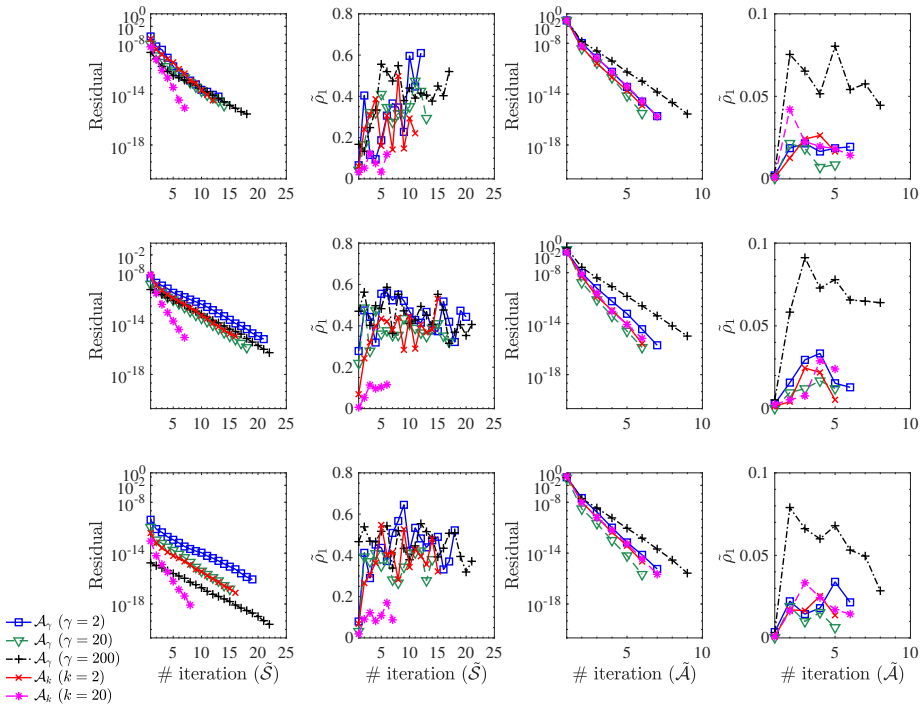

Figure 4.9. Test A, setting 3. Residuals (first and third columns) and estimated convergence rate $\tilde{\rho}_1$ (second and fourth columns) for the solution of $\tilde{\mathscr{S}}$ and $\tilde{\mathscr{A}}$ considered against the number of iteration for the SMGP strategy. Obtained results are reported for the first, the second and the second to last nonlinear iterations in the first, second and third rows, respectively.

Strong scalability

We investigate how the number of cores affects the mean number of iterations for the solution of $\tilde{\mathscr{S}}$ and of $\tilde{\mathscr{A}}$ at a given nonlinear iteration. We also investigate the strong scaling in which we keep fixed the size of the problem and increase the number of processors. We consider a two-grid and a three-grid approach for the solution of the inflation-contraction problem on $\mathscr{T}_1$ and $\mathscr{T}_2$, respectively. We fixed $k = 50$, $s_{\tilde{\mathscr{S}}} = 2$, and $s_{\tilde{\mathscr{A}}} = 5$.

Fig. 4.17, left panel, shows the mean number of iterations for the solution of $\tilde{\mathscr{S}}$ and of $\tilde{\mathscr{A}}$ against the number of computing cores. The average is computed over all the solutions of $\tilde{\mathscr{S}}$ and $\tilde{\mathscr{A}}$ over all the nonlinear steps. On the right of the figure, the mean run times (in seconds) per nonlinear step against the number of cores considered are shown. The higher number of iterations for the solution on $\mathscr{T}_2$ is due to the increase of the number of levels from 2 to 3. The solution of $\tilde{\mathscr{A}}$ is slightly affected by the increase of the number of cores. In contrast, the solution of $\tilde{\mathscr{S}}$ is independent on the considered number of cores and on the problem-size. Differently from standard smoothing approaches with classic iterative solvers, the dependence on the number of cores is mitigated by the use of a GMRES smoother. In fact, this optimality with respect to the number of cores affects its scaling properties. We observe from right panel of Fig. (4.17) that the

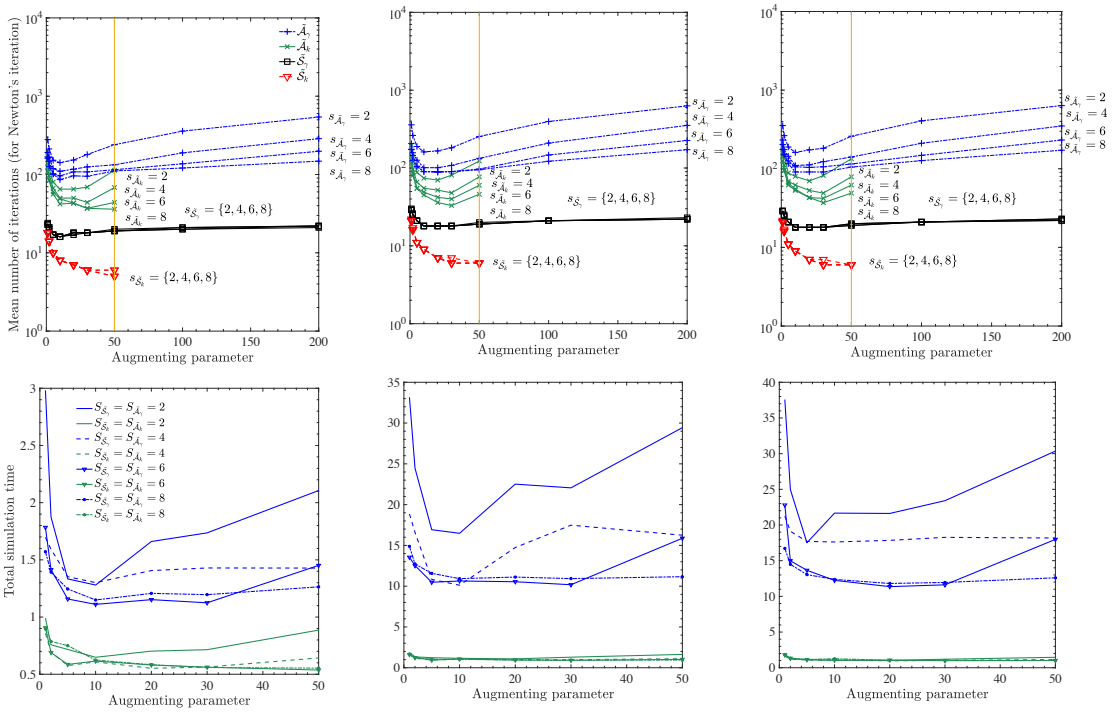

Figure 4.10. Test A, setting 3. First row: mean number of iterations (for a single iteration of the Newton's method) for $\tilde{\mathscr{S}}$ and $\tilde{\mathscr{A}}$ for the SMGP strategy against the augmenting parameter. Second row: total simulation time (in seconds) for the solution of the beam problem against the considered augmenting parameter. As number of smoothing steps we consider the couples $(s_{\tilde{\mathscr{S}}}, s_{\tilde{\mathscr{A}}}) \in \{(2,2),(4,4),(6,6),(8,8)\}$ (reported in the figure). Results for two-grid SMGP approach for the solution on $\mathscr{H}_1$ (left) and on $\mathscr{H}_2$ (center) and three-grid SMGP approach for the solution on $\mathscr{H}_2$ (right) are reported.

scaling is not optimal for a large number of cores.

Effect of the active stress contribution

The components of the active stress in the Jacobian are usually believed to negatively affect the convergence of the linear and nonlinear solution methods [Gurev et al., 2015]. In particular, the mass matrix defined on the pressure space is not an optimal preconditioner for the Schur complement. In order to study the impact of the active stress contribution on the Newton's strategy, the passive inflation and the active contraction phases have been decoupled by first applying the maximum force on the endocardium (diastolic phase) in twenty incremental loading steps and then by applying the active stress (systolic phase) in twenty steps. Maximum values are the same as the ones reported in Sec. 4.3.2. For each of these forty steps, Fig. 4.18 reports the number of Newton's iterations (left) and the mean number of iterations for the solution of $\tilde{\mathscr{A}}$ and of $\tilde{\mathscr{S}}$ (right). We consider $(s_{\tilde{\mathscr{S}}}, s_{\tilde{\mathscr{A}}}) = (2,5)$ and $(s_{\tilde{\mathscr{S}}}, s_{\tilde{\mathscr{A}}}) = (4,7)$ smoothing steps. Newton's method coupled with physics-based SMGP approach performs similarly during the passive and active phases. In this latter phase, increasing the smoothing steps from $(s_{\tilde{\mathscr{S}}}, s_{\tilde{\mathscr{A}}}) = (2,5)$ to

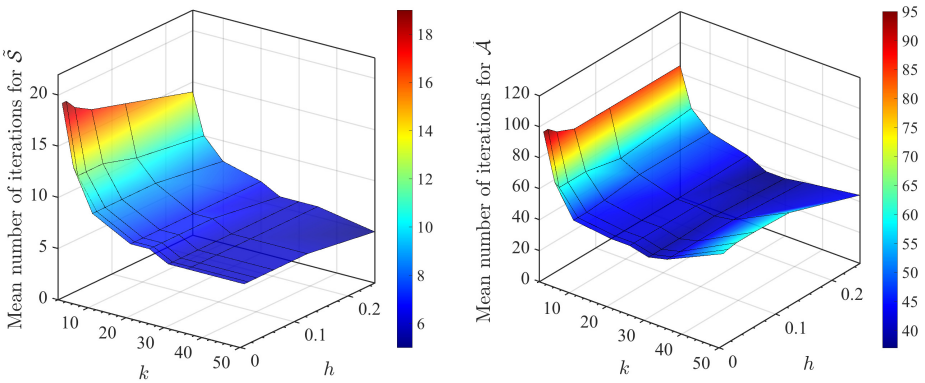

Figure 4.11. Test A, setting 3: mean number of iterations for $\tilde{\mathscr{S}}$ (left) and for $\tilde{\mathscr{A}}$ (right) for the two-grid physics-based SMGP approach plotted against the considered mesh size and augmenting parameter.

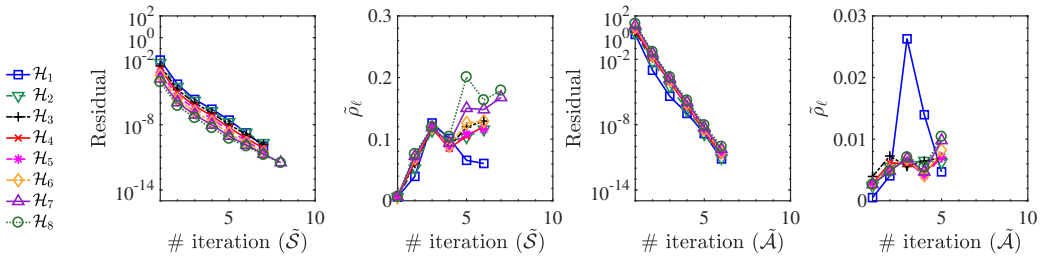

Figure 4.12. Test B, setting 3: two-grid physics-based SMGP approach. Residuals (first and third columns) and estimated convergence rate $\tilde{\rho}_l$ (second and fourth columns) for the solution of $\tilde{\mathscr{S}}$ and $\tilde{\mathscr{A}}$ considered against the number of iteration.

$(s_{\tilde{\mathscr{S}}}, s_{\tilde{\mathscr{A}}}) = (4,7)$ results in a small decrease of the number of iterations. The highest numbers of iterations for the solution of $\tilde{\mathscr{S}}$ and $\tilde{\mathscr{A}}$ are obtained around the incremental steps 20 and 40 which are associated to the maximum values of forces imposed on the domain. However, no significant differences are obtained for the solution of $\tilde{\mathscr{A}}$ and of $\tilde{\mathscr{S}}$ during the two phases.

4.4 Conclusions

We presented a novel Schur-complement-based segregated strategy for the solution of saddle point problems arising from mixed finite element discretizations in incompressible nonlinear mechanics. The arising tangent problem, which has a saddle point structure, is solved in a segregated fashion employing a GMRES solver for the Schur complement preconditioned by means of a pressure mass matrix. Hence, at each iteration of the Schur complement, a multigrid strategy has been employed to solve both the elasticity operator and the mass matrix. In order to remove the singularity of the elasticity matrix two different augmenting strategies have been tested: the physics-based and the augmented Lagrangian approaches. The physics-based segregated multigrid-preconditioned approach is applicable to incompressible elasticity. It has the main

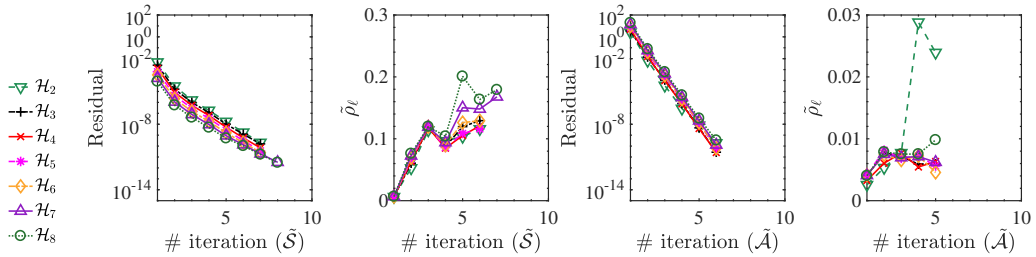

Figure 4.13. Test C, setting 3: three-grid physics-based SMGP approach. Residuals (first and third columns) and estimated convergence rate $\tilde{\rho}_l$ (second and fourth columns) for the solution of $\tilde{\mathscr{S}}$ and $\tilde{\mathscr{A}}$ considered against the number of iteration.

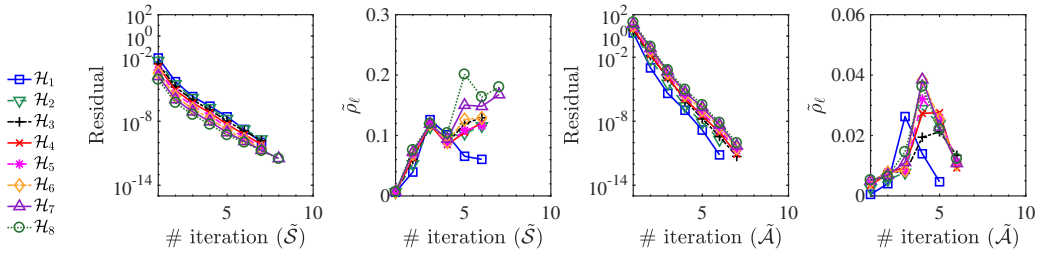

Figure 4.14. Test D, setting 3: multi-level physics-based SMGP approach. Residuals (first and third columns) and estimated convergence rate $\tilde{\rho}_l$ (second and fourth columns) for the solution of $\tilde{\mathscr{S}}$ and $\tilde{\mathscr{A}}$ considered against the number of iteration.

advantage of preserving the sparsity pattern of the stiffness matrix. Compared to standard augmenting Lagrangian methods, this physics-based approach presents better convergence rates. By means of several numerical tests, we showed the optimality of the proposed strategy with respect to the augmenting parameter, the mesh-size, and the number of multigrid levels. In conclusion, the extensive comparative study performed suggest that the proposed Schur-complement-based segregated strategy coupled with the physics-based augmenting approach represents an efficient solution strategy for the solution of the equations describing incompressible nonlinear materials for the augmenting parameter belonging to the range $[20, 50]$.

Level	Grid	# Vertices	# DOFs
0	$\mathcal{T}_0$	~4 k	~14 k
1	$\mathcal{T}_1$	~32 k	~100 k
2	$\mathcal{T}_2$	~235 k	~738 k
3	$\mathcal{T}_3$	~1820 k	~5696 k

Table 4.3. Idealized left ventricle: table associated to the refinement history.

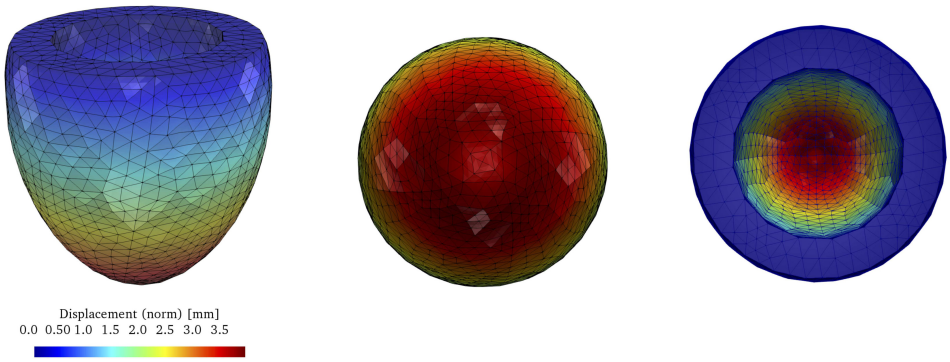

Figure 4.15. Snapshots of the idealized left ventricle after 10 incremental loading steps. In detail, norm of the displacement in anterior view (left), in bottom view (center) and in top view (right). Results on the grid $\mathcal{T}_0$ are reported.

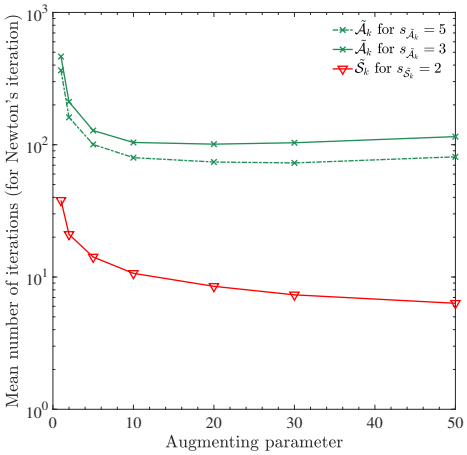

Figure 4.16. Mean number of iterations (for a single iteration of the Newton's method) for $\tilde{\mathcal{F}}$ and $\tilde{\mathcal{S}}$ for the two-grids physic-based SMGP strategy against the considered augmenting parameter. As number of smoothing steps we consider the couples $(s_{\tilde{\mathcal{F}}}, s_{\tilde{\mathcal{A}}}) \in \{(2,3),(2,5)\}$ (reported in figure).

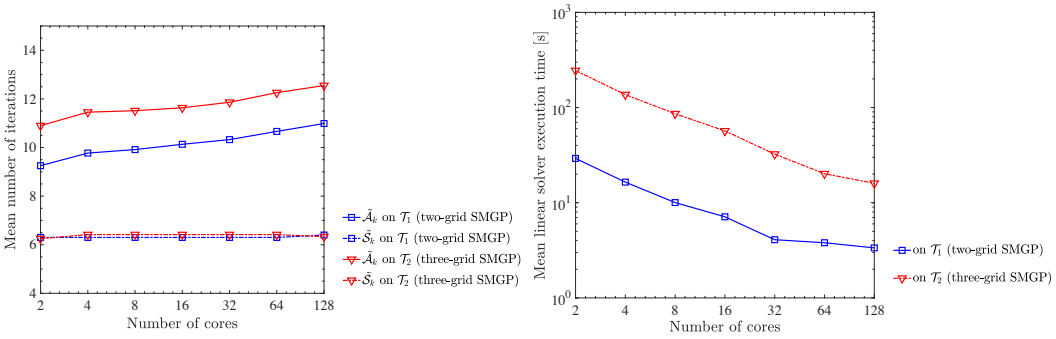

Figure 4.17. Left: mean number of iterations for the solution of the block $\tilde{\mathscr{A}}$ and of the Schur complement $\tilde{\mathscr{S}}$ against the number of cores. Right: mean run times for nonlinear iteration against the number of cores.

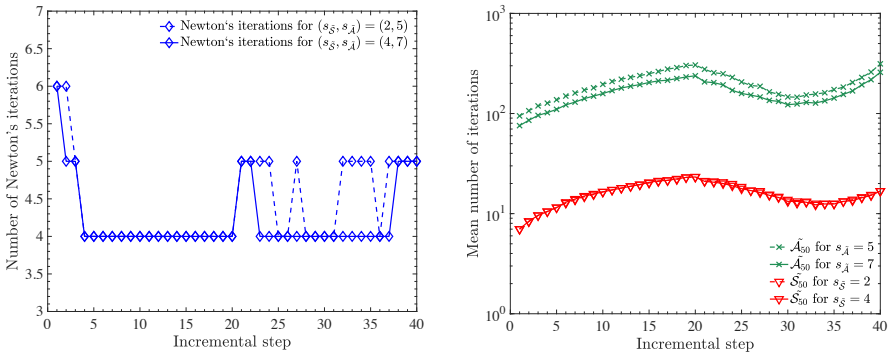

Figure 4.18. Left: number of Newton's iterations against the number of the current incremental loading step. Right: mean number of iterations for the solution of $\tilde{\mathscr{A}}$ and of $\tilde{\mathscr{S}}$ against the number of the current incremental loading step are reported. Results are shown considering $(s_{\tilde{\mathscr{S}}}, s_{\tilde{\mathscr{A}}}) = (2,5)$ and $(s_{\tilde{\mathscr{S}}}, s_{\tilde{\mathscr{A}}}) = (4,7)$ smoothing steps.

Chapter 5

Coupled numerical simulations

5.1 Impact of mechanical deformation on pseudo-ECGs: a simulation study

The spatio-temporal morphology of the ECG is the result of the relative motion of the cardiac extracellular action potentials with respect to the position of the electrodes. ECG is usually computed as static process, without considering the mechanical deformation due to the beating heart and breathing. In detail, in the computation of the ECG, often a fixed geometry of the heart in the torso is assumed. Based on this approximation, patient-tailored ECGs can be simulated in a few minutes on HPC architectures with anatomically detailed cardiac electrophysiology models [M. Potse et al., 2006; Villongco et al., 2014]. However, the heart is mechanically active and several model studies showed that the T-wave in the ECGs is influenced by the volume of blood in the cavity [Cluitmans et al., 2015] and hence by the current configuration of the heart [Keller et al., 2011; Smith et al., 2003a; De Oliveira et al., 2013]. This indicates that the commonly used pure electrophysiology (PE) scenario may be too simple.

From a *geometrical point of view*, mechanics plays a double role in possible modifications of the ECG signals in contrast to a purely electrophysiological (PE) scenario: one is due to the effects of mechanical contraction on the electrical activation front and the second one is related to the change of distance from the electrodes during the cardiac cycle (see Sec. 1.3.2). Aim of this simulation study is to investigate the impact of the above-mentioned geometrical effects on simulated pseudo-ECGs. For this purpose two coupling strategies have been presented in Sec. 1.3.3. We employ a MD coupling scenario to isolate the role of the distance from the electrodes and a BD coupling scenario to understand the combined role of the two effects. MD coupling strategy allows to remove all mechano-electrical feedbacks (MEFs) which may affect the AP propagation. Additionally, this study results also in a comparison of the PE, MD and BD computational scenarios.

Experimental setup

We consider the monodomain system (1.90) coupled with the BOCF (see Sec. 1.2.7) ionic model and the fully incompressible Guccione-Costa hyperelastic law (see Sec. 1.1.8) with the GK model (see Sec. 1.3.1) for the mechanical description of the cardiac elastic active response. We consider $k_{T_a} = 50$ kPa, $\epsilon_0 = 1$ ms^{-1} and $\epsilon_\infty = 0.01$ ms^{-1}, $V_s = -30$ mV, and $\xi_r = 0.3$ mV^{-1}. The

conductivity tensor is assumed to be transversely isotropic. Electrophysiology material properties are homogeneous in space and taken from [Niederer et al., 2011]. We aim to systematically study the effect of the mechanical deformation on pseudo-ECGs. Thus we reduce the complex effects due to geometry and fiber orientation, considering the following three settings in which $\mathscr{B}_r$ is a

setting 1: cube with edge of 7 mm and fibers aligned along x-axis,

setting 2: slab of size 20 mm × 7 mm × 3 mm and fibers aligned along x-axis, and

setting 3: slab of size 20 mm × 7 mm × 3 mm and fibers aligned along y-axis.

In order to avoid rigid-body motion, the boundary faces along the planes $x = 0$, $y = 0$, and $z = 0$ are fixed in the normal direction. Setting 2. represents the electro-mechanical enrichment of the purely electrophysiological test studied presented in [Niederer et al., 2011].

We computed the pseudo-ECG signals as described in Sec. 1.3.2 at six unipolar electrodes $Z_{i,\pm}$, two for each Cartesian axis $i = x, y, z$. They are arranged symmetrically with respect to the center of the domain and are 10 cm apart from the boundary faces. In addition, the unipolar signals from electrodes aligned in the same direction are combined into a single bipolar pseudo-ECG, with the electrode in the positive direction being the cathode and the opposite one being the anode, defining $Z_i = Z_{i,+} - Z_{i,-}$.

The time integration of the monodomain system is performed by means of the qN-BDF-ETDStab$_1$ scheme described in Chpt. 3. The linear system arising from the implicit linearization of the nonlinear monodomain equation has been solved with an algebraic multigrid solver (BoomerAMG, PETSc suite). The non-linear mechanical model has been solved with Newton's SMGP strategy described in Chpt. 4. The spatial computational meshes of the electrophysiology have a resolution of 0.125 mm. Since no steep gradients in the deformation are present, the mechanical solver employs a coarser mesh of step-size 1 mm. Both solvers employ a temporal mesh with mesh size 0.05 ms.

Numerical Results

The AP and the pseudo-ECGs computed with the three computational scenarios are shown in Fig. 5.1, Fig. 5.2, and Fig. 5.3 for settings 1, 2, and 3, respectively. To compare zero potential isosurfaces considering MD and BD coupling approaches, the simulated AP have been mapped to the reference geometry. The isosurfaces of PE are equal to those of the MD since the electrophysiology problems are solved on the same domain for both the scenarios. The two leftmost upper panels of Fig. 5.1 depict the deformed states (reported in colors) of the two electro-mechanical approaches and they are compared with the undeformed state (computational grid is reported). The activation starts from the rightmost corner (marked with a green dot) closed to the clamped faces $x = 0$, $y = 0$, and $z = 0$. On the other faces, a stress-free boundary condition is imposed. The AP is depicted after 25 ms: the green region is in a depolarized state and the red region is in a resting condition. It can be seen that in the MD simulation the wavefront has progressed less, especially in the XZ- and XY-planes (parallel to the fiber direction, marked in red). Front of the BD method is also flatter. The influence of deformation on the activation wavefronts at different times is reported in the right upper panel. In general, due to the contraction of the tissue the BD scenario gave a faster activation front in the interior of the tissue and close to the stress-free faces along fiber direction. Hence, with the BD coupling strategy the same point activated earlier. Instead, in the cross fiber direction a slower activation has been noticed. An

opposite behavior has been observed close to the clamped edge along fiber direction. Specifically, the point located at $(0, 0, 7)$ activated 0.2 ms earlier with PE and MD. The influence of mechanical deformations is then reflected in the computed pseudo-ECGs. As a consequence of the simple axis aligned geometry, pseudo-ECG potential was basically dominated by the activated areas orthogonal to positive-to-negative electrode direction, weighted by the distance from the electrodes. The differences in the propagation are mostly visible in the X-direction where larger deformations occur. Initially, the potential increased since the activated area on the $x = 0$ face increased. Since no changes in configuration are present at this point, computed pseudo-ECGs are almost equal. After reaching its peak value, when the opposite face started to activate the potential abruptly decreased. Here differences are reflected in the notching present in the QRS complex of X-direction around the S-wave. MD scenario was responsible for a sharp notch, compared to the PE and BD. This was a consequence of the varying distance of the electrodes from the tissue. The activated areas between the approaches were comparable, but they were located at different distances from the electrode $Z_{i,+}$. The difference between BD and PE approaches is less appreciable, due to the change of conductivity, that compensated for the relative variation of the electrode location with slower areal velocity. For the other two electrodes, the QRS complex duration and shape were similar among PE, MD and BD approaches. In general, PE and BD produced T-waves of different amplitude. The discrepancy varied among the electrodes and test cases, with either higher or lower amplitudes. MD coupling scenario always provided a good approximation of the BD coupling one. In order to show more clearly the effect of conduction and contraction along the fibers, simulations were performed in two flatter and longer tissue slabs. For setting 2 (see Fig. 5.2) the effect of the boundary condition on the propagation was more apparent due to the orientation of the fibers along the major axis. MD and BD provided similar activation patterns until the signal reached the top face (around 7 ms after the electrical activation of the tissue). Then, since the signal has reached the stress- free top face, the tissue slab started to contract and thus the interplay between mechanics and electrophysiology became manifest. The propagation for BD approach resulted faster on the top face and slower close to the bottom face of the preparation. In particular, the zero-potential isosurfaces from MD and BD coupling approaches intersected on the reference geometry, certifying a face-to-face smooth variation in conduction velocity (see right panel of Fig. 5.2). Concerning the pseudo-ECG, the PE simulation gave a slightly smaller potential at the peak of the QRS complex compared to the other two approaches while the Y-lead of the pseudo-ECGs showed an opposite effect (see Fig. 5.2). No large differences were observed between MD and BD. Actually, the tissue is long enough along the fiber direction to decouple the activation of the two opposite faces, and thus easing the pseudo-ECGs interpretation. Differently from the previous case, accounting for deformation in the BD resulted in a larger and slightly earlier T-wave along the x- axis than in the MD and PE approaches. Finally, setting 3. (reported in Fig. 5.3) confirmed the results of the previous two cases, with a faster activation front of BD along fiber directions. In the pseudo-ECG, differences were noticeable in the S-wave between the different approaches in the fiber direction (see bottom panel of Fig. 5.3). As for setting 1, larger potential in the QRS complex were given by the BD and even larger by the MD. A delayed and amplified T-wave was observed for the Y-axis. Again, the MD approximation is not satisfactory for the computation of pseudo-ECGs. Even if the overall shape of the QRS complex, overestimated values are observed (for example peak of S-wave for y-axis was 0.09270 mV) and surprisingly a change of the sign of the T-wave was also present.

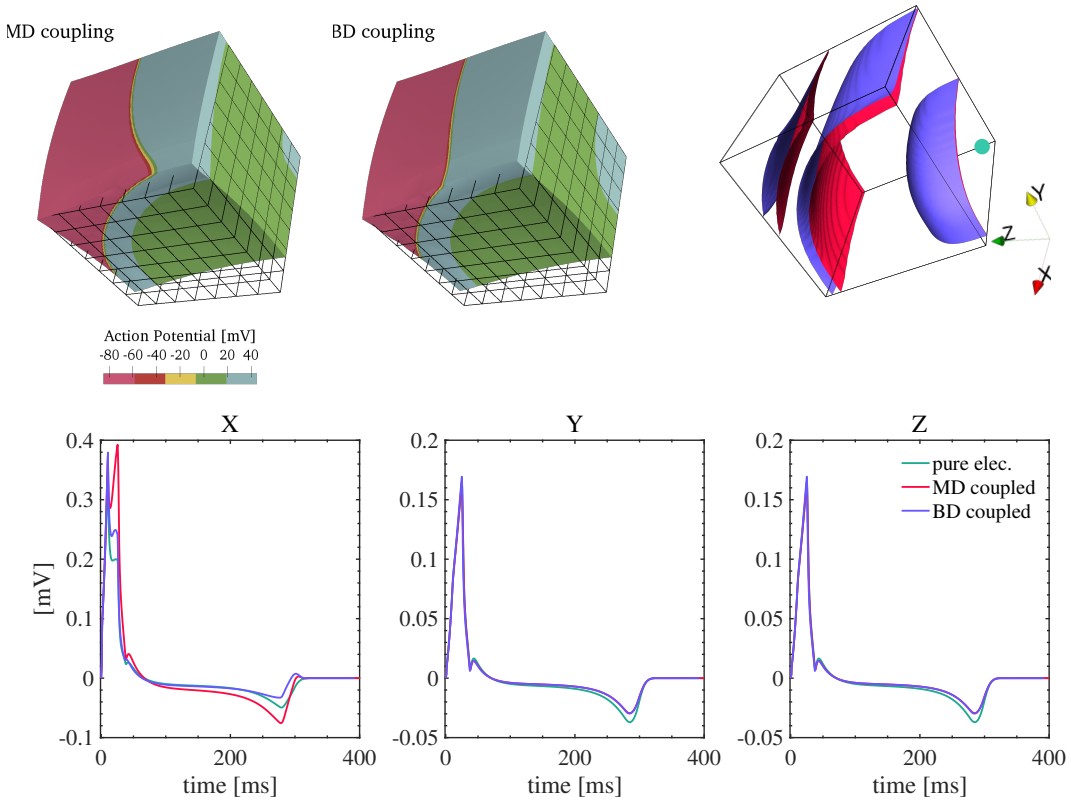

Figure 5.1. Setting 1. Top left: snapshots of the spatial distribution of the action potential from the MD and BD for a cube of tissue with fibers aligned along the x-axis. Configurations are reported 25 ms after applying an electrical stimulus at the location of the green dot. The grid reflects the mechanical mesh of the static configuration. Top right: comparison of zero isopotential surfaces obtained from the MD scenario (red surface) and BD scenario (blue surface) for different time steps (10 ms, 25 ms, 30 ms). In order to compare them, the different activations have been projected on the reference configuration. Bottom: simulated pseudo-ECGs. The three bipolar pseudo-ECGs along the Cartesian axes are shown here. Green, red and blue lines represent results for the pure-electrophysiology approach, the MD approach and the BD approach, respectively.

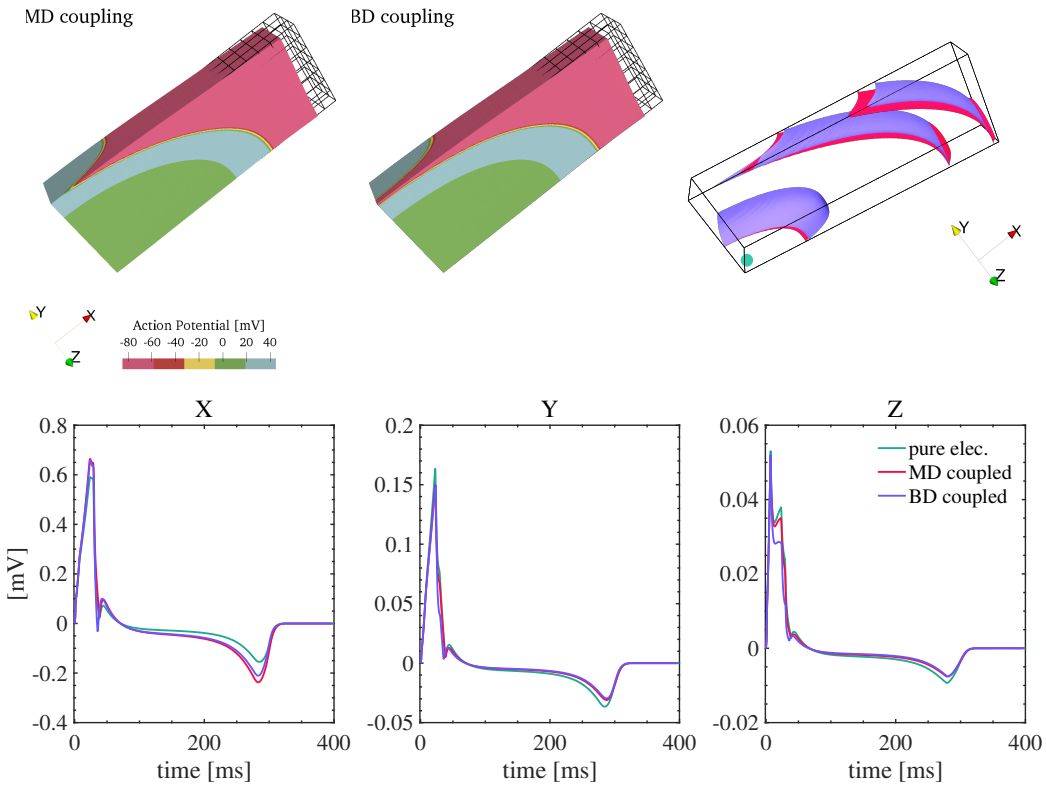

Figure 5.2. Setting 2. Top left: snapshots of the spatial distribution of the action potential from the MD and BD for a slab of tissue with fibers aligned along the x-axis. Configurations are reported 25 ms after applying an electrical stimulus at the location of the green dot. The grid reflects the mechanical mesh of the static configuration. Top right: comparison of zero isopotential surfaces obtained from the MD scenario (red surface) and BD scenario (blue surface) for different time steps (10 ms, 25 ms, 30 ms). In order to compare them, the different activations have been projected on the reference configuration. Bottom: simulated pseudo-ECGs. The three bipolar pseudo-ECGs along the Cartesian axes are shown here. Green, red and blue lines represent results for the pure-electrophysiology approach, the MD approach and BD approach, respectively.

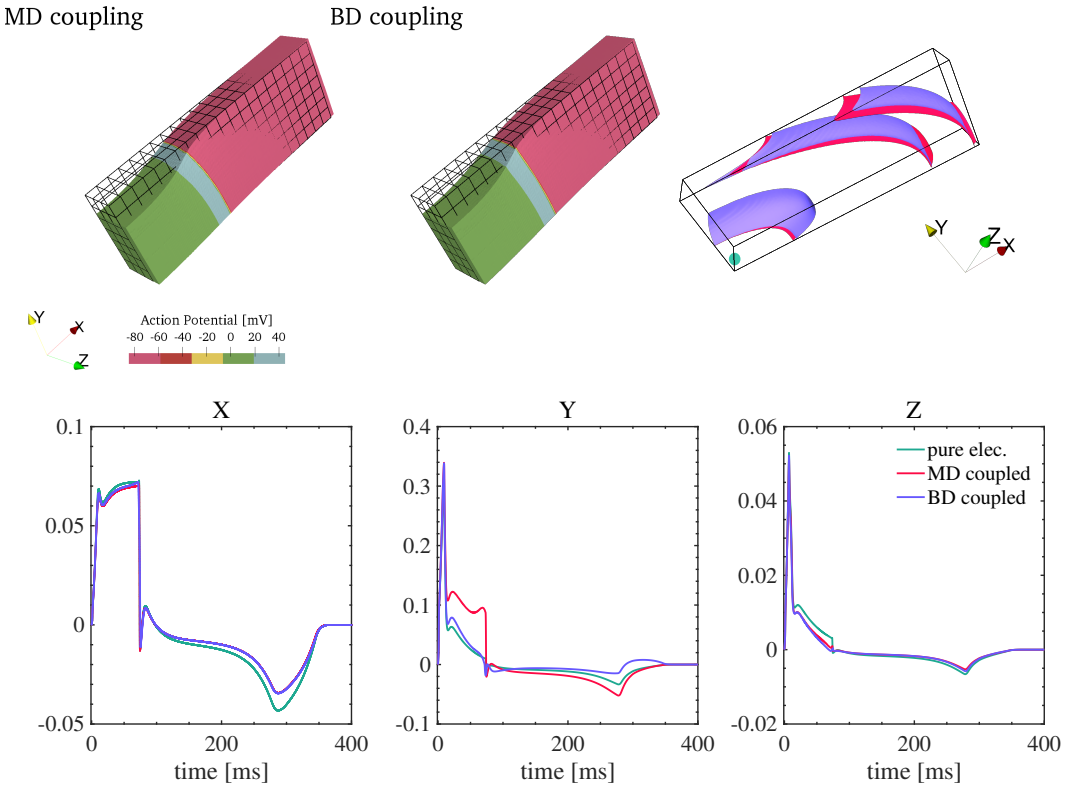

Figure 5.3. Setting 3. Top left: snapshots of the spatial distribution of the action potential from the MD and BD for a slab of tissue with fibers aligned along the y-axis. Configurations are reported 25 ms after applying an electrical stimulus at the location of the green dot. The grid reflects the mechanical mesh of the static configuration. Top right: comparison of zero isopotential surfaces obtained from the MD scenario (red surface) and BD scenario (blue surface) for different time steps (10 ms, 25 ms, 30 ms). In order to compare them, the different activations have been projected on the reference configuration. Bottom: simulated pseudo-ECGs. The three bipolar pseudo-ECGs along the Cartesian axes are shown here. Green, red and blue lines represent results for the pure-electrophysiology approach, the MD approach and BD approach, respectively.

Comments

ECG is usually computed as static process, without considering the mechanical deformation due to the beating heart and breathing. Our results confirm the importance to account for mechanical deformation while simulating the ECG. Moreover, they significantly extend previous knowledge indicating that different ways of coupling electrophysiology and cardiac mechanics may result in different propagation patterns and ECGs. Mechanical changes have been shown to have major effects on potential propagation both at the macroscopic level [Nguyên et al., 2015], depending on the position of the heart in the torso, and at cellular level [Smith et al., 2003b; Dos Santos et al., 2006; Trayanova et al., 2011]. In this study, we focused on the changes in the pseudo-ECG signals due to the different propagation pattern given by the mechanical deformations and due to the changes in the relative distance from the electrodes. The purely electrophysiological, the MD, and the BD coupling approaches of electrophysiology and mechanics had the role to the separate these two effects. The numerical experiments show an impact of mechanics on the T-wave and, under specific circumstances, on the QRS complex as well. At the T-wave, the shortening along the fiber direction has its maximal value, and hence the major differences between the electro-mechanical models and the PE one are noticeable. On the other hand, smaller differences are usually observed between the two electro-mechanical scenarios. This demonstrates that the change in conductivity is mostly a dynamical effect: deformations are slower during repolarization. Also Cluitmans et al. in [Cluitmans et al., 2015] confirmed that the differences in the repolarization phase are mostly due to the difference location of the heart, performing a static comparison of electrograms in systolic and diastolic cardiac geometries. Differences between the MD and BD scenarios, when present, become more relevant at the QRS complex. During the depolarization phase, faster and larger changes occur in the active force and hence in the deformation. The position of the tissue in the ideal torso appears to be counteracted in the BD approach by the effect of deforming myocardium on its conduction velocity. This can be seen observing that the calculated pseudo-ECGs in the BD simulations were closer to those from the PE simulations. Changes in both the QRS complex and the T-wave were observed in [Smith et al., 2003b]. In a two-dimensional comparison between BD and PE they motivated the early T-wave partially by the geometrical changes and partially by phenomena at the cellular level. In our simulations, an altered T-wave both in time and amplitude had been observed but, differently from the previous studies, time shift depends on the geometry and fiber orientation. Actually for the cubic case, reported in Fig. 5.1, the T-wave with mechanics has a larger amplitude while for the tissue slab, reported in Fig. 5.2, an opposite effect was noticeable. Our results confirmed the findings of Smith et al. also concerning the QRS complex. The BD approach is responsible for a larger potential in QRS complex. The MD approach in this cases is responsible also for an early S-wave and for a notch that are in particular visible for the leads located along the propagation direction (see Fig. 5.1 and Fig. 5.3). The expected larger conduction velocities are usually visible on the non-clamped sides of the preparations. On the other sides, PE and MD had a faster velocity. This means that mechanical boundary condition may have a significant impact on the propagation of the activation potential. This effect is mostly challenging in its understanding but, in any case, it suggests that mechanical boundary conditions have to be accurately chosen in fully coupled simulations in order not to introduce disturbance on the propagation, and hence invalidate the results. The use of the MD coupling, and to a lesser extent the BD coupling, resulted in some cases in QRS complexes characterized by a notch that was less visible in the PE simulations. This observation suggests that the occurrence of notches in the QRS complex may in part be related to the effect of deformation. A well-known pseudo-ECG condition, where

notching appears, is left bundle branch block (LBBB). In LBBB, due to a delay (or disruption) of conduction of the left bundle, the right ventricle is activated first and then the activation front spreads from right-to-left through the septum. The typical notching observed in the pseudo-ECG of patients with LBBB, may be due to a slow trans-septal conduction. Our simulations represent a proof of concept of a possible explanation for notching in LBBB. The septum undergoes a complicated paradoxical deformation, often referred to as *septal flash* [Leenders et al., 2012] while the action potential is traveling through it LV. This is similar to pseudo-ECG along fiber direction occurring, for example, reported in Fig. 5.1 and Fig. 5.3. In this simulation, propagation was orthogonal to the fibers, and thus the cube or the slab started to contract before the entire block had been activated. Because of the incompressibility of the material, a contraction in the fiber direction translated into an expansion in the cross-fiber plane, thus introducing a relative motion of the action potential with respect to the electrodes.

Note on choice of the active force

The choice of the active stress parameters, in some cases, led to an unstable behavior of the mechanical solver. This instability generally occurred during the repolarization phase and it was due to a singularity in the linearized mechanical problem. A possible explanation comes from a buckling phenomenon given by active stress model under compression [Ambrosi and Pezzuto, 2012; Augustin et al., 2016]: fibers can exert an active force only under extension. We conducted the same simulation study for the NP model (see Sec. 1.3.1) for the active stress. In this case we considered $k_{T_a} = 30$ kPa, and $\epsilon_0 = \epsilon_\infty = 0.01$ mV^{-1} obtaining, for a single cell, the smooth active stress function reported in Fig. 5.4. The considerations above apply also for the NP model [Favino et al., 2016]. No remarkable differences had arisen for the simulated pseudo-ECG with the NP and the GK activation model. As shown in Fig. 5.4, a delay of approximatively 200 ms is obtained between upstroke of the action potential and the onset of force development considering the NP and the GK activation models for the chosen parameters. For this reason, in simulations involving the complete cardiac geometry we do not expect the mechanical deformation to impact the simulated QRS-complex. However in our simulations, the simplified shape of the considered geometries and the boundary effects damp the outcomes associated to this electromechanical delay in the resulting QRS-complex. Additional simulations on the biventricular geometry would support a more robust understanding of the impact of the mechanical deformation on simulated pseudo-ECG.

Limitations

The model adopted in this study comes with some simplifications: the active force generation is phenomenological and not integrated into the cellular model. Moreover, used fiber orientations were uniform and aligned along one axis of the pseudo-ECG electrodes. Also, the rectangular arrangement of the six pseudo-ECG electrodes and the space they surround are a simplification of the actual shape of a human torso. These simplifications were used in order to more clearly demonstrate the proof of principle of the impact of deformation on the pseudo-ECG. Further investigations are, hence, necessary in order to understand the role of fibers distribution, e.g. employing slabs with non-uniform fiber directions, and of the geometry, e.g. employing a truncated ellipsoids or realistic hearts.

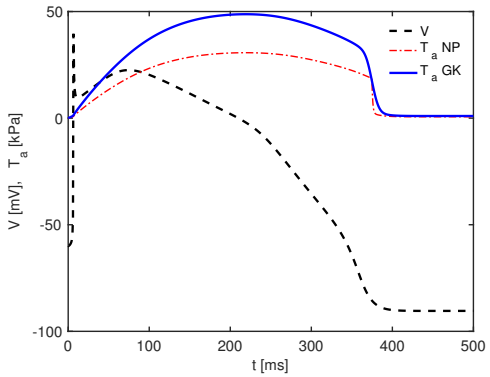

Figure 5.4. Comparison of the Nash Panfilov (NP) and Göktepe and Kuhl (GK) active stress models and action potential considered in the simulation study.

5.2 Simulated patient-specific pV-loop

Goal of this chapter is to study the effect of synchronous and asynchronous activation of the myofibers on the pressure-volumes loops obtained for the ventricular cavities. For this purpose we consider the LMC - FE electromechanical model described in with the closed-loop lumped model of circulation (LMC). In the LMC - FE incompressible elasticity coupled model, we consider the Guccione-Costa constitutive law [Guccione et al., 1995] described in Sec. 1.1.8. The constitutive parameters for the incompressible elasticity model are taken from [Land et al., 2015a] and reported in Tab. 5.1. Additionally, Tab. 5.1 reports the parameters for the Eikonal-diffusion model described in Sec. 1.2.13.

The novelty of our work is represented by the study of the effects of asynchronous activation of the myofibers on the pressure-volumes loops obtained for the ventricular cavities. In the LMC originally proposed by Kerckhoffs et al. [Kerckhoffs et al., 2007], synchronous activation of ventricular cardiac cells is considered in which the ventricular chambers are described as 0D variables. Coupling the LMC with the FE electromechanical model we consider different synchronous and asynchronous experimental setups. In asynchronous settings, the cellular start time of first active ventricular contraction t_{active} is shifted by the simulated electrical activation time ψ, i.e. we consider

$$t_{\text{active,AT}}(\mathbf{x}) = t_{\text{active}} + \psi(\mathbf{x}). \tag{5.1}$$

ATs are computed considering the reduced Eikonal-diffusion model described Sec. 1.2.13. In detail, we consider

setting 1: synchronous mechanical activation of myocardial cell, i.e. t_{active} to constant on $\mathscr{B}_r$.

setting 2: asynchronous mechanical activation of myocardial cells, with activation delay prescribed by the Eikonal-diffusion model with early activated site represented by a group of cells located in the ventricular septal (represented by a blue region in Fig. 5.5).

setting 3: asynchronous, mechanical activation of myocardial cells, with delay prescribed by the Eikonal-diffusion model with as early activated site 18 groups of cells representing the termination of Purkinje fibers (represented by a blue regions in Fig. 5.6). Nine groups of cells are located in the LV and nine in the RV.

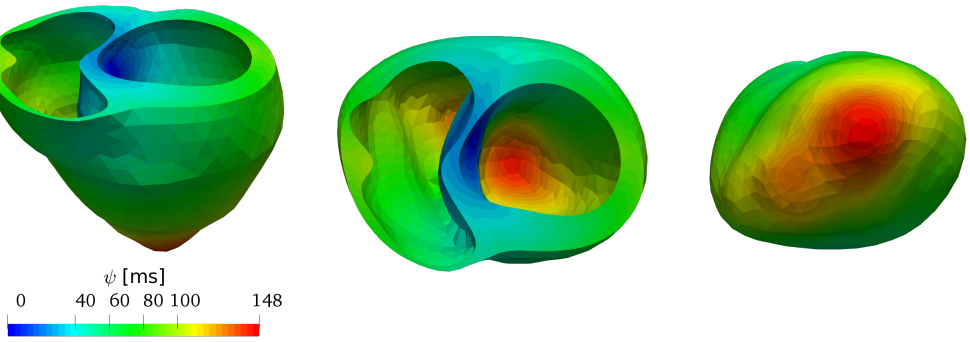

Figure 5.5. Activation times ψ in milliseconds obtained with the reduced Eikonal-diffusion model in anterior (left), top (center) and bottom (right) views. The early activated site is represented by a group of cells (here represented by the blue area of the domain) located in the ventricular septal.

First row of Fig. 5.7 shows the four chambers volumes (left) and pressures (right) obtained for the canine LMC [Kerckhoffs et al., 2007]. Second row of Fig. 5.7 shows the pV-loops for the left (left) and right (center) ventricular cavities and the trigonometric functions (right) controlling the mechanical activation of the atrium and ventricles. In case the biventricular geometry is considered, circulation parameters such as the total blood volume and suitable initial conditions for the pure LMC have to be determined. In this case, data for the different circulatory segments have been estimated from magnetic resonance imaging (MRI) of the ventricular cavities considering the frame after mitral valve closure (MVC) taking into account epidemiologic data. Volumetric and time parameters have been scaled accordingly to the biventricular geometry and the human basic cycle length. Considered parameters and initial conditions for the patient-specific LMC are reported in Tab. 5.1. First row of Fig. 5.8 shows the four chambers volumes (left panel) and pressures (right panel) obtained with the Kerckhoffs et al. LMC with the parameters tuned for the biventricular geometry. Second row of Fig. 5.8 shows the pV-loops for the left (left) and right (center) ventricular cavities and the trigonometric functions (right) controlling the mechanical activation of the atrium and ventricles. Independent on mechanical deformation of the geometry, the Eikonal-diffusion model was first solved with the Newton's method. The solution was computed on the FE anatomical biventricular geometry discretized considering ≈820k tetrahedral elements and then interpolated on a coarser grid of ≈102k elements. Incompressible elasticity is then solved with the Newton's method on the coarser grid. As a non-linear convergence criteria we considered the absolute tolerance of tol =1e-10. The system arising from the linearization of the Eikonal-diffusion model and of the mechanical equations were solved with a direct solver (MUMPS of the PETSc suite [Balay et al., 2017]).

5.2.1 Numerical results

In this section, we compare the numerical results obtained for the three numerical setting described above in terms of resulting pV-loops and ventricular ejection fraction (EF). In Fig. 5.9 snapshots of the displacement for the simulated pV-loops for the setting 1 are reported. In detail,

Equation	Symbol	Quantity	Canine geometry geometry	Biventricular geometry
Circulation	V_{tot}	total blood	1.7 l	4.4 l
lumped model	V_{LA}	volume of left atrium	37.3 ml	39.0 ml
	V_{LV}	volume of left ventricle	45.4 ml	84.61 ml
	V_{as}	volume of systemic arteries and capillares	352 ml	900 ml
	V_{vs}	volume of systemic veins	1040 ml	2700 ml
	V_{RA}	volume of right atrium	35 ml	32 ml
	V_{RV}	volume of right ventricle	34.7 ml	48.56 ml
	V_{ap}	volume of pulmonic arteries and capillaries	84.9 ml	245 ml
	V_{pv}	volume of pulmonic veins	93 ml	245 ml
	t_{active}	start time of first ventricular contraction	200 ms	200 ms
	t_{cycle}	basic cycle length	600 ms	1100 ms
	t_{twitch}	duration of ventricular twitch	300 ms	400 ms
Incompressible	mu		-	2.0kPa
elasticity	bf		-	8.0
	bt		-	2.0
	bfs		-	4.0
Eikonal model	χ	surface to volume ratio	-	1440 cm^{-1}
	c_0	diffusivity parameter	-	0.03 μ $\mathrm{F}^{-1}\mathrm{cm}^{3}$
	θ		-	3.5 cm ms^{-1} $\mathrm{mS}^{-\frac{1}{2}}$

Table 5.1. Simulated pV-loop: parameters calibration for the canine and the biventricular geometry.

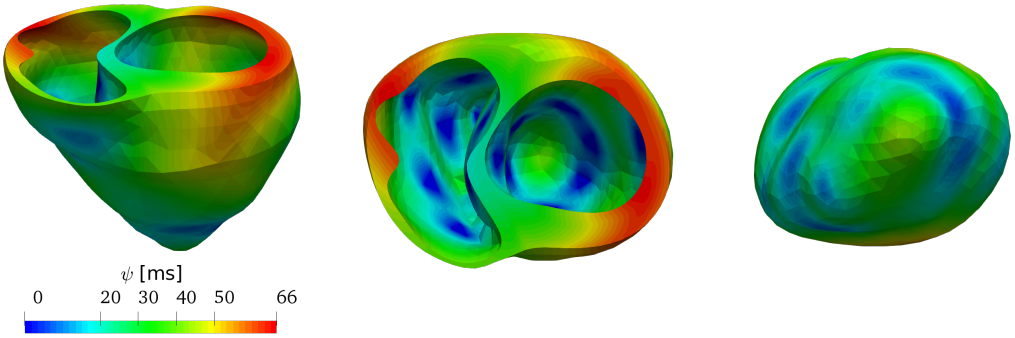

Figure 5.6. Activation times ψ in milliseconds obtained with the reduced Eikonal-diffusion model in anterior (left), top (center) and bottom (right) views. The set of early activated sites (here represented by the blue areas of the domain) represent the cells located close to the terminations of Purkinje fibers.

unloaded geometry at $t = 0$ ms is reported in the top left corner of the figure. For the first heartbeat the first 200 ms of the simulation are devoted to a preload of the geometry, representing the ventricular filling phase. The loaded geometry at time $t = 200$ ms is reported in the top right corner of Fig. 5.9. Second row of Fig. 5.9 reports the deformed geometry at $t = 400$ ms (left) and $t = 600$ ms (right). Fig. 5.10 reports the obtained results for the three different settings for the LMC - FE electromechanical model with parameters tuned for the biventricular geometry. In detail, first row of the figure shows the ventricular (solid line) and atrial (dashed line) volumes. Second row of the figure reports the obtained ventricular pressure for the left (left) and for the right (right) ventricular cavities. Third row of the figure shows the pV-loops for the left (left) and right (center) ventricular cavities. For all the considered settings, the simulated ventricular pressure underestimate normal hemodynamic parameters. Tab. 5.2 reports for the 10th beat for the three different settings, the end-diastolic pressure (EDP), the end-diastolic volume (EDV), the peak pressure (P_{max}), the end-systolic pressure (ESP), the stroke volumes (SV) and the ejection fraction EF. The ventricular EF is expressed as the ratio of the ventricular stroke volume (SV) to the ventricular end-diastolic volume (EDV). SV is obtained by subtracting the ventricular end-systolic volume (ESV) from EDV. Therefore, EF is calculated as

$$\mathrm{EF} = \frac{\mathrm{EDV} - \mathrm{ESV}}{\mathrm{EDV}} \times 100(\%). \tag{5.2}$$

EF for setting 2 is smaller than the one for setting 1 in the percentage of the 2.3% for the LV and of the 1% for the RV. EF for setting 3 is smaller than the one for setting 1 in the percentage of the 0.8% for the LV and of the 0.2% for the RV. If compared to setting 1, setting 2 results in a delay of the 39% in time for the achievement of the pressure peak value and setting 3 in a delay of the 17%. Moreover asynchronous settings result in variations of the peak pressures. In detail, setting 2 results in a decrease of the 2.7% for the LV and of the 4.8% for the RV and setting 3 results 0.8% for the LV and of the 2.9% for the RV.

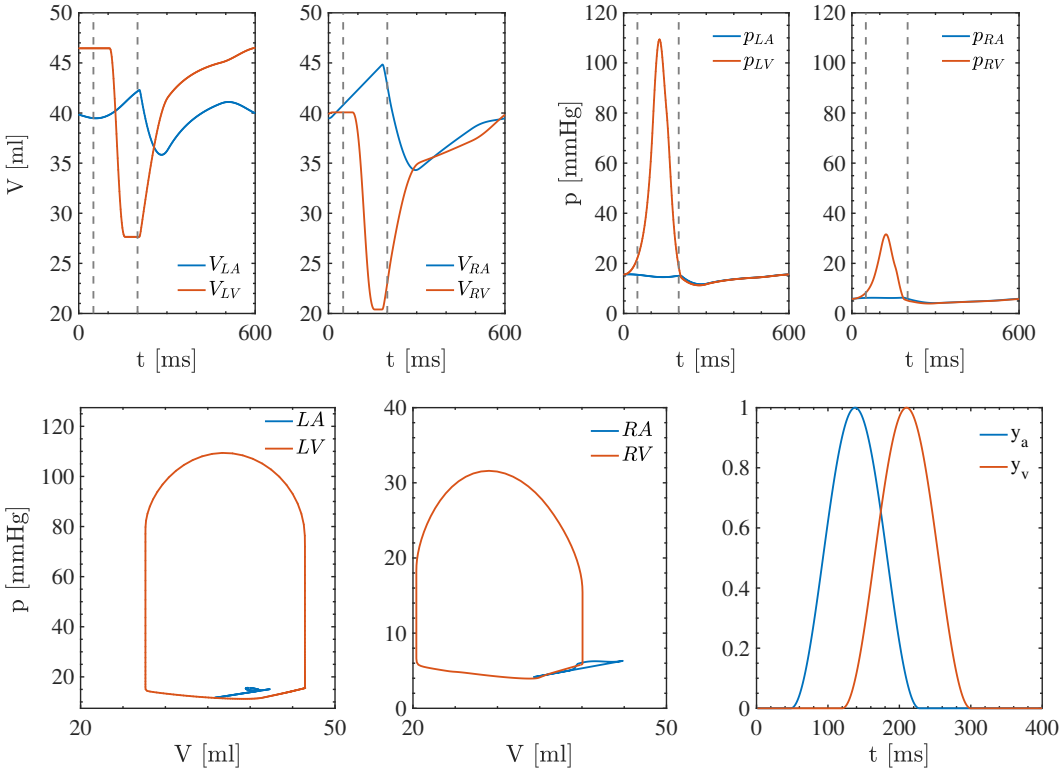

Figure 5.7. LMC canine model: first row: four chambers volumes (left) and cavity pressures (right) obtained with the LMC [Kerckhoffs et al., 2007]. Second row: pV-loops for the left (right) and right (center) ventricular cavities and (right) the trigonometric functions y_a and y_v controlling the elastances of the atria and ventricles, respectively.

Limitations

Parameters of the compliance matrix have been obtained rescaling the ones of the LMC by the ratio between the unloaded volumes of the biventricular and of the canine geometry. Entries of the matrix should be obtained from the non-linear pressure-volumes relationships and as a qualification of direct ventricular interaction for the FE mechanical model. Obtained results demonstrate the proof of principle of the impact of the asynchronous activation of the cardiac tissue on the simulated pV-loops. Limitations of this work include that the proposed study has be performed on a single patient-specific case. Moreover, as discussed for the test case presented in Sec. 5.1, in the model adopted the active force generation is phenomenological. The LMC - FE electromechanical model proposed involves the computation of the electrical activation times considering the reduced Eikonal-diffusion model. As a further investigation the LMC could be coupled to the fully coupled 3D electromechanical model in which the propagation of the AP is computed on the deformed geometry.

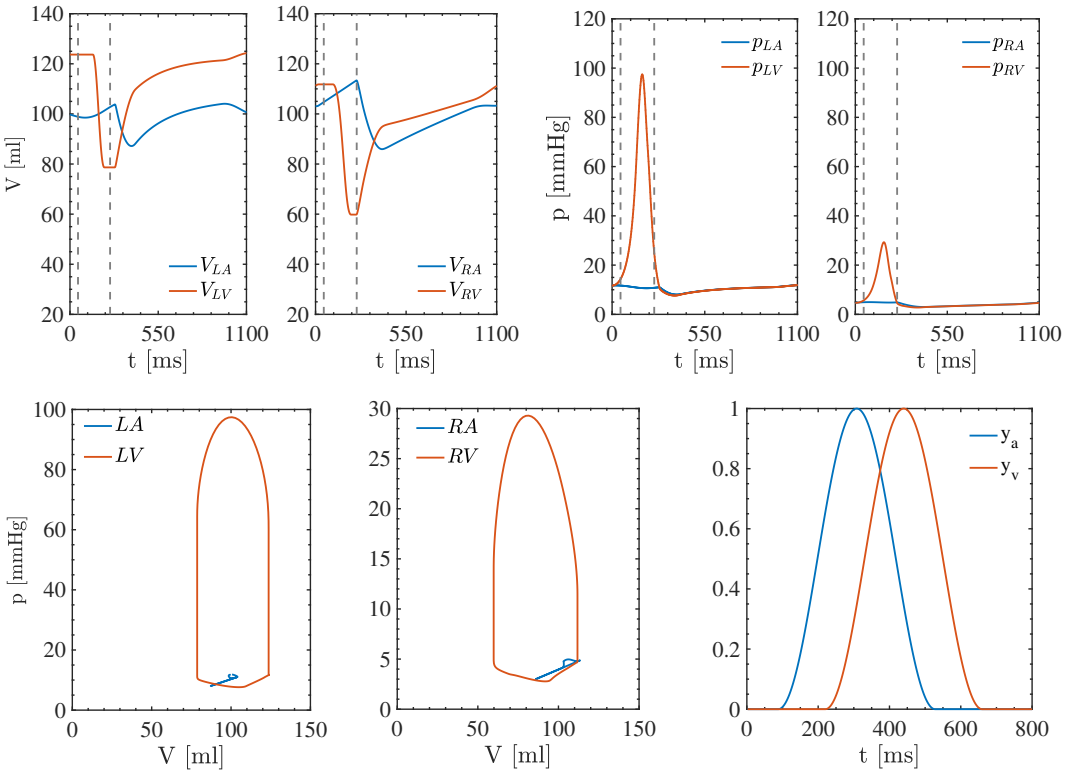

Figure 5.8. LMC patient-specific model: first row: four chambers volumes (left) and cavity pressures (right) obtained with the LMC [Kerckhoffs et al., 2007] with the parameters tuned for the biventricular geometry. Second row: pV-loops for the left (right) and right (center) ventricular cavities and (right) the trigonometric functions y_a and y_v controlling the elastances of the atria and ventricles, respectively.

		Setting 1		Setting 2		Setting 3	
		LV	RV	LV	RV	LV	RV
EDP	[mmHg]	12.67	8.33	12.94	8.14	12.74	8.26
EDV	[ml]	163.13	101.78	164.18	101.69	163.43	101.77
P_{max}	[kPa]	69.13	22.15	67.26	23.23	68.57	21.50
ESP	[mmHg]	58.51	13.81	57.96	13.60	58.05	14.05
SV	[ml]	67.59	70.60	66.41	69.82	67.15	70.40
EF	[%]	41.44	69.37	40.45	68.67	41.09	69.17

Table 5.2. The 10th beat for the three different settings, EDP, end-diastolic pressure; EDV, end-diastolic volume; P_{max}, peak pressure; ESP, end-systolic pressure; SV, stroke volumes; EF, ejection fraction.

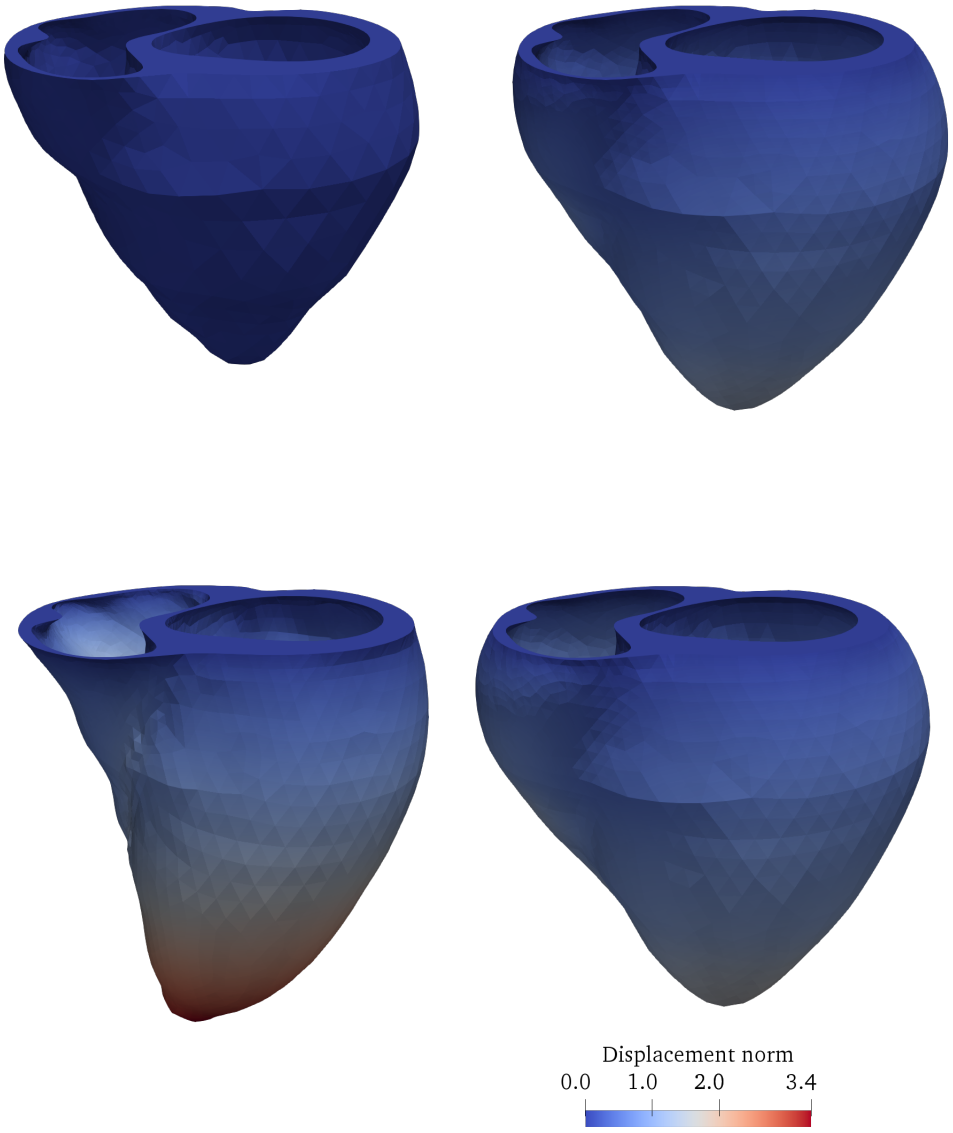

Figure 5.9. LMC - FE electromechanical patient-specific model: snapshots of the displacement for the simulated pV-loops at time $t = 0$ ms (top left), $t = 200$ ms (top right), $t = 400$ ms (bottom left) and $t = 600$ ms (bottom right). Results for setting 1 are reported.

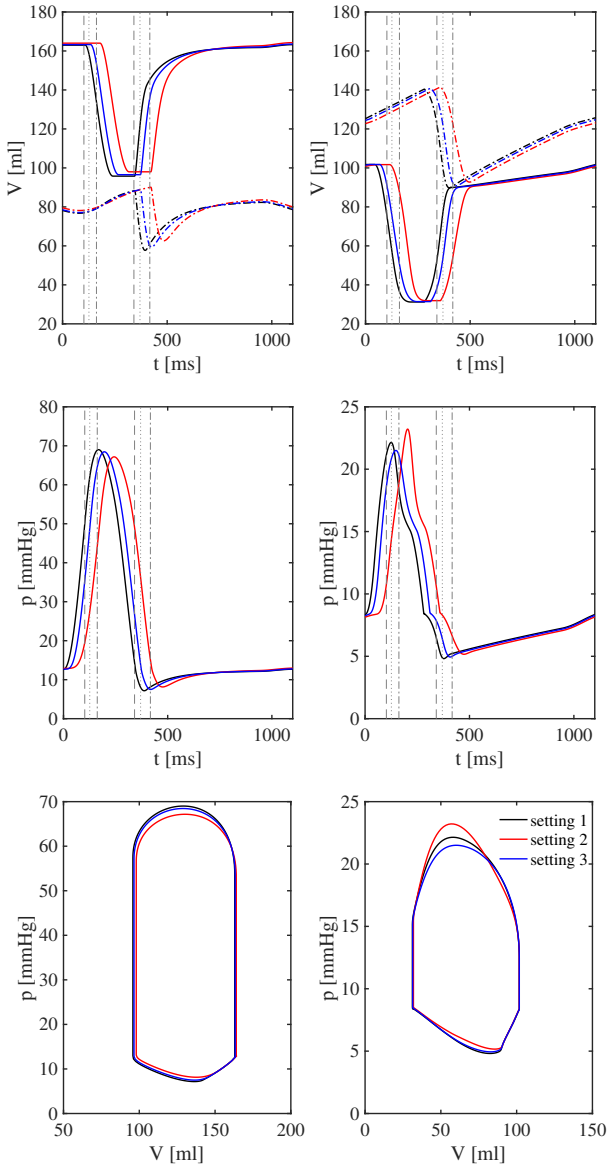

Figure 5.10. LMC - FE electromechanical patient-specific model: first row: left ventricle and left atrium (dashed) volumes (left) and right ventricle and right atrium (dashed) volumes (right). Second row: left ventricular pressure (left) and right ventricular pressure (right). Thirs row: pV-loops for the left (right) and right (center) ventricular cavities. Results are reported for the three different settings for $\tau = 2$ms.

Final remarks

In this work, we developed discretization and solution methods for the simulation of a fully-coupled electromechanical model of the heart. We presented high-order schemes for time integration of the monodomain system based on an extension of the well-known Rush-Larsen scheme. Moreover, we presented a novel segregated solution strategy for the saddle-point system arising from the discretization of the equations of incompressible nonlinear elasticity.
The main novel results of this work can be summarized as follow.

- The Rush-Larsen scheme for the integration of the monodomain equation has been reinterpreted as an exponential integrator. Hence, by generalizing this latter, we developed high-order exponential schemes for the time integration of the gating variables. The developed schemes have been coupled with high-order backward differentiation methods for the time integration of the reaction-diffusion equation. An additional contribution comes from a novel quasi-Newton method for the implicit discretization of the monodomain equation based on the specific form of the ionic currents. As an alternative, we also proposed to evaluation of the complicated Jacobian by means of a complex step differentiation technique.

- We developed an efficient solution strategy for the solution of the linear system with a saddle-point structure arising from the finite element discretization of the tangent problem in the simulation of incompressible nonlinear elasticity. In details, to increase the minimum eigenvalue of the elasticity operator in the tangent problem, we considered and compared two penalty volumetric terms: a linear and a nonlinear augmenting strategies. This allows to remove the possible singularity in the elasticity block and hence makes possible to use segregated approaches to solve the augmented linear system. This approach corresponds to the solution of the Schur complement of the augmented system, for which a mass matrix was used as a preconditioner. Two multigrid preconditioners have been used to solve the Schur complement associated: one for the elasticity operator and one for the mass matrix preconditioner. A particular choice in our multigrid strategy was the use of a GMRES solver as a smoother. We have also investigated the effect of the augmenting parameters in the convergence and the optimality of the proposed multigrid strategy with respect to the mesh-size and number of multigrid levels. With these choices the linear solver converged with a fixed number of Newton iterations and demonstrated good scalability properties. We showed the stability of the linear and nonlinear solution methods for a purely passive response of the material and the weak dependence of the solver on the active contribution to the elastic response.

We considered the following applications of the coupled electromechanical model:

- We studied the impact of geometrical changes on the electrical activation front and of the change of distance from the electrodes during the cardiac cycle on simulated electrocardiograms. The study of three different coupling scenarios (defined as purely electrophysiological, mono-directional and bi-directional electromechanical coupling strategies) allowed us to show the impact of mechanical deformation on simulated pseudo-ECGs.
- The developed finite element electromechanical model was coupled to a lumped model of circulation. This allowed us to simulate complete cardiac cycles and, as a result, to obtain pressure-volume loops in a patient-specific setting. In the simulated pressure-volumes loops, we highlighted significant differences arising from synchronous and asynchronous mechanical activation of the cardiac muscle.

Finally, we point out the following future research.

- High-order time integration schemes should be extended to deal with discontinuous descriptions of the behavior of the gating variables. High-order integration schemes lead to an accurate solution of equation governing electrophysiology. However, the requirement of small time steps does not allow to fully exploit high-order strategies to reduce the computational time needed for the solution of the monodomain system. This is due to stiffness of the gating variables. For this reason, high-order time integration schemes should be coupled to adaptive time integration schemes.
- In the solver for the equations describing of incompressible behavior of the tissue, I employed the GMRES solver as a smoother. Other more efficient smoothers should be investigated.
- At the price of the development of appropriately fitted block-element smoothers, coupled solvers for the equations arising in cardiac mechanics should be considered.
- An extension to the model should be performed: in the model adopted the active force generated is not integrated into the cellular model.
- Parameters of the compliance matrix for the finite element electromechanical model coupled with the lumped model of circulation should be computed from the nonlinear pressure-volume relationships. The proposed model involved the computation of the electrical activation times considering the reduced Eikonal-diffusion model. As a further investigation the considered lumped model of circulation should be coupled to the fully coupled electromechanical FE model in which the AP is computed on the deformed geometry.
- In the study of the impact of geometric changes due to mechanical deformation of the tissue on simulated electrocardiograms, fiber orientations were considered to be uniform and aligned along one axis of the pseudo-ECG electrodes. To understand the role of fiber distribution, the results for the patient-specific geometry should be investigated.

Publications

M. Favino, S. Pozzi, S. Pezzuto, F. W. Prinzen, A. Auricchio, and R. Krause. **Impact of mechanical deformation on pseudo-ecg: a simulation study.** EP Europace, 18(suppl_4):iv77-iv84, 2016.

S. Pozzi, M. Favino, R. Krause. **Segregated Multigrid Methods for Incompressible Nonlinear Elasticity with Application to Cardiac Mechanics** submitted in International Journal for Numerical Methods in Biomedical Engineering

S. Pozzi, M. Favino, R. Krause. **Backward Differentiation Strategies in Cardiac Electrophysiology** in preparation

S. Pozzi, M. Favino, R. Krause. **Higher-order integrators for the cell membrane equations and the mono-domain system in cardiac electrophysiology** in preparation

Talks and Posters

05.06.2016 **Fully Coupled Solution Strategies for Electro - Mechanics in the Heart**
Eccomas, Crete, GR
Person involved: Prof. Rolf Krause & Marco Favino
Link: www.eccomas2016.org

04.22.2016 **Numerical Strategies for Saddle Point Formulation in Cardiology**
Colloque Numerique Suisse, Fribourg, CH
Person involved: Prof. Rolf Krause & Marco Favino
Link: http://math.unifr.ch/colloqnum2016/history.php

05.29.2015 **A New Reduced Dual Basis Approach for Parametrized Contact Problem in Elasticity**. ICCM15, Hannover, DE
Person involved: Prof. Rolf Krause & Marco Favino

07.20.2014 **A lightweight approach to parallel adaptivity in electrophysiology**
WCCM XI, ECCM V, Barcelona, ES
Person involved: Prof. Rolf Krause & Dorian Krause
Link: http://congress.cimne.com/iacm-eccomas2014

06.13.2018 **Multigrid augmented Lagrangian preconditioners for incompressible cardiac mechanics**. ECCM -ECDF 2018
Person involved: Prof. Rolf Krause & Marco Favino

28.04.2017 Poster: **Higher Order Exponential Time Integrators in Cardiac Electrophysiology**. Colloque Numerique Suisse, Basel, CH
Person involved: Prof. Rolf Krause & Marco Favino
Link: https://colloqnum17.dmi.unibas.ch/en/

06.12.2016 Poster: **Fully Coupled Staggered and Monolithic Approaches**
8th TRM Forum on Computer Simulation and Experimental Assessment of Cardiac Function. USI, Lugano, CH Link: http://trm-forum.ics.usi.ch/

Bibliography

D. Ambrosi and S. Pezzuto. Active stress vs. active strain in mechanobiology: constitutive issues. *Journal of Elasticity*, 107(2):199–212, 2012.

D. Ambrosi, A. Quarteroni, and G. Rozza. *Modeling of physiological flows*, volume 5. Springer Science & Business Media, 2012.

H. Arce, A. Xu, H. Gonzalez, and M. Guevara. Alternans and higher-order rhythms in an ionic model of a sheet of ischemic ventricular muscle. *Chaos 10*, pages 411–426, 2000.

C. M. Armstrong and F. Bezanilla. Inactivation of the sodium channel. ii. gating current experiments. *The Journal of general physiology*, 70(5):567–590, 1977.

C. M. Augustin, A. Neic, M. Liebmann, A. J. Prassl, S. A. Niederer, G. Haase, and G. Plank. Anatomically accurate high resolution modeling of human whole heart electromechanics: a strongly scalable algebraic multigrid solver method for nonlinear deformation. *Journal of computational physics,*, 305:pp. 622–646, 2016.

C. Bacuta. A unified approach for uzawa algorithms. *SIAM Journal on Numerical Analysis*, 44(6): 2633–2649, 2006.

C. Bacuta and L. Shu. Multilevel gradient uzawa algorithms for symmetric saddle point problems. *Journal of Scientific Computing*, 57(1):105–123, 2013.

S. Balay, S. Abhyankar, M. Adams, J. Brown, P. Brune, K. Buschelman, L. Dalcin, V. Eijkhout, W. Gropp, D. Kaushik, et al. Petsc users manual revision 3.8. Technical report, Argonne National Lab., Argonne, IL, 2017.

P. Balbi, P. Massobrio, and J. Hellgren Kotaleski. A single markov-type kinetic model accounting for the macroscopic currents of all human voltage-gated sodium channel isoforms. *PLOS Computational Biology*, 13(9):1–29, 09 2017. doi: 10.1371/journal.pcbi.1005737. URL `https://doi.org/10.1371/journal.pcbi.1005737`.

J. M. Ball. Convexity conditions and existence theorems in nonlinear elasticity. *Archive for Rational Mechanics and Analysis*, 63(4):337–403, 1976. ISSN 0003-9527. doi: 10.1007/BF00279992. URL `http://dx.doi.org/10.1007/BF00279992`.

O. Barnich and M. Van Droogenbroeck. Vibe: A universal background subtraction algorithm for video sequences. *IEEE Transactions on Image processing*, 20(6):1709–1724, 2011.

J. Bayer, A. J. Prassl, A. Pashaei, J. F. Gomez, A. Frontera, A. Neic, G. Plank, and E. J. Vigmond. Universal ventricular coordinates: A generic framework for describing position within the heart and transferring data. *Medical image analysis*, 45:83–93, 2018.

G. Beeler and H. Reuter. Reconstruction of the action potential of ventricular myocardial fibres. *J Physiol.*, 268(1):177–210, 1977 Jun.

M. Benzi and J. Liu. Block preconditioning for saddle point systems with indefinite (1, 1) block. *International Journal of Computer Mathematics*, 84(8):pp. 1117–1129, 2007.

M. Benzi and M. A. Olshanskii. An augmented lagrangian-based approach to the oseen problem. *SIAM Journal on Scientific Computing*, 28(6):2095–2113, 2006.

M. Benzi and M. Tuma. A comparative study of sparse approximate inverse preconditioners. *Applied Numerical Mathematics*, 30(2-3):305–340, 1999.

M. Benzi, G. H. Golub, and J. Liesen. Numerical solution of saddle point problems. *Acta numerica*, 14:pp. 1–137, 2005.

C. Bernardi, Y. Maday, and F. Rapetti. Basics and some applications of the mortar element method. *GAMM-Mitteilungen*, 28(2):97–123, 2005.

O. Bernus and R. W. et al. A computationally efficient electrophysiological model of human ventricular cells. *Am J. Physiol. - Heart C.*, 282 (6):H2296–H2308, 2002.

G. Beylkin, J. M. Keiser, and L. Vozovoi. A new class of time discretization schemes for the solution of nonlinear pdes. *J. Comput. Phys.*, 147:362–387, 1998.

Blender Online Community. *Blender - a 3D modelling and rendering package*. Blender Foundation, Blender Institute, Amsterdam. URL `http://www.blender.org`.

D. Bonet, J.and Wood. *Nonlinear continuum mechanics for finite element analysis*. Cambridge, 2 edition, 2008.

J. Bonet and R. D. Wood. *Nonlinear continuum mechanics for finite element analysis*. Cambridge university press, 1997.

R. Bordas, B. Carpentieri, et al. Simulation of cardiac electrophysiology on next- generation high-performance computers. *Philios. T. Roy. Soc. A*, 367 (1895):1951–1969, 2009.

J. P. Boyd. Chebyshev and fourier spectral methods. *Dover, New York*, pages 203 (1):72–88, 2001.

D. Braess. *Finite Elements : Theory, Fast Solvers, and Applications in Solid Mechanics*. Cambridge University Press, 2009. ISBN 9780521588348. URL `http://www.worldcat.org/isbn/9780521588348`.

F. Brezzi and M. Fortin. *Mixed and Hybrid Finite Element Methods*. Springer-Verlag, Berlin, Heidelberg, 1991. ISBN 0-387-97582-9.

A. Bueno-Orovio, E. M. Cherry, and F. H. Fenton. Minimal model for human ventricular action potentials in tissue. *Journal of theoretical biology*, 253(3):544–560, 2008.

J. O. Campos, R. Weber dos Santos, J. Sundnes, and B. M. Rocha. Preconditioned augmented lagrangian formulation for nearly incompressible cardiac mechanics. *International journal for numerical methods in biomedical engineering*, 34(4):e2948, 2018.

R. S. Campos, F. O. Campos, J. Gomes, C. de Barros Barbosa, M. Lobosco, and R. Dos Santos. Comparing high performance techniques for the automatic generation of efficient solvers of cardiac cell models. *Computing*, 95(1):pp. 639–660, 2013a.

R. S. Campos, F. O. Campos, J. M. Gomes, C. de Barros Barbosa, M. Lobosco, and R. W. Dos Santos. Comparing high performance techniques for the automatic generation of efficient solvers of cardiac cell models. *Computing*, 95(1):639–660, 2013b.

R. Chadwick. Mechanics of the left ventricle. *Biophysical journal*, 39(3):279–288, 1982.

C. Cherubini, S. Filippi, P. Nardinocchi, and L. Teresi. An electromechanical model of cardiac tissue: Constitutive issues and electrophysiological effects. *Progress in biophysics and molecular biology*, 97(2-3):562–573, 2008.

Y. J. Choi, J. Constantino, V. Vedula, N. Trayanova, and R. Mittal. A new mri-based model of heart function with coupled hemodynamics and application to normal and diseased canine left ventricles. *Frontiers in bioengineering and biotechnology*, 3:140, 2015.

R. H. Clayton. Models of cardiac tissue electrophysiology: progress, challenges and open questions. *Prog. Biophys. Mol. Biol.*, pages 104:22–48, 2011.

M. J. M. Cluitmans, R. Peeters, R. Westra, and P. Volders. Noninvasive reconstruction of cardiac electrical activity: update on current methods, applications and challenges. *Netherlands Heart Journal*, 23(6):301–311, 2015.

P. Colli Franzone and L. Guerri. Spreading of excitation in 3-d models of the anisotropic cardiac tissue. i. validation of the eikonal model. *Mathematical biosciences*, 113(2):145–209, 1993.

P. Colli Franzone and L. F. Pavarino. A parallel solver for reaction–diffusion systems in computational electrocardiology. *Mathematical models and methods in applied sciences*, 14(06): 883–911, 2004.

P. Colli Franzone, L. Guerri, M. Pennacchio, and B. Taccardi. Spread of excitation in 3-d models of the anisotropic cardiac tissue. ii. effects of fiber architecture and ventricular geometry. *Mathematical Biosciences*, 147(2):131–171, 1998.

P. Colli Franzone, L. F. Pavarino, and S. Scacchi. Mathematical and numerical methods for reaction-diffusion models in electrocardiology. In *Modeling of Physiological flows*, pages 107–141. Springer, 2012.

P. Colli Franzone, L. F. Pavarino, and S. Scacchi. *Mathematical Cardiac Electrophysiology*. Springer International Publishing, 1 edition, 2014. ISBN 978-3-319-04800-0,978-3-319-04801-7. URL `http://gen.lib.rus.ec/book/index.php?md5=327854feefb21815d0ce6de14c8ac600`.

P. Colli Franzone, L. F. Pavarino, and S. Scacchi. Parallel multilevel solvers for the cardiac electromechanical coupling. *Applied Numerical Mathematics*, 95:pp. 140–153, 2015.

P. Colli Franzone, L. F. Pavarino, and S. Scacchi. Bioelectrical effects of mechanical feedbacks in a strongly coupled cardiac electro-mechanical model. *Mathematical Models and Methods in Applied Sciences*, 26(01):27–57, 2016.

P. Colli Franzone, L. F. Pavarino, and S. Scacchi. Effects of mechanical feedback on the stability of cardiac scroll waves: A bidomain electro-mechanical simulation study. *Chaos: An Interdisciplinary Journal of Nonlinear Science*, 27:093905, 09 2017. doi: 10.1063/1.4999465.

P. Colli Franzone, L. F. Pavarino, and S. Scacchi. A numerical study of scalable cardiac electromechanical solvers on hpc architectures. *Frontiers in physiology*, 9:268, 2018.

C. Conti, E. Votta, C. Corsi, D. De Marchi, G. Tarroni, M. Stevanella, M. Lombardi, O. Parodi, E. Caiani, and A. Redaelli. Left ventricular modelling: a quantitative functional assessment tool based on cardiac magnetic resonance imaging. *Interface focus*, 1(3):384–395, 2011.

K. D. Costa, P. J. Hunter, J. Rogers, J. M. Guccione, L. Waldman, and A. D. McCulloch. A three-dimensional finite element method for large elastic deformations of ventricular myocardium: IâĂŤcylindrical and spherical polar coordinates. *Journal of biomechanical engineering*, 118(4): pp. 452–463, 1996.

K. D. Costa, J. W. Holmes, and A. D. McCulloch. Modelling cardiac mechanical properties in three dimensions. *Philosophical Transactions of the Royal Society of London A: Mathematical, Physical and Engineering Sciences*, 359(1783):1233–1250, 2001.

S. M. Cox and P. C. Matthews. Exponential time differencing for stiff systems. *J. Comput. Phys.*, pages 176 (2):430–4557, 2002.

B. De Oliveira, B. Rocha, L. Barra, E. Toledo, J. Sundnes, and R. Weber dos Santos. Effects of deformation on transmural dispersion of repolarization using in silico models of human left ventricular wedge. *International journal for numerical methods in biomedical engineering*, 29 (12):1323–1337, 2013.

H. Demiray. Stresses in ventricular wall. *Journal of Applied Mechanics*, 43(2):194–197, 1976.

S. Dokos, B. H. Smaill, A. A. Young, and I. J. LeGrice. Shear properties of passive ventricular myocardium. *American Journal of Physiology-Heart and Circulatory Physiology*, 283(6):H2650–H2659, 2002.

R. W. Dos Santos, F. Otaviano Campos, L. Neumann Ciuffo, A. Nygren, W. Giles, and H. Koch. Atx-ii effects on the apparent location of m cells in a computational model of a human left ventricular wedge. *Journal of cardiovascular electrophysiology*, 17:S86–S95, 2006.

A. El Maliki, M. Fortin, N. Tardieu, and A. Fortin. Iterative solvers for 3d linear and nonlinear elasticity problems: Displacement and mixed formulations. *International Journal for Numerical Methods in Engineering*, 83(13):1780–1802, 2010.

H. Elman, V. E. Howle, J. Shadid, R. Shuttleworth, and R. Tuminaro. Block preconditioners based on approximate commutators. *SIAM Journal on Scientific Computing*, 27(5):1651–1668, 2006.

H. C. Elman, D. J. Silvester, and A. J. Wathen. *Finite elements and fast iterative solvers: with applications in incompressible fluid dynamics*. Numerical Mathematics and Scientific Computation, 2014.

L. Endresen and N. Skarland. Limit cycle oscillations in pacemaker cells. *IEEE Trans. Biomed. Eng.*, vol 47: 1134-1137, 2000.

T. S. Eriksson, A. Prassl, G. Plank, and G. A. Holzapfel. Influence of myocardial fiber/sheet orientations on left ventricular mechanical contraction. *Mathematics and Mechanics of Solids*, 18(6):592–606, 2013.

M. Ethier and Y. Bourgault. Semi-implicit time-discretization schemes for the bidomain model. *SIAM J. Numer. Anal*, 46:2443–2468, 2008a.

M. Ethier and Y. Bourgault. Semi-implicit time-discretization schemes for the bidomain model. 46(5):2443–2468, 2008b.

M. Favino, S. Pozzi, S. Pezzuto, F. W. Prinzen, A. Auricchio, and R. Krause. Impact of mechanical deformation on pseudo-ecg: a simulation study. *EP Europace*, 18(suppl_4):iv77–iv84, 2016.

F. Fenton and A. Karma. Vortex dynamics in three-dimensional continuous myocardium with fiber rotation: Filament instability and fibrillation. *Chaos: An Interdisciplinary Journal of Nonlinear Science*, 8(1):20–47, 1998.

F. Fenton, A. B. Orovio, E. Cherry, and S. Evans. Basis for the induction of phase-two reentry in the brugada syndrome: Insights from computer simulations. *Circulation*, 105:1208–1213, 2002.

F. H. Fenton. *Theoretical investigation of spiral and scroll wave instabilities underlying cardiac fibrillation: a dissertation*. PhD thesis, Northeastern University, 1999.

M. Fortin and R. Glowinski. *Augmented Lagrangian methods: applications to the numerical solution of boundary-value problems*, volume 15. Elsevier, 2000.

P. C. Franzone and L. Pavarino. A parallel solver for reaction-diffusion systems in computational electrocardiology. *Math. Models Methods Appl. Sci.*, 14:883–911, 2004.

P. C. Franzone, P. Deuflhard, B. Erdmann, and J. L. L. F. Pavarino. Adaptivity in space and time for reaction-diffusion systems in electrocardiology. *SIAM J. Sci. Comput*, 28:942–962, 2006.

T. Fritz, C. Wieners, G. Seemann, H. Steen, and O. Dössel. Simulation of the contraction of the ventricles in a human heart model including atria and pericardium. *Biomechanics and modeling in mechanobiology*, 13(3):627–641, 2014.

D. B. Geselowitz. On the theory of the electrocardiogram. *Proceedings of the IEEE*, 77(6):857–876, 1989.

S. H. Gilbert, A. P. Benson, P. Li, and A. V. Holden. Regional localisation of left ventricular sheet structure: integration with current models of cardiac fibre, sheet and band structure. *European journal of cardio-thoracic surgery*, 32(2):231–249, 2007.

R. Glowinski and P. Le Tallec. *Augmented Lagrangian and operator-splitting methods in nonlinear mechanics*, volume 9. SIAM, 1989.

S. Göktepe and E. Kuhl. Electromechanics of the heart: a unified approach to the strongly coupled excitation–contraction problem. *Computational Mechanics*, 45(2-3):227–243, 2010.

J. M. Gomes and R. W. dos Santos. *A Time Adaptive Scheme Based on the Rush-Larsen Method for Solving Cardiac Cell Models*, pages 896–899. Springer International Publishing, Cham, 2015. ISBN 978-3-319-13117-7. doi: 10.1007/978-3-319-13117-7_227. URL https://doi.org/10.1007/978-3-319-13117-7_227.

E. Grandi, F. S. Pasqualini, and D. M. Bers. A novel computational model of the human ventricular action potential and ca transient. *Journal of molecular and cellular cardiology*, 48(1):112–121, 2010.

J. M. Guccione, K. Costa, and A. D. McCulloch. Finite element stress analysis of left ventricular mechanics in the beating dog heart. *Journal of Biomechanics*, 28(10):pp. 1167–1177, 1995.

M. Gulliksson, X.-Q. Jin, and Y.-M. Wei. Perturbation bounds for constrained and weighted least squares problems. *Linear algebra and its applications*, 349(1-3):pp. 221–232, 2002.

C. Gupta, V. Palimar, A. Saxena, A. S. D'souza, et al. A morphometric study of measurements of heart in adults and its relation with age and height of the individual: A post-mortem study. *CHRISMED Journal of Health and Research*, 1(4):263, 2014.

V. Gurev, P. Pathmanathan, J.-L. Fattebert, H.-F. Wen, J. Magerlein, R. A. Gray, D. F. Richards, and J. J. Rice. A high-resolution computational model of the deforming human heart. *Biomechanics and modeling in mechanobiology*, 14(4):pp. 829–849, 2015.

M. Hadjicharalambous, J. Lee, N. P. Smith, and D. A. Nordsletten. A displacement-based finite element formulation for incompressible and nearly-incompressible cardiac mechanics. *Computer methods in applied mechanics and engineering,*, 274:pp. 213–236, 2014.

M. Hochbruck and A. Ostermann. Explicit exponential runge?kutta methods for semilinear parabolic problems. *SIAM J. Numer. Anal.*, 2005.

A. Hodgkin and A. Huxley. J physiol (lond). *A quantitative description of membrane current and its application to conduction and excitation in nerve*, 117: 500-544, 1952.

G. Holzapfel. *Nonlinear Solid Mechanics. A continuum approach for engineering*. J. Wiley and Sons, Chichester, 2000.

G. Holzapfel and R. Ogden. Constitutive modelling of passive myocardium: a structurally based framework for material characterization. *Computer Methods in Applied Mechanics and Engineering*, 367:3445–3475, 2009.

T. J. R. Hughes. *The finite element method, linear static and dynamic finite element analysis*. Prentice Hall, 2009. URL http://www.worldcat.org/isbn/9780521588348.

J. Humphrey, R. Strumpf, and F. Yin. Determination of a constitutive relation for passive myocardium: I. a new functional form. *Journal of biomechanical engineering*, 112(3):333–339, 1990.

W. Hundsdorfer and J. G. Verwer. *Numerical solution of time-dependent advection-diffusion-reaction equations*, volume 33. Springer Science & Business Media, 2013.

P. J. Hunter, M. Nash, and G. Sands. Computational electromechanics of the heart. *Computational biology of the heart*, 12:347–407, 1997.

R. Kannan. An implicit lu-sgs spectral volume method for the moment models in device simulations: Formulation in 1d and application to ap-multigrid algorithm. *International Journal for Numerical Methods in Biomedical Engineering*, 27(9):1362–1375, 2011.

R. Kannan and Z. J. Wang. A study of viscous flux formulations for a p-multigrid spectral volume navier stokes solver. *Journal of Scientific Computing*, 41(2):165, 2009.

L. V. Kantorovich. Functional analysis and applied mathematics. *Uspekhi Matematicheskikh Nauk*, 3(6):89–185, 1948.

J. Keener and A. Panfilov. Three-dimensional propagation in the heart: the effects of geometry and fiber orientation on propagation in myocardium. *Cardiac Electrophysiology: From Cell to Bedside*, pages 335–347, 1995.

J. Keener and J. Sneyd. *Mathematical Physiology: II: Systems Physiology*. Interdisciplinary Applied Mathematics. Springer, 2nd edition, 2008a.

J. Keener and J. Sneyd. *Mathematical Physiology: I: Cellular Physiology*. Interdisciplinary Applied Mathematics. Springer, 2nd edition, 2008b.

J. P. Keener. An eikonal-curvature equation for action potential propagation in myocardium. *Journal of mathematical biology*, 29(7):629–651, 1991.

D. U. Keller, O. Jarrousse, T. Fritz, S. Ley, O. Dossel, and G. Seemann. Impact of physiological ventricular deformation on the morphology of the t-wave: a hybrid, static-dynamic approach. *IEEE Transactions on Biomedical Engineering*, 58(7):2109–2119, 2011.

C. T. Kelley. *Solving nonlinear equations with Newton's method*. SIAM, 2003.

R. C. Kerckhoffs, M. L. Neal, Q. Gu, J. B. Bassingthwaighte, J. H. Omens, and A. D. McCulloch. Coupling of a 3d finite element model of cardiac ventricular mechanics to lumped systems models of the systemic and pulmonic circulation. *Annals of biomedical engineering*, 35(1): 1–18, 2007.

R. Klabunde. *Cardiovascular physiology concepts*. Lippincott Williams & Wilkins, 2011.

P. Kohl, P. Hunter, and D. Noble. Stretch-induced changes in heart rate and rhythm: clinical observations, experiments and mathematical models. *Progress in biophysics and molecular biology*, 71(1):91–138, 1999.

D. Krause. *Scalable space-time adaptive simulation tools for computational electrocardiology*. PhD thesis, Università della Svizzera italiana, 2013.

D. Krause, M. Potse, T. Dickopf, R. Krause, A. Auricchio, and F. W. Prinzen. Hybrid parallelization of a large-scale heart model. In R. Keller, D. Kramer, and J.-P. Weiss, editors, *Facing the Multicore-Challenge II*, volume 7174 of *Lecture Notes in Computer Science*, pages 120–132. Springer, 2012.

R. Krause and P. Zulian. A parallel approach to the variational transfer of discrete fields between arbitrarily distributed unstructured finite element meshes. *SIAM Journal on Scientific Computing*, 38(3):C307–C333, 2016.

S. Krogstad. Generalized integrating factor methods for stiff pdes. *J. of Comp. Phys.*, pages 203(1):72–88, 2005.

S. Land, S. A. Niederer, and N. P. Smith. Efficient computational methods for strongly coupled cardiac electromechanics. *IEEE Transactions on Biomedical Engineering,*, 59(5):pp. 1219–1228, 2012.

S. Land, V. Gurev, S. Arens, C. M. Augustin, L. Baron, R. Blake, C. Bradley, S. Castro, A. Crozier, M. Favino, et al. Verification of cardiac mechanics software: benchmark problems and solutions for testing active and passive material behaviour. *Proc. R. Soc. A*, 471(2184):20150641, 2015a.

S. Land, S. A. Niederer, P. Lamata, and N. P. Smith. Improving the stability of cardiac mechanical simulations. *IEEE Transactions on Biomedical Engineering*, 62(3):939–947, 2015b.

D. J. Lawson. Generalized runge-kutta processes for stable systems with large lipschitz constants. *SIAM J. Numer. Anal.*, pages 4:372–380, 1967.

G. E. Leenders, J. Lumens, M. J. Cramer, B. W. De Boeck, P. A. Doevendans, T. Delhaas, and F. W. Prinzen. Septal deformation patterns delineate mechanical dyssynchrony and regional differences in contractility: analysis of patient data using a computer model. *Circulation: Heart Failure*, 5(1):87–96, 2012.

I. LeGrice, B. Smaill, L. Chai, S. Edgar, et al. Laminar structure of the heart: ventricular myocyte arrangement and connective tissue architecture in the dog. *American Journal of Physiology - Heart and Circulatory Physiology*, 269(2):H571–H582, 1995.

I. LeGrice, P. Hunter, A. Young, and B. Smaill. The architecture of the heart: a data–based model. *Philosophical Transactions of the Royal Society of London A: Mathematical, Physical and Engineering Sciences*, 359(1783):1217–1232, 2001a.

I. LeGrice, P. Hunter, A. Young, and B. Smaill. The architecture of the heart: a data–based model. *Philosophical Transactions of the Royal Society of London A: Mathematical, Physical and Engineering Sciences*, 359(1783):1217–1232, 2001b.

I. J. LeGrice, P. J. Hunter, and B. Smaill. Laminar structure of the heart: a mathematical model. *American Journal of Physiology-Heart and Circulatory Physiology*, 272(5):H2466–H2476, 1997.

C. Liang, R. Kannan, and Z. Wang. A p-multigrid spectral difference method with explicit and implicit smoothers on unstructured triangular grids. *Computers & fluids*, 38(2):254–265, 2009.

D. Lin and F. Yin. A multiaxial constitutive law for mammalian left ventricular myocardium in steady-state barium contracture or tetanus. *Journal of biomechanical engineering*, 120(4): 504–517, 1998.

J. Lindenstrauss and D. Preiss. On Frèchet differentiability of Lipschitz maps between Banach spaces. *Annals of Mathematics*, 2003.

C. D. Lontsi, Y. C. , and C. Pierre. Efficient high order schemes for stiff odes in cardiac electrophysiology. *<hal-01445817>, https://hal.archives-ouvertes.fr/hal-01445817*, 2017.

C. Luo and Y. Rudy. A model of the ventricular cardiac action potential. depolarization, repolarization, and their interaction. *Circ Res.*, 68(6):1501–1526, 1991 Jun.

C. Luo and Y. Rudy. A dynamic model of the cardiac ventricular action potential. i. simulations of ionic currents and concentration changes. *Circ Res.*, 74(6):1071–1096, 1994.

J. N. Lyness. Numerical algorithms based on the theory of complex variable. In *Proceedings of the 1967 22nd national conference*, pages 125–133. ACM, 1967.

J. N. Lyness and C. B. Moler. Numerical differentiation of analytic functions. *SIAM Journal on Numerical Analysis*, 4(2):202–210, 1967.

M. M. Potse, , B. Dubé, et al. A comparison of monodomain and bidomain reaction-diffusion models for action potential propagation in the human heart. *IEEE Trans. Biomed. Eng.*, 53(12): 2425–2435, 2006.

J. E. Marsden and T. J. Hughes. *Mathematical foundations of elasticity*. Courier Corporation, 1994a.

J. E. Marsden and T. J. R. Hughes. *Mathematical Foundation of Elasticity*. Dover editions, 1 edition, 1994b.

J. R. Martins, P. Sturdza, and J. J. Alonso. The complex-step derivative approximation. *ACM Transactions on Mathematical Software (TOMS)*, 29(3):245–262, 2003.

R. Mcfee and F. D. Johnston. Electrocardiographic leads: I. introduction. *Circulation*, 8(4):554–568, 1953.

B. V. Minchev and W. M. Wright. A review of exponential integrators for first order semi-linear problems. *Norges Teknisk-Naturvitenskapelige Universitet*, Preprint Numerics No. 2, 2005.

R. Mittal, J. H. Seo, V. Vedula, Y. J. Choi, H. Liu, H. H. Huang, S. Jain, L. Younes, T. Abraham, and R. T. George. Computational modeling of cardiac hemodynamics: Current status and future outlook. *Journal of Computational Physics*, 305:1065–1082, 2016.

P. Nardinocchi and L. Teresi. On the active response of soft living tissues. *Journal of Elasticity*, 88 (1):27–39, 2007.

M. P. Nash and A. V. Panfilov. Electromechanical model of excitable tissue to study reentrant cardiac arrhythmias. *Progress in biophysics and molecular biology*, 85(2-3):501–522, 2004.

U. C. Nguyên, M. Potse, F. Regoli, M. L. Caputo, G. Conte, R. Murzilli, S. Muzzarelli, T. Moccetti, E. G. Caiani, F. W. Prinzen, et al. An in-silico analysis of the effect of heart position and orientation on the ecg morphology and vectorcardiogram parameters in patients with heart failure and intraventricular conduction defects. *Journal of electrocardiology*, 48(4):617–625, 2015.

S. A. Niederer and N. P. Smith. An improved numerical method for strong coupling of excitation and contraction models in the heart. *Progress in biophysics and molecular biology*, 96(1-3): 90–111, 2008.

S. A. Niederer, E. Kerfoot, A. P. Benson, M. O. Bernabeu, O. Bernus, C. Bradley, E. M. Cherry, R. Clayton, F. H. Fenton, A. Garny, et al. Verification of cardiac tissue electrophysiology simulators using an n-version benchmark. *Philosophical transactions. Series A, Mathematical, physical, and engineering sciences*, 369(1954):4331, 2011.

D. Noble, A. Varghese, P. Kohl, and P. Noble. Improved guinea-pig ventricular cell model incorporating a diadic space, ikr and iks, and length-and tension-dependent processes. *Canadian Journal of Cardiology*, 14(1):123–134, 1998.

S. Nørsett. Master's thesis, university of oslo. *Numerisk integrasjon av stive likninger*, 1969.

T. O'Hara, L. Virág, A. Varró, and Y. Rudy. Simulation of the undiseased human cardiac ventricular action potential: model formulation and experimental validation. *PLoS computational biology*, 7(5):e1002061, 2011.

A. V. Panfilov, R. Keldermann, and M. Nash. Self-organized pacemakers in a coupled reaction-diffusion-mechanics system. *Physical review letters*, 95(25):258104, 2005.

P. Pathmanathan, S. Chapman, D. Gavaghan, and J. Whiteley. Cardiac electromechanics: the effect of contraction model on the mathematical problem and accuracy of the numerical scheme. *The Quarterly Journal of Mechanics & Applied Mathematics*, 63(3):375–399, 2010.

L. Pavarino, S. Scacchi, and S. Zampini. Newton-krylov-bddc solvers for nonlinear cardiac mechanics, 2015. ISSN 00457825. URL `http://hdl.handle.net/10754/561071`. The aim of this work is to design and study a Balancing Domain Decomposition by Constraints (BDDC) solver for the nonlinear elasticity system modeling the mechanical deformation of cardiac tissue. The contractionâĂŞrelaxation process in the myocardium is induced by the generation and spread of the bioelectrical excitation throughout the tissue and it is mathematically described by the coupling of cardiac electro-mechanical models consisting of systems of partial and ordinary differential equations. In this study, the discretization of the electro-mechanical models is performed by Q1 finite elements in space and semi-implicit finite difference schemes in time, leading to the solution of a large-scale linear system for the bioelectrical potentials and a nonlinear system for the mechanical deformation at each time step of the simulation. The parallel mechanical solver proposed in this paper consists in solving the nonlinear system with a Newton-Krylov-BDDC method, based on the parallel solution of local mechanical problems and a coarse problem for the so-called primal unknowns. Three-dimensional parallel numerical tests on different machines show that the proposed parallel solver is scalable in the number of subdomains, quasi-optimal in the ratio of subdomain to mesh sizes, and robust with respect to tissue anisotropy.

M. Perego and A. Veneziani. An efficient generalization of the rush-larsen method for solving electro-physiology membrane equations. *ETNA. Electronic Transactions on Numerical Analysis [electronic only]*, 35,, http://eudml.org/doc/232711:234–256, 2009.

C. S. Peskin. Fiber architecture of the left ventricular wall: An asymptotic analysis. *Communications on Pure and Applied Mathematics*, 42(1):79–113, 1989.

S. Pezzuto, J. Hake, and J. Sundnes. Space-discretization error analysis and stabilization schemes for conduction velocity in cardiac electrophysiology. *International journal for numerical methods in biomedical engineering*, 32(10):e02762, 2016.

S. Pezzuto, P. Kal'avskÃi, M. Potse, F. W. Prinzen, A. Auricchio, and R. Krause. Evaluation of a rapid anisotropic model for ecg simulation. *Frontiers in Physiology*, 8:265, 2017.

R. Plonsey. Volume conductor fields of action currents. *Biophysical journal*, page 4: p. 317, 1964.

M. Potse, D. Krause, L. Bacharova, R. Krause, F. W. Prinzen, and A. Auricchio. Similarities and differences between electrocardiogram signs of left bundle-branch block and left-ventricular uncoupling. *Europace*, 14(suppl_5):v33–v39, 2012.

M. Powell. A method for nonlinear constraints in minimization problems in optimization, 1969.

L. Priebe and D. J. Beuckelmann. Simulation study of cellular electric properties in heart failure. *Circulation research*, 82(11):1206–1223, 1998.

A. J. Pullan, K. A. Tomlinson, and P. J. Hunter. A finite element method for an eikonal equation model of myocardial excitation wavefront propagation. *SIAM Journal on Applied Mathematics*, 63(1):324–350, 2002.

Z. Qu and A. Garfinkel. An advanced algorithm for solving partial differential equation in cardiac conduction. *IEEE Trans. Biomed. Eng.*, 46:11660–1168, 1999.

A. Quarteroni. *Numerical Models for Differential Problems*. Springer, 2009a.

A. Quarteroni. *Numerical modeling for differential problems*. Springer Milan, 4 edition, 2009b.

A. Quarteroni, T. Lassila, S. Rossi, and R. Ruiz-Baier. Integrated heart-coupling multiscale and multiphysics models for the simulation of the cardiac function. *Computer Methods in Applied Mechanics and Engineering*, 314:345–407, 2017.

D. R Gaston, C. Permann, J. Peterson, A. Slaughter, D. Andrs, Y. Wang, M. Short, D. M Perez, M. Tonks, J. Ortensi, L. Zou, and R. Martineau. Physics-based multiscale coupling for full core nuclear reactor simulation. 211, 11 2014.

R. Rasmusson, J. Clark, W. Giles, K. Robinson, R. Clark, E. Shibata, and D. Campbell. A mathematical model of electrophysiological activity in a bullfrog atrial cell. *American Journal of Physiology-Heart and Circulatory Physiology*, 259(2):H370–H389, 1990.

R. Rivlin. Large elastic deformations of isotropic materials iv. further developments of the general theory. *Phil. Trans. R. Soc. Lond. A*, 241(835):pp. 379–397, 1948.

J. M. Rogers and A. D. McCulloch. A collocation-galerkin finite element model of cardiac action potential propagation. *IEEE Transactions on Biomedical Engineering*, 41(8):743–757, 1994.

S. Rossi, R. Ruiz-Baier, L. F. Pavarino, and A. Quarteroni. Orthotropic active strain models for the numerical simulation of cardiac biomechanics. *International journal for numerical methods in biomedical engineering*, 28(6-7):761–788, 2012.

S. Rush and H. Larsen. A practical algorithm for solving dynamic membrane equations. *IEEE Trans. Biomed. Eng.*, pages p. 389–392, 1978.

R. S. Sampath and G. Biros. A parallel geometric multigrid method for finite elements on octree meshes. *SIAM Journal on Scientific Computing*, 32(3):1361–1392, 2010.

H. Saraf, K. Ramesh, A. Lennon, A. Merkle, and J. Roberts. Mechanical properties of soft human tissues under dynamic loading. *Journal of biomechanics*, 40(9):1960–1967, 2007.

H. Schmid, M. Nash, A. Young, and P. Hunter. Myocardial material parameter estimationâĂŤa comparative study for simple shear. *Journal of biomechanical engineering*, 128(5):742–750, 2006.

J. H. Seo and R. Mittal. Effect of diastolic flow patterns on the function of the left ventricle. *Physics of Fluids*, 25(11):110801, 2013.

N. Smith, M. Buist, et al. Altered t wave dynamics in a contracting cardiac model. *Journal of cardiovascular electrophysiology*, pages S203–S209, 2003a.

N. Smith, D. Nickerson, E. Crampin, and P. Hunter. Multiscale computational modelling of the heart. *Acta Numerica*, 13:371–431, 2004.

N. P. Smith, M. L. Buist, and A. J. Pullan. Altered t wave dynamics in a contracting cardiac model. *Journal of cardiovascular electrophysiology*, 14(s10), 2003b.

J. Sundnes, G. T. Lines, and A. Tveito. An operator splitting method for solving the bidomain equations coupled to a volume conductor model for the torso. *Math. Biosci*, 194 no. 2:233–248, 2005.

J. Sundnes, R. Artebrant, O. Skavhaug, and A. Tveito. A second-order algorithm for solving dynamic cell membrane equations. *IEEE Trans. Biomed. Eng.*, 56 no. 10:2546–2548, 2009.

L. Taber. On a nonlinear theory for muscle shells: part iiâĂŤapplication to the beating left ventricle. *Journal of biomechanical engineering*, 113(1):63–71, 1991.

L. A. Taber and R. Perucchio. Modeling heart development. *Journal of elasticity and the physical science of solids*, 61(1-3):165–197, 2000.

A. Tagliabue, L. Dede, and A. Quarteroni. Fluid dynamics of an idealized left ventricle: the extended nitsche's method for the treatment of heart valves as mixed time varying boundary conditions. *International Journal for Numerical Methods in Fluids*, 85(3):135–164, 2017a.

A. Tagliabue, L. Dede, and A. Quarteroni. Fluid dynamics of an idealized left ventricle: the extended nitsche's method for the treatment of heart valves as mixed time varying boundary conditions. *International Journal for Numerical Methods in Fluids*, 85(3):135–164, 2017b.

R. J. Tallarida, B. F. Rusy, and M. H. Loughnane. Left ventricular wall acceleration and the law of laplace. *Cardiovascular research*, 4(2):217–223, 1970.

P. L. Tallec. Numerical methods for nonlinear three-dimensional elasticity. In P. G. Ciarlet and J. L. Lions, editors, *Handbook of Numerical Analysis*, volume 3, pages 465 – 622. Elsevier, 1994. doi: http://dx.doi.org/10.1016/S1570-8659(05)80018-3. URL `http://www.sciencedirect.com/science/article/pii/S1570865905800183`.

K. ten Tusscher, D. Noble, P. Noble, and A. Panfilov. A model for human ventricular tissue. *American Journal of Physiology - Heart and Circulatory Physiology*, 286(4):H1573–H1589, 2004. ISSN 0363-6135. doi: 10.1152/ajpheart.00794.2003,http://ajpheart.physiology.org/content/286/4/H1573.

K. H. Ten Tusscher and A. V. Panfilov. Alternans and spiral breakup in a human ventricular tissue model. *American Journal of Physiology-Heart and Circulatory Physiology*, 291(3):H1088–H1100, 2006.

N. A. Trayanova, J. Constantino, and V. Gurev. Electromechanical models of the ventricles. *American Journal of Physiology-Heart and Circulatory Physiology*, 301(2):H279–H286, 2011.

L. Tung. A bi-domain model for describing ischemic myocardial d-c potentials. *PhD Thesis, MIT, Cambridge, MA*, 1978.

S. Vanka. Block-implicit multigrid solution of navier-stokes equations in primitive variables. *Journal of Computational Physics*, 65(1):138 – 158, 1986. ISSN 0021-9991. doi: https://doi.org/10.1016/0021-9991(86)90008-2.

R. Verfurth. A combined conjugate gradient-multi-grid algorithm for the numerical solution of the stokes problem. *IMA Journal of Numerical Analysis*, 4(4):pp. 441–455, 1984.

E. J. Vigmond, F. Aguel, and N. A. Trayanova. Computational techniques for solving the bidomain equations in three dimensions. 49(11):1260–1269, 2002.

C. T. Villongco, D. E. Krummen, P. Stark, J. H. Omens, and A. D. McCulloch. Patient-specific modeling of ventricular activation pattern using surface ecg-derived vectorcardiogram in bundle branch block. *Progress in biophysics and molecular biology*, 115(2-3):305–313, 2014.

T. Wakatsuki, M. S. Kolodney, G. I. Zahalak, and E. L. Elson. Cell mechanics studied by a reconstituted model tissue. *Biophysical journal*, 79(5):2353–2368, 2000.

H. Watanabe, S. Sugiura, H. Kafuku, and T. Hisada. Multiphysics simulation of left ventricular filling dynamics using fluid-structure interaction finite element method. *Biophysical journal*, 87(3):2074–2085, 2004.

B. I. Wohlmuth. A mortar finite element method using dual spaces for the lagrange multiplier. *SIAM journal on numerical analysis*, 38(3):989–1012, 2000.

F. Yin, C. Chan, and R. M. Judd. Compressibility of perfused passive myocardium. *American Journal of Physiology-Heart and Circulatory Physiology*, 271(5):H1864–H1870, 1996.

X. Zheng, J. Seo, V. Vedula, T. Abraham, and R. Mittal. Computational modeling and analysis of intracardiac flows in simple models of the left ventricle. *European Journal of Mechanics-B/Fluids*, 35:31–39, 2012.